Study of smart antennas and MU-MIMO techniques for indoor radio engineering and planning tools

Khouloud Issiali

Thèse

THESE INSA Rennes
sous le sceau de l'Université européenne de Bretagne
pour obtenir le titre de
DOCTEUR DE L'INSA DE RENNES
Spécialité : Electronique et Télécommunications

présentée par
Khouloud ISSIALI
ECOLE DOCTORALE : *MATISSE*
LABORATOIRE : *IETR*

Study of smart antennas and MU-MIMO techniques for indoor radio engineering and planning tools

Thèse soutenue le 08.12.2015
devant le jury composé de :

Geneviève Baudoin
Professeur, ESIEE - Noisy le Grand / Présidente
Karine Amis Cavalec
Maître de Conférences - HDR, Télécom Bretagne - Brest / Rapporteur
Alain Sibille
Professeur, Télécom Paris Tech / Rapporteur
Jean-François Diouris
Professeur, Ecole Polytechnique - Université de Nantes / Examinateur
Ali Louzir
Technical Manager, Technicolor R&D France - Cesson-Sévigné/ Examinateur
Valéry Guillet
Ingénieur de recherche, Orange Labs Belfort / Co-encadrant
Gheorghe Zaharia
Maître de Conférences, INSA de Rennes / Co-encadrant
Ghaïs El Zein
Professeur, INSA de Rennes / Directeur de thèse

Study of smart antennas and MU-MIMO techniques for indoor radio engineering and planning tools

Khouloud ISSIALI

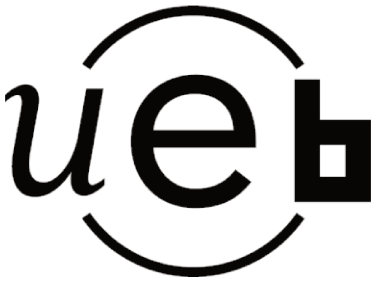

En partenariat avec

Abstract

The deployment facility and flexibility of wireless technologies have allowed considerable evolution of IEEE 802.11 standards. The arrival of the optical fiber to the home has further motivated research studies to increase data rates and capacity. In this context, the latest IEEE 802.11ac standard ratified in 2014 proposes new technologies to achieve maximum data rates above 1 Gbit/s. In particular, 802.11ac includes the Multi-User Multiple Input Multiple Output (MU-MIMO) and Transmit Beamforming (TxBF). These smart antenna technologies assume a variable transmit antenna pattern in function of the users' position and the corresponding multipath propagation channel characteristics. However, the current radio planning tools give a fixed coverage map independent of any adaptive or smart antenna processing.

This thesis studies the impact of the MU-MIMO and TxBF techniques on radio engineering, system optimization as well as radio planning tools. Indeed, the first part of this thesis deals with refining the sum rate capacity gains by identifying interesting system configurations and optimal system parameters (antenna spacing, tradeoff between antenna number and number of spatial streams, antenna arrangement...). The second part addresses the beamforming gains in terms of the Signal-to-Noise Ratio (SNR) gain and interference level to have realistic radio coverage modeling.

Hence, we have firstly analyzed the MU-MIMO to Single User MIMO (SU-MIMO) sum rate capacity gain based on the 802.11ac correlated MU-MIMO channel models. By analyzing the results, we have proposed system recommendations to optimize the MU-MIMO in a residential environment, mainly related to system configuration. We have also highlighted a relevant correlation coefficient which can be used to decide whether MU-MIMO or SU-MIMO is suitable and to select users in MU-MIMO group. Moreover, we have formulated the convex optimization problem of maximizing the capacity in a Multi-User Multiple Input Multiple Output (MU-MIMO) context with multiple receiving antennas taking into account the Equivalent Isotropically Radiated Power (EIRP) constraint for Wireless Local Area Network (WLAN) in Europe.

Secondly, we have conducted a 2-user Multiple-Input Multiple-Output (MIMO) propagation channel measurement campaign in a residential environment to confirm the obtained radio engineering and system optimization recommendations. We have been able to extend this study to other potential parameters which have influence on MU-MIMO to SU-MIMO capacity gain such as path loss and antenna array geometries.

Finally, we have evaluated the performance of TxBF by analyzing the Signal-to-Noise Ratio (SNR) gain as well as the interference reduction. This part identifies the system parameters which have the biggest influence on the realistic radio coverage simulation. It proposes a statistical modeling to predict the beamforming gains achieved by the antenna processing.

Keywords : MU-MIMO ; IEEE 802.11ac ; capacity ; antenna arrays ; indoor propagation measurements ; TGac channel models ; transmit beamforming ; EIRP.

Dedication

To my family...

To the memory of my mother Rachida DARIF...

A great women who has sacrificed so much for us, and whom I still miss every day...

To my father Ramdane ISSIALI...
To my brother Walid ISSIALI...

This humble work is a sign of my love for you...

Thank you...

Acknowledgements

This thesis took place in Orange Labs Belfort within the Wireless Engineering Propagation (WEP) team in the context of a CIFRE contract.

First of all, I would like to thank the team manager Daniel MILLI for welcoming me into the WEP team and offering me the opportunity to be a member of them. I would also like to express my gratitude to my advisor Dr Valery GUILLET for the faith he has shown in me. I am very grateful for his availability and encouragement from the early beginning to the manuscript writing.

I am most grateful to my advisors, Dr Ghais EL ZEIN and Dr Gheorghe ZAHARIA, for their feedback, advices and for guiding my work through these three years.

I would also like to express my appreciation to all the friends and people I met during my thesis : Mounir, Sabine, Jean-Claude, Philippe, Lionel, Patrice, Nadine, Michèle, Annie, Michel,Gilles...

I am most grateful to my husband, Marouane TADILI, for his love, his constant support and patience. Thank you for making my journey very pleasant and enjoyable.

I am especially grateful to my parents and my brother for their prayers and encouragements. Thank you for always supporting me, and being there for me even though we are a thousand miles apart.

Many thanks go to my special friend, Fatima Zara MOATAZ for her support and her unlimited kindness. You have made the good times better and the hard ones easier.

Contents

Résumé étendu en français

1 Introduction

Le contexte global de cette thèse est celui de la montée en débit au-delà de 500 Mbit/s, voire de 1 Gbit/s sur l'accès radio, notamment en environement résidentiel. Pour cela, différents standards sont en fin de normalisation, notamment le standard IEEE 802.11ac dans la bande 5 GHz. Pour répondre à ce besoin de montée en débit, de nouvelles techniques sont mises en œuvre comme l'utilisation de largeurs de bande plus importantes (jusqu'à 160 MHz), la formation de faisceaux connue sous "transmit beamforming (TxBF)" , puis, dans un second temps, l'utilisation du MIMO multi-utilisateurs (MIMO-MU) permettant une réutilisation spatiale du spectre. En outre, l'arrivée de la fibre optique a davantage motivé l'exploration de nouvelles solutions pour augmenter le débit au sein des réseaux locaux domestiques.

Pour réaliser l'ingénierie radio, les outils d'ingénierie actuels supposent tous que le réseau d'antennes de bornes Wi-Fi a un diagramme de rayonnement indépendant des positions des stations clientes et constant dans le temps. Les nouveaux systèmes MIMO-MU, ou même MIMO mono-utilisateur notés MIMO-SU avec "transmit beamforming" remettent en cause cette modélisation dans la mesure où le diagramme d'antennes formé devient dépendant du canal multi-trajets et de chacun des terminaux clients servis à un instant donné. L'objet de la thèse est d'analyser l'impact de ces nouvelles techniques MIMO sur l'ingénierie radio et notamment sur la modélisation des couvertures et des interférences pour contribuer à la conception de la prochaine génération d'outils d'ingénierie.

Le premier objectif de la thèse consiste à affiner les gains de capacité et surtout préciser les domaines d'emploi en indoor du MIMO-MU par rapport au MIMO-SU (lien en vue directe (LOS) ou avec obstacle (NLOS), comment constituer les groupes d'utilisateurs...). Les travaux s'appuient sur une modélisation réaliste du canal de propagation MIMO indoor, basée sur des canaux standardisés indoor dans un premier temps. Ensuite, une campagne de mesures a été réalisée au cours de cette thèse pour confirmer et compléter les résultats obtenus.

Le second objectif de la thèse consiste à identifier quelle modélisation de l'ensemble propagation, antennes et ses traitements, permettrait de simuler une couverture radio réaliste pour l'ingénierie de ces nouveaux systèmes (802.11ac) tant du critère de puissance reçue que des interférences.

2 Techniques MIMO-MU pour les réseaux locaux sans fil

Les communications sans fil utilisent le rayonnement des ondes dans un environnement donné par un émetteur (Tx). L'onde émise interagit avec l'environnement physique d'une manière complexe avant d'arriver au récepteur (Rx). En effet, l'onde se propage et est soumise à plusieurs phénomènes : réflexions, diffractions, transmissions... L'onde reçue dépend de l'environnement, de l'emplacement des objets et de l'activité humaine. Cet environnement souvent dynamique exige une analyse approfondie du canal de propagation radio afin d'estimer avec précision les paramètres des signaux reçus.

Pour tirer profit de la propagation multi-trajets à l'intérieur des bâtiments, les techniques MIMO ont fait l'objet d'une attention particulière. Celles-ci ont été proposées pour augmenter la capacité, en exploitant les propriétés spatiales du canal à trajets multiples. Ces techniques MIMO ont d'abord été étudiées dans des scénarios mono-utilisateur, puis étendues à des scénarios multi-utilisateurs. Dans ce contexte, la nouvelle norme IEEE 802.11ac finalisée en janvier 2014 normalise le MIMO-MU pour augmenter la capacité pour le sens descendant. Ce chapitre rappelle d'abord les caractéristiques principales de la couche physique de la nouvelle norme 802.11ac avant d'énumérer en détail les phénomènes de propagation influant le canal de propagation dans les reséaux sans fil. Ensuite, nous décrivons la liaison descendante MIMO-MU, les techniques de précodage proposées dans la littérature pour permettre la réutilisation spatiale et les capacités liées.

2.1 Le standard 802.11ac

La norme IEEE 802.11ac permet d'atteindre des débits allant jusqu'à $6,9$ Gbit/s au niveau de la couche physique pour la bande de 5 GHz. Par conséquent, cette norme est destinée aux services qui requièrent des débits élevés, tels que la télévision haute définition, l'affichage sans fil (interface multimédia haute définition (HDMI) sans fil), les stations d'accueil sans fil (connexion sans fil avec des périphériques), et autres. Ci-après, nous passons en revue quelques-unes des principales caractéristiques de la norme IEEE 802.11ac (Tableau 1).

2.2 Les techniques MIMO-MU

Dans les systèmes MIMO-MU, le point d'accès communique simultanément avec plusieurs terminaux clients en exploitant la dimension spatiale. Ceci est possible en utilisant la connaissance de chacun des canaux reliant les antennes de l'émetteur aux différentes antennes des récepteurs en s'appuyant sur la technique de "feedback" explicite. Dans le contexte MIMO-MU, l'émetteur doit gérer l'interférence inter utilisateurs. Pour ce faire, plusieurs méthodes, nommées méthodes de précodage, sont proposées dans la littérature. La diagonalisation par blocs, la plus étudiée, consiste premièrement à annuler l'interférence inter-utilisateurs, et ensuite à optimiser la capacité de chacun des liens. Les résultats proposés dans cette thèse se basent principalement sur cette technique vu

Bande de fréquence	5 GHz: environ 400 MHz du spectre disponible en Europe
Modulation	modulation d'amplitude en quadrature (MAQ): MAQ256, MAQ64...
Nombre maximum de flux spatiaux	8 flux spatiaux
Portée	selon environnement 35 m à 150 m
Largeur de bande	20/40/80, 160, and 80 + 80 MHz
Débit maximal	6, 9 Gbit/s obtenu avec: 160 MHz, 8 flux spatiaux, MAQ 256 avec un taux de codage $\frac{5}{6}$, et un intervalle de garde de 400 ns.

Table 1 – Caractéristiques du standard 802.11ac.

qu'elle offre des performances assez proches de la borne théorique de capacité appliquant le principe du "dirty paper coding".

3 Simulation de capacités multi-utilisateurs basées sur des canaux normalisés (TGac)

Dans ce paragraphe, nous considérons la liaison descendante d'un scénario MIMO-MU dans laquelle un point d'accès IEEE 802.11ac est équipé de plusieurs antennes dipôles (jusqu'à 10 antennes) et transmet à deux récepteurs, chacun avec deux antennes dipôles. Ce chapitre propose des recommandations pour optimiser les performances MIMO-MU en se basant sur les canaux standardisés pour 802.11ac (TGac). Tout d'abord, nous décrivons brièvement ce modèle. Ensuite, nous donnons les résultats numériques pour l'impact du nombre d'antennes d'émission sur le gain de capacité MIMO-MU par rapport au MIMO-SU. Nous expliquons les résultats obtenus en mettant en évidence un coefficient de corrélation qui décrit la similarité entre les canaux de deux utilisateurs. Enfin, nous formulons le problème d'optimisation de la capacité au sens Shannon du MIMO-MU en tenant compte de la contrainte de Puissance Isotrope rayonnée équivalente (PIRE). Il s'agit de la puissance répondant aux exigences de la réglementation européenne pour les réseaux WLAN dans la bande de fréquence 5 GHz: $PIRE \leq 23$ dBm pour la bande basse, $PIRE \leq 30$ dBm pour la bande haute.

3.1 Modèle TGac

Les modèles normalisés ou standardisés sont un outil important pour la conception des nouveaux systèmes radio. Ils permettent d'évaluer les avantages et les performances de différentes techniques (modulation, codage...) d'une manière unifiée. C'est dans ce cadre que les canaux 802.11 sont proposés pour les milieux indoor. Le modèle IEEE 802.11 TGn a été développé pour les canaux WLAN MIMO aux fréquences de 2.4 GHz

et 5 GHz, puis étendus au MIMO-MU (TGac). Le modèle 802.11 TGn est considéré comme étant un modèle utilisant une approche stochastique non-géométrique. La réponse impulsionnelle est décrite par une somme de clusters. Ce modèle compte six environnements de type «indoor» en LOS et NLOS comme les bureaux de grande et de petite surface, les maisons, appartements, ainsi que les espaces ouverts de type « open space ». Vu que le milieu considéré par le sujet de thèse concerne le résidentiel, nous avons basé nos simulations sur le modèle TGac-B. Celui-ci est composé de deux clusters. Chaque cluster se compose de 9 trajets (appelés « Taps ») séparés de 10 ns. A chaque trajet est associé un spectre Doppler, une loi de fading, un spectre de répartition de puissance (en azimut et en élévation) en émission et en réception généré selon une distribution de Laplace, avec un étalement angulaire variant de 20° à 40°. Le nombre de clusters ainsi que l'étalement des retards sont déduits de résultats de mesures. La figure 1 donne le profil de puissance moyenne pour ce modèle en fontion du temps de retard des taps. A noter que le modèle TGn, initialement destiné à

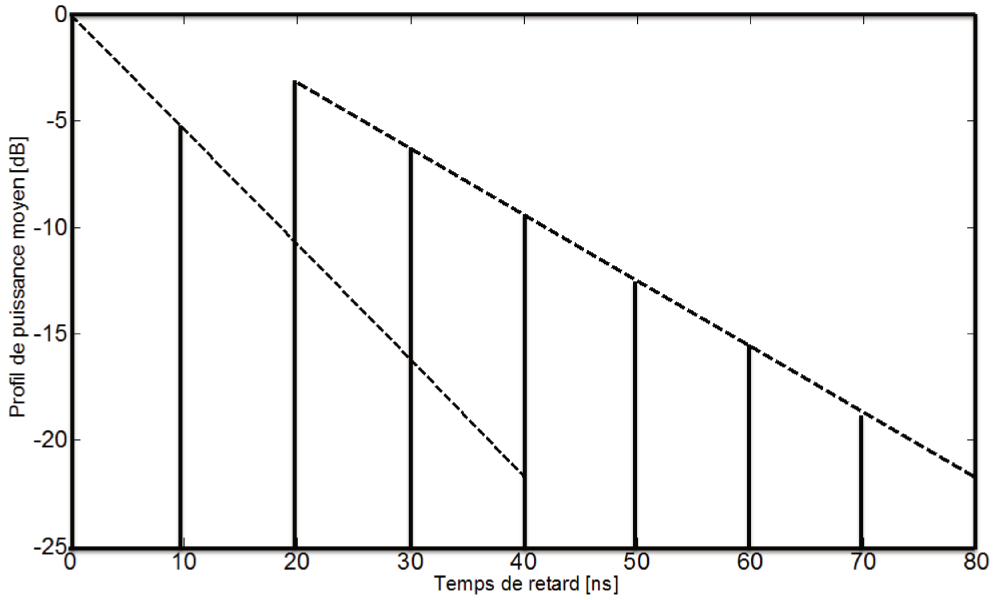

Figure 1 – Profil de puissance pour le modèle TGac-B en fontion du retard des taps.

simuler des canaux du 802.11n, a été étendu au nouveau standard 802.11ac en apportant des modifications au code Matlab. La caractéristique MIMO-MU est simulée en tirant aléatoirement deux indices pour simuler les deux canaux d'utilisateurs. Nous avons fixé à 100 le nombre de tirages alétoires pour avoir des résultats statistiques.

3.2 Nombre d'antennes d'émission et corrélation

Dans ce paragraphe, nous évaluons l'impact de l'augmentation du nombre d'antennes d'émission sur le gain de capacité MIMO-MU par rapport au MIMO-SU. Nous examinons ce gain de capacité en considérant que la répartition de la puissance totale d'émission est équitable entre les différents flux spatiaux et sous porteuses. Le SNR est défini comme le rapport entre puissance totale émise et la puissance du bruit, et est fixé ici à 20 dB. Le canal est normalisé pour avoir une atténuation moyenne de 0 dB. La figure 2 donne la moyenne du gain de capacité MIMO-MU par rapport au MIMO-SU en fonction du nombre d'antennes d'émission. On considère deux canaux: le canal normalisé TGac-B dans les conditions NLOS et le canal i.i.d Rayleigh décorrélé. Le graphe affiche les valeurs moyennes et les quantiles à 10% et 90% (q_{10} et q_{90}) servant à estimer l'intervalle de confiance. La première observation tirée de la figure 2 est que le gain de capacité MIMO-MU par rapport au MIMO-SU augmente lorsque le nombre d'antennes d'émission augmente. Le gain passe de $1,2$ à $1,65$ pour l'environnement résidentiel: jusqu'à 45% de gain de capacité. Nous observons également que le gain de capacité obtenu passant de $n_T = 4$ à $n_T = 6$ est plus élevé que celui observé en passant de $n_T = 6$ à $n_T = 8$. Ceci peut être expliqué par le fait que nous ne pouvons pas tirer profit du "transmit beamforming" lorsque $n_T = 4$, c'est à dire lorsque le nombre d'antennes d'émission est le même que le nombre total de flux spatiaux. Une autre explication concernant le coefficient de corrélation est donnée ci-après.

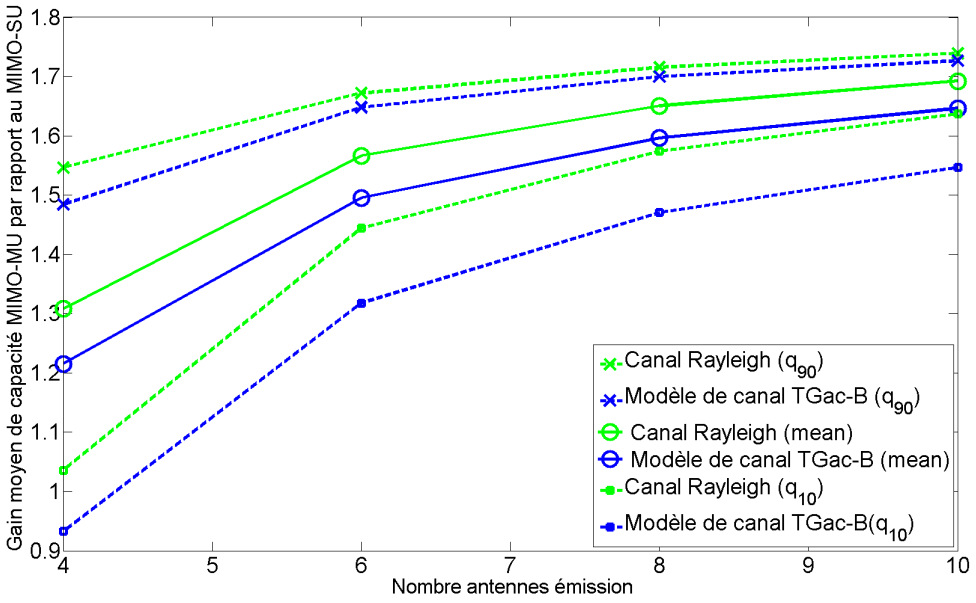

Figure 2 – Moyenne du gain de capacité MIMO-MU par rapport au MIMO-SU en fonction du nombre d'antennes d'émission.

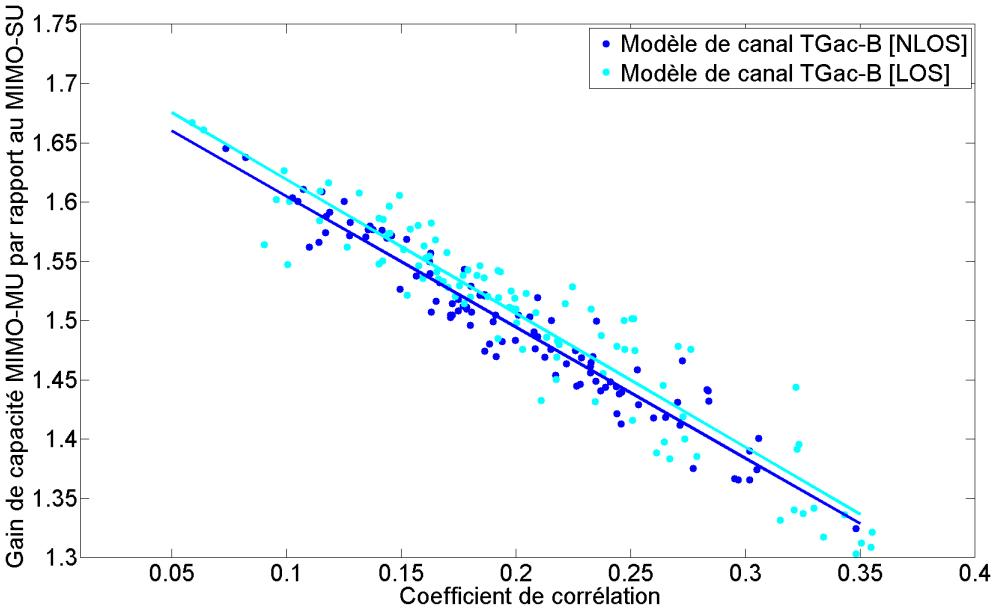

Figure 3 – La moyenne du gain de capacité MIMO-MU par rapport au MIMO-SU en fonction de la moyenne du coefficient de correlation($n_T = 6$).

Dans cette partie, nous définissons un coefficient de corrélation qui décrit le degré de similarité entre les canaux de 2 utilisateurs. La moyenne du gain de capacité MIMO-MU par rapport au MIMO-SU en fonction de la moyenne du coefficient de corrélation est donnée sur la figure 3. Le nombre d'antennes d'émission est égal à 6. La moyenne est calculée par rapport au temps, et chaque point représente l'un des 100 tirages de 2 utilisateurs. Lorsque le coefficient de corrélation augmente, le gain de capacité diminue: plus de 30% de capacité en moins lorsque le coefficient de corrélation passe de 0,05 à 0,35. En effet, lorsque les canaux des deux utilisateurs sont corrélés, l'algorithme de précodage se montre moins performant. Ce coefficient de corrélation a un autre avantage: il peut être utilisé comme critère pour regrouper les utilisateurs dans un scénario MIMO-MU. Enfin, une analyse basée sur la régression linéaire est effectuée: les résultats suggèrent une relation linéaire entre gain de capacité et corrélation. Le gain de capacité MIMO-MU par rapport à MIMO-SU estimé y' peut être exprimé en fonction de la corrélation x sous forme:

$$y' = a_1 x + a_0 \tag{1}$$

où y', a_1 et a_0 désignent respectivement le gain de capacité estimé, la pente de régression et l'ordonnée à l'origine. Dans le cas précis $n_T = 6$, les valeurs numériques sont listées dans le tableau 2.

Scenario	a_0	a_1	r	Root Mean Square Error (RMSE)
LOS	1.7319	-1.1290	0.9425	0.0379
NLOS	1.7153	-1.1046	0.9682	0.0226

Table 2 – Résultats numériques des paramètres de régression linéaire pour 6 antennes d'émission.

3.3 Contrainte de PIRE dans un contexte multi-utilisateurs

Le gain de capacité MIMO-MU par rapport au MIMO-SU est étudié en appliquant la contrainte de limitation de PIRE cette fois-ci. Deux méthodes de répartition de la puissance totatle d'émission sont analysées: répartition équitable et non de la puissance parmi les flux spatiaux. Dans notre formulation, nous étudions le cas de 2 utilisateurs, mais les résultats et les algorithmes présentés dans cette section peuvent être généralisés à n'importe quel nombre d'utilisateurs.

Les techniques MIMO-MU consistent à appliquer un précodage linéaire transmis aux flux spatiaux. Par conséquent, le diagramme d'antenne ainsi que son gain sont modifiés en fonction de l'emplacement d'utilisateurs et les paramètres de propagation. La valeur de PIRE est ainsi modifiée. La régulation européenne a fixé la PIRE dans les bandes de fréquence 5 GHz à 200 mW (bande basse) ou 1 W (bande haute). Cette contrainte peut être différente dans d'autres pays où elle est plutôt basée sur la puissance totale émise.

Nous avons formulé le problème de maximisation de capacité MIMO-MU sous la contrainte de la limitation de PIRE. La figure 4 présente les résultats du gain de capacité MIMO-MU par rapport au MIMO-SU pour les systèmes tenant compte ou non de la contrainte de PIRE. Les valeurs moyennes et les quantiles à 10% et 90% (q_{10} and q_{90}) servant à estimer l'intervalle de confiance sont représentés. Le cas où la contrainte de PIRE est considérée est noté *eirp-égal*. Nous notons le cas habituel où la puissance d'émission est directement liée au SNR par *basic*. Le rapport signal à bruit est fixé à 20 dB dans les deux cas. Le nombre d'antennes d'émission varie de 4 à 10. La figure 4 montre que le gain de capacité MIMO-MU augmente quand le nombre d'antennes d'émission augmente pour le modèle de canal TGac-B. Ce gain passe de 1,2 à 1,77 pour un système tenant compte de la contrainte de PIRE dans un milieu résidentiel, ce qui représente plus de 50% de gain de capacité. A noter que ce gain est égal à 45% pour un système ne tenant pas compte de la contrainte de PIRE (*basic*). Ces résultats montrent que l'augmentation du nombre d'antennes d'émission est également favorable au gain de capacité MIMO-MU par rapport au MIMO-SU pour des canaux corrélés en respectant la contrainte de PIRE.

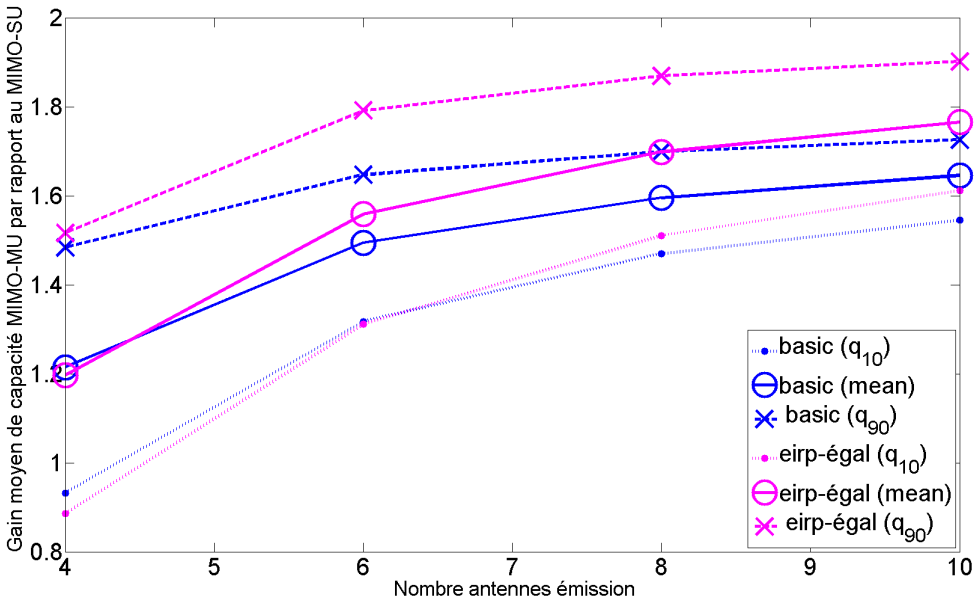

Figure 4 – La moyenne du gain de capacité MIMO-MU par rapport au MIMO-SU pour IEEE TGac-B channel (residential).

4 Capacité MIMO-MU en environment réel de type résidentiel

Ce chapitre présente les résultats numériques basés sur une campagne de mesures menée au cours de la thèse dans un environnement résidentiel typique rencontré au sein des réseaux domestiques. Afin d'avoir une comparaison significative, nous avons effectué une comparaison entre le modèle de canal TGac-B et de l'environnement mesuré. Le premier objectif de cette campagne de mesures est de confirmer les résultats précédents et de valider les conclusions d'ingénierie radio basées sur des modèles de canaux, puis d'étendre les résultats à différentes géométries de réseaux d'antennes et à d'autres paramètres de propagation comme l'atténuation. Nous avons également évalué l'impact de l'augmentation du nombre de flux spatiaux et des valeurs de SNR. Enfin, nous avons élaboré une étude comparative entre les résultats simulés et mesurés.

4.1 Campagnes de mesures

La Figure 5 montre l'environnement où nous avons mené la campagne de mesure: un milieu résidentiel. Il s'agit d'un appartement réel de 12 m ×7 m formé de matériaux et meubles européens. Le plafond est à 2,53 m. Les deux scénarios LOS et NLOS ont

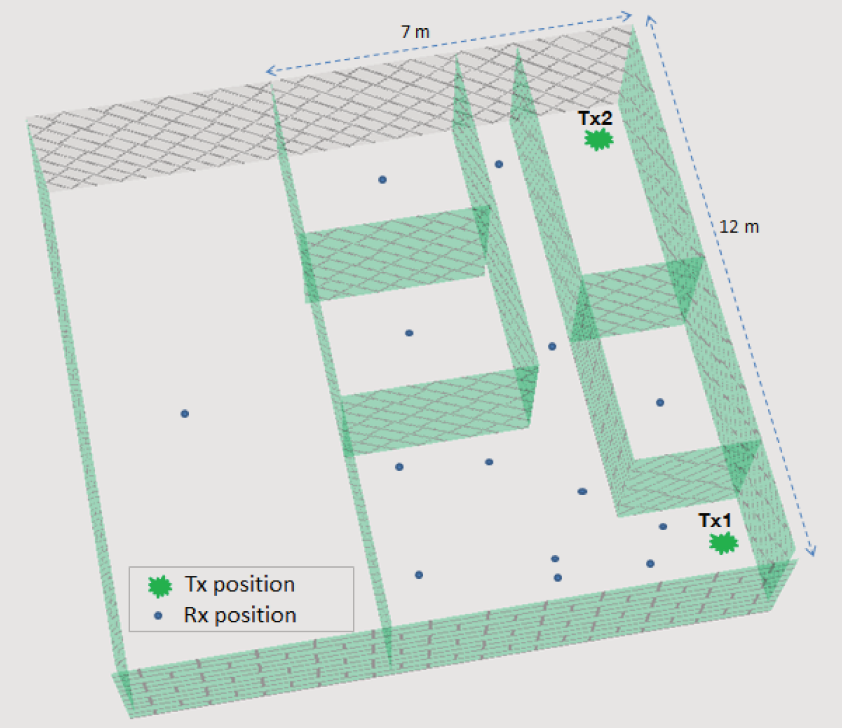

Figure 5 – L'environnement de mesure indoor, les 2 positions de l'émetteur et les 12 positions de réception.

été sondés. Cependant, seuls les résultats globaux sont présentés ci-après: des mesures en quantité plus importantes seraient nécessaires pour comparer les situations LOS / NLOS. Deux emplacements d'émetteur sont considérés, notés Tx_1 Tx_2. Pour chaque position d'émetteur, plusieurs emplacements de récepteurs sont évalués. Au cours des mesures, aucun meuble et aucune personne ne se déplace afin de maintenir les mêmes conditions de mesure. Enfin, la base de données de mesures obtenue correspond à 67 configurations différentes de 2 utilisateurs. Le canal MIMO-MU est sondé en collectant le paramètre S_{21} à l'aide d'un analyseur de réseau vectoriel. L'émetteur est équipé de 8 antennes espacées de $\frac{\lambda}{2}$ arrangées en un réseau linéaire uniforme et montées sur un bras tournant. Deux antennes sont placées sur les deux extrémités pour avoir des effets de couplage symétriques. Le bras tourne d'un pas de 6° permettant ainsi l'obtention d'un réseau virtuel de 480 antennes.

4.2 Géométrie de réseaux d'antennes

Dans cette partie, nous analysons l'effet de la géométrie réseaux de 8 antennes d'émission sur le système MIMO-MU avec deux récepteurs et deux antennes chacun. Le SNR est défini de manière à respecter la contrainte de PIRE, et est fixé à 20 dB.

Avant de comparer le gain de capacité MIMO-MU par rapport MIMO-SU, nous

définissons d'abord les types de géométries de réseaux d'antennes étudiés. Nous évaluons un Tx avec 8 antennes disposées en un réseau linéaire uniforme (ULA), un réseau circulaire croisé (CCA) avec $0,5$ λ d'espacement, et réseau circulaire irrégulier (ICA) avec différents rayons comme illustré sur la figure 6. Les résultats sont présentés en fonction du coefficient de corrélation entre canaux. A noter que nous ne tenons pas compte dans notre étude de l'effet de couplage à part pour ULA puisqu'il s'agit d'un réseau réel, les autres étant des réseaux virtuels.

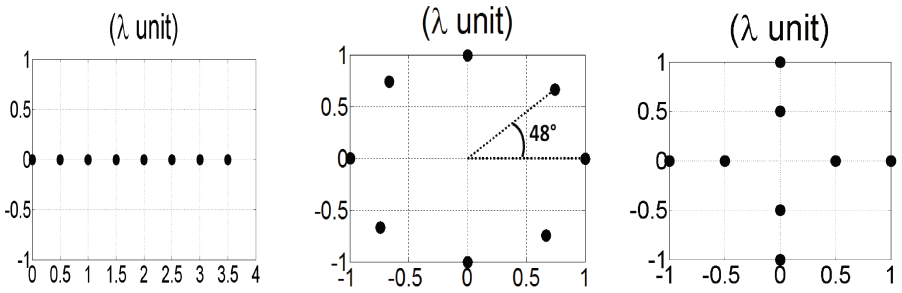

(a) ULA (b) ICA 1 λ (c) CCA

Figure 6 – Les différentes géométries de réseaux d'antennes Tx.

La Figure 7 donne la moyenne du gain de capacité MIMO-MU par rapport au MIMO-SU en fonction de la moyenne du coefficient de corrélation. Le gain le plus élevé est obtenu pour un réseau d'antennes CCA. Celui-ci montre des valeurs de corrélation relativement petites. Par conséquent, nous recommandons l'utilisation d'une géométrie CCA dans le cas d'un émetteur avec 8 antennes. En plus du gain élevé, et des valeurs de corrélation relativement faibles, CCA permet d'avoir un réseau d'antennes de taille réduite.

5 Analyse des gains de beamforming dans un milieu résidentiel

Le design radio joue un rôle primordial dans la conception et la plannification des nouveaux systèmes radio. Dans ce contexte, le logiciel Wireless Local Area Network Design et Analysis (WANDA), a été développé à Orange Labs Belfort. C'est un outil pour la conception et l'ingénierie de réseaux sans fil indoor. La couverture radio proposée par cet outil est fixe et indépendante de l'emplacement des récepteurs. Ce chapitre évalue la méthode du "transmit beamforming" côté émission en se basant sur les données de mesures collectées dans un contexte MIMO-SU. Par ailleurs, MIMO-SU devrait avoir plus de gain de "beamforming" par rapport au MIMO-MU à nombre d'antennes identiques. Nous avons utilisé deux métriques: le gain sur le SNR et la réduction d'interférence.

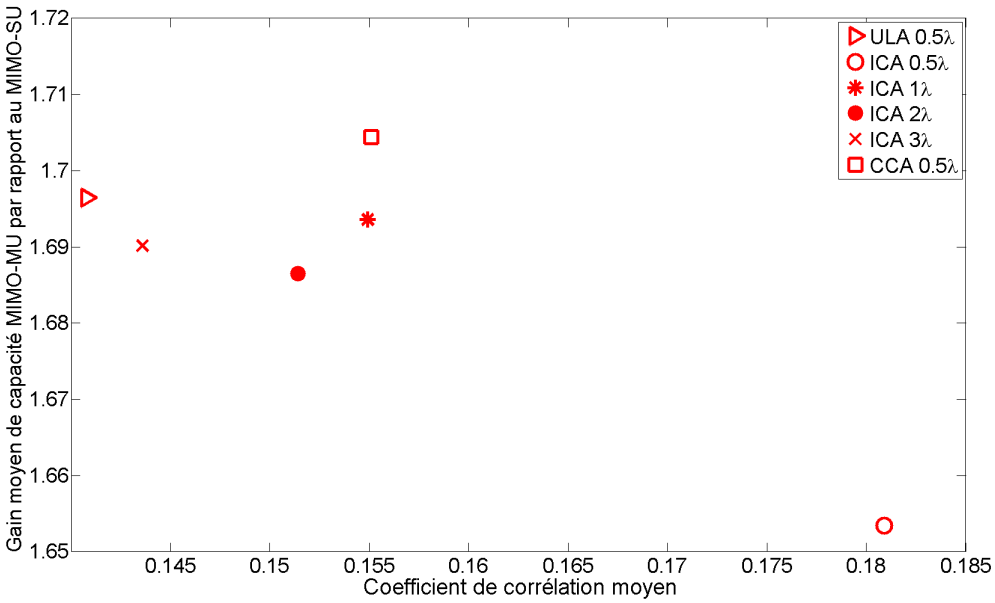

Figure 7 – Moyenne du gain de capacité MIMO-MU par rapport au MIMO-SU en fonction de la moyenne du coefficient de corrélation.

5.1 Gain de beamforming

Nous présentons le gain sur le SNR comme métrique d'évaluation du gain de "beamforming". Nous évaluons la capacité MIMO en respectant la contrainte de la limitation de PIRE: $PIRE = 23$ dBm et en variant les valeurs d'atténuation de canal pour prendre en compte différentes valeurs de SNR. En effet, en utilisant les 67 configurations différentes de 2 utilisateurs, nous avons normalisé le canal pour avoir des atténuations comprises dans l'intervalle: $[\![45 \text{ dB}, 110 \text{ dB }]\!]$. Pour chaque valeur d'atténuation, on simule la valeur médiane de la capacité MIMO. En tenant compte de la tendance linéaire décroissante des valeurs médianes de capacités en fonction du path loss, nous avons appliqué une régression linéaire comme le montre l'exemple Figure 8. La figure montre les valeurs médianes de capacité MIMO avec et sans "transmit beamforming" pour un système avec deux antennes à l'émission, une antenne en réception et un flux spatial en fonction de l'atténuation moyenne de propagation. Le gain sur le SNR est défini comme la différence entre les deux droites de régression en dB comme montre la figure.

Le gain sur le SNR a été évalué pour différentes configurations en fonction du nombre d'antennes d'émission et de réception. La Figure 9 donne le gain sur le SNR en fonction du nombre d'antennes d'émission pour un seul flux spatial. Le gain sur le SNR augmente avec l'augmentation du nombre d'antennes d'émission, alors qu'il diminue lorsque le nombre d'antennes de réception augmente. Outre, la figure 9 montre qu'il y a toujours

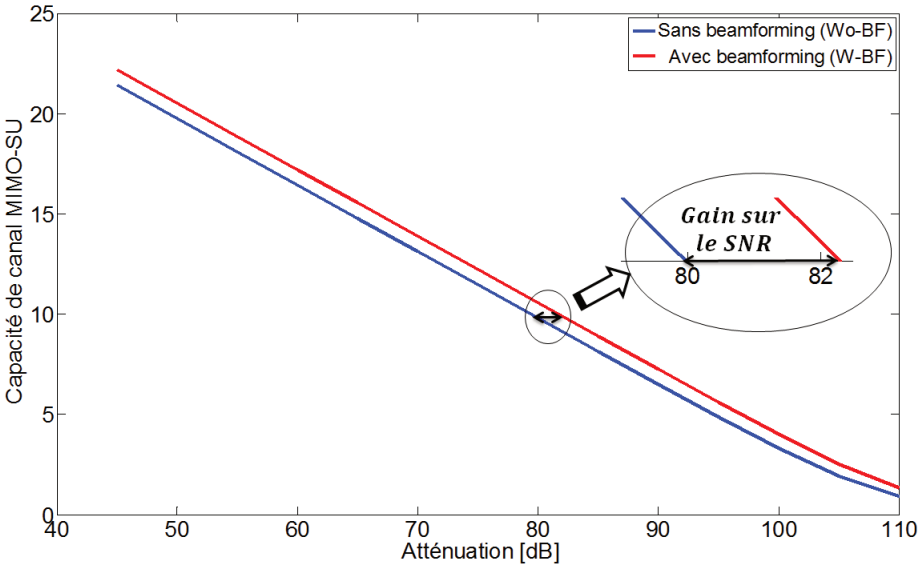

Figure 8 – Gain moyen de SNR obtenu en activant TxBF.

un gain de "beamforming" même en appliquant la contrainte de PIRE, ce qui peut s'expliquer par une recombinaison optimisée des multitrajets, même si la PIRE ne change pas avec TxBF. Ce gain passe de 2 à 4 dB. Le gain le plus élevé de 6 dB de SNR est obtenu avec un émetteur équipé de 8 antennes d'émission et une antenne en réception. Par conséquent, nous pouvons profiter pleinement du "transmit beamforming" lorsque le nombre d'antennes d'émission est largement supérieur au nombre d'antennes de réception et au nombre de flux spatiaux, même avec une PIRE limitée et identique à un système sans TxBF.

5.2 Réduction d'interférence

Un aspect pertinent en relation avec la technique du "transmit beamforming" côté émission est sa capacité ou non à réduire les interférences dans les réseaux sans fil. Il modifie le rayonnement de l'émission et favorise le récepteur ciblé. Le "transmit beamforming" tel qu'utilisé par 802.11ac n'est pas cependant optimisé pour réduire les interférences. La puissance reçue et le niveau d'interférence sont des paramètres importants déterminant la qualité de transmission. Nous définissions une métrique appelée réduction d'interférence, calculée en fonction de la puissance reçue. On considère un système à deux utilisateurs. On applique le "transmit beamforming" vers le premier utilisateur, noté sur la Figure 10 comme *targeted user*. Nous relevons la puissance reçue par un deuxième récepteur noté *interfered user* dans les deux cas: cas où la méthode du "transmit beamfoming" est appliquée ou non au *targeted user*. La réduction d'interférence est obtenue pour le 2^{nd} utilisateur comme la différence entre la puissance reçue moyenne (exprimée en dB) par le second utilisateur avec et sans

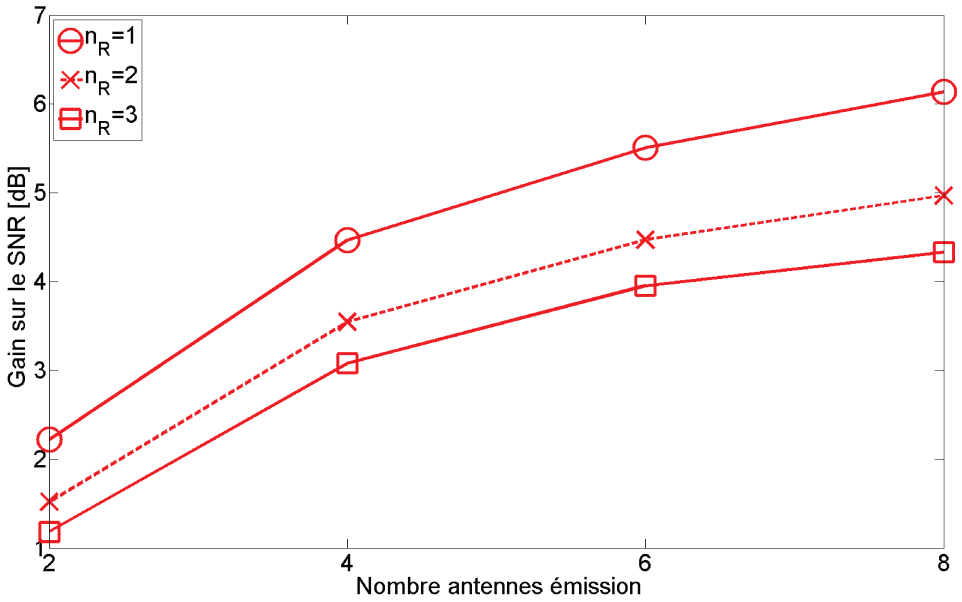

Figure 9 – Gain sur le SNR en fonction du nombre d'antennes d'émission pour $N_{ss} = 1$.

méthode du "transmit beamforming" appliquée au user 1.

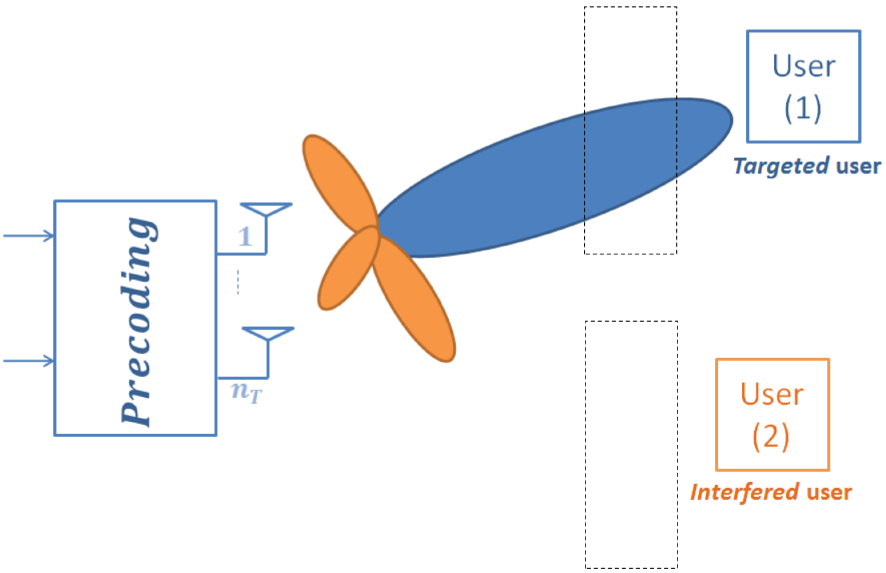

Figure 10 – Le schéma de caractérisation d'interférence.

La réduction d'interférence est évaluée en fonction du nombre d'antennes d'émission et de flux spatiaux. La Figure 11 donne la réduction d'interférence moyenne en fonction du gain moyen sur le SNR pour un réseau linéaire. L'augmentation du nombre d'antennes de transmission permet de diminuer le niveau d'interférence. Le niveau d'interférence est réduit de 1,5 dB à près de 3 dB lorsque le nombre d'antennes d'émission passe de 2 à 8 antennes. Cependant, l'augmentation du nombre d'antennes de réception n'a presque pas d'impact sur le niveau d'interférence. La valeur la plus élevée de réduction d'interférence, 3,5 dB, est obtenue dans le cas d'un flux spatial, 3 antennes de réception, et 8 antennes d'émission.

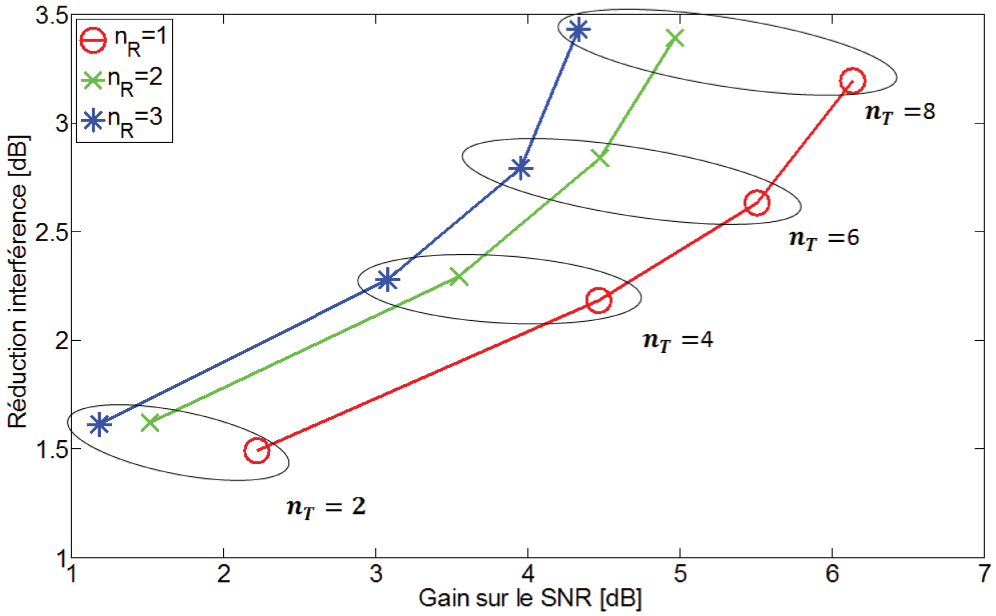

Figure 11 – La réduction d'interférence en fonction de la moyenne du gain sur le SNR pour $N_{ss} = 1$.

6 Conclusion et perspectives

Les technologies MIMO ont motivé ces dernières années de nombreux travaux de recherche pour leur potentiel à augmenter la capacité du canal. Les techniques MIMO-MU ont été proposées pour augmenter davantage cette capacité à travers la réutilisation spatiale. Cependant, à ce jour, aucune étude ne donne des résultats expérimentaux quant au choix de l'utilisation MIMO multi-utilisateurs ou mono-utilisateur dans un milieu résidentiel. En outre, aucune étude ne s'est intéressée à proposer une configuration optimale pour profiter pleinement de ces techniques. Par ailleurs, aucun modèle n'est proposé à ce jour pour les outils d'ingénierie radio actuels qui ignorent les traitements d'antennes adaptatives du côté de l'émission dans la simulation de couverture radio.

Dans cette thèse, nous avons abordé les problématiques ci-dessus liées aux techniques MIMO-MU et aux antennes intelligentes.

Tout d'abord, nous avons résumé les caractéristiques de la nouvelle norme 802.11ac ainsi que les mécanismes de base de la propagation radio. Les différents modèles de canaux MIMO ont également été présentés. En particulier, nous avons détaillé le canal TGac utilisés pour nos simulations. Ensuite, nous avons décrit un modèle de système MIMO-MU, les techniques de précodage et les méthodes de calcul de capacités.

Ensuite, nous avons proposé des recommandations pour optimiser les performances MIMO-MU en se basant sur les canaux standardisés TGac. Ces recommandations sont données en termes de paramètres systèmes/antennes et de la disposition des utilisateurs: LOS, NLOS... Tout d'abord, nous avons détaillé le processus des de simulation, le modèle de canal évalué et ses paramètres. Ensuite, nous avons fourni les résultats de gain de capacité MIMO-MU par rapport au MIMO-SU en fonction des configurations d'antennes et des paramètres de canaux de propagation. Enfin, nous avons mené une étude sur ces gains de capacité en tenant compte de la contrainte de la PIRE. En particulier, nous avons démontré qu'une légère augmentation du nombre d'antennes d'émission par rapport au nombre total de flux spatiaux transmis améliore significativement le gain en capacité MIMO-MU sur MIMO-SU. Nous avons également mis en évidence une définition de la corrélation des canaux correspondant qui est utile pour décider si MIMO-MU apporte plus de capacité que le MIMO-SU. Ce paramètre permettrait de sélectionner les utilisateurs dans un groupe d'utilisateurs MIMO-MU, et également d'optimiser la conception des antennes MIMO. Ensuite, nous avons formulé le problème d'optimisation de la capacité MU-MIMO en tenant compte de la contrainte de la PIRE. Nous avons montré que la technique de précodage MIMO-MU tire profit de la contrainte de la PIRE.

Nous avons ensuite présenté les résultats d'une campagne de mesures réalisée au sein d'Orange Labs Belfort en utilisant un analyseur de réseau. Cette campagne a été menée au cours de la thèse dans un environnement résidentiel typique des réseaux domestiques. Le premier objectif de cette campagne de mesures était de confirmer les résultats précédents et ainsi valider les conclusions d'ingénierie radio basées sur des modèles de canaux, puis d'étendre ces résultats à différentes géométries de réseaux d'antennes et à d'autres paramètres potentiels tels que l'atténuation de propagation. Les résultats obtenus confirment les recommandations basées sur des simulations TGac. En outre, nous avons étendu ces conclusions en étudiant l'impact de la configuration des antennes de réception, le nombre de flux spatiaux et les valeurs de SNR. En particulier, l'augmentation du nombre d'antennes de réception augmente légèrement le gain en capacité du MIMO-MU par rapport au MIMO-SU. En outre, la sélection de différentes antennes de réception n'a pas d'impact significatif sur ce gain de capacité. Ensuite, nous avons évalué l'atténuation du canal et son impact sur le gain de capacité MU-MIMO en utilisant différentes méthodes d'accès au canal. Une différence d'atténuation entre récepteurs peut être bénéfique pour le gain de capacité MIMO-MU par rapport au MIMO-SU selon le type de la méthode d'accès.

Enfin, le dernier chapitre évalue la méthode du "transmit beamforming" en se basant sur les données de mesure dans un contexte MIMO-SU. Pour évaluer les

performances de cette technique, nous avons défini deux métriques: le gain sur le SNR et la réduction d'interférence. Plusieurs configurations MIMO (nombre d'antennes émettrices et réceptrices, nombre de flux spatiaux, géométries de réseaux d'antennes) ont été comparées pour identifier celle qui fournit les meilleurs gains sur le SNR. En particulier, nous avons prouvé que l'augmentation du gain sur le SNR est possible lorsque nous augmentons le nombre d'antennes d'émission, diminuons le nombre d'antennes de réception, ou diminuons le nombre de flux spatiaux. Ces conclusions permettraient d'ajouter les gains de "beamforming" aux cartes de couverture simulées par les outils d'ingénierie actuels. En outre, nous avons cherché à savoir si l'introduction de cette technique de "transmit beamforming" pourrait augmenter ou réduire l'effet des interférences générées par un lien interférant. Nous avons pu montrer qu'utiliser la technique de "transmit beamforming" peut réduire dans certaines directions les interférences.

Les travaux de cette thèse pourraient être poursuivis par le développement des points suivants:

- Cette thèse suppose que l'émetteur connaît parfaitement le canal. Il est donc pertinent d'évaluer l'impact d'une estimation imparfaite du canal sur les résultats obtenus.
- Une analyse approfondie des caractéristiques spatiales du canal de propagation (direction du départ, direction d'arrivée) permettrait une comparaison plus poussée des résultats des modèles de canal MIMO et de la campagne de mesure.
- Il serait intéressant de mener une campagne de mesures avec un réseau d'antennes compact incluant ainsi l'effet de couplage des antennes. Dans notre campagne de mesures, nous avons évalué le seul cas avec 8 antennes d'émission disposées en réseau linéaire uniforme, les autres géométries se basant sur des réseaux virtuels.
- Il serait possible d'aller plus loin dans l'analyse des tirages aléatoires des 8 antennes d'émission pour proposer une géométrie de réseaux optimisée à 8 antennes et la tester dans d'autres environnements résidentiels pour généraliser les résultats.
- Il est pertinent de développer un algorithme rapide simulant le traitement d'antenne pour l'associer à un canal simulé par tracé/lancer de rayons afin de prédire les gains de "transmit beamforming" en chaque point de la carte de couverture au lieu d'une correction statistique globale.

Acronyms

AoA	Angle of Arrival
AoD	Angle of Departure
AP	Access Point
AS	Angular Spread
BC	Broadcast Channel
BD	Block Diagonalization
BER	Bit Error Rate
BF	Beamforming
BS	Base Station
CSD	Cyclic Shift Delay
CCA	Crossed Circular Array
CDF	Cumulative Distribution Function
CI	Channel Inversion
CIR	Channel Impulse Response
CFR	Channel Frequency Response
CSI	Channel State Information
CSIT	Channel State Information at the Transmitter
CSMA/CA	Carrier Sense Multiple Access/Collision Avoidance
DL	Downlink
DS	Delay Spread
DPC	Dirty Paper Coding
EIRP	Equivalent Isotropically Radiated Power
GI	Guard Interval
i.i.d.	independent and identically distributed
IP	Internet Protocol
ICA	Irregular Circular Array
IDC	International Data Corporation

IUI	Inter User Interference
ISI	Inter-Symbol Interference
LOS	Line-Of-Sight
MIMO	Multiple-Input Multiple-Output
MU-MIMO	Multi-User Multiple Input Multiple Output
MCS	Modulation and Coding Schemes
NLOS	Non-Line-Of-Sight
OFDM	Orthogonal Frequency-Division Multiplexing
PAS	Power Angular Spectrum
PAPR	Peak-to-Average Power Ratio
per-SS	per-Spatial Stream
PHY	PHYsical layer
PDP	Power Delay Profile
PDS	Power Delay Spectrum
QAM	Quadrature Amplitude Modulation
Rx	receiver
RMS	Root Mean Square
RMSE	Root Mean Square Error
RCI	Regularized Channel Inversion
SISO	Single-Input Single-Output
SINR	Signal-to-Interference-plus-Noise Ratio
SNR	Signal-to-Noise Ratio
SS	Spatial Stream
SU-MIMO	Single User MIMO
SVD	Singular Value Decomposition
Tx	transmitter
TxBF	Transmit Beamforming
UL	Uplink
ULA	Uniform Linear Array
TDMA	Time Division Multiple Access
THP	Tomlinson-Harashima Precoding
VNA	Vector Network Analyzer
VHT	Very High Throughput
VP	Vector Perturbation
Wo-BF	Without Beamforming
W-BF	With Beamforming
Wi-Fi	Wireless Fidelity
WLAN	Wireless Local Area Network

List of Figures

List of Tables

Notation

We briefly summarize below the main notations used throughout this report. Wherever possible, we have tried to keep the same notations from one chapter to another. The matrices and vectors are indicated with boldface.

t	Time
τ	Delay
f	Frequency
$\mathbf{H}_k$	Channel matrix for user k (Transfer channel function at a given frequency)
$\mathbf{W}_k$	Precoding matrix for user k
$diag(\mathbf{v})$	Diagonal matrix formed using the vector $\mathbf{v}$
$diag(\mathbf{M})$	Diagonal matrix formed using the diagonal of matrix $\mathbf{M}$
$*$	Convolution
$(.)^T$	Transposition
$\|\| . \|\|$	Vector norm-2
$\| . \|$	Absolute value
$\bar{(.)}$	Complex conjugate
$(.)^H$	Transpose conjugate
$E(.)$	Expectation || Mean
$\|\| . \|\|_F$	Frobenius norm
N	Number of 802.11ac subcarriers
n_T	Number of transmitting antennas
n_R	Number of receiving antennas
n_{R_k}	Number of receiving antennas for the k^{th} user
K	Number of users
k	User index running from 1 to K
$trace()$	Trace
$\mathbf{H}^\dagger$	Pseudo inverse
$\mathbf{I}$	Identity matrix

Chapter 1

Introduction

Contents

1.1 Context

Wireless communication is one of the most vibrant, challenging and interesting areas in the communication field today. Over the past two decades, wireless technologies have thrived and have even become standard for household and office appliances. The deployment facility and freedom of movement they enable have made them a very attractive solution for setting up local access networks.

The Enterprise Wireless Local Area Network (WLAN) market has become highly competitive and the vendors are proposing vast offerings and unique solutions. WLAN is affordable, easy to deploy and manage. That is why, recent trends in the industry have shown increase in the demand for enterprise WLAN. According to the International Data Corporation (IDC) [1], the Worldwide WLAN Market has shown solid growth (12.8%) in the third Quarter of 2013 [3]. Also, the overall WLAN market revenues are forecast to exceed 11 billion in 2017 and nearly 50 percent greater than 2012 revenues, according to Dell'Oro Group [4](this growth includes deployment of the 802.11ac upgrade cycle). In home networks, more than 10 millions of residential gateways are deployed in France.

The major standards for WLANs are the Institute of Electrical and Electronics Engineers (IEEE) 802.11 family, commonly known as Wireless Fidelity (Wi-Fi). Since its 1997 initial specification, the IEEE 802.11 standard has gone through several

1. IDC is the premier global provider of market intelligence, advisory services, and events for the information technology, telecommunications, and consumer technology markets.

designations starting with the initial IEEE 802.11b till its emerging standard IEEE 802.11ac which has been recently ratified (final approval released in 2014).

This thesis is proposed in order to face the explosion of traffic demand, by exploring new solutions for home networks while taking benefit from high-speed on the radio access networks offered by the arrival of the optical fiber to home networks.

1.2 Motivations and objectives

The ability to accurately predict radio-propagation behavior for wireless communication systems, is becoming crucial to system design and radio planning. Depending on the type of transmitting and receiving antennas and the physical location of the access points, the range and throughput may vary significantly. However, current network planning tools and models assume each Access Point (AP) has an antenna pattern which is independent of users' positions and constant over time. The new MU-MIMO systems proposed in the 802.11ac standard, or even Single User MIMO (SU-MIMO) with Transmit Beamforming (TxBF), challenge this practice considering that the antenna pattern of a wireless system with smart antennas depends on multipath phenomenon. MU-MIMO technique is an enhanced form of the Multiple-Input Multiple-Output (MIMO) technology. Combined with TxBF, MU-MIMO enables an AP to transmit simultaneously multiple spatial streams to multiple users. This provides significant performance gains over the original MIMO technology. These techniques shape the overall pattern of the received signal towards the direction of the main propagation paths arriving to the targeted user, as depicted in Figure 1.1. This supposes a variable antenna pattern changing as a function of users' positions and traffic. Thereby, the study of the impact of these new MIMO technologies on radio engineering is necessary to describe the impact of antenna processing.

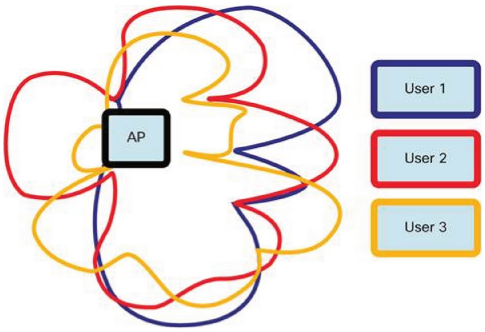

Figure 1.1 – MU-MIMO combined to TxBF techniques [1].

The purpose of this thesis is to analyze the impact of these new MIMO techniques on radio engineering, particularly on the modeling of radio coverage and interference. This would help in the design of the next generation of radio engineering tools. In

order to evaluate radio wave propagation in an indoor environment, various techniques may be used such as ray tracing launching technique, channel measurements and channel models. The 2D and 3D ray tracing models are both used widely in the literature. However, these techniques have not been normalized for MU-MIMO. Moreover, they would need very high computation time. The task group of 802.11ac (TGac) has designed standardized channel models for indoor wireless local area networks by including MU-MIMO techniques. We have first based our research approach on these standardized channel models. Since MU-MIMO TGac channel models are mainly based on measurement campaigns in Line-Of-Sight (LOS) scenarios like in offices [5][6][7][8], we have conducted afterwards a measurement campaign to confirm and complete our results based on TGac simulations. However, since the measurement equipment was not available until the end of the 2^{nd} year of this Ph.D work, the measurement analysis began at the end of 2014 and was hence scheduled for less than one year. With this constraint, we could not go further in the measurement analysis.

Thereby, in the first part of this thesis, the objective is to refine the capacity gains for indoor MU-MIMO compared to the SU-MIMO systems by identifying interesting system configurations (deployment recommendations such as LOS or Non-Line-Of-Sight (NLOS), impact of distances or other environmental parameters ..) and optimal system parameters (like number and arrangement of antennas, number of spatial streams, ..). The results are based on both a standardized MIMO channel modeling and a measurement campaign conducted in an indoor environment. This part concludes system and deployment recommendations. In the second part of the thesis, the objective is to define how smart antenna affects radio coverage and interference. This characterization could be included in radio planning tools. This part identifies the propagation parameters which have the biggest influence on the realistic radio coverage simulation in terms of received power and interference level.

1.3 Main contributions

During this thesis, we have focused our study on identifying the deployment recommendations or optimal system configuration of MU-MIMO techniques compared to SU-MIMO from a physical point of view. We have studied the impact of antennas and propagation channels on the Block Diagonalization (BD) capacity gain in home networks under a total transmitted power constraint. Note that the BD is a precoding technique that cancels the interference between users in a MU-MIMO context. We have also highlighted a relevant channel correlation definition that is useful to decide whether MU-MIMO outperforms SU-MIMO and to select the users into a MU-MIMO user group. We have formulated the optimization problem for computing capacity satisfying the Equivalent Isotropically Radiated Power (EIRP) constraint in MU-MIMO context. We have confirmed the results based on measured channels in a residential environment. The measurement campaign we have conducted, extended the study to various antenna array geometries, as well as path loss impact. Finally, we

have proposed a statistical model that describes the TxBF processing in terms of received power gain and interference reduction. Based on this model, we will be able to apply the beamforming gains in the upcoming radio planning tools.

1.4 Contents

The remainder of the report is divided as follows. In Chapter 2, we first introduce the fundamentals of WLAN. Afterwards, we give the new features implemented in the latest IEEE 802.11ac standard. We then present the basics of a wireless channel and an overview of the channel models. We finish by presenting the different MU-MIMO techniques and related capacity formulas. Chapter 3 analyzes and summarizes the recommendations based on IEEE 802.11ac standardized channel for a two-user case, taking or not into account the European regulation in terms of EIRP. In Chapter 4, we present the results based on our measurement campaign conducted in a residential environment. This environment is compared to the simulated TGac-B channel model. This chapter completes the findings of the simulation results in terms of system optimization. It also extends the study to reveal the impact of path loss on MU-MIMO performance. Chapter 5 investigates the modeling of radio coverage using smart antennas in terms of received power gain of the TxBF and interference level reduction. Finally, we conclude this thesis and give some potential further research directions in Chapter 6.

1.5 List of publications

Journal papers

— K. Issiali, V. Guillet, G. El Zein and G. Zaharia. Impact of Antennas and Correlated Propagation Channel on BD Capacity Gain for 802.11ac Multi-User MIMO in Home Networks. *Mediterranean Telecommunication Journal (RMT)*, June 2015.

— K. Issiali, V. Guillet, G. El Zein and G. Zaharia. MU-MIMO 802.11ac Capacity Gain under EIRP Constraint for a Typical Home Environment. *Lecture Notes in Electrical Engineering (LNEE)*, April 2016.

International conferences

— K. Issiali, V. Guillet, G. El Zein and G. Zaharia. Impact of Antennas and Correlated Propagation Channel on BD Capacity Gain for 802.11ac Multi-User MIMO in Home Networks. *In WIreless Technologies, embedded and Intelligent Systems (WITS)*, April 2015: **selected paper** for publication in *RMT* journal.

— K. Issiali, V. Guillet, G. El Zein and G. Zaharia. Impact of EIRP Constraint on MU-MIMO 802.11ac Capacity Gain in Home Networks. *In Mediterranean Conf. On Inf. and Com. Techn. (MedICT)*, May 2015: **best selected paper** for publication in extended version in *MDPI* journal.

— K. Issiali, V. Guillet, G. El Zein and G. Zaharia. IEEE 802.11ac Multi-user MIMO capacity and impact of antenna array geometry based on indoor measurements. *In Personal, Indoor and Mobile Radio Communications (PIMRC)*, August 2015.

Chapter 2

MU-MIMO techniques for wireless local area networks

Contents

2.1 Introduction

Radio propagation study is an essential step to perform appropriate design, deployment, and management strategies for any wireless network. The transmitted wave interacts with the physical environment in a complex way before arriving at the receiver (Rx). Indeed, radio propagation is heavily site-specific and can vary depending on the terrain, velocity of communicating devices, interacting objects and movement of people.

Under the suggested solutions to overcome the issues related to multipath propagation, MIMO communications have attracted considerable attention. They have demonstrated the potential for increased Shannon capacity by exploiting the spatial properties of the multipath channel [9]. If the channel is rich scattering (independent and identically distributed (i.i.d.) Rayleigh channel) then a linear increase in capacity is possible by simultaneously increasing the number of receiving and transmitting antennas (the capacity increases according to the min of the number of transmitting and receiving antennas). MIMO techniques were first investigated in single-user scenarios, then extended to multi-user MIMO scenarios. The MU-MIMO technology uses *adaptive antenna*[1] arrays to provide high spectral efficiency with moderate receiver complexity. In this context, the new IEEE 802.11ac standard ratified in January 2014 normalizes the MU-MIMO for increased data rates (above 1 Gbit/s). The aim behind these techniques is to improve the system performance by increasing channel capacity and spectrum efficiency extending coverage range. These techniques also reduce multipath fading, co-channel interference, system complexity and cost, Bit Error Rate (BER), and outage probability [10].

This chapter first gives the physical features of the new standard 802.11ac in Section 2.2, before listing in details the basic propagation mechanisms which impact the propagation channel in wireless communication (Section 2.3). Afterwards, we describe the MU-MIMO downlink system, the precoding techniques in Section 2.5 and their related capacities in Section 2.6. Finally, the conclusion is drawn in Section 2.7.

2.2 The 802.11ac standard

The IEEE 802.11ac standard is an emerging Very High Throughput (VHT) WLAN standard that can achieve PHYsical layer (PHY) data rates of up to 6.9 Gbit/s for the

1. Adaptive antenna is as example a phased array where the gains and the phases of the signals induced in the various elements are weighted to adjust the gain of the array in a dynamic manner along a particular direction, while simultaneously placing nulls along undesired directions.

5 GHz frequency band [11]. Note that the rates at the Internet Protocol (IP) layer are lower in practice.

The scope of IEEE 802.11ac includes single link throughput supporting at least 500 Mbit/s, multiple-stations throughput of at least 1 Gbit/s, and backward compatibility and coexistence with legacy IEEE 802.11n devices in the 5 GHz band. Consequently, this standard is targeted at higher data rate services such as high-definition television, wireless display (high-definition multimedia interface (HDMI) replacement), wireless docking (wireless connection with peripherals), and rapid sync-and-go (quick upload/download). The IEEE 802.11ac standardization process started in 2008 and finished in December 2014.

In general, IEEE 802.11ac could be schematized as a lateral extension of IEEE 802.11n in which the two basic notions of MIMO and wider channel bandwidth are enhanced. PHY and Multiple-Access Channel (MAC) layers modifications have been introduced with the VHT standard. In addition, channelization has been modified and MU-MIMO has been introduced for greater spectral efficiency.

Hereafter, we review some of the key features of IEEE 802.11ac such as larger bandwidth, higher order modulation, and MU-MIMO transmission mode.

2.2.1 Mandated use of the 5 GHz band

The WLAN market is now transitioning from IEEE 802.11n to IEEE 802.11ac [2], due to the promise of higher throughput and more reliable performance available in the 5 GHz unlicensed band. IEEE 802.11ac mandates the use of the 5 GHz frequency band, a band with the availability of more significant spectrum compared to the commonly used 2.4 GHz band. Indeed, in Europe, there is approximately 400 MHz of spectrum available. In contrast, the 2.4 GHz band can accommodate only three non-overlapping 20 MHz wide channels. This has led to many competing devices per channel and heavy levels of interference. The larger spectrum availability in the 5 GHz band provides more network capacity, and leads to fewer competing devices per channel and thus reduced interference compared to traditional single-band 2.4 GHz IEEE 802.11n networks.

2.2.2 Maximum data rate

One key feature of IEEE 802.11ac is the increase in data rate compared to IEEE 802.11n. This is achieved through the use of expanded channel bandwidth and higher-order modulation. Figure 2.1 shows the peak data rate and the per-Spatial Stream (per-SS) data rate for various WLAN standards that have evolved over the years. Spatial streams are composed of independent data streams. 802.11b and 802.11g support peak data rates of 11 and 54 Mbit/s, respectively. IEEE 802.11n increased the peak data rate to 600 Mbit/s. IEEE 802.11ac has further increased the peak data rate to 6.9 Gbit/s, over ten times that of 802.11n.

A maximum data rate of 6.93 Gbit/s is thus obtained using: 160 MHz bandwidth, 8 Spatial Stream (SS), 256-Quadrature Amplitude Modulation (QAM) with coding rate 5/6, and short Guard Interval (GI) (400 ns) [2].

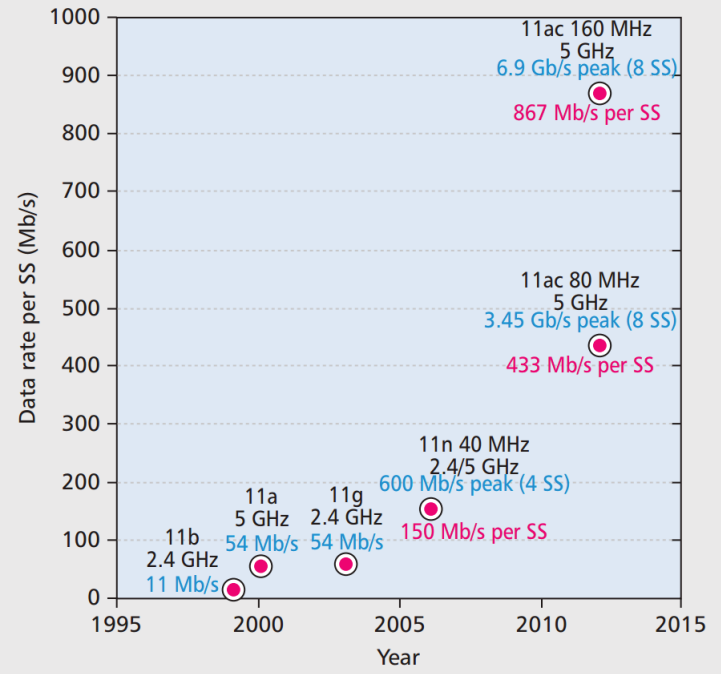

Figure 2.1 – Peak data rate and per-SS data rate of WLAN technologies [2].

2.2.3 Wider bandwidth and higher modulation order

IEEE 802.11ac introduces three new modes of expanded channel bandwidth: 80 MHz, 160 MHz, and 80 + 80 MHz, while also defining support for 20 and 40 MHz bandwidth modes to match channel bandwidth modes of IEEE 802.11n. The 80 and 160 MHz transmissions use contiguous spectrum, while the 80 + 80 MHz mode allows the construction of the transmitted signal to occupy separate 80 MHz segments. The 80 MHz transmissions use 234 data tones per Orthogonal Frequency-Division Multiplexing (OFDM) symbol, which more than doubles the data rate compared to an 802.11n 40 MHz transmission that only uses 108 data tones. Note that 234 and 108 represent the number of usable subcarriers while 114 and 242 are respectively the total number of the subcarriers for 40 MHz and 80 MHz. The 160 and 80 + 80 MHz transmissions use exactly twice the number of data tones as the 80 MHz transmission, thereby doubling further the data rate. In this report, we mainly study the 20 MHz bandwidth. It uses 56 subcarriers ranged from $-28\Delta f + f_0$ to $-\Delta f + f_0$ and from $+\Delta f + f_0$ to $+28\Delta f + f_0$, where $\Delta f = 312.5$ kHz and $f_0 = 5.25$ GHz are respectively the subcarrier frequency spacing and the studied central frequency. There is a total of 19 channels covered in Europe for the 802.11ac standard [12] (central frequency between 5.18 GHz and 5.32 GHz). The $+/-7\Delta f + f_0$ and $+/-21\Delta f + f_0$ represent the 4 pilot subcarriers [13]. We denote by N the total number of subcarriers as defined in the standard ($N = 56$ for 802.11ac in the 20 MHz band).

802.11ac introduces the use of 256-QAM [12]. Two forward error correction (FEC)

coding rates are defined: 3/4-rate and 5/6-rate. For comparison, 802.11n supports up to 64-QAM with the same coding rates. Thus, 802.11ac achieves a 33% increase in peak data rate over 802.11n. The combination of higher-order modulation and increased channel bandwidth enables an 802.11ac device to support approximately three to six times higher data rate compared to an 802.11n device for the same number of antennas or SS [2]. 802.11n achieves a maximum of 150 Mbit/s per-SS (108 data tones in 40 MHz of bandwidth with a maximum of 5.0 bits per tone). This results in a maximum data rate of 600 Mbit/s, assuming the maximum supported 4 SS MIMO transmission of 802.11n. 802.11ac reaches 433 Mbit/s per-SS using 80 MHz channel bandwidth (234 data tones with 6.67 bits per tone), and 867 Mbit/s per-SS using 160 or $80 + 80$ MHz bandwidth. This results in a maximum data rate of 6.9 Gbit/s, assuming the maximum supported 8 SS MIMO transmission of 802.11ac. While 6.9 Gbit/s is an eye-catching maximum data rate, a more commonly cited advantage of 802.11ac is the ability to cross the 1 Gbit/s barrier with small form-factor devices [2]. A two-antenna 802.11ac device (using a maximum of two SS) can support a maximum data rate of 1.73 Gbit/s. Furthermore, an 802.11ac device can surpass the data rate of an 802.11n device, with much lower complexity and cost but with an increased bandwidth range. For example, an 802.11n device requires three antennas (three spatial streams) to achieve a similar maximum data rate (450 Mbit/s) as a single-antenna 802.11ac device.

2.2.4 Rate-range

In addition to increasing the maximum data rate, these enhancements also lead to improved rate over-range performance of 802.11ac compared to 802.11n. Figure 2.2 shows simulated performance of both technologies [2], using a path loss model validated with measurements within a large building. Both technologies support three spatial streams, and have three transmitting and receiving antennas (3×3). The figure shows the TCP/IP throughput vs. the distance between the wireless devices. It can be seen that the 802.11ac devices can connect at twice the range of the 802.11n devices, at the maximum TCP/IP throughput of the 802.11n device (approximately 280 Mbit/s). For an end user, this translates to 802.11ac devices experiencing higher throughput across most locations in a home/office environment. Another observation from Figure 2.2 is that the peak rate of the 802.11ac device is three times that of the 802.11n device. For the end user, this translates to 802.11ac-enabled devices experiencing much higher throughput for in room and peer-to-peer scenarios.

However, the use of 80 MHz is guaranteed in optimal cases only where 80 MHz bandwidth can be available. In the case of a reduced available bandwidth, as in dense environments with many AP, in order to increase the throughput, the standard increases the number of SS to eight, as well as it proposes the MU-MIMO processing as solution to enhance the spectral efficiency.

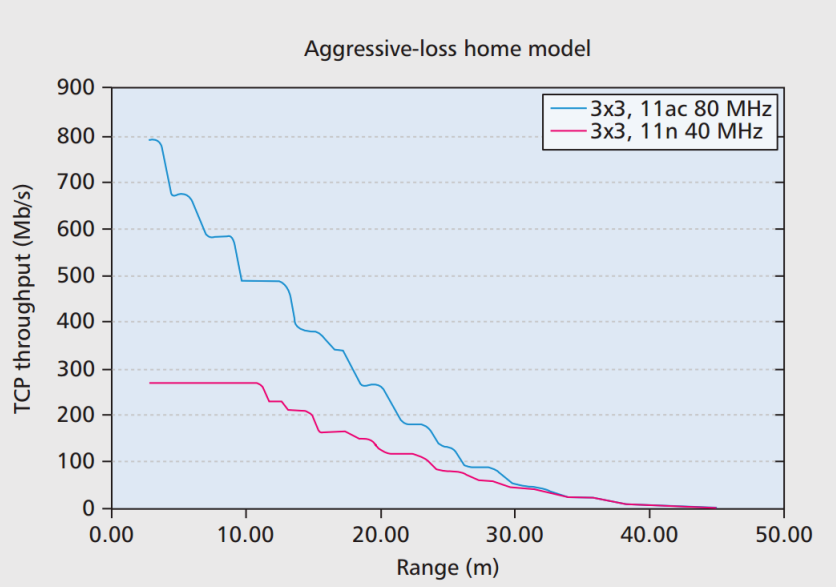

Figure 2.2 – Rate-over-range of three spatial streams 802.11ac and 802.11n devices [2].

2.2.5 Eight spatial streams

802.11ac introduces support for up to eight SS, compared to 802.11n, which defines up to four SS. In 802.11ac, the same modulation is applied to all SS for a particular user. Specifically, the transmitter bits are encoded, interleaved and modulated according to one of 10 prescribed Modulation and Coding Schemes (MCS) and then spatially mapped to physical antennas. The spatial mapping between the SS and antennas is implementation-specific, and may be frequency dependent and include transmit steering or precoding matrices [12]. This feature is interesting when combined with MU-MIMO technique since the end users are rarely equipped with 8 antennas, whereas the AP can easily be equipped with 8 antennas [14].

2.2.6 Transmit beamforming

Beamforming is an optional feature of 802.11n/ac standards but there is a growing industry demand for it in various wireless applications. In the case of TxBF, by controlling the power and the phase of the transmitted signals, it is possible to shape the effective radiation pattern of the antennas pointing towards the direction of the dominant propagation paths to improve the received power, as shown in Figure 2.3.

What 802.11ac adds is a standardized channel sounding which enables the transmitter (Tx) to precisely steer its transmitted power toward the targeted receiver. 802.11ac defines a single protocol for one 802.11ac device to sound other 802.11ac devices. The selected protocol closely follows the 802.11n explicit compressed feedback protocol. However, because of some subtle differences, the 802.11ac sounding is not

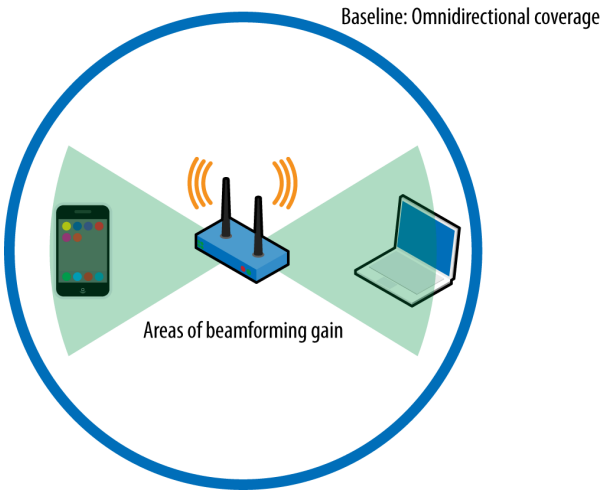

Figure 2.3 – Beamforming basics.

backward compatible with 802.11n devices.

Explicit compressed feedback (ECFB) is known to provide the most precise estimate of the channel, taking into account all the imperfections at the transmitter and the receiver. However, ECFB comes with a lot of overhead. For an AP with four antennas, the compressed feedback varies from 180 to 1800 bytes, depending on the number of client antennas and level of compression. For an 80 MHz client, sounding with just one single antenna takes about 250 microseconds.

2.2.7 MU-MIMO

In 802.11n, a transmission to a device happens using SU-MIMO modes, where the data rate to a device scales with the minimum number of antennas of each device and with the signal to noise ratio. An 802.11n AP must transmit data to different devices, attempting to divide up the network throughput between stations based on Carrier Sense Multiple Access/Collision Avoidance (CSMA/CA) which acts to prevent collisions before they happen. Unfortunately, 802.11n network capacity is then limited by lower-cost devices that have a smaller number of antennas [15]. For instance, with single-antenna receivers, the 802.11n does not take benefit from MIMO advantages to improve throughput. In this context, 802.11ac MU-MIMO transmission modes allow simultaneous transmissions to multiple devices, as depicted in Figure 2.4. This significantly improves the spectral efficiency of a WLAN when there are stations with limited numbers of antennas. Essentially, MU-MIMO captures the maximum spatial capacity without requiring all individual stations to have a large number of antennas. The 802.11ac standard allows a MU-MIMO transmission to send up to four stations simultaneously. Each station may receive up to four SS, but the total number of SS in a MU-MIMO transmission is limited to eight SS summed across all stations.

Transmit beamforming and MU-MIMO require knowledge of the channel state to

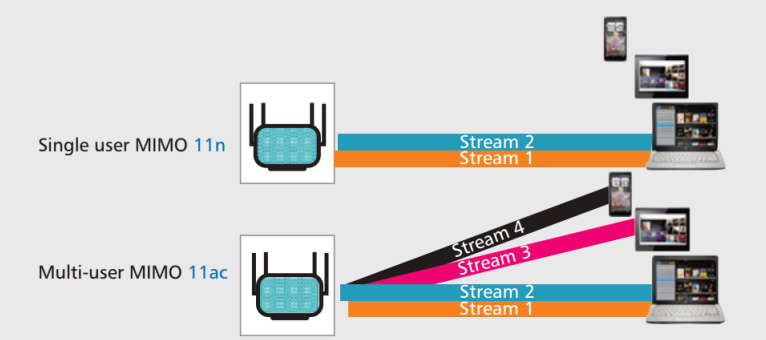

Figure 2.4 – Illustration of MU-MIMO 802.11ac and SU-MIMO 802.11n [2].

compute a precoding or steering matrix that is applied to the transmitted signal to optimize reception at one or more stations. The 802.11ac standard employs an explicit channel sounding and feedback protocol that works as follows. Upon gaining access to the medium, the AP transmits a Null Data Packet (NDP) Announcement Frame, identifying the stations for which it wants to collect channel state information for a subsequent MU-MIMO transmission, followed by an NDP frame. The first identified station in the NDP Announcement Frame then estimates the downlink channel from the NDP and feeds back the Channel State Information (CSI) to the AP. The remaining identified stations send CSI feedback upon subsequently being polled. The AP can then calculate the MU-MIMO precoding weights and use them in subsequent MU-MIMO data transmissions to the relevant stations. One positive consequence of the 802.11ac MU-MIMO specification is that it led to a unification of an underlying transmit beamforming feedback mechanism. This fact accelerated the industry adoption of transmit beamforming, and cleared up the confusion surrounding the multiple defined methods of 802.11n. In [16], it has been proven that the channel sounding overhead may impact badly the performance of MU-MIMO by preventing perfect CSI at the Tx.

2.3 Basics of propagation channel in wireless networks

In indoor WLAN, walls, floors, furniture, movement of people and objects within buildings may obstruct the direct path between the transmitter and receiver (LOS path). In addition, the transmitted wave arrives at the receiver along a number of paths after being transmitted, reflected or diffracted by different interacting objects in the surrounding environment. Furthermore, the propagation environment is often dynamic because of the mobility of communicating nodes and/or of objects and people within the environment. Therefore, the direct path, i.e. directly linking the Tx to the Rx, is not the only transmission path. There are multiple copies of a signal that may arrive with different phases, different powers (attenuations), delays and directions of arrival. This is called multipath propagation. Indeed, the signals may reflect on a

variety of surfaces and reach the receiving antenna via paths other than the direct line of sight path, as depicted in Figure 2.5. In these conditions, the propagation channel can be selective in time, frequency and space. In digital radio communications, multipath propagation can cause errors and affect the quality of communications. Multipath can be also beneficial for MIMO systems to increase throughput and to maintain a communication when the direct path is obstructed. We discuss all the related issues in this section.

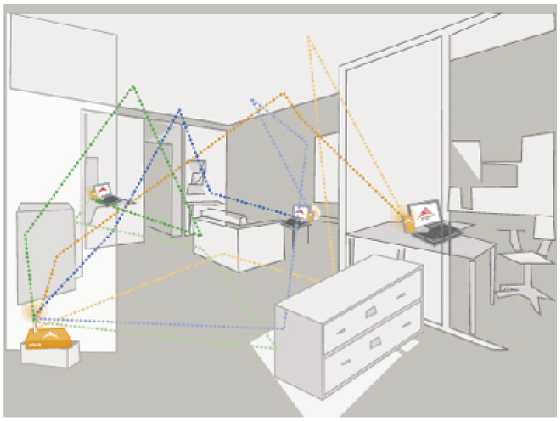

Figure 2.5 – Multipath propagation in an indoor environment.

2.3.1 Multipath propagation mechanisms

Multipath radio signal propagation occurs due to several propagation mechanisms. Reflection, transmission, diffraction and scattering are the basic propagation mechanisms encountered in an indoor environment resulting on a multipath propagation (Figure 2.6).

2.3.1.1 Reflection

Reflections occur when the propagating electromagnetic wave impinges upon an object (smooth surface) that has large dimensions compared to the wavelength of the propagating wave. In a indoor area, it occurs from the surface of the ground, from walls, and from furniture. Depending on the reflection surface, we can distinguish whether the reflection is specular or diffuse. Reflection on smooth surfaces is called specular, while reflection on rough surfaces is considered diffuse.

2.3.1.2 Diffraction

Diffraction is the mechanism by which waves enter into the shadow of an obstacle. It occurs at the edge of an impenetrable body that is large compared to the wavelength. A radio wave that meets an obstacle has a natural tendency to bend around the obstacle.

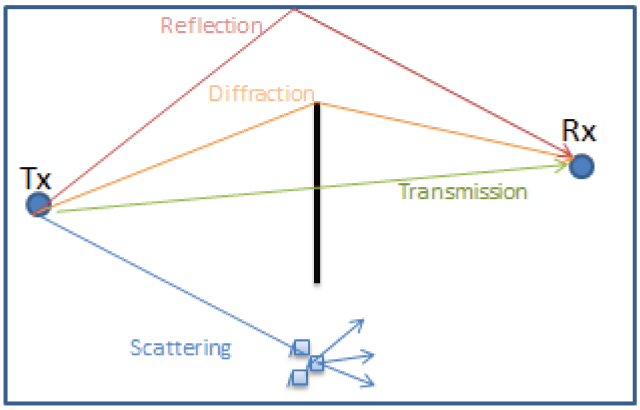

Figure 2.6 – Propagation phenomena.

The waves produced by the obstructing surface are present throughout space and even behind the obstacle, giving rise the bending of waves around the obstacle, even when a LOS path does not exist between Tx and Rx.

2.3.1.3 Scattering

Scattering occurs when waves reach irregular objects such as walls with rough surfaces and furniture which scatter radio waves in all directions. This occurs when objects are of dimensions in the order of a wavelength (or less) of the electromagnetic wave, and where the number of obstacles per unit volume is large. Propagation in many directions results in reduced power levels, especially far from the scatterer. That's why in most cases, the scattering can be neglected [10], at least for the 2.4 GHz and 5 GHz Wi-Fi frequencies.

2.3.1.4 Refraction

Refraction is the bending of the waves as they move from one medium into another in which the velocity of propagation is different. This changes the direction of the wave. A radio signal may refract through certain types of glass and other materials that are found in indoor environment.

2.3.1.5 Waveguiding

Waveguiding is an important process modeling propagation in street canyons, corridors and tunnels. Those waveguides occurring in wireless communications deviate from the idealized assumptions of theoretical work due to several factors, such as the lossy materials, the discontinuous walls of corridors, the rough surfaces and the metallic and dielectric objects existing in these waveguides.

2.3.2 Multipath propagation channel modeling

The channel refers to the medium between the transmitter and the receiver. We have seen in the previous section that the real wireless channel is complicated due to complex propagation environment. The transmitted signal may be reflected, diffracted and scattered by surrounding obstacles, or attenuated and absorbed by obstructions causing a fluctuation of signal power. Hence, multipath signals are received in a terrestrial environment, i.e., where different forms of propagation are present and the signals arrive at the receiver from transmitter via a variety of paths, causing multipath interference. This is known as multipath fading. Adding the effect of movement of either the Tx or Rx, the received overall signal amplitude or phase changes over a small amount of time.

Consider a single-input single-output system, the overall transmission channel (propagation channel as well as the transmitting and receiving antennas) can be represented as a linear filter with time varying impulse response in continuous time $h(\tau, t)$. The received signal $y(t)$ at time t is expressed using complex baseband equivalent signals and filter as:

$$y(t) = x(t) * h(\tau, t) + n(t) = \int_{-\infty}^{+\infty} h(\tau, t)s(t - \tau)\,\mathrm{d}\tau + n(t) \tag{2.1}$$

where $x(t)$ is the transmitted signal, $n(t)$ is the corrupting noise, and $*$ denotes the convolution operation.

As channel can be time-varying, time t is needed, and τ is the multipath delay. The Channel Impulse Response (CIR) $h(\tau, t)$ for a single-input single-output system experiencing multipath fading with L paths is given by:

$$h(\tau, t) = \sum_{l=0}^{L-1} \alpha_l(t)\delta(\tau - \tau_l(t)) \tag{2.2}$$

where $\alpha_l(t)$ and $\tau_l(t)$ are respectively the complex attenuation and the delay of the l^{th} propagation path at time t. We denote $L(t)$ by L for sake of simplicity.

The characteristics of the channel can also be represented in the frequency domain by the Channel Frequency Response (CFR). CFR can be obtained by applying Fourier transform to the CIR in the time-delay domain τ:

$$\mathbf{H}(f, t) = \int_{-\infty}^{+\infty} h(\tau, t)exp\{-j2\pi f\tau\}\,\mathrm{d}\tau = \sum_{l=0}^{L-1} \alpha_l(t)exp\{-j2\pi f\tau_l(t)\} \tag{2.3}$$

The continuous-time system model is generally sampled into an equivalent discrete time model. The received signal is given by:

$$y_k = \sum_{l=0}^{L-1} h_{l,k}s_{k-l} + n_k \tag{2.4}$$

where $y_k = y(kT_{sym})$, k is an integer and T_{sym} is the sampling period. L is the number of taps, $h_{l,k}$ is the l^{th} channel tap. The frequency domain response becomes:

$$\mathbf{H}(f,k) = \sum_{l=0}^{L-1} h_{l,k} exp\{-j2\pi l f T_{sym}\} \tag{2.5}$$

2.3.3 Propagation channel parameters

The average Power Delay Profile (PDP), referred to as $E(PDP(\tau,t))$, gives the distribution of signal average power received over a multipath channel as a function of propagation delays [17]. The influence of particular obstacles can be noticed in the PDP, where the peaks, echoes, and other irregularities are displayed. The PDP can be thought of as a density function, of the form:

$$PDP(\tau,t) = \frac{\mid h(\tau,t) \mid^2}{\int_0^{+\infty} \mid h(\tau',t) \mid^2 \, \mathrm{d}\tau'} \tag{2.6}$$

Mean Excess Delay, denoted $\tau_e(t)$ is the first moment of the power-delay profile (as shown in Figure 2.7) [17]. It is expressed as:

$$\tau_e(t) = \int_0^{+\infty} \tau PDP(\tau,t) \, \mathrm{d}\tau \tag{2.7}$$

The time reference 0 is given by the first path of the channel.

Root Mean Square (RMS) Delay Spread (DS) $\tau_{RMS}(t)$ is the square root of the second central moment of a power-delay profile [17], as seen in Figure 2.7. It is the standard deviation of the mean excess delay as expressed in Equation 2.8. The RMS delay is a good measure of the multipath delay spread. It gives an indication of the importance of the Inter-Symbol Interference (ISI). Strong echoes (relative to the shortest path) with long delays contribute significantly to $\tau_{RMS}(t)$.

$$\tau_{RMS}(t) = \sqrt{\int_0^{+\infty} (\tau - \tau_e)^2 PDP(\tau,t) \, \mathrm{d}\tau} \tag{2.8}$$

Maximum Excess Delay τ_m is measured with respect to a specific power level, which is characterized as the threshold of the signal [17]. When the signal level is lower than the threshold, it is processed as noise. For example, the maximum excess delay can be specified as the excess delay τ_m for which the average $PDP(\tau)$ falls below -30 dB with respect to its peak value, as shown in Figure 2.7.

Figure 2.7 summarizes the delay dispersion parameters characterizing the propagation channel defined above.

The coherence bandwidth B_{coh} is the statistical average bandwidth of the radio channel, over which signal propagation characteristics are frequency correlated at a given correlation level. It characterizes the range of frequencies over which the channel can be considered correlated or nearly flat. It is usually defined as the bandwidth over which

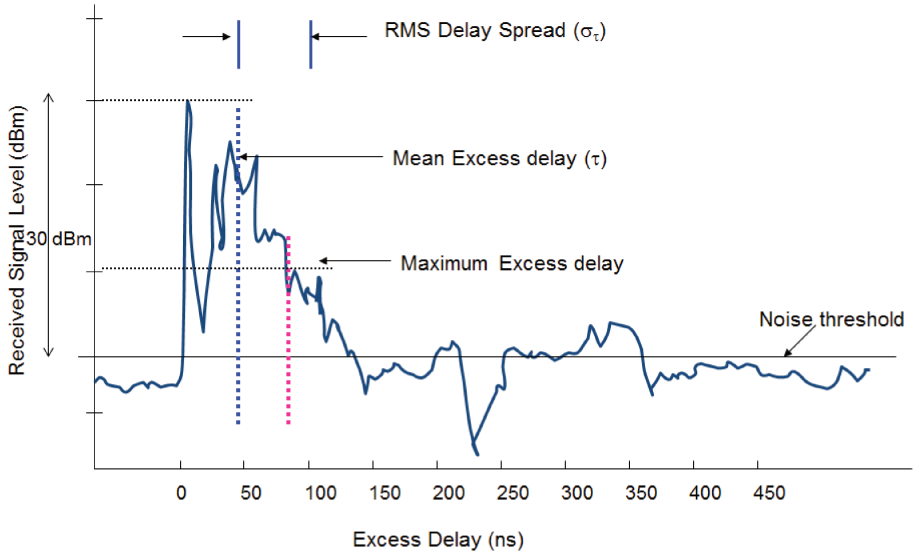

Figure 2.7 – An illustration of a typical power-delay profile and the definition of the delay parameters.

the variation of the correlation is 50% or 90%, and is approximated to be inversely proportional to the root mean square delay spread of the channel τ_{RMS} [10] as:

$$B_{coh} \alpha \frac{1}{\tau_{RMS}} \tag{2.9}$$

The channel can be also time selective due to the Doppler effect. The channel coherence time T_{coh} is defined by the duration over which the channel impulse response can be considered nearly constant over time t. It is often approximated by the inverse of the Doppler spread: $T_{coh} = \frac{1}{B_d}$, with $B_d = 2f_{D,max}$ where $f_{D,max}$ is the maximum Doppler frequency.

2.3.4 Classification of multipath channels

The multipath fading phenomenon can be classified into two different types: large-scale fading and small-scale fading as illustrated in Figure 2.8. Actually, due to the motion into the channel, the term *small-scale fading*, means rapid fluctuations of the amplitudes, phases, or multipath delays of a radio signal over a short period or short travel distance. This might be so severe that large scale radio propagation loss effects, referred to as *large-scale fading*, might be ignored.

Firstly, the phenomenon of large-scale fading is affected by the motion over large areas (presence of hills, forests, buildings) in outdoor or by the presence of walls, furniture in indoor. The analysis of large-scale fading provides a way of computing an estimate of the path loss as a function of distance and other factors. It includes *path loss* due

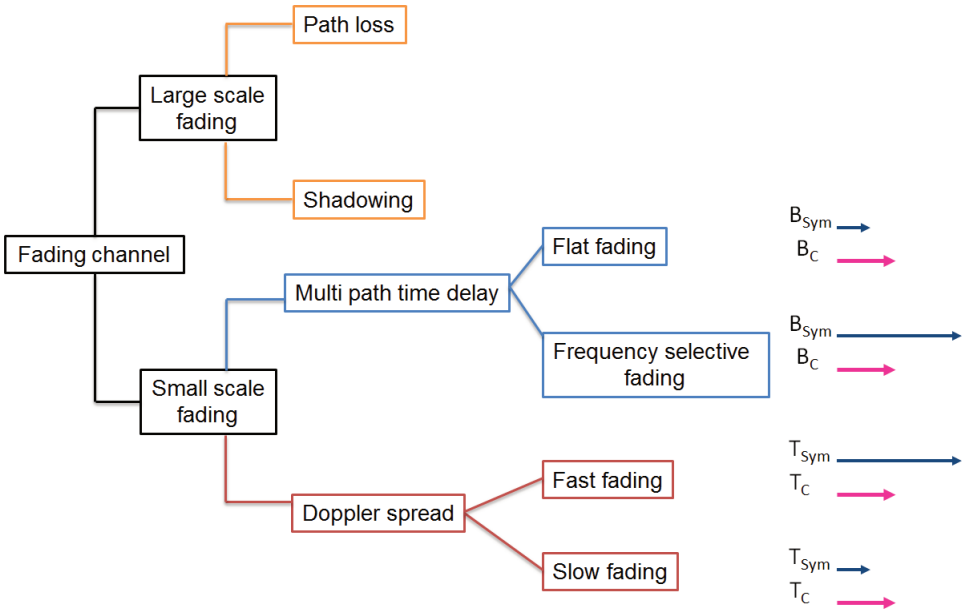

Figure 2.8 – Classification of fading channels.

to the large distance between the Tx and Rx, and *shadowing* caused by the presence of obstructions.

The type of fading experienced by the signal through a wireless channel depends on the relation between the signal parameters (bandwidth B_{sym} and symbol period T_{sym}) and the channel parameters (RMS delay spread $\tau_{RMS} \alpha \frac{1}{B_{coh}}$, Doppler spread $= \frac{1}{T_{coh}}$). Hence, we have four different types of small-scale fading, as in Figure 2.8. There are two types of fading due to the time dispersive nature of the channel.

Due to delay dispersion and multipath propagation, the channel can be categorized as frequency flat fading or frequency selective fading. A channel is said to exhibit *frequency-selective fading* when the delay spread is greater than the symbol period ($\tau_{RMS} > T_{sym}$ which implies $B_{sym} > B_{coh}$). This condition occurs whenever the received multipath components of a symbol extend beyond the time duration of the symbols. Such multipath dispersion of the signal yields a kind of ISI called channel-induced ISI.

When the delay spread is less than the symbol period ($\tau_{RMS} < T_{sym}$, i.e. $B_{sym} < B_{coh}$), a channel is said to exhibit *flat fading*, and there is no channel-induced ISI distortion. But there can still be performance degradation, due to the irresolvable phasor components that add up destructively to yield a substantial reduction in SNR at the receiver.

Fast fading and slow fading are classified on the basis of how rapidly the transmitted baseband signal changes, compared to the rate of the parameter changes of the channel. If the channel impulse response changes at a rate much faster than the transmitted signal: $T_{sym} > T_{coh}$, i.e. $B_{sym} < B_d$, the channel may be assumed to be a *fast-fading* channel.

The fast fading is modeled using either Rician distribution or Rayleigh fading. Rayleigh fading occurs when there are multiple indirect paths between the transmitter and receiver and no distinct dominant path, such as LOS path. Sometimes the dominant non fading signal due to line-of-sight in the channel superimposes itself on the random multipath components. The effect of the dominant signal over the weaker multipath signal gives rise to a Rician distribution. The Rician distribution is described by a parameter K, which is defined as the ratio of signal power in dominant component over the (local-mean) scattered power. The absence of direct line-of-sight signal $K \Rightarrow \infty$ degenerates Rician distribution into Rayleigh.

Otherwise, it is assumed to be a *slow-fading* channel if $T_{sym} < T_{coh}$, i.e. $B_{sym} > B_d$. It is important to note that the velocity of the mobile unit or the velocity of objects using the channel through a baseband signal determines whether a signal undergoes fast fading or slow fading.

2.4 MIMO propagation channel modeling for systems

The design guidelines and performance evaluation of radio communication require developing effective propagation models featuring the relevant characteristics of the radio propagation in an operating environment. MIMO channel propagation models have been developed as a suitable, low-cost, and convenient alternative, since the site-measurements are expensive and time consuming.

2.4.1 Power angular spectrum

Since the spatial (angular) distribution of the multi-path components is important in determining the MIMO system performance [18], this paragraph highlights the incorporate additional concepts such as Angular Spread (AS), Angle of Arrival (AoA), Angle of Departure (AoD), Power Angular Spectrum (PAS) and the antenna array correlation matrices for the Tx and Rx combinations, as illustrated in Figure 2.9.

Power angular spectrum defines the average received power as a function of Θ, where Θ represents either the angle-of arrival for receiving antenna or angle-of-departure for transmitting antenna. The AoD is defined to be the angle with which a departing ray's power is transmitted by the Tx array with respect to the broadside. Inversely, the AoA is defined to be the angle with which an arriving ray's power is received by the Rx array with respect to the broadside. The power angular spectrum value, denoted PAS, at an angle $\theta \in]-\pi, \pi]$ is given by:

$$PAS(\theta) = E(\int_{-\infty}^{+\infty} \mid h(\tau, \theta) \mid^2 \, \mathrm{d}\tau) \tag{2.10}$$

where $h(\tau, \theta)$ defines the CIR as a function of the delay τ and the angle θ.

Similar to PDP, we can define the mean angle $\bar{\theta}$, and the RMS AS θ_{RMS}. This determines how spread out multipath power is about the horizon. It is defined as the standard deviation of the PAS.

The coherence distance D_{coh} defines the maximum distance between two antenna elements so that their channel responses are still strongly correlated. In practice, it corresponds to the spatial separation for which autocorrelation of coefficient of spatial fading drops to 0.7 and is inversely proportional to θ_{RMS}.

The spatial correlation r is expressed as a function of PAS in the case of linear array antennas spaced by d as [19]:

$$r = \int_{-\pi}^{+\pi} PAS(\theta) e^{-j\frac{2\pi}{\lambda} d cos(\theta)} \, \mathrm{d}\theta \tag{2.11}$$

r is used to compute the transmit and correlation matrix elements, depending on the antenna element spacing d.

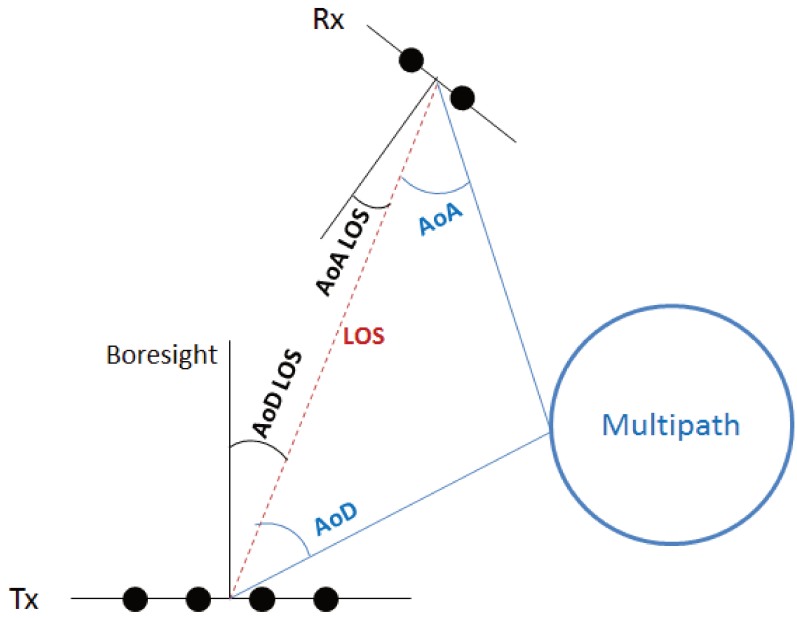

Figure 2.9 – The MIMO channel angular parameters at both Tx and Rx.

2.4.2 Classification of the MIMO channel models

There are two main models for propagation channel: empirical (or statistical) models, and site-specific (or deterministic) models, as can be seen in Figure 2.10. The statistical models are based on the statistical characterization of the channel. They are easier to implement, require less computational effort, and are less sensitive to the geometry of the environment. Several stochastic models have been developed to predict the channel properties for wideband applications. The deterministic models have a certain physical basis, and require a vast amount of data regarding geometry, terrain profile, locations of building and of furniture in buildings, and so on. These deterministic models require more computations, and are more accurate and include site-specific (ray-tracing) models.

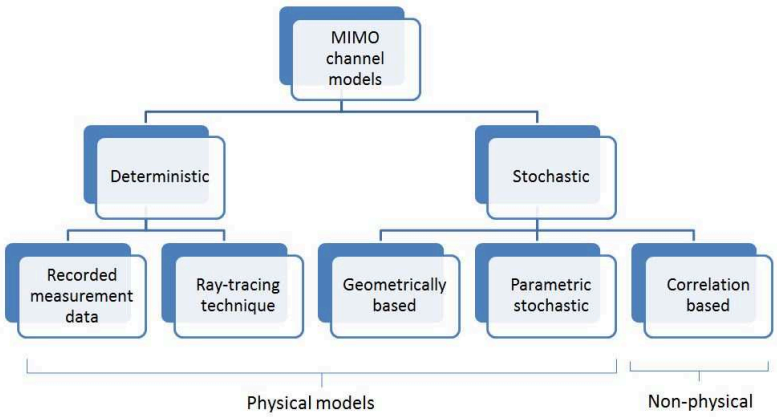

Figure 2.10 – MIMO channel models.

2.4.3 TGn channel models

Standardized models are an important tool for the development of new radio systems. They allow to assess and compare the benefits of different transmission techniques to enhance capacity and improve performance, in a manner that is unified for many parties.

In indoor area, radio propagation is influenced by the presence of building materials. The transmitted signal reaches the receiver through more than one path, due to reflection, refraction, and diffraction of the radio wave by objects such as walls, windows, and doors inside a building. The IEEE 802.11n task group proposes in [20] a set of channel models applicable to indoor MIMO WLAN systems as an extension of the Single-Input Single-Output (SISO) channel models proposed by Medbo et al. These models are the TGn channel models and are classified to be stochastic in Figure 2.10. The newly developed MIMO models are based on the cluster model developed by Saleh and Valenzuela [20].

The channel models comprise a set of 6 profiles, labeled A to F, which cover the scenarios of Rayleigh flat fading, residential, residential/small office, typical office, large office, and large space (indoors and outdoors). Each channel model has a path loss model including shadowing, and a MIMO multipath fading model, which describes the multipath delay profile, the spatial properties, the K-factor distribution, and the Doppler spectrum.

Each channel model has a certain number of taps (one for model A, and 9 to 18 for models $B - F$). Each model further comprises a number of clusters, which correspond to overlapping subsets of the tap delays. Each tap is characterized by a relative delay (with respect to the first path delay). Table 2.1 summarizes the basic model parameters.

The average power of each tap in a particular cluster was determined so that the sum of the powers of overlapping taps corresponding to different clusters corresponds to the powers of the original average power delay profiles. Next, AS, AoA, and AoD

2. Not Applicable

Parameters/Environment	A	B	C	D	E	F
Avg 1^{st} Wall Distance (m)	5	5	5	10	20	30
RMS Delay Spread (ns)	0	15	30	50	100	150
Maximum Delay (ns)	0	80	200	390	730	1050
Number of Taps	1	9	14	18	18	18
Number of Clusters	N/A [2]	2	2	3	4	6

Table 2.1 – Basic channel model parameters.

values were assigned to each tap and cluster (using statistical methods) that agree with experimentally determined values reported in the literature. Cluster AS was experimentally found to be in the 20° to 40° range, and the mean AoA was found to be random with a uniform distribution. With the knowledge of each tap power, AS, and AoA (AoD) and for a given antenna configuration, TGn generates the correlation matrix. The correlation matrix for each tap is based on the PAS with AS being square root of the second moment of PAS.

The various steps of the cluster modeling approach are briefly described below.

— Start with delay profiles of models, designed as A for Rayleigh, B, C, D, E and F for other specific environments.
— Manually identify clusters in each of the five models.
— Extend clusters so that they overlap, determine tap powers (see Appendix A).
— Assume Laplacian PAS shape of each cluster and corresponding taps.
— Assign AS to each cluster and corresponding taps.
— Assign mean AoA and AoD to each cluster and corresponding taps.
— Assume antenna configuration.
— Calculate correlation matrices for each tap as in [20].

Figure 2.11 and Figure 2.12 show model B and its delay profile with clusters. Clearly, two clusters can be identified: cluster 1 corresponds to tap delays 0 to 40 ns (in steps of 10 ns), while cluster 2 corresponds to tap delays 20 to 80 ns (also in steps of 10 ns). Hence, clusters 1 and 2 comprise 5 and 7 tap delays, respectively, and they overlap in 3 tap delays (20, 30 and 40 ns). Each cluster is assigned a set of spatial properties: a mean AoA, a mean AoD, an AS at the receiver, and an AS at the transmitter. These parameters assume the same values for all tap delays related to a given cluster. These parameters determine the transmit and receive correlation matrices associated with each tap delay.

The IEEE 802.11n channel models make the following assumptions:

— The PAS and the Power Delay Spectrum (PDS) are separable: each tap is modeled independently.
— The PAS and the Doppler spectrum for each tap are separable: the spatial correlation (correlation matrices) and temporal correlation (Doppler spectrum) for each tap are modeled independently.
— Each tap is modeled using the Kronecker model for Rician correlated channels,

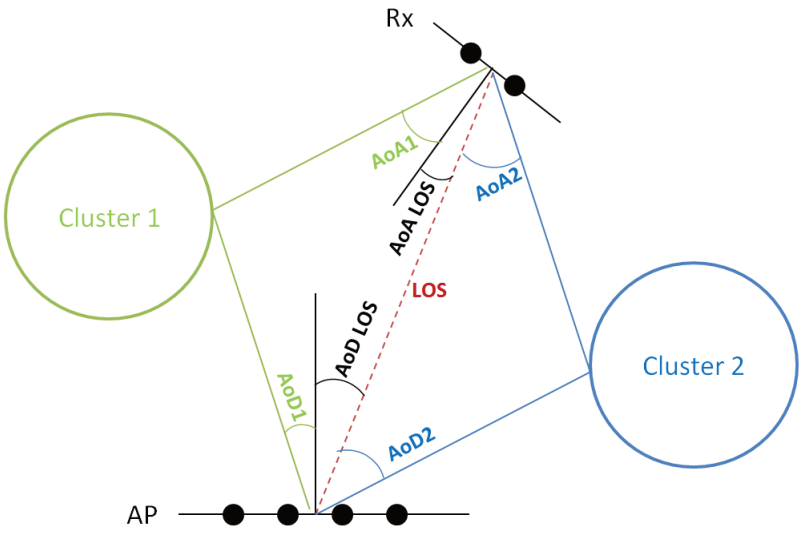

Figure 2.11 – Cluster based channel model B (2 clusters).

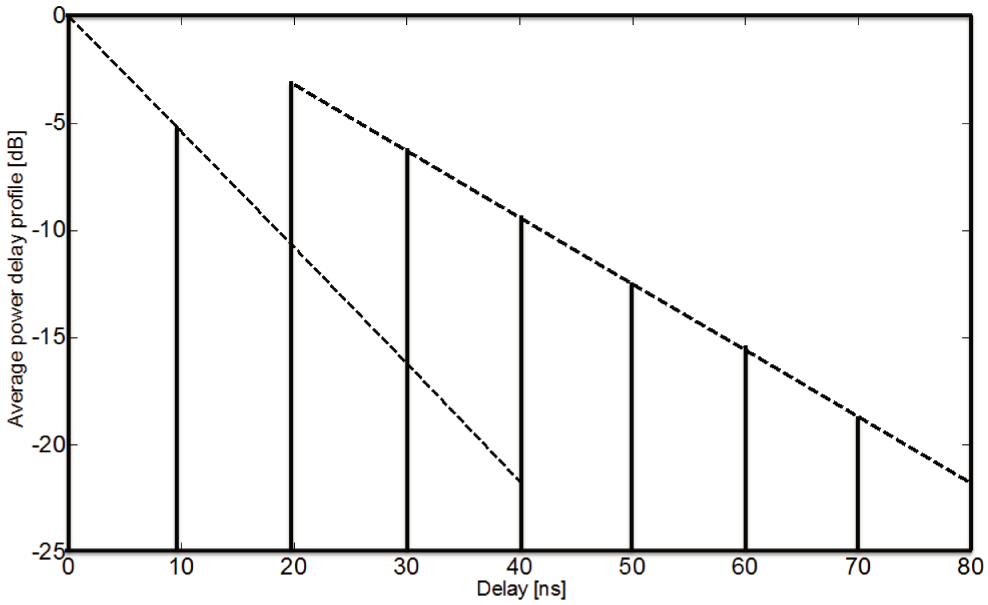

Figure 2.12 – TGac-B model average power delay profile with cluster extension (overlapping clusters).

hence it is assumed that the transmit and receive correlation matrices are separable for each tap.

2.4.4 TGac channel models

In order to support MAC throughput above 1 Gbit/s using one or more of the following technologies: higher order MIMO ($\geq 4 \times 4$), or higher bandwidth (≥ 40 MHz), or the MU-MIMO technology with ≥ 4 transmitting antennas, the TGac task group proposes modifications to the basic TGn model [21].

The TGn channel models assume minimum tap spacing of 10 ns and were employed for system bandwidth of up to 40 MHz. TGac systems may have much larger bandwidth. Hence, the channel sampling rate is increased by reducing the PDP tap spacing by a factor defined in [21].

The TGn channel models were originally conceived for MIMO systems with a transmitter with four antennas and a receiver with four antennas, and are based on the Kronecker channel correlation model assumption. TGn proposes that it is sufficient for channel models to tightly bound and sweep the range of performance in real environments. Furthermore, it is desirable that the channel model is simple enough and builds on TGn channel models to allow a fair and efficient comparison of different standards proposals.

Finally, to support MU-MIMO scenarios, the TGac proposed modifications to the power angular spectrum. These modifications are summarized as follows [20]:

— The defined TGn azimuth spread for each cluster remains the same for all users.
— For each user, independent random offsets between $+/-180°$ are introduced for the AoA, the direct tap and the NLOS taps.
— For each user, independent random offsets between $+/-30°$ are introduced for the AoD, the direct tap and the NLOS taps.

In fact, it is shown [21] that for the same transmitter location, different receiver locations lead to a different AoA at the receiver as depicted in Figure 2.13. Specifically, the measurements report that clusters AoA vary by $0-20$ degrees in NLOS scenario (classroom) and $0-60$ degrees in LOS scenario (great hall), depending on location. This is equivalent to a MU-MIMO scenario with a fixed transmitter location and receivers at different locations as depicted in Figure 2.13. Hence, the TGac conjectures that for the same transmitter location, different receiver locations lead to a different AoD at the transmitter. This conjecture is justified based on simulations evaluating the channel capacity [21].

2.5 MU-MIMO techniques

In this section, we give an overview about the MU-MIMO techniques. First, we present the assumed hypothesis throughout this thesis. Afterwards, we give the MU-MIMO system model as described in the literature. Finally, we synthesize the most explored MU-MIMO techniques in research distinguishing two cases: the single-antenna users and the multiple antennas users.

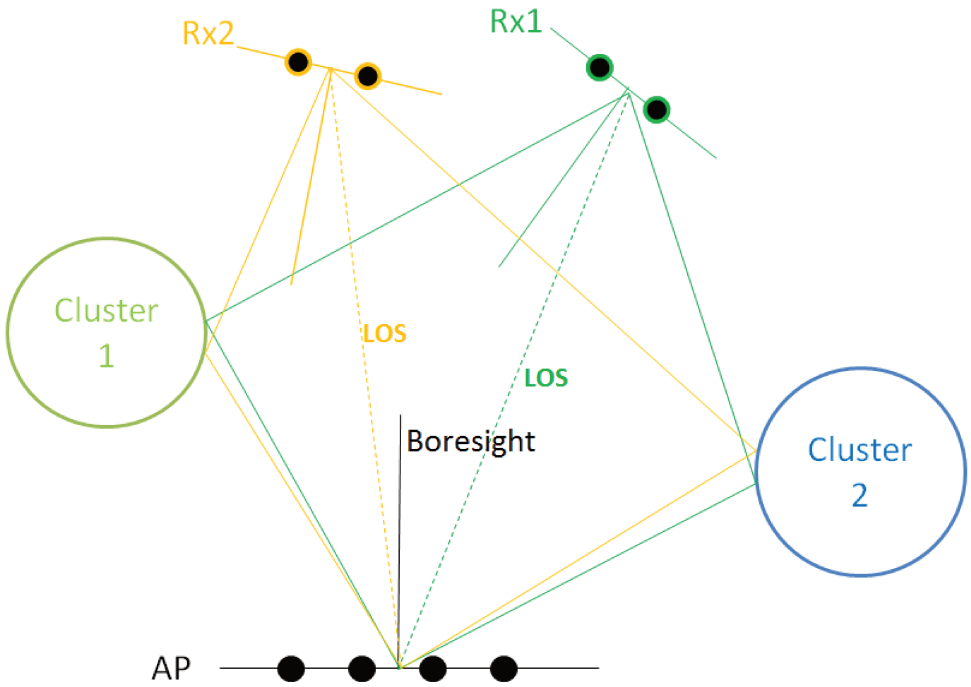

Figure 2.13 – AoA and AoD for two-users MU-MIMO system.

2.5.1 Overview

In this thesis, there are mainly two important assumptions. We consider that the transmitter has a perfect knowledge of the transmission channel. Moreover, we consider we are operating in a narrowband channel or on a subchannel for OFDM. Explanations are given below.

In a multi-user downlink scenario, the AP is equipped with multiple antennas and is simultaneously transmitting several independent spatial streams to a group of users. Each of these users is also equipped with a single or multiple antennas. The management of multiple users by the AP generates a new interference called Inter User Interference (IUI) seen by each user. In fact, when there are multiple users, the noise term of each user includes the interference. This interference term contains the signals intended for the other users.

To overcome this issue in IEEE 802.11ac AP, the MU-MIMO operates best with accurate knowledge of the downlink channel response between each transmitting antenna and each receiving antenna: CSI at the transmitter using feedback. In fact, when a perfect CSI is provided at the access point, zero IUI is achievable at every receiver, enabling thereby a simple receiver at each user. To obtain the CSI, most existing approaches use a combination of strategies such as feedback using downlink training data, where the AP obtains a measure of the CSI. To achieve CSI in IEEE

802.11ac, the standard specifies a single compressed beamforming method that relies on the use of explicit feedback to implement MU-MIMO [11][16]. However, propagation channels change over time in actual radio environments due to moving people resulting in Doppler effect for example. Hence, CSI is not perfect. A simple channel prediction scheme to provide CSI is proposed in [22], and its effectiveness is demonstrated through simulations of BER performance using a measurement campaign in a meeting room.

To mitigate the effects of intersymbol interference in frequency selective channels, OFDM is now a simple and well-accepted technique which converts a broadband frequency selective channel into a series of narrowband channels by transmitting data in parallel over many subcarriers. Combining OFDM with MIMO, producing so called MIMO-OFDM, significantly reduces receiver complexity in wireless multiuser broadband systems. Since OFDM uses multiple subcarriers, optimal linear precoding for MIMO-OFDM can be implemented by deriving linear precoders for each subcarrier independently. Hereafter, we assume either the channel experiences a flat fading so that the channel is frequency non-selective or we operate in narrowband subchannels guaranteed by the use of OFDM. Hence, the channel fading characteristic can be considered to be narrowband for each frequency bin. This assumption is satisfied in the case of the environment considered by TGac channel models. In fact, the subcarrier frequency spacing defined in the 802.11ac standard [12] is $\Delta f = 312.5$ kHz, and the measured coherence bandwidths are $\geq$ 1 MHz: $B_{coh} \gg \Delta f$ [23] in most of the indoor environments in the 5 GHz frequency band.

2.5.2 MU-MIMO system model

In a MU-MIMO transmission, there are two challenges in a MU-MIMO scenario: Uplink (UL) and Downlink (DL) channels as depicted in Figure 2.14. The UL channel, is used to model multiple users transmitting simultaneously to a single AP. The DL or Broadcast Channel (BC) is used to model the case where the AP is transmitting simultaneously to multiple users. The UL challenge is addressed using array processing and multi-user detection techniques by the AP in order to separate the signals transmitted by the users. The challenge for BC is that the interference cancellation is required at the AP to have cheap terminals with low power consumption. This report focuses on the capacity of the MU-MIMO DL channels. The UL MU-MIMO is not considered by the 802.11ac standard. Thereby, a presentation of the mathematical model can be quite useful. Indeed, techniques MU-MIMO processing techniques are based on such approaches.

In the following, we describe the typical system model considered in this thesis. The studied IEEE 802.11ac MU-MIMO system is composed of K users connected to one AP, as shown in Figure 2.15.

The AP has n_T antennas and communicates with K users simultaneously. Each user k has n_{R_k} antennas. We define $n_R = \sum_{k=1}^{K} n_{R_k}$, as the total number of the receiving antennas.

According to Equation 2.1, the channel from the AP to the k^{th} user is represented by a $n_{R_k} \times n_T$ channel matrix $\mathbf{H}_k$. It is the MIMO subchannel transfer function for a

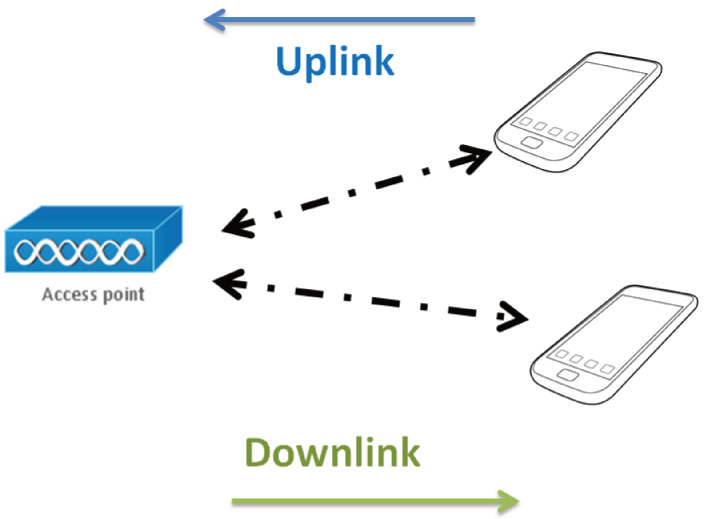

Figure 2.14 – Uplink and downlink MU-MIMO systems.

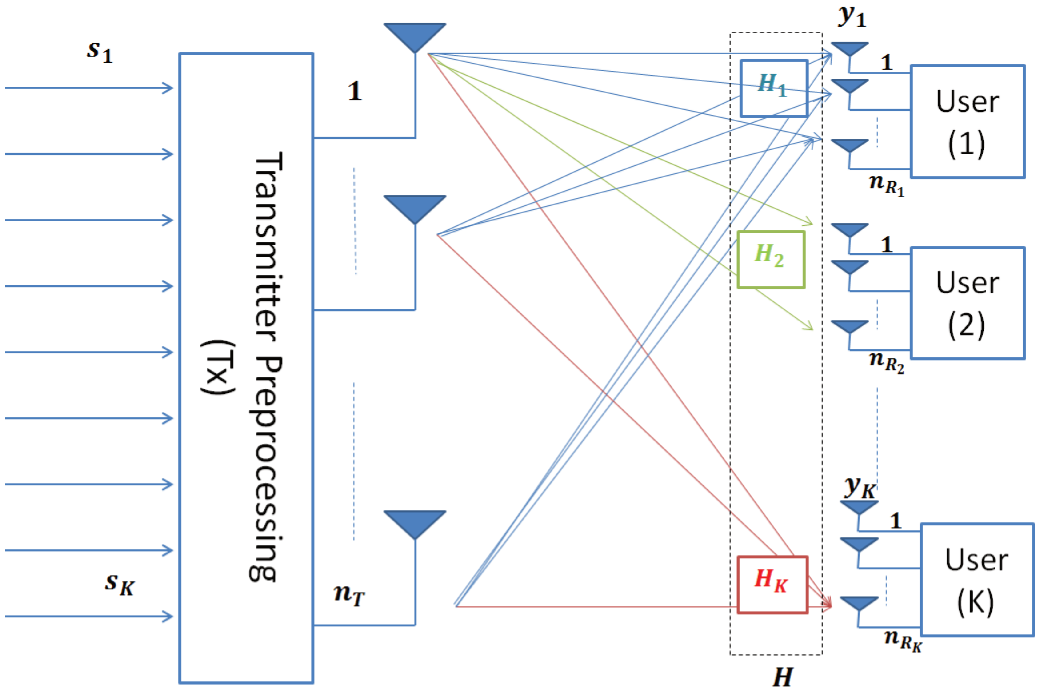

Figure 2.15 – Diagram of MU-MIMO system.

subcarrier. For the sake of simplification, the subcarrier index is not mentionned. We define the $n_R \times n_T$ channel matrix $\mathbf{H}$ as $\mathbf{H} = [\mathbf{H}_1^T \dots \mathbf{H}_K^T]^T$, and its elements H_{ij} as $\mathbf{H} = \Big(H_{ij}\Big)_{\substack{1 \leq j \leq n_T \\ 1 \leq i \leq n_R}}$. Note that each element H_{ij} of $\mathbf{H}$ is the CFR presented in Subsection 2.3.2 between i^{th} receiving antenna and the j^{th} transmitting antenna and for a particular subcarrier. The received signal is written as:

$$\mathbf{y} = \mathbf{HX} + \mathbf{n} \tag{2.12}$$

where $\mathbf{X}$ is the transmitted signal.

Let $\mathbf{s}_k$ represents the $N_{ss,k} \times 1$ transmit data symbol vector for user k, where $N_{ss,k}$ is the number of independent spatial streams transmitted simultaneously for the k^{th} user. The total number of spatial streams is $N_{ss} = \sum_{k=1}^{K} N_{ss,k}$. We define the $N_{ss} \times 1$ transmit data symbol vector as: $\mathbf{s} = [\mathbf{s}_1{}^T \mathbf{s}_2{}^T \dots \mathbf{s}_K{}^T]^T$.

Next section addresses how $\mathbf{X}$ can be designed based on $\mathbf{s}$ using precoding techniques for MU-MIMO.

2.5.3 Precoding techniques

Precoding technique is the process of using the information at the transmitter in a way that mitigates multi-user interference on the one hand, and maximizes the sum rate capacity on the other. The non-linear techniques are known to achieve optimum capacity. Actually, it has been proven that the capacity region of the DL MU-MIMO systems is achieved with Dirty Paper Coding (DPC) method [24] called also the capacity bound. This non-linear technique consists of precoding the data in order to avoid the effect caused by the interference without canceling it. However, it has high computational complexity. The capacity bound can be approached by linear techniques. Linear precoding techniques are low-complexity transmission techniques compared to non-linear techniques [22].

Linear precoding techniques, supported by the standard IEEE 802.11ac, assume that the transmitted signal $\mathbf{X}$ is generated by a linear combination of data symbols contained in a vector $\mathbf{s}$. It has been shown that linear precoding techniques can achieve sum rate capacity close to the DPC capacity bound with lower complexity [24]. Next, we will present some precoding techniques proposed in the literature in order to identify a relevant method for our study in next chapters. First, the simple case of single antenna receivers is detailed in next subsection. Afterwards, we present the precoding techniques taking into account multiple antennas per user.

2.5.4 Linear precoding techniques for single antenna receivers

Each user has only one receive antenna ($n_{R_k} = 1$ for $k = 1, .., K$). In this case, we have $n_R = K$. Various approaches exist to solve the problem of designing linearly $\mathbf{X}$ given $\mathbf{s}$. Some of these techniques are Channel Inversion (CI) and regularized channel inversion methods [25].

2.5.4.1 Channel inversion

The channel inversion technique consists in canceling the effects of the channel by precoding $\mathbf{s}$ with the pseudo inverse $\mathbf{H}^{\dagger}$ of the channel matrix [26]:

$$\mathbf{X} = \mathbf{H}^{\dagger}\mathbf{s} = \mathbf{H}^{\mathbf{H}}(\mathbf{H}\mathbf{H}^{\mathbf{H}})^{-1}\mathbf{s} \qquad for: \quad n_T \geq n_R = K \tag{2.13}$$

The inversion in the Equation 2.13 can be done only when $n_T \geq n_R = K$. In [27], it has been proven that the sum rate as K goes to infinity is constant when $n_T = K$ unlike the capacity bound of a classical SU-MIMO system [28] which increases linearly with $\min(n_R, n_T)$[29].

This poor capacity is explained by looking at the eigenvalues of the matrix $(\mathbf{H}\mathbf{H}^{\mathbf{H}})^{-1}$. This matrix is not well conditioned for random complex Gaussian matrices when $\mathbf{H}$ is square, resulting in a very low SNR at the receivers. The CI technique is then a good solution for low noise or high-power situations [27].

Therefore, any approach to improve channel inversion must seek to reduce the effects of ill-conditioned channel matrices.

2.5.4.2 Regularized channel inversion

One technique used to *regularize* an inverse is to add a multiple of the identity matrix before inverting. This technique is called regularized channel inversion and is written:

$$\mathbf{X} = \mathbf{H}^{H}((\mathbf{H}\mathbf{H}^{H} + \zeta\mathbf{I})^{-1})\mathbf{s} \tag{2.14}$$

where ζ is the regularization parameter.

In practice, the regularization factor, as a function of the total transmitted power P_{Tx}, is commonly chosen as $\zeta = \frac{n_T}{P_{Tx}}$ [27]. It is shown in [27] that this expression approximately maximizes the Signal-to-Interference-plus-Noise Ratio (SINR) at each receiver, and leads to linear capacity growth with n_T[30] [31]. Using this technique, each user sees some interference. Actually, if $\zeta \neq 0$, the transmitter does not cancel out perfectly all interference. Furthermore, this method has less flexibility in adjusting the transmitted power to each user: changing the transmitted power to one user changes the interference for all other users.

2.5.4.3 Discussion

The achievable sum rates for channel inversion and regularized channel inversion methods are explicitly given in [32]. The authors in [27] have discussed their performance versus the increase of the number of users as well as high SNR. The sum rate of regularized inversion has linear growth with K, although its slope is different from the sum capacity. The regularization channel inversion method shows a big improvement over channel inversion method, a gap to capacity bound however remains, especially at high SNR.

The channel inversion and regularized channel inversion methods could be used with multiple antennas ($n_{R_k} > 1$). However, system performance is not optimal. Several

linear methods that take advantage of the presence of multiple antennas at the receivers have been proposed by [33] [34]. The technique that was widely explored for multiple antenna receivers is block diagonalization which is discussed in Subsection 2.5.5.1. This technique relaxes the interference cancellation constraint between spatial streams to interference cancellation between users only.

The rate gap between the BD and CI techniques with perfect Channel State Information at the Transmitter (CSIT) is given in [35]. According to [36], a difference of 3.2 bits/s/Hz is seen between CI and BD sum-rates for the 2-user equipped with 2 antennas case connected to a transmitter with 4 transmitting antennas in indoor scenarios.

2.5.5 Linear precoding techniques for multiple antenna receivers

2.5.5.1 Block diagonalization

Block diagonalization [33], also referred to as block channel inversion, is a generalization of the channel inversion technique when there are multiple antennas at each user. BD scheme is one popular alternative due its low implementation complexity and its capability of approaching the capacity bound at high SNR.

The AP employs a BD precoding matrix $\mathbf{W}_k$ of size $n_T \times N_{ss,k}$ for each user, which transforms the data $\mathbf{s}_k$ to the transmitted vector $\mathbf{W_k s}_k$. The $n_T \times N_{ss}$ precoding matrix is hence defined as: $\mathbf{W} = [\mathbf{W}_1 \dots \mathbf{W}_K]$. For each IEEE 802.11ac OFDM subcarrier, the received signal vector at the k^{th} user is given by:

$$\mathbf{y}_k = \mathbf{H}_k \mathbf{W}_k \mathbf{s}_k + \mathbf{H}_k \sum_{i=1, i \neq k}^{K} \mathbf{W}_i \mathbf{s}_i + \mathbf{n_k} \tag{2.15}$$

where $\mathbf{n_k} = [n_{k,1}, \dots, n_{k,n_{R_k}}]^T$ is the noise vector composed of complex Gaussian random variables for the k^{th} user. The components $n_{k,i}$ are i.i.d. with zero mean and variance σ_n^2 for $k = 1, \dots, K$ and $i = 1, \dots, n_{R_k}$. We define the noise vector $\mathbf{n}$ as: $\mathbf{n} = [\mathbf{n}_1{}^T \mathbf{n}_2{}^T \dots \mathbf{n}_K{}^T]^T$. The corresponding signals $\mathbf{y} = [\mathbf{y}_1^T \mathbf{y}_2^T \dots \mathbf{y}_K^T]^T$ at all users can be arranged as:

$$\mathbf{y} = \mathbf{HWs} + \mathbf{n} \tag{2.16}$$

According to Equation 2.15, the component $\mathbf{H}_k \mathbf{W}_k \mathbf{s}_k$ denotes the desired signal for the k^{th} user, and the other components are the interference values between the k^{th} and the other $K - 1$ users. Hereafter, noise components are ignored. Therefore, it is important for the MU-MIMO technique to eliminate these interference values. In this direction, the BD precoding matrix must satisfy for any $\mathbf{H}_k$ and $\mathbf{s}_i$ with $i \neq k$:

$$\mathbf{H}_k \sum_{i=1, i \neq k}^{K} \mathbf{W}_i \mathbf{s}_i = 0 \tag{2.17}$$

It follows that $\mathbf{H}_i\mathbf{W}_k = 0$ for $i \neq k$ and $1 \leq i, k \leq K$. Here, we define the following new MIMO channel matrix $\tilde{\mathbf{H}}_k$ except for the k^{th} user as:

$$\tilde{\mathbf{H}}_k = \begin{bmatrix} \mathbf{H}_1^T & \dots \mathbf{H}_{k-1}^T & \mathbf{H}_{k+1}^T & \dots & \mathbf{H}_K^T \end{bmatrix} \tag{2.18}$$

The condition in Equation 2.17 implies that $\mathbf{W}_k$ needs to be in the nullspace of $\tilde{\mathbf{H}}_k$ of dimension $dim(Null(\tilde{\mathbf{H}}_k)) = n_T - rank(\tilde{\mathbf{H}}_k)$. Note that the precoding matrix $\mathbf{W}_k$ should be a nonzero matrix, otherwise, no signal is transmitted. To guarantee the existence of a nonzero precoding matrix, a sufficient condition is that the number of the transmit antennas is larger than the sum of the receive antennas of any $K-1$ users [34] and is written as

$$n_T > \max(\sum_{i=1, i\neq k}^{K} n_{R_i}, k = 1, 2, \dots, K) \tag{2.19}$$

The BD precoding matrix $\mathbf{W}_k$ is a cascade of two precoding matrices $\mathbf{A}_k$ and $\mathbf{B}_k$. $\mathbf{W}_k = \mathbf{A}_k\mathbf{B}_k$, where $\mathbf{A}_k$ is computed by Singular Value Decomposition (SVD) in order to nullify the IUI and $\mathbf{B}_k$ is designed using any classical method for optimizing SU-MIMO capacity.

The SVD of the matrix $\tilde{\mathbf{H}}_k$ is defined in Equation 2.20 where $\tilde{\mathbf{U}}_k$, $\tilde{\mathbf{A}}_k$, and $\tilde{\mathbf{V}}_k$ are the left singular vector matrix, the matrix of singular values of $\tilde{\mathbf{H}}_k$ and the right singular vector matrix respectively.

$$\tilde{\mathbf{H}}_k = \tilde{\mathbf{U}}_k\tilde{\mathbf{A}}_k\tilde{\mathbf{V}}_k^H \tag{2.20}$$

We set $\tilde{\mathbf{V}}_k = [\tilde{\mathbf{V}}_k^{(1)}\tilde{\mathbf{V}}_k^{(0)}]$ where $\tilde{\mathbf{V}}_k^{(1)}$ denotes the right singular matrix corresponding to non-zero singular values, referred to as the single space of all users except for the k^{th} user. Term $\tilde{\mathbf{V}}_k^{(0)}$ denotes the right singular matrix corresponding to zero singular values, i.e. singular vectors in the null space which does not interfere with the other $K-1$ users. In order to produce zero interference at the other users, the matrix $\mathbf{A}_k$ is chosen by using the weight matrix $\mathbf{A}_k$ as the null space $\tilde{\mathbf{V}}_k^{(0)}$: $\mathbf{A}_k = \tilde{\mathbf{V}}_k^{(0)}$.

We can see that the dimension of $\tilde{\mathbf{V}}_k^{(0)}$ is $n_T \times N_{ss,k}$. Under the sufficient condition given in Equation 2.19 and the assumption of i.i.d. channel, we can obtain than the dimension $N_{ss,k}$ of the null subspace is $N_{ss,k} = n_T - \sum_{i=0, i\neq k}^{K} n_{R_i}$ [34].

By substituting into Equation 2.15, we obtain Equation 2.21 where the MU-MIMO system denoted by Equation 2.15 has been decoupled to K parallel SU-MIMO systems as depicted in Figure 2.16.

$$\mathbf{y}_k = \mathbf{H}_k\tilde{\mathbf{V}}_k^{(0)}\mathbf{B}_k\mathbf{s}_k + \mathbf{n_k} \tag{2.21}$$

A close observation from Equation 2.21 and Figure 2.16 shows that we can think of an equivalent SU-MIMO channel of user k as $\mathbf{H}_k\tilde{\mathbf{V}}_k^{(0)}$ and the equivalent transmit preprocessing for the equivalent SU-MIMO channel for user k can be represented as $\mathbf{B}_k$. The design of $\mathbf{B}_k$ is the same as designing the transmit preprocessing for a SU-MIMO system. In this report, it is designed to optimize the channel capacity [29] and based

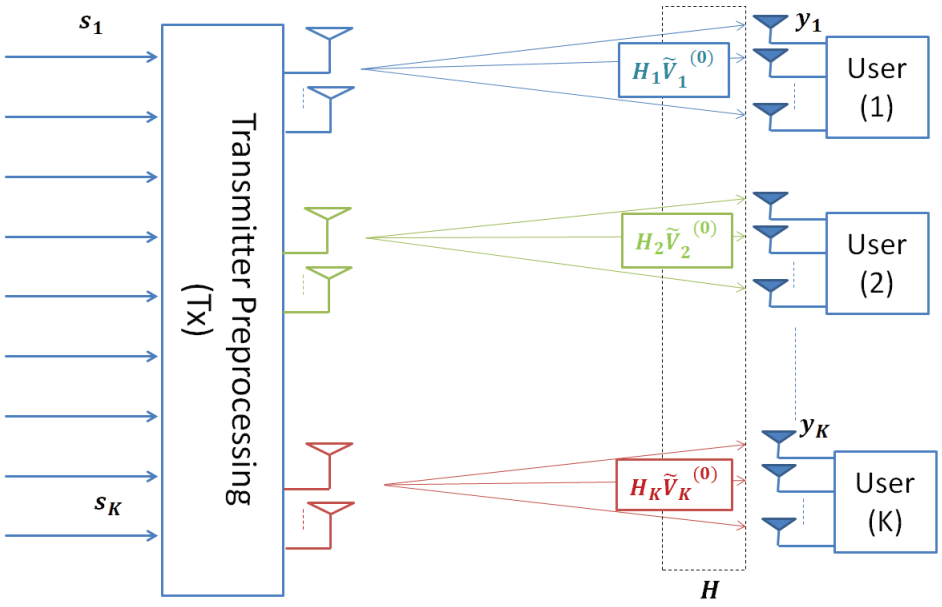

Figure 2.16 – K parallel SU-MIMO channels.

on SVD transmit beamforming. Hence, let us consider the SVD of the new equivalent SU-MIMO channel matrix $\hat{\mathbf{H}}_k = \mathbf{H}_k\tilde{\mathbf{V}}_k^{(0)}$ as:

$$\hat{\mathbf{H}}_k = \hat{\mathbf{U}}_k\hat{\mathbf{A}}_k[\hat{\mathbf{V}}_k^{(1)}\hat{\mathbf{V}}_k^{(0)}]^H \tag{2.22}$$

where $\hat{\mathbf{U}}_k$ and $\hat{\mathbf{V}}_k$ are the left and right singular vectors respectively. $\hat{\mathbf{A}}_k$ is the diagonal matrix whose elements are the the singular values of $\hat{\mathbf{H}}_k$. In order to maximize channel capacity, $\mathbf{B}_k$ matrix is chosen as follows: $\mathbf{B}_k = \hat{\mathbf{V}}_k^{(1)}$.

Therefore, the BD weight matrix at the transmitter is given as

$$\mathbf{W}_k = \tilde{\mathbf{V}}_k^{(0)}\hat{\mathbf{V}}_k^{(1)} \tag{2.23}$$

In this report, we study the two-user case ($K = 2$). The sufficient condition in Equation 2.19 for IUI cancellation is then written as: $n_T > \max(n_{R_1}, n_{R_2})$. The BD precoding implies also that: $N_{ss,k} = \max(0, n_T - \sum_{i=1, i\neq k}^{K} n_{R_i})$ for each user k with the assumption of i.i.d. channel [34].

2.5.5.2 Discussion

The BD scheme has been widely evaluated based on theoretical and measured channels. According to simulations done in [37], it is shown that BD precoding is more effective compared to CI precoding. Actually, the effective channel matrix of the CI precoding is the diagonal matrix at the receiver side. On the other hand, the effective

channel matrix of the BD precoding is a block diagonal matrix. Hence MIMO decoders can take advantage of the diversity present in the inter stream interference for each user.

The authors in [38] evaluate the BD technique using a limited feedback system. They have established the advantage of using BD technique compared to CI in terms of feedback load quantifying the loss based on the throughput as a function of the feedback level.

Based on experimental mobile WiMAX system with real implementation of BD technique, it has been shown in [39] that BD throughput is almost the same using either measured or simulated channels.

The BD scheme is just one of many linear precoding techniques that can be used on the MU-MIMO broadcast channel with multiple user antennas. It is primarily limited when the number of receiving antennas is greater than the number of transmitting antennas.

To overcome the dimensionality constraint, [40] have proposed successive Minimum Mean Square Error (MMSE) precoding (SMMSE). SMMSE provides higher antenna and diversity gain than MMSE by suppressing the interference only between the antennas located at the two different terminals.

In [41], the authors use a different approach by separating the problem of IUI mitigation and the optimization of the overall system performance with respect to the different optimization criteria. The proposed method is called Regularized block diagonalization (RBD).

Different modifications of the original RBD algorithm provide different performance improvements. RBD is capable to adapt to different levels of SNR in order to provide a higher information sum rate of the system. At high SNR and high IUI it is able to provide the high diversity. RBD represents a good compromise between capacity/BER performance and computational complexity.

In [42], the authors propose a linear transmission technique based on the BD technique using joint coordinated transmit-receive processing using a receiver beamformer to select a subset of the eigenmodes of a given user, and a transmitter beamformer in order to guarantee the orthogonality between the different users. This method is evaluated based on numerical results. It has been shown how the proposals achieve a significant fraction of the DPC sum rate for practical systems with finite K, and outperform previous BD schemes.

To sum up, there are various linear precoding techniques and their performance evaluation are compared in the literature. They achieve almost the same capacity with relatively the same complexity. Since BD is the one that has been widely explored in the literature and is used as reference for further improvement or extensions, this report will focus on simulating the MU-MIMO processing based on its principle.

Note also that in the standard 802.11ac uses the feedback to obtain the CSI. Hence, the MU-MIMO is chosen when the SNR is sufficiently high to get an acceptable feedback.

2.5.6 Non-linear precoding techniques

Non-linear precoding techniques are known to be capacity achieving using the notion of DPC, which originates from [43]. This reveals that any known interference at the transmitter can be subtracted without the penalty of radio resources if the optimal precoding scheme is applied on the transmit signal. In other words, it proposes to benefit from the known CSI at the Tx to transmit information, instead of fighting against this interference. Optimal performance can be achieved this way. But this technique is very difficult to be implemented in practice.

There are several suboptimal and simplified variants of dirty paper coding. Other non-linear precoding techniques are Tomlinson-Harashima Precoding (THP), Vector Perturbation (VP) and Lattice Reduction Aided (LRA) methods. However, these techniques have a very computational complexity and are not supported by IEEE 802.11ac.

We present in Appendix B a comparison of BD and DPC capacities based on the correlated TGac-B channel model.

2.6 Channel capacity of wireless channels

An important tool for characterizing the performance of any communication channel is the Shannon capacity. It is the maximum rate of communication for which arbitrarily small error probability can be achieved [29].

A transmission scheme that maximizes the capacity for one user in the network might result in unacceptably high interference for the other users, rendering their links useless. If high throughput is the goal, a better approach might be to maximize the **sum** capacity of the network, or the maximum sum transmission rate, where the IUI is taken into consideration.

2.6.1 SU-MIMO capacity

The capacity of SU-MIMO additive white Gaussian noise channels with CSI known at the transmitter was first studied by Telatar[29] and Foschini [9]. It is the maximum amount of information that can be transmitted as a function of available bandwidth given a constraint power.

The considered SU-MIMO system applies a singular value decomposition and its capacity is computed for each OFDM subcarrier as detailed in [44]:

$$C_{SU-MIMO,k} = \sum_{i=1}^{N_{ss,k}} \log_2(1 + \frac{p_{ik}}{\sigma_n^2}\sigma_{ik}^2) \tag{2.24}$$

where p_{ik} is the allocated power to the i^{th} spatial stream for the k^{th} user, σ_{ik} are the singular values of the channel matrix for the k^{th} user after the singular value decomposition, and σ_n^2 is the noise power.

Since we evaluate in this thesis the case of two users $K = 2$, we denote C_1 and C_2 the provided capacities for these two users respectively.

We evaluate two types of channel access: Time Division Multiple Access (TDMA) usually used in published results and CSMA/CA specific to 802.11ac. Let L_i and t_i the frame length and time slot corresponding to the i^{th} user where $i \in [\![1, 2]\!]$, as depicted in Figure 2.17.

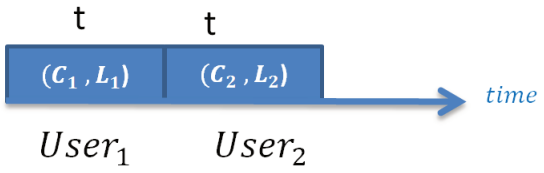

(a) TDMA (same time slot t)

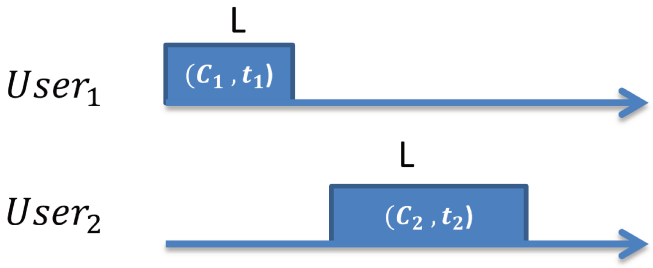

(b) CSMA/CA (same frame length L)

Figure 2.17 – TDMA and CSMA/CA channel access methods.

We assume a perfect CSI at the transmitter. Furthermore, for the sake of simplification, we do not take into account the schemes of the CSMA/CA protocol like the channel sounding. In fact, the 802.11ac standard is based on CSMA/CA protocol. The SU-MIMO capacity for a 2-user system is expressed according to the applied channel access method. We give further the capacity for the two channel access methods.

2.6.1.1 TDMA method

In the literature, the SU-MIMO sum capacity is often computed considering the deterministic TDMA which allows several users to share the same frequency channel by dividing the signal into equal time slots.

Let us consider the time slot $t = t_1 = t_2$. According to Figure 2.17(a), the frame length of the SU-MIMO, denoted L_{SU}, is as: $L_{SU} = L_1 + L_2$ where $L_1 = C_1 \times t_1$ and $L_2 = C_2 \times t_2$. Thus, the TDMA sum capacity of the SU-MIMO system $C_{SU,TDMA} \times (2t) = C_1 \times t + C_2 \times t$. Therefore, the TDMA SU-MIMO sum capacity is computed using the

arithmetic mean of C_1 and C_2 as can be seen in Equation 2.25.

$$C_{SU,TDMA} = \frac{C_1 + C_2}{2} \tag{2.25}$$

2.6.1.2 CSMA/CA method

The IEEE 802.11ac standard uses for the channel access the CSMA/CA method, where each user verifies the absence of other co-channel signals before transmitting a frame. The data frames are supposed to have equal size for each user, denoted below $L = L_1 = L_2$, which implies a variable transmission duration [15]. According to Figure 2.17(b), the time duration of the SU-MIMO, denoted t_{SU}, is as: $t_{SU} = t_1 + t_2$. Thus, the CSMA/CA sum capacity of the SU-MIMO system $\frac{(2\times L)}{C_{SU,CSMA}} = \frac{L}{C_1} + \frac{L}{C_2}$. Hence, the CSMA/CA SU-MIMO sum capacity is then equal to the harmonic mean of C_1 and C_2 expressed as in Equation 2.26. We recall that ideal CSI is considered with no protocol or frame overhead in this ideal case.

$$C_{SU,CSMA} = \frac{2}{\frac{1}{C_1} + \frac{1}{C_2}} \tag{2.26}$$

2.6.2 MU-MIMO capacity

For a MU-MIMO system with K users and n_{R_k} receiving antennas for each user k, the sum rate using BD [32] for a particular propagation channel sample is expressed for each OFDM subcarrier by Equation 2.27.

$$C_{MU-MIMO} = \sum_{k=1}^{K} \sum_{i=1}^{N_{ss,k}} \log_2(1 + \frac{p_{ik}}{\sigma_n^2} \mu_{ik}^2) \tag{2.27}$$

where p_{ik} is the power dedicated to the i^{th} spatial stream for the k^{th} user, μ_{ik} are the singular values of the effective channel for the k^{th} user after applying the IUI cancellation, and σ_n^2 is the noise power. The methods of scaling the power will be analyzed in the following chapter.

2.7 Main existing results and future works

Compared to a SU-MIMO TDMA system, DPC can bring a theoretical performance gain in terms of channel capacity of up to $\max(\min(n_T/n_{R_k}, K), 1)$ in an i.i.d. Rayleigh fading channel [32]. The expected loss in Rayleigh fading due to block diagonalization compared to DPC is given in Appendix B.

BD and DPC techniques are shown to be equivalent at low and very high SNR, small number of users (low K), and high number of transmitting antennas [32][35].

Most MU-MIMO studies are based on Rayleigh channels, and only few articles addresses the MU-MIMO challenges based on indoor measurements (see Appendix C).

Some measured channels show an increase of the sum rate capacity over SU-MIMO by a factor of 3.2 using DPC and by a factor of 2.7 using Regularized Channel Inversion (RCI) with four transmit and four users with one receive antenna each at high SNR[45]. These results encourage us to simulate the MU-MIMO processing based on BD technique since it outperfoms the RCI technique. The DPC gain compared to BD is however important with large number of users [35] which is not the case with 802.11ac standard. It actually limits the max number of users to 4 in a MU-MIMO group.

It has been shown in [46] that channel correlation impacts capacity gap. Still, this result is based on single antenna users. The authors in [47] prove that MU-MIMO capacity gain becomes insignificant comparing to SU-MIMO when n_R increases with 16 transmitting antennas. Furthermore, the MU-MIMO is highly sensitive to Doppler [48],[49].

Chapter 3

MU-MIMO capacity simulations for standardized indoor channels (TGac)

Contents

3.1 Introduction

The first objective of this thesis is to refine the capacity gains by identifying deployment recommendations or optimal system configuration for indoor MU-MIMO compared to the SU-MIMO systems. Accordingly, the aim of this chapter is to give recommendations to optimize MU-MIMO performance based on TGac simulations in

terms of channel propagation parameters and users' configuration: LOS, NLOS, distances...

Consequently, this chapter is organized as follows. First, a detailed description of the simulation process, the evaluated channel model and its parameters are given in Section 3.2. Next, we provide the simulation results of the impact of antennas and propagation channels on the BD capacity gain over SU-MIMO in Section 3.3. Afterwards, we study in Section 3.4 the impact of transmit power control meeting the European regulation requirements for WLAN in the 5 GHz frequency band in terms of EIRP. Finally, we conclude in Section 3.5 by summarizing system recommendations for an optimal use of MU-MIMO compared to SU-MIMO.

3.2 TGac-B channel model

3.2.1 Simulation setup

Since we study the benefit of using MU-MIMO techniques in home networks in the context of the arrival of the optical fiber to the home, this chapter shows results according to the channel model TGac$-B$. Actually, the TGac-B channel model covers the scenarios of residential environments. It has a path loss model including shadowing, and a MIMO multipath fading model which describes the multipath power delay profile, the spatial properties, the Rician K-factor, the Doppler spectrum and the PAS.

Typically, the fading process is characterized by a Rayleigh distribution for the non line-of-sight paths and a Rician distribution for a line-of-sight path. The TGac-B channel model has 9 Rayleigh-fading taps, and each tap has a Bell Doppler spectrum to consider the random time variability of an indoor channel due to human activity for example. Each tap is characterized by a relative delay (with respect to the first path delay). It further comprises a number of clusters, which correspond to overlapping subsets of the tap delays. Each cluster is assigned a set of spatial properties: a mean AoA, a mean AoD, an AS at the receiver, and an AS at the transmitter. These parameters assume the same values for all tap delays pertaining to a given cluster. These parameters determine according to the procedure given in [20] the transmit and correlation matrices associated with each tap delay. The relative motion between the transmitter and receiver causes Doppler shifts. Local scattering typically comes from many angles around the user. This scenario causes a range of Doppler shifts, known as the Doppler spectrum. The maximum Doppler shift corresponds to the local scattering components whose direction exactly opposes the user's trajectory.

A Matlab source code [20] was used to compute the different 802.11ac channel samples based on the implementation of fading channels as objects. The main loop of the source code is designed to process *Fading Number Of Iterations* bursts of samples. In our case, its value is set in the Matlab channel model to 512. The length of a burst can be expressed in coherence times, where the coherence time is defined in the TGn channel models as the inverse of the *Cut-off frequency* $f_{D_{Hz}} = 5.8333$ Hz which is the ratio between the wavelength and the movement speed of the scattering environment v_0. In

our simulation, we use a simulation length equal to 55 coherence times of the MIMO channel to simulate the fast fading. The choice of the value 55 for coherence times is justified by the convergence of the MU-MIMO to SU-MIMO capacity gain as the value of coherence times is increasing as can be seen in Figure 3.1. The figure gives the MU-MIMO to SU-MIMO capacity gain versus the simulation length in coherence times for a system with two receivers with two antennas each, both in NLOS with the Tx equipped with 4 antennas. The antennas are spaced with half wavelength. The capacity is computed using an average $SNR = 20$ dB. The simulation values stabilize after the fictive threshold of 50 coherence times. Table 3.1 summarizes the input parameters used for our simulations.

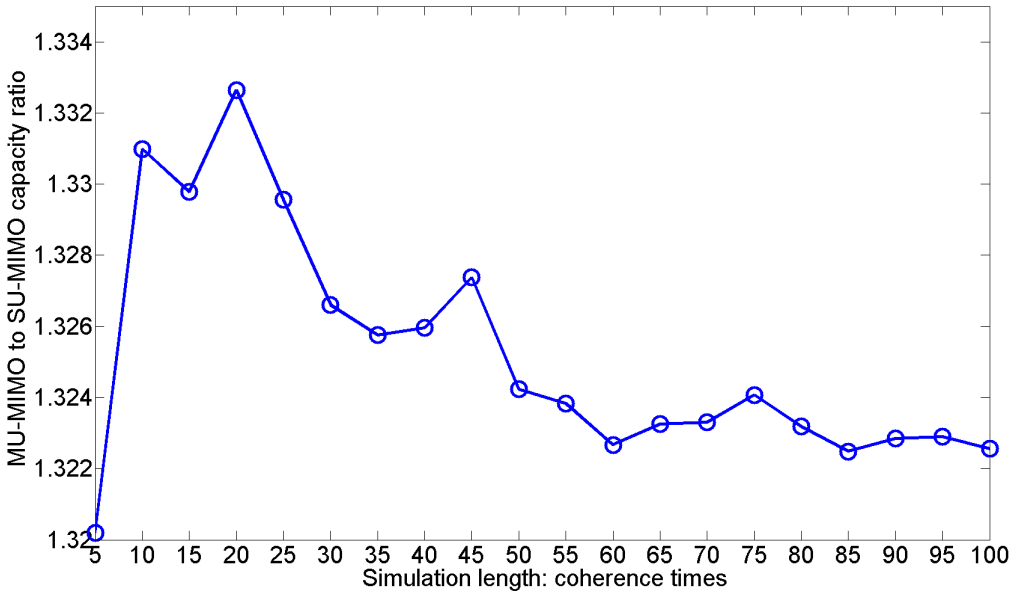

Figure 3.1 – MU-MIMO to SU-MIMO capacity gain versus the simulation length values.

Number of iterations of the vector of fading coefficients $FadingNumberOfIterations$	512
Length of simulation in CoherenceTimes $SimulationLengthInCoherenceTimes = \frac{1}{f_{D_{Hz}}}$	55
Sampling rate of the simulation $SamplingRate$	2500 Hz
Speed of moving scattering environment v_0	1.2 km/h

Table 3.1 – Global parameters set for TGac-B channel model.

To have statistical results and various AoA and AoD angles, 100 couples of two

users ($K = 2$) are randomly drawn around the access point. For each drawing, 488 interpolated channel time samples, denoted $N_{samples}$, are collected for each couple of users.

The delay domain channel was converted to frequency domain by discrete Fourier transform taking into account the characteristics of IEEE 802.11ac: $N = 56$ subcarriers spaced by $\Delta f = 312.5$ kHz.

Thereafter, a uniform linear array of antennas at the AP is simulated with the propagation channel model TGac-B (15 ns RMS delay spread) for the 5.25 GHz frequency band. Note that linear array antenna is the only antenna array geometry supported by TGac channel model. The simulated system is composed of one access point equipped with multiple antennas (linear array of 0 dBi omnidirectionnal and vertically polarized antennas), and two receivers. Each receiver has two 0 dBi omnidirectionnal antennas. By default, the antenna spacing is set to 0.5 λ for both the transmitter and the receiver.

3.2.2 Normalization

It is demonstrated in [50] that the physics of antenna arrays and propagation channel should be taken into account when the normalization of the channel matrix is chosen, so that SNR has proper physical meaning. The conclusions are physical and correspond to realistic systems. The paper pointed out various normalizations and gave equivalent formulas for different parameters needed. The antenna array geometry and the transmission strategy (coherent/non-coherent) limit the choice of normalization and determine how the capacity and other performance metrics scale with the number of antennas, which is more pronounced for densely-populated antenna arrays. The commonly used normalization is $E(\|\mathbf{H}\|_F^2) = n_T n_R$. It corresponds to a 0 dB average path loss. This normalization implies the equality in Equation 3.1.

$$\frac{1}{N_{samples}} \sum_{p=1}^{N_{samples}} \sum_{i=1}^{n_R} \sum_{j=1}^{n_T} |H_{ij}|^2 = n_T n_R \tag{3.1}$$

For the sake of simplicity, we omit to write the components of the channel matrix as a function of the index of the channel sample p ($N_{samples} = 488$).

We denote the normalized channel matrix $\mathbf{H}^{'}$. We have $\mathbf{H}^{'} = \alpha \mathbf{H}$ where α is the normalization constant. Thus, the normalized channel matrices $\mathbf{H}_1^{'}$ and $\mathbf{H}_2^{'}$ for each user are given in Equation 3.2.

$$\begin{cases} \mathbf{H}_1^{'} = \sqrt{\dfrac{n_T n_{R_1} N_{samples}}{\sum_{p=1}^{N_{samples}} \sum_{i=1}^{n_{R_1}} \sum_{j=1}^{n_T} |H_{1ij}|^2}} \mathbf{H}_1 \\ \mathbf{H}_2^{'} = \sqrt{\dfrac{n_T n_{R_2} N_{samples}}{\sum_{p=1}^{N_{samples}} \sum_{i=1}^{n_{R_2}} \sum_{j=1}^{n_T} |H_{2ij}|^2}} \mathbf{H}_2 \end{cases} \tag{3.2}$$

3.2.3 TGac and Rayleigh channel

Rayleigh fading is exhibited for each tap (except for the LOS tap which follows a Rice fading with a 0 dB Rician factor), with the assumption that the real and imaginary parts of the taps are modeled by i.i.d. zero-mean Gaussian processes so that different taps are uncorrelated.

By setting the distance between the Tx and the Rx, the TGac-B channel model simulates either the LOS or NLOS. Indeed, LOS conditions are assumed only up to a breakpoint distance $d_{BP} = 5$ m ($d_{BP} = 5$ m for TGac-B channel). Since the Rician factor for LOS is set to 0 dB which is very close to a Rayleigh channel, almost similar results are obtained with the TGac-B LOS and NLOS scenarios. This 0 dB weak Rice factor of the model B clearly appears in the Cumulative Distribution Function (CDF) of the first tap of Figure 3.2. It almost merges with the CDF of the Rayleigh distributed amplitude of the other taps. In Figure 3.2, the curve in green corresponds to the reference values, whereas the blue curves are the outcomes of the simulation for the 9 taps. This chapter is focusing on the TGac-B NLOS channel model after giving an example of LOS numerical results.

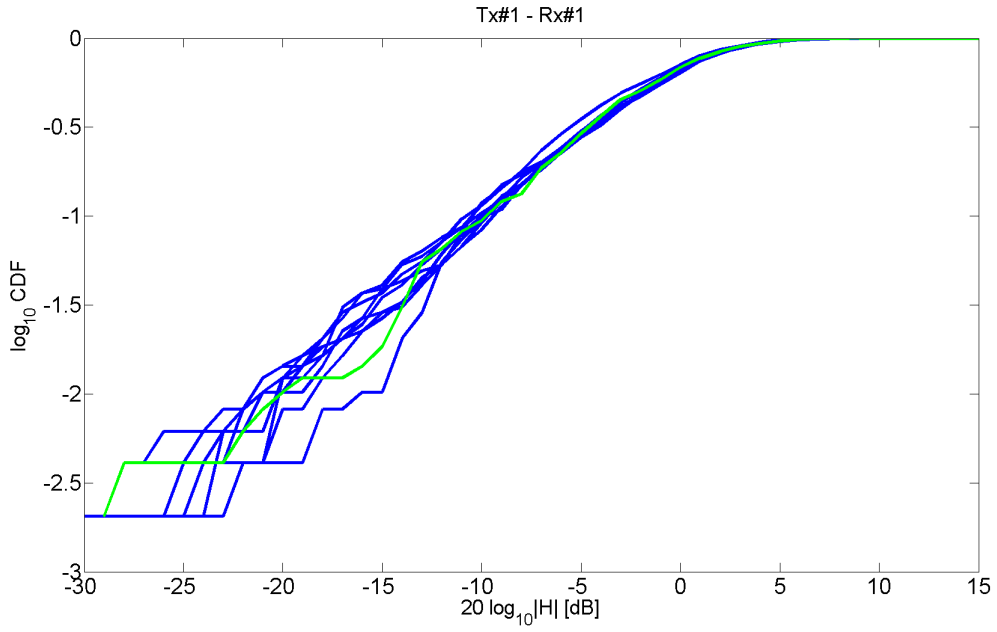

Figure 3.2 – CDF of the taps power of TGn Channel Model Case B (9 taps)

We recall that for each IEEE 802.11ac OFDM subcarrier, the channel matrix is computed through a discrete Fourier transformation ($N = 56$ subcarriers for a 20 MHz channel) of the tap delay representation. To have comparisons with an ideal case, we also study a non-correlated Rayleigh channel.

3.3 Impact of antennas and spatially correlated propagation channel on BD capacity gain

The objective of this thesis it to know which among the MU-MIMO and SU-MIMO techniques is better in a residential environment. Thereby, most graphs in this chapter highlight the MU-MIMO capacity gain over SU-MIMO expressed as the average of MU-MIMO (simulated BD method) to SU-MIMO capacity ratio. For 2 users, the optimal value of MU-MIMO to SU-MIMO capacity gain is theoretically proven to be 2 for TDMA system based on a Rayleigh channel. Indeed, compared to a SU-MIMO TDMA system, DPC can bring a theoretical performance gain of up to $\max(\min(n_T/n_R, K), 1)$ in an i.i.d. Rayleigh fading channel [51].

We first study in this section the impact of antennas and propagation channel on the BD capacity gain for IEEE 802.11ac MU-MIMO in home networks. No EIRP constraint is considered in this section. We examine the effect of the number of the transmitting antennas, their spacing, and the average SNR, defined as the ratio of P_{Tx} to the average noise power: $SNR = \frac{P_{Tx}}{N\sigma_n^2}$, where $N = 56$ is the total number of subcarriers defined in IEEE 802.11ac standard for a 20 MHz bandwidth.

P_{Tx} is considered equally shared among the N subcarriers throughout this thesis. Other strategies could be considered as in [52]. However, the impact of Peak-to-Average Power Ratio (PAPR) should be globally studied. We also draw for comparative study the results for i.i.d. Rayleigh channels. The aim of this study is to assess the weight of each parameter on the BD capacity gain over SU-MIMO and to give recommendations to optimize MU-MIMO performance.

3.3.1 Transmit antenna spacing effect

For the following, the number of transmitting antennas is fixed to $n_T = 6$, and $SNR = 20$ dB. To study the impact of the transmitting antenna spacing, six values are used: 0.25 λ, 0.5 λ, 0.75 λ, 1 λ, 1.25 λ and 1.5 λ. No antenna coupling is considered [53][54][49].

In Figure 3.3, the first value (0.25 λ) presents an isolated and very low gain (33%) compared to the other spacings. For a transmit antenna spacing of 0.5 λ and 0.75 λ, the capacity gain of MU-MIMO compared to SU-MIMO is around 50%. For a transmit antenna spacing of 1 λ and above, the capacity gain of MU-MIMO compared to SU-MIMO is around 53% and it almost attains the gain in a Rayleigh channel. Antenna spacing has no effect on the Rayleigh channel since its MU-MIMO channel matrix elements are complex Gaussian and independent. Considering a trade-off between the overall antenna size and the MU-MIMO capacity gain, we recommend an antenna spacing equal to 0.5 λ. This is set as the default value for the rest of this report.

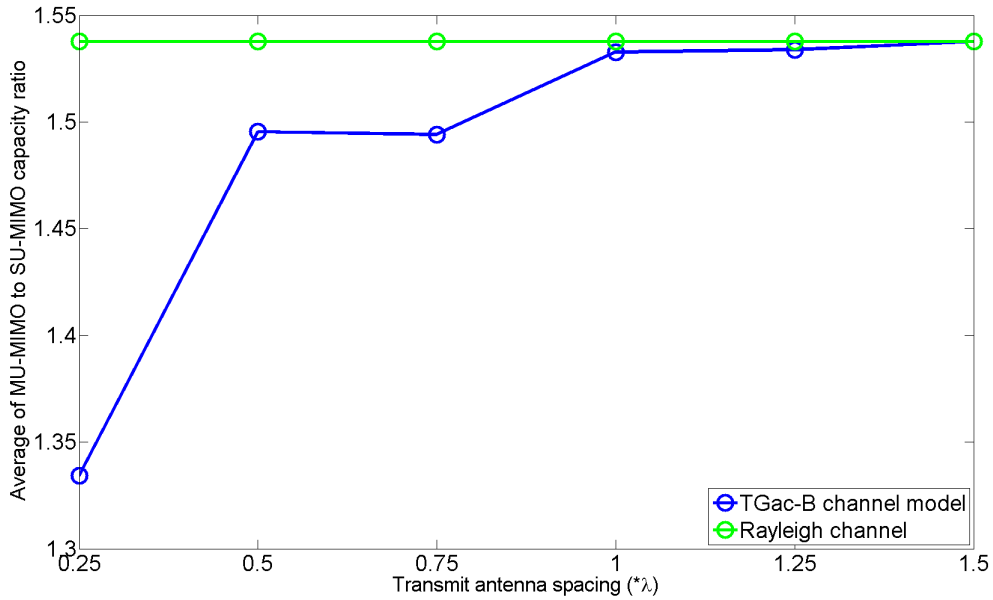

Figure 3.3 – Average of MU-MIMO to SU-MIMO capacity ratio versus transmit antenna spacing.

3.3.2 SNR effect

Figure 3.4 shows the MU-MIMO capacity gain over SU-MIMO versus SNR with 6 transmitting antennas spaced by 0.5 λ in NLOS conditions. For high SNR, MU-MIMO outperforms SU-MIMO in terms of capacity with gain changing from 10% till 70%. Nevertheless, for low SNR, SU-MIMO performs better than MU-MIMO in terms of capacity which has been described already in the limitations of BD scheme. Note that it is not practical to have too low SNR for MU-MIMO as it would not be possible to have CSI with no errors to apply the precoding.

The MU-MIMO to SU-MIMO capacity gain is 30% when the SNR increases from 0 to 10 dB, from 10 to 20 dB, or from 20 to 30 dB, and around 10% when it changes from 30 to 40 dB. To conclude about the SNR, the desired range and the desired bit rate are put forward. For the following results, a middle case is evaluated with $SNR = 20$ dB.

3.3.3 Number of transmitting antennas

In this subsection, we assess the impact of increasing the number of transmitting antennas on MU-MIMO to SU-MIMO capacity gain. Under the same total transmitted power, we have considered two transmitted power allocation strategies. We first share the allocated power equally among the spatial streams. Secondly, we optimize the power allocation using the Water-filling algorithm. In both cases, the SNR is set to $SNR = 20$ dB.

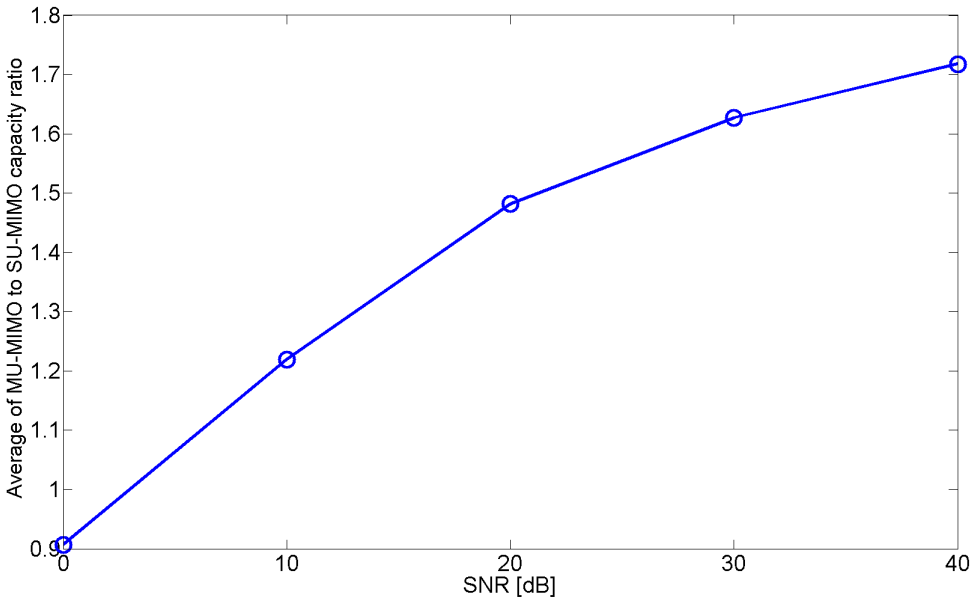

Figure 3.4 – Average of MU-MIMO to SU-MIMO capacity ratio versus the SNR with 6 transmitting antennas spaced by 0.5 λ in NLOS conditions.

3.3.3.1 Equal power sharing

We assume here that the transmitted power is equally shared among the spatial streams. Figure 3.5 gives the average of MU-MIMO to SU-MIMO capacity ratio versus the number of transmitting antennas for the TGac-B NLOS and Rayleigh channels. Average values, 10% and 90% quantiles (q_{10} and q_{90}) are represented to estimate the confidence intervals. The first observation drawn from Figure 3.5 is that the MU-MIMO capacity gain over SU-MIMO increases with the number of transmitting antennas. It changes from 1.2 to 1.65 for the residential environment, i.e. around 45% of capacity gain. We also observe that the gain from $n_T = 4$ to $n_T = 6$ is much higher than the one observed from $n_T = 6$ to $n_T = 8$ or the one observed from $n_T = 8$ to $n_T = 10$. This can be explained by the fact that we cannot take benefit of the transmit beamforming for $n_T = 4$, since the number of transmitting antennas is the same as the total number of spatial streams. Another explanation concerning the channel correlation is given hereafter.

In order to optimize the MU-MIMO capacity gain and have a less congested system, we recommend using $n_T = 6$, when we have a system with two receivers and two antennas each. Figure 3.6 shows the average capacity value for MU-MIMO and SU-MIMO. The capacity value for MU-MIMO increases more rapidly than SU-MIMO. It achieves 27.5 bits/s/Hz versus 16.5 bits/s/Hz for SU-MIMO for $n_T = 10$.

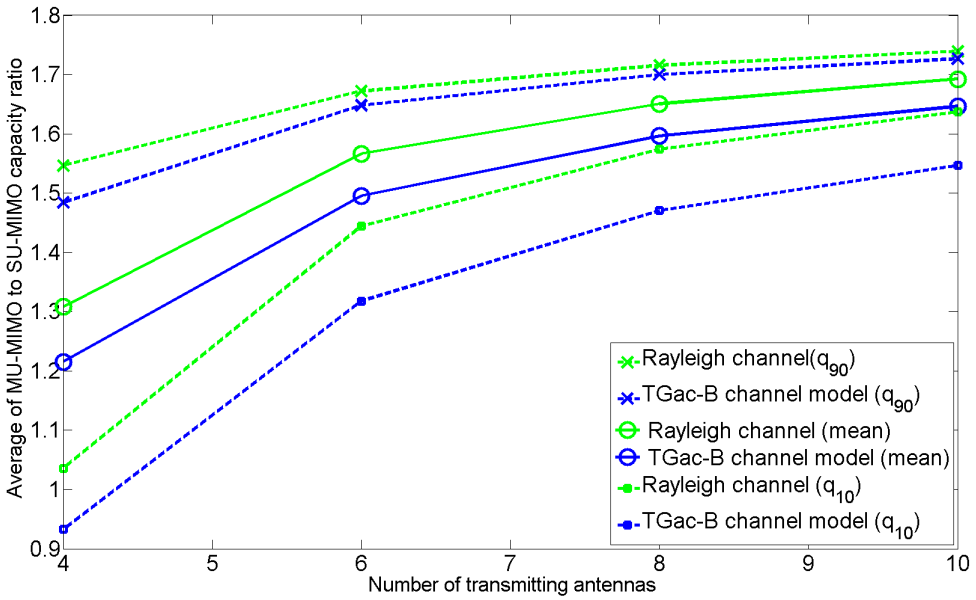

Figure 3.5 – Average of MU-MIMO to SU-MIMO capacity ratio versus the versus the number of transmitting antennas.

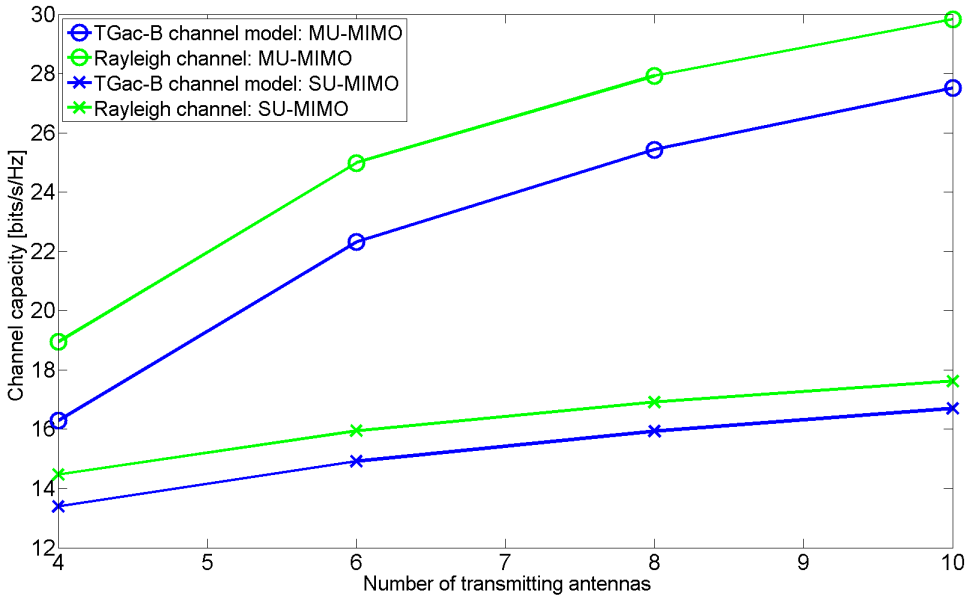

Figure 3.6 – Channel capacity values versus the number of transmitting antennas.

3.3.3.2 Optimized power sharing: Water-filling algorithm

The capacity of the MU-MIMO system can be further increased if we assign extra power at the transmitter by allocating the power according to the Water-filling algorithm to all the channels. The capacity optimization problem is presented in Equation 3.3

$$\begin{cases} \max \limits_{subcarrier} \sum_{k=1}^{K} \sum_{i=1}^{N_{ss,k}} \log_2(1 + \frac{p_{ik}}{\sigma_n^2}\mu_{ik}^2) \\ \text{such that} \quad \sum_{k=1}^{K} \sum_{i=1}^{N_{ss,k}} p_{ik} = \frac{P_{Tx}}{N} \end{cases} \tag{3.3}$$

The power p_{ik} is allocated according to the Water-filling algorithm. The problem 3.3 is a constrained maximization problem solved based on Lagrange technique. This technique is characterized by the Lagrange multiplier $\lambda_{Lagrange}$ by maximizing the function F defined in Equation 3.4. In our case, we have considered a maximization for each subcarrier separately.

$$F = \sum_{k=1}^{K} \sum_{i=1}^{N_{ss,k}} \log_2(1 + \frac{p_{ik}}{\sigma_n^2}\mu_{ik}^2) - \lambda_{Lagrange}(\frac{P_{Tx}}{N} - \sum_{k=1}^{K} \sum_{i=1}^{N_{ss,k}} p_{ik}) \tag{3.4}$$

From Equation 3.4, we deduce the expression of $p_{ik} = (\frac{1}{\lambda_{Lagrange}} - \frac{\sigma_n^2}{\mu_{ik}^2})^+$, where $(.)^+$ is defined as: $(x)^+ = x$ if $x \geq 0$ and $(x)^+ = 0$ if $x < 0$. The Lagrange multiplier is found based on the constraint of the optimization problem. The process of Water-filling algorithm is similar to pouring the water in the vessel. The unshaded portion of the graph in Figure 3.7 represents the inverse of the power gain of a specific channel. The shadow portion represents the power allocated or the water. In [55], a practical algorithm is detailed to evaluate numerically a general Water-filling solution.

Figure 3.8 analyzes the benefit of using Water-filling algorithm in optimizing the MU-MIMO capacity gain over SU-MIMO. It shows the average of MU-MIMO to SU-MIMO capacity ratio versus the number of transmitting antennas for TGac-B channel NLOS using or not the Water-filling algorithm.

Average values, 10% and 90% quantiles (q_{10} and q_{90}) are represented to estimate the confidence intervals. The first observation drawn from Figure 3.8 is that the average MU-MIMO capacity gain over SU-MIMO is almost the same as the obtained gain using the Water-filling algorithm with slight gain in 90% quantiles: around 5%. This is explained by the fact that both MU-MIMO and SU-MIMO systems take benefit from the Water-filling algorithm as was proven widely in the literature. Hence, using this complex algorithm for increasing MU-MIMO capacity gain is not necessary. Next section will explore other ways in optimizing MU-MIMO system satisfying a given power or EIRP constraint.

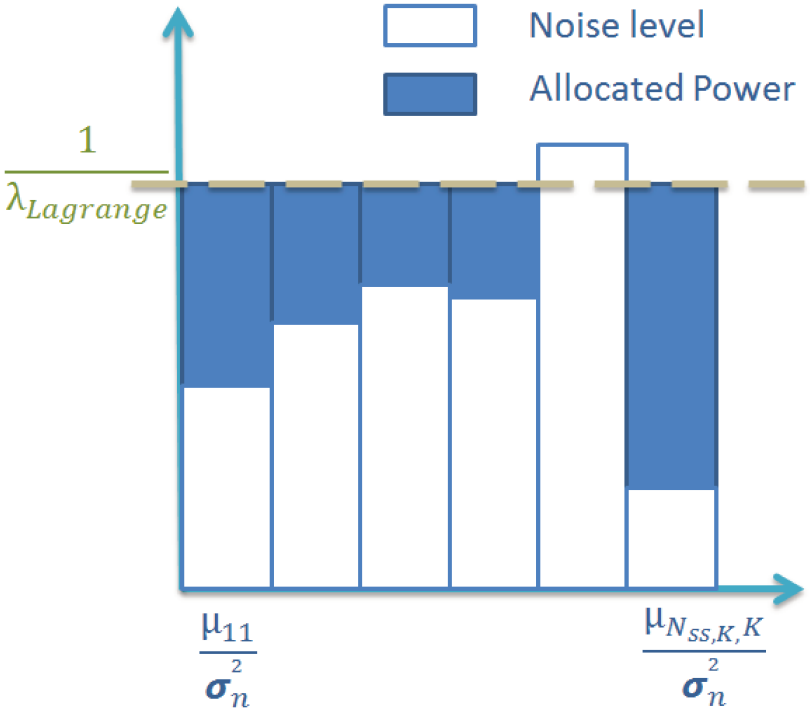

Figure 3.7 – Water-filling model.

3.3.4 Correlation coefficient

3.3.4.1 Definition and overview

In this section, a correlation parameter is explored as a relevant parameter to explain the previous results related to the increase of the number of transmitting antennas n_T and MU-MIMO capacity gain. This parameter is used to analyze the correlation of the MIMO channels $\mathbf{H}_1$ and $\mathbf{H}_2$ between the AP and each user.

MU-MIMO channel correlation coefficient ρ was previously studied for the particular case of receivers with a single antenna [56]. In the case of of multi-antenna receivers, there is not a single definition of the channel correlation. Several possibilities exist in the literature. We can define the matrix distance dM [57] [58]. It is expressed in Equation 3.5. This metric measures the *orthogonality* between the considered channel matrices.

$$dM = \frac{\mid trace(\mathbf{H}_1 {\mathbf{H}_2}^H) \mid}{\mid\mid \mathbf{H}_1 \mid\mid_F \mid\mid {\mathbf{H}_2}^H \mid\mid_F} \tag{3.5}$$

We can also explore the orthogonality related coefficient ro [56] expressed as:

$$ro = \frac{\left\| \mathbf{H}_1 {\mathbf{H}_2}^H \right\|_F^2}{n_{R_1} n_{R_2}} \tag{3.6}$$

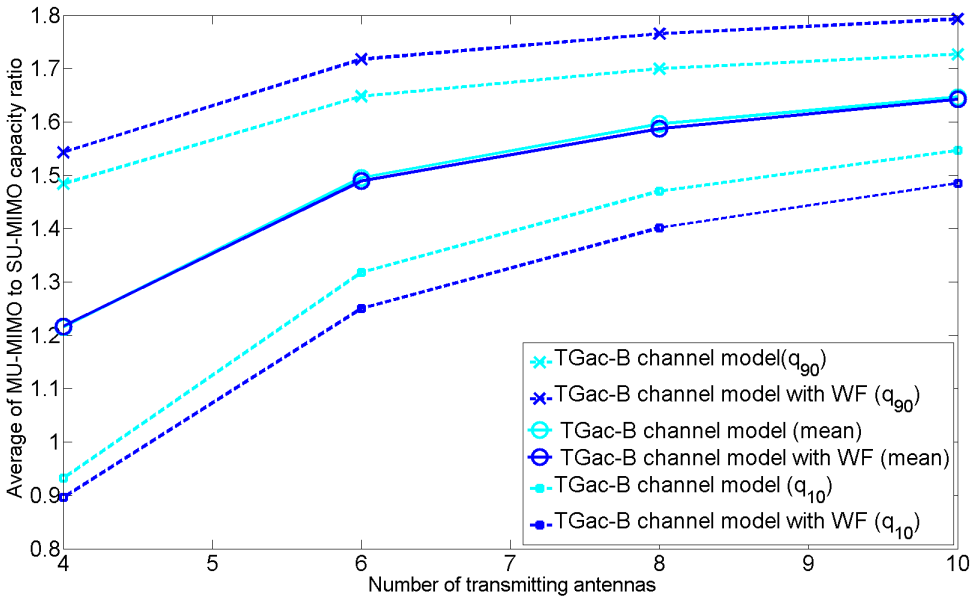

Figure 3.8 – Average of MU-MIMO to SU-MIMO capacity ratio versus the number of transmitting antennas.

Theoretical studies comparing BD to DPC have proved that in the particular case where $n_T > n_R$, BD achieves the DPC optimal bound if $\mathbf{H}_1\mathbf{H}_2{}^H = 0$ [59]. This result means that when the user channels are mutually orthogonal, BD can achieve the DPC capacity bound. The opposite side ($\mathbf{H}_1 = \mathbf{H}_2{}^H$) is considered to be the worst case for MU-MIMO [33]. Actually, with BD, each user precoding matrix lies in the null space of all other users' channels. Hence, if $\mathbf{H}_1 = \mathbf{H}_2$, then $\mathbf{H}_2 = \tilde{\mathbf{V}}_1^{(0)}$.

These theoretical results for extreme cases and our simulations revealed that the definition in Equation 3.7 was the most relevant to explain MU-MIMO to SU-MIMO capacity gain [60].

$$\rho = \frac{\left\|\mathbf{H}_1\mathbf{H}_2{}^H\right\|_F^2}{n_{R_1} n_{R_2}} \tag{3.7}$$

Let us define the rows of the channel matrix of the j^{th} user as: $\mathbf{H}_j = (\mathbf{L}_1^j, \ldots, \mathbf{L}_{n_{R_j}}^j)^T$ where $\mathbf{L}_i^j = (l_{i,1}^j, \ldots, l_{i,n_T}^j)$ represents the i^{th} row of dimension $1 \times n_T$. The applied channel normalization implies that $|| \mathbf{L}_i^j ||= 1$.

The product $\mathbf{H}_1\mathbf{H}_2{}^H = (\mathbf{L}_1^1, \ldots, \mathbf{L}_{n_{R_1}}^1)^T(\mathbf{L}_1^2, \ldots, \mathbf{L}_{n_{R_2}}^2)^H$ is a matrix whose elements

are: $\left(\mathbf{L}^1{}_i\mathbf{L}^2{}_j{}^H\right)_{\substack{1\leq j\leq n_{R_1}\\1\leq i\leq n_{R_2}}}$. Hence, the correlation coefficient can be expressed as:

$$\rho = \frac{1}{n_{R_1} n_{R_2}} \sum_{i=1}^{n_{R_1}} \sum_{j=1}^{n_{R_2}} || \mathbf{L}_i{}^1\mathbf{L}_j{}^{2H} ||^2 \tag{3.8}$$

The component $|| \mathbf{L}_i{}^1\mathbf{L}_j{}^{2H} ||^2$ represents the correlation between each single receiving antenna subsystem of the first user and each single receiving antenna subsystem of the second user. This is the more common correlation coefficient used in the case of single antenna receivers. $E(\rho)$ represents an average value of the correlation coefficient between any single antenna receiver subsystem combination.

The impact of the number of transmitting antennas versus average correlation coefficient $E(\rho)$ is presented in Figure 3.9. The averaging is performed over all the MU-MIMO channel samples. The average correlation coefficient decreases with the increase of the number of transmitting antennas. The two types of residential channel (LOS, NLOS) follow the same trend. The values are higher but remain relatively close to the ones obtained for i.i.d. Rayleigh channel. We can observe that even if the simulated Rayleigh channel has independent elements in $\mathbf{H}_1$ and $\mathbf{H}_2$, the average correlation coefficient $E(\rho)$ is not zero, which is not an intuitive result. Through analytic calculation (see next subsection), the average correlation coefficient ρ for an i.i.d. MIMO Rayleigh fading channel is proven to be: $E(\rho) = \frac{1}{n_T}$.

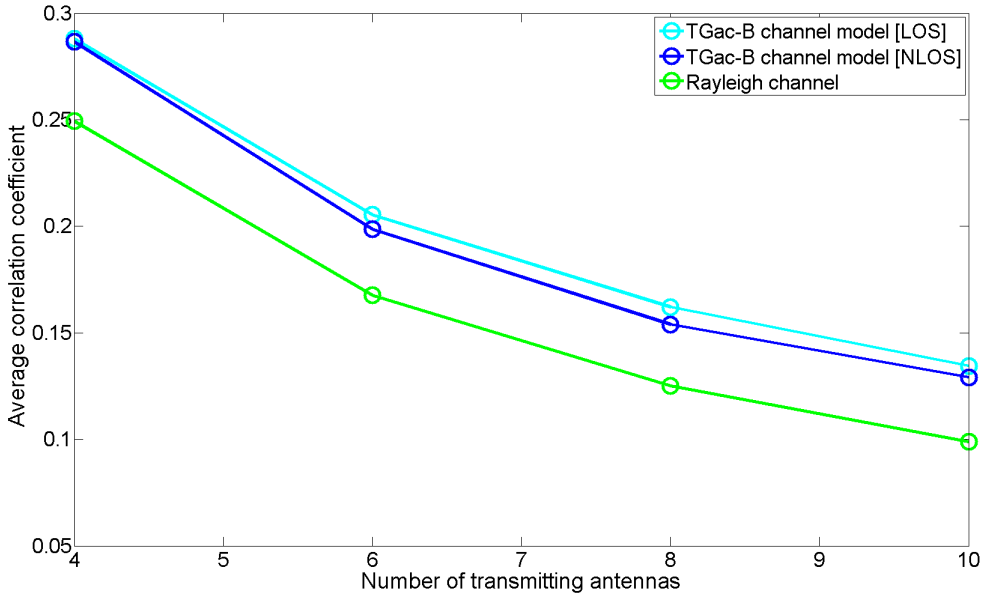

Figure 3.9 – Average correlation coefficient versus the number of transmitting antennas.

In Figure 3.10, we highlight the effect of transmit antenna spacing on the defined correlation coefficient for a Tx with 6 transmitting antennas in NLOS conditions. The figure shows that increasing the antenna spacing decorrelates the channels to attain the optimum value 0.17 obtained for the Rayleigh channel. The recommended value of 0.5 λ spacing gives a correlation coefficient value of 0.2 which is very close to the optimal value.

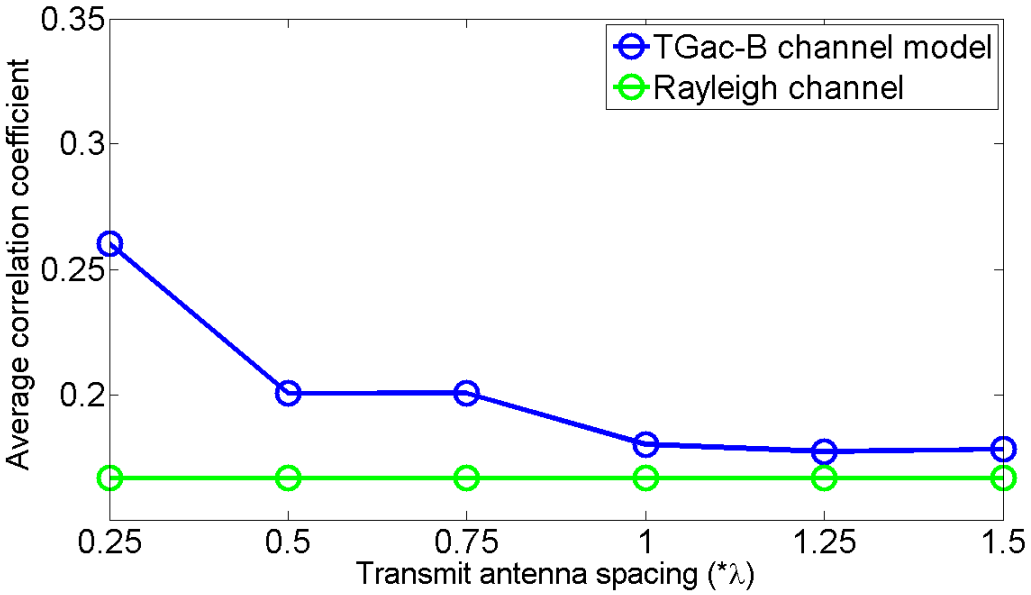

Figure 3.10 – Average correlation coefficient versus transmit antenna spacing.

3.3.4.2 Impact of correlation coefficient on capacity gain

The average of MU-MIMO to SU-MIMO capacity ratio versus the average of the correlation coefficient $E(\rho)$ is presented in Figure 3.11 considering $n_T = 6$. The average is computed here only over time, and each point represents one of the 100 samples of user couples. When the correlation coefficient increases, the capacity gain decreases: more than 30% of capacity loss when the correlation coefficient goes from 0.05 to 0.35. Actually, when both channels ($\mathbf{H}_1$ and $\mathbf{H}_2$) are correlated, close in other words, the BD algorithm does not show great performance since the existence of the precoding matrix is not guaranteed [33]. Thus, the gain decreases. It could be the case when the two users are close. This correlation coefficient has another advantage: it can be computed to optimize the users grouping in a MU-MIMO scenario. For example, a system could be optimized by selecting the K users minimizing $\sum_{i=1}^{n_{R_1}} \sum_{j=1}^{n_{R_2}} \frac{||\mathbf{H_1}\mathbf{H_2}^H||^2}{n_{R_1} n_{R_2}}$ between any 2−user.

Since Figure 3.11 reveals a linear trend between correlation ρ and the capacity gain, an analysis based on the supervised linear regression is carried out. To formulate the

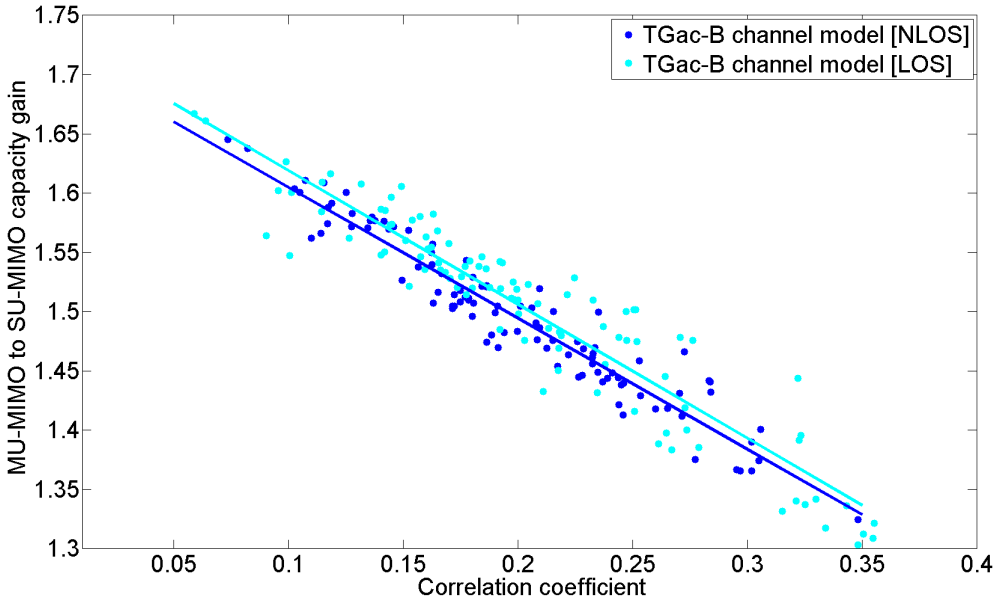

Figure 3.11 – Average of MU-MIMO to SU-MIMO capacity ratio versus the average correlation coefficient ($n_T = 6$).

problem, the linear regression will determine how the MU-MIMO to SU-MIMO capacity gain y is affected by the changes in the correlation coefficient x according to the regression line in Equation 3.9.

$$y' = a_1 x + a_0 \tag{3.9}$$

where y', a_1 and a_0 denote respectively the estimated capacity gain, the regression slope of the line and the intercept. The fitted line minimizes the error variance.

Besides, a coefficient of determination denoted r^2 is defined in Equation 3.10 as the ratio between the variance of y' and the variance of y. Note that r is referred to as correlation coefficient between x and y in the particular case of linear regression.

$$r^2 = \frac{Var(y')}{Var(y)} \tag{3.10}$$

Finally, the RMSE, also termed standard error of the regression is calculated by dividing the error variance by $n - 2$ (n is the number of samples, in our case $n = 100$ number of random draws). In fact, linear regression removes two degrees of freedom from the data (by estimating two parameters a_0 and a_1). The RMSE is simplified as can be seen in Equation 3.11:

$$RMSE = \sqrt{Var(y)(1 - r^2)(\frac{n-1}{n-2})} \tag{3.11}$$

The numerical values of the different parameters are summarized in Table 3.2. It shows that setting the Rician factor to 0 dB for LOS scenarios in TGac-B channel models gives almost similar results with slightly high capacity gain for LOS: 73 % for LOS compared to 71 % for NLOS case.

Scenario	a_0	a_1	r	RMSE
LOS	1.7319	-1.1290	0.9425	0.0379
NLOS	1.7153	-1.1046	0.9682	0.0226

Table 3.2 – Numerical results of linear regression parameters for 6 transmitting antennas.

The y intercept for LOS scenario is slightly greater than the one in NLOS conditions: almost 2% of capacity gain.

The coefficient of determination r^2 (equivalently the correlation coefficient r between x and y) tends to 1, and the RMSE tends to 0. This confirms the validity of predicting the capacity gain based on the correlation coefficient.

These results will be confirmed next chapter based on measurements. Note also that this linear regression analysis could be performed for other transmitting antennas number.

3.3.4.3 Correlation coefficient for Rayleigh fading channel

For a MIMO i.i.d. Rayleigh fading channel, each element of the channel matrix follows a zero mean complex Gaussian process (with the same standard deviation σ) and all these elements are independent. Hence, the complex Gaussian coefficients $\mathbf{L}_1^1(p)$ and $\mathbf{L}_1^2(q)$ where $1 \leq p, q \leq n_T$ can be written in terms of their amplitudes r_p^1, r_q^2, and phases ϕ_p^1, ϕ_q^2 as:

$$\mathbf{L}_1^1(p) = \frac{r_p^1 e^{j\phi_p^1}}{\sum_{m=1}^{n_T} (r_m^1)^2} \quad and \quad \mathbf{L}_1^2(q) = \frac{r_q^2 e^{j\phi_q^2}}{\sum_{m=1}^{n_T} (r_m^2)^2} \tag{3.12}$$

where ${r_p}^1$, ${r_q}^2$ follow a Rayleigh law, and ${\phi^1}_p$, ${\phi^2}_q$ a uniform low in $[0, 2\pi]$. Note that ${r_p}^1$, ${r_q}^2$, ${\phi^1}_p$, ${\phi^2}_q$ are independent. The denominators stand for for channel normalization.

The expression of the correlation coefficient in Equation 3.8 is thus simplified as:

$$E(\rho) = \frac{1}{n_{R_1} n_{R_2}} \sum_{i=1}^{n_{R_1}} \sum_{j=1}^{n_{R_2}} E(||\ \mathbf{L}_i^1 {\mathbf{L}_j^2}^H\ ||^2) \tag{3.13}$$

The components $E(||\ \mathbf{L}_i^1 {\mathbf{L}_j^2}^H\ ||^2)$ do not depend on the indexes i and j since the corresponding laws for the matrix elements $\mathbf{L}_i^1$ and ${\mathbf{L}_j^2}^H$ do not. The equation in 3.13 is

then simplified as:

$$E(\rho) = E(|| \mathbf{L}_1^1 \mathbf{L}_1^{2H} ||^2) \tag{3.14}$$

$$= E\Big(| \sum_{p=1}^{n_T} \mathbf{L}_1^1(p)\mathbf{L}(p)_1^{2H} |^2 \Big)$$

$$= E\Big(| \sum_{p=1}^{n_T} \frac{r_p^1 r_p^2}{\sqrt{\sum_{m=1}^{n_T}(r_m^1)^2}\sqrt{\sum_{m=1}^{n_T}(r_m^2)^2}} e^{j(\phi_p^1 - \phi_p^2)} |^2 \Big) \tag{3.15}$$

Based on the statistical independence r_p^1, r_p^2, ϕ_p^1, ϕ_p^2, we can write:

$$E(\rho) = \sum_{p=1}^{n_T} E\Big(\frac{(r_p^1 r_p^2)^2}{\sum_{m=1}^{n_T}(r_m^1)^2 \sum_{m=1}^{n_T}(r_m^2)^2}\Big) + 0 \tag{3.16}$$

Since all terms in the sum are identical, we can write:

$$E(\rho) = n_T E\Big(\frac{(r_1^1 r_1^2)^2}{\sum_{m=1}^{n_T}(r_m^1)^2 \sum_{m=1}^{n_T}(r_m^2)^2}\Big) \tag{3.17}$$

We can deduce the equation below since r_1^1 and r_1^2 are independent:

$$E(\rho) = n_T E\Big(\frac{(r_1^1)^2}{\sum_{m=1}^{n_T}(r_m^1)^2}\Big)\Big(\frac{(r_1^2)^2}{\sum_{m=1}^{n_T}(r_m^2)^2}\Big) \tag{3.18}$$

Let us define A as $A = E\Big(\frac{(r_1^1)^2}{\sum_{m=1}^{n_T}(r_m^1)^2}\Big)$. We have:

$$A = E\Big(\frac{(r_1^1)^2}{\sum_{m=1}^{n_T}(r_m^1)^2}\Big) \tag{3.19}$$

$$= E\Big(\frac{(r_1^1)^2}{(r_1^1)^2 + (r_2^1)^2 + \ldots + (r_{n_T}^1)^2}\Big)$$

$$= E\Big(\frac{(r_1^1)^2 + (r_2^1)^2 + \ldots + (r_{n_T}^1)^2}{(r_1^1)^2 + (r_2^1)^2 + \ldots + (r_{n_T}^1)^2} - \frac{(r_2^1)^2}{(r_1^1)^2 + (r_2^1)^2 + \ldots + (r_{n_T}^1)^2} - \ldots - \frac{(r_{n_T}^1)^2}{(r_1^1)^2 + (r_2^1)^2 + \ldots + (r_{n_T}^1)^2}\Big) \tag{3.20}$$

$$= 1 - (n_T - 1)A \tag{3.21}$$

The quantity A is consequently equal to $A = \frac{1}{n_T}$. Similarly, we have $E\Big(\frac{(r_1^2)^2}{\sum_{m=1}^{n_T}(r_m^2)^2}\Big) = \frac{1}{n_T}$. Finally, we prove that the average of the correlation coefficient

defined in Equation 3.7 is the inverse of the total number of the transmitting antennas as can be seen in Equation 3.22. This result is validated through simulations (Figure 3.9).

$$E(\rho) = \frac{1}{n_T} \tag{3.22}$$

In this section, we have studied the impact of antennas and propagation channel on the BD capacity gain based on a same total transmitted power. Based on simulations, we have given recommendations to optimize MU-MIMO capacity in terms of number of transmitting antennas, their spacing and SNR effect. In the case of the EIRP constraint, it may not be evident that TxBF and MU-MIMO linear precoding still improve the system performance. Therefore, next section evaluates the impact of the EIRP constraint on IEEE 802.11ac MU-MIMO capacity gain using simulations based on the IEEE 802.11ac channel models.

3.4 EIRP constraint in a multi-user context

In this section, we still consider the downlink MU-MIMO scenario, in which an IEEE 802.11ac access point with multiple antennas (up to 10) is transmitting to two receivers, each one with two antennas. The BD method is investigated under the EIRP constraint. Two different power allocation schemes of the spatial streams are analyzed to optimize MU-MIMO capacity: equal and unequal power sharing among the spatial streams under the same EIRP constraint. In our formulation, we study $K = 2$ but the results and algorithms presented in this section can be generalized to any number of users K.

3.4.1 Related work

The MU-MIMO techniques consist of applying a linear precoding to the transmitted spatial streams based on the channel matrices $\mathbf{H}_1$, $\mathbf{H}_2$. Consequently, the antenna array pattern and gain are modified as functions of the user location and their corresponding propagation channel properties. This directly impacts the EIRP. The European regulation sets the EIRP limit in the 5 GHz frequency bands to 200 mW or 1 W depending on the frequency channels. This constraint may differ in other countries where it can be rather based on the total transmitted power. The EIRP constraint is rarely evaluated in the literature for MIMO systems. In most of the MIMO performance results, the packet error rate or the capacity value is evaluated based on the same total transmitted power (denoted throughout this report as P_{Tx}) which is related to the SNR. The used SNR is commonly defined as the ratio of P_{Tx} to the average noise power as in the previous section with 0 dB average path loss normalized channel. Few recent studies have focused on the capacity optimization problems under total transmitted power constraint [52, 61, 33]. Sometimes, this optimization is performed on each subcarrier of the 802.11 OFDM signal [52]. In [62], a new EIRP-based solution for IEEE 802.11 power scaling is proposed. However, this

study is dedicated to only one single user system with a single spatial stream and receiving antenna. MU-MIMO linear precoding, like BD [61, 34], modifies dynamically the antenna array pattern and gain as function of the current MU-MIMO propagation channel. This may change the EIRP of the transmitting antenna array if transmitted power remains unchanged. MU-MIMO and TxBF are commonly associated with a large number of transmitting antennas used to improve the antenna array gain and performance, as stated for MIMO i.i.d. Rayleigh channel [33, 34].

3.4.2 Problem statement

3.4.2.1 EIRP in linear precoding

For any receiver location, i.e. for any **H** matrix, the transmitting antenna array pattern is modified by the **W** precoding matrix. We have used a linear array of n_T omnidirectional 0 dBi gain antennas with a regular spacing Δ, typically $\Delta = \lambda/2$. The manifold of the transmitter antenna array $a(\Theta)$ can be expressed in function of the Θ angle with the antenna array axis, a $n_T \times 1$ vector as written in Equation 3.23.

$$\mathbf{a}(\Theta)^T = [1, e^{-2j\pi\Delta\cos(\Theta)/\lambda}, ..., e^{-2j\pi(n_T-1)\Delta\cos(\Theta)/\lambda}] \tag{3.23}$$

In practice with real antennas, a 3D antenna pattern can be included in this processing. Since the used TGac channel model is only a 2D model, the antenna array pattern expression is simplified to a 2D problem. The average radiated power $d(\Theta)$ in any direction Θ relative to the antenna array direction is expressed in Equation 3.24 as a function of the antenna input signals defined as $\mathbf{X} = \mathbf{W}\mathbf{s}$.

$$d(\Theta) = E(\mid \mathbf{a}(\Theta)^T\mathbf{X} \mid^2) \tag{3.24}$$

The radiated power contribution of any subcarrier is simply expressed as a function of the transmit diagonal correlation matrix $\mathbf{B} = E(\bar{\mathbf{s}}\mathbf{s}^T) = E(diag(\bar{\mathbf{s}_1}\mathbf{s}_1^T, \ldots, \bar{\mathbf{s}_K}\mathbf{s}_K^T)) = \Big(diag(p_{ik}), 1 \leq i \leq N_{ss,k}, 1 \leq k \leq K\Big)$ as:

$$d(\Theta) = \mathbf{a}(\Theta)^H\bar{\mathbf{W}}\mathbf{B}\mathbf{W}^T\mathbf{a}(\Theta) \tag{3.25}$$

The total radiated power $d_{total}(\Theta)$ of all the subcarriers of the IEEE 802.11ac system is expressed as:

$$d_{total}(\Theta) = \sum_{subcarrier} d(\Theta) \tag{3.26}$$

The EIRP is then deduced as follows:

$$EIRP = \max_{\Theta} d_{total}(\Theta) \tag{3.27}$$

In the particular case in which the total transmitted power P_{Tx} is equally shared among the spatial streams and subcarriers, we have $p_{ik} = \frac{P_{Tx}}{NN_{ss}}$, where N_{ss} denotes the total number of spatial streams. Thus, $d(\Theta)$ can be simplified as:

$$d(\Theta) = \frac{P_{Tx}}{NN_{ss}} \mathbf{a}(\Theta)^H \bar{\mathbf{W}} \mathbf{W}^T \mathbf{a}(\Theta) \tag{3.28}$$

3.4.2.2 Optimization problems

The capacity optimization process consists of finding the optimal value of the transmitted power values p_{ik} compatible with the $EIRP$ constraint. Considering the spatial streams, two power allocation schemes are evaluated: equal power allocation and unequal power allocation.

The European regulation sets the maximum EIRP in an indoor area to 23 dBm for the lower band ($5150 - 5350$ MHz) for the 5 GHz frequency. For practical reasons, such as the computation time, this section focuses on the case where each subcarrier has the same allocated total transmitted power. Furthermore, an unequal subcarrier power allocation may not have a favorable impact on the peak-to-average power ratio of the OFDM signal. The general optimization problem is thus expressed in this case as:

$$\begin{cases} \max \limits_{subcarrier} \sum_{k=1}^{K} \sum_{i=1}^{N_{ss,k}} \log_2(1 + \frac{p_{ik}}{\sigma_n^2} \mu_{ik}^2) \\ \text{such that} \quad EIRP \leq 23\ dBm \end{cases} \tag{3.29}$$

As we have a sum of logarithmic functions, our problem is a standard convex optimization problem with constraint and is resolved using the Matlab-based library for convex optimization namely CVX [63] to find the optimal solution. A simpler optimization problem consists in solving the case with equally distributed powers, i.e. $p_{ik} = \frac{P_{Tx}}{NN_{ss}}$. This optimization problem has only one unknown variable P_{Tx}. This problem is simplified by seeking the maximum antenna array gain $\frac{d_{total}(\Theta)}{P_{Tx}}$ and then scaling the power according to the EIRP limit. The case $K = 1$ uses the same optimization method for computing the SU-MIMO capacity for both equal and unequal power allocation under EIRP constraint.

3.4.2.3 Evaluated systems and SNR considerations

The 802.11ac MU-MIMO systems based on BD schemes are evaluated. The results are presented in Section 3.4.3 and are compared to SU-MIMO systems relying on the same antennas and total power or EIRP constraint. Three capacity optimization techniques are evaluated and compared.

The first one is the usual MIMO system (denoted *basic*), with a constant transmitted power P_{Tx} equally shared among the spatial streams. *BD-basic* and *SU-basic* denote the corresponding studied systems. For this case, the average signal to noise ratio SNR per subcarrier is defined as $SNR = \frac{P_{Tx}}{N\sigma_n^2}$. This is the common SNR definition adopted in most of the published MIMO capacity studies.

The second optimization considers a 23 dBm EIRP constraint and a total transmitted power equally shared among the spatial streams. This optimization is labeled *eirp-equal*. A dynamic power scaling is applied, as detailed above, as a function of each

channel matrix snapshot $\mathbf{H}$. *SUeirp-equal* and *BDeirp-equal* denote respectively the corresponding SU-MIMO and MU-MIMO systems applying this technique.

The third one (*eirp-unequal*) considers a 23 dBm EIRP constraint and a total transmitted power unequally and dynamically shared among the spatial streams. *SUeirp-unequal* and *BDeirp-unequal* denote the corresponding systems applying this technique.

For *eirp-equal* and *eirp-unequal* systems, the common SNR definition is biased since P_{Tx} is no more constant, and depends on each channel matrix computation. We subsequently define the average SNR_{EIRP} under EIRP constraint as $SNR_{EIRP} = \frac{EIRP}{N\sigma_n^2}$ for *eirp-equal* and *eirp-unequal* systems.

Note that the maximum antenna array gain is n_T. Since $SNR = \frac{P_{Tx}}{N\sigma_n^2}$ for a *basic system*, it implies that its corresponding SNR_{EIRP} value is upper bounded by $\frac{n_T P_{Tx}}{N\sigma_n^2}$. However, direct comparison between the two systems remains unfair.

3.4.3 Simulation results and analysis

3.4.3.1 Results for equal power allocation

In this section, we consider a system with an equal power allocation among the spatial streams.

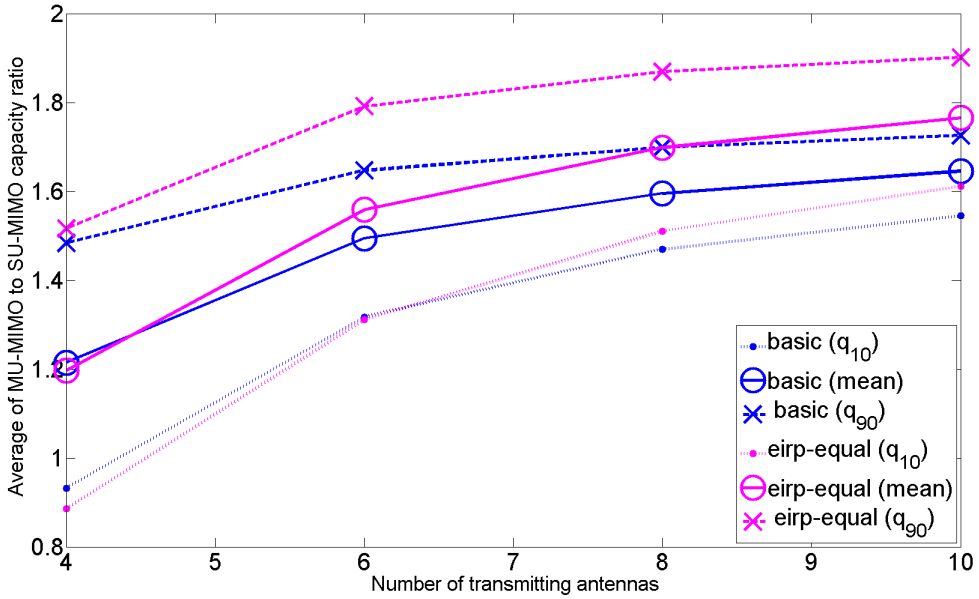

Figure 3.12 – MU-MIMO to SU-MIMO capacity ratio for an IEEE TGac-B channel (residential).

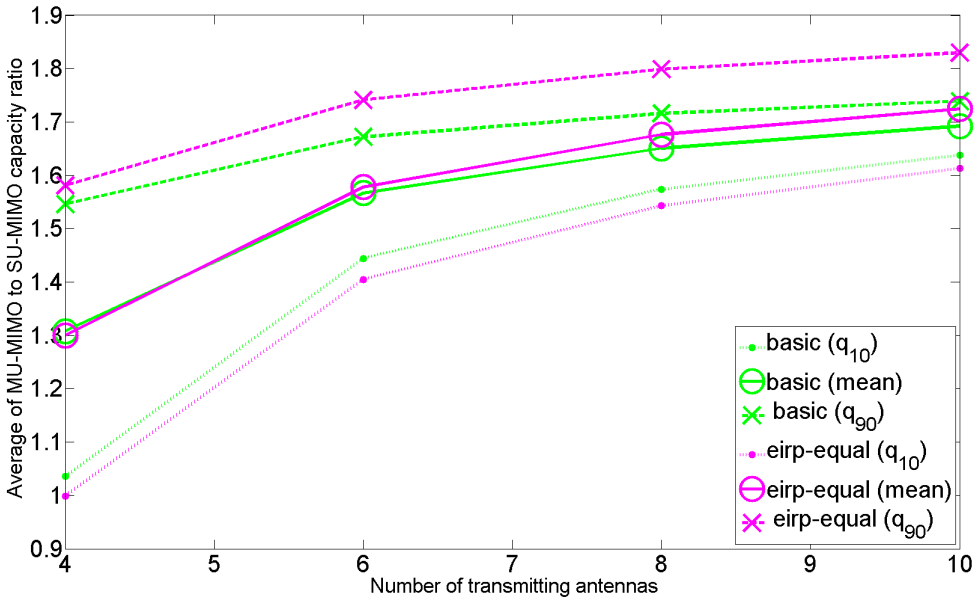

Figure 3.13 – MU-MIMO to SU-MIMO capacity ratio for an i.i.d Rayleigh channel.

Figures 3.12 and 3.13 present the simulation results in terms of the MU-MIMO to SU-MIMO capacity ratio for *basic* and *eirp-equal* systems. Average values, 10% and 90% quantiles (q_{10} and q_{90}) are represented to estimate the confidence intervals. SNR_{EIRP} is set to 20 dB for *eirp-equal* and SNR for *basic* is also set to 20 dB. n_T varies from 4 to 10 transmitting antennas.

These figures show that the MU-MIMO to SU-MIMO capacity ratio increases with the number of transmitting antennas for TGac-B (Figure 3.12) and Rayleigh (Figure 3.13) channels. The capacity ratio changes from 1.2 to 1.77 for the *eirp-equal* system in a residential environment, which represents more than 50% of capacity gain. Note that the gain without the EIRP constraint is around 45% [64]. It has been shown in previous studies that increasing the number of transmitting antennas favorably impacts the capacity gain on an i.i.d. Rayleigh channel under SNR constraint [33, 34]. We have been able to prove in this section that this result holds even under the EIRP constraint and with correlated channels as in TGac models. The difference between the 10% and 90% quantiles reduces as the number of antennas increases. This shows that fading has less impact on the capacity values which become less scattered.

The *basic* and *eirp-equal* comparisons are biased. In fact, a system relying on a total transmitted power does not satisfy a constant $EIRP$ constraint since it may have an increasing $EIRP$ as n_T increases. Intuitively, we could expect that for a *basic* system, the MU-MIMO to SU-MIMO capacity ratio increases more rapidly in function of n_T than for an *eirp-equal* system, but simulations prove the opposite. In fact, SU-MIMO takes

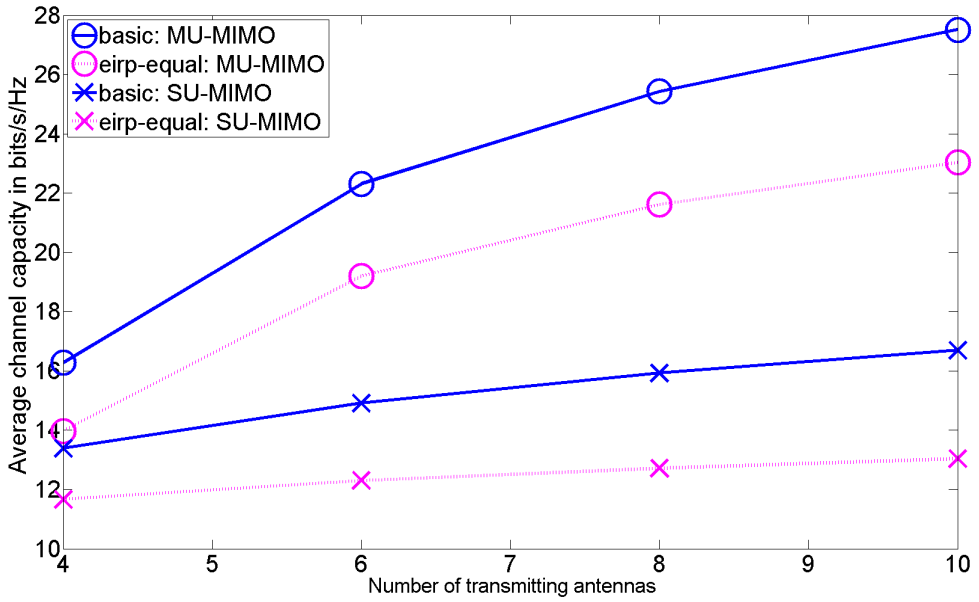

Figure 3.14 – Average of capacity values achieved by the *basic* and *eirp-equal* systems.

advantage of the power P_{Tx} when the system is not under EIRP constraint. For instance in our simulated case ($K = 2$) where $N_{ss} = 4$ for MU-MIMO and $N_{ss} = 2$ for each one of the single users, the reached $EIRP$ by the MU-MIMO system $EIRP_{MU-MIMO}$ is expressed as $EIRP_{MU-MIMO} = \frac{P_{Tx}}{NN_{ss}}[\max_{\Theta} \sum_{subcarrier}(\mathbf{a}(\Theta)^H \bar{\mathbf{W}}\mathbf{W}^T\mathbf{a}(\Theta))]$ and is upper bounded by $n_T\frac{P_{Tx}}{4}$. Similarly, for the same value of P_{Tx}, the single user EIRP is upper bounded by $n_T\frac{P_{Tx}}{2}$. This means that for a system under the same EIRP constraint, the allocated power tends to be lower for SU-MIMO than for MU-MIMO. For the basic system, the allocated power is the same for SU-MIMO and MU-MIMO. Figure 3.14 shows the average capacity values for MU-MIMO and SU-MIMO. It is well observed that the MU-MIMO capacity increases more rapidly with n_T compared to SU-MIMO.

3.4.3.2 Impact of power allocation strategy

The previous results have been obtained under the EIRP constraint with equally shared power among the spatial streams. In this section, the impact of allocating an unequal and optimized power to each spatial stream according to Equation 3.29 is highlighted. Figure 3.15 compares the average of MU-MIMO to SU-MIMO capacity ratio versus the number of transmitting antennas for *eirp-equal* and *eirp-unequal* systems. As the number of the transmitting antennas increases, the capacity gain of the MU-MIMO to SU-MIMO of the *eirp-unequal* becomes greater than the one achieved of the *eirp-equal* system. However, this gain is not significant compared to the

computational complexity: it is around 5% for 4 transmitting antennas, and it decreases to 1% for 10 transmitting antennas.

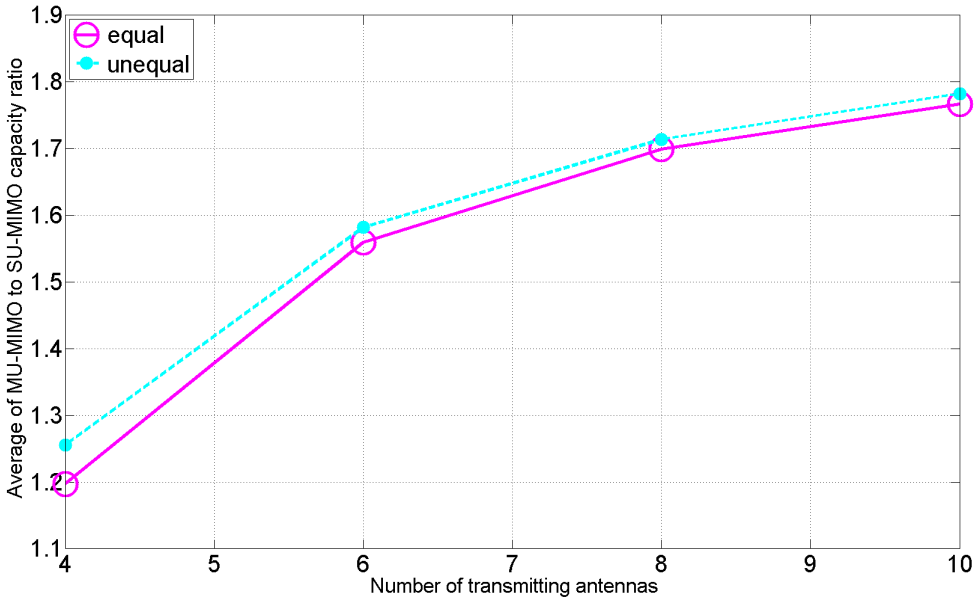

Figure 3.15 – Average of MU-MIMO to SU-MIMO capacity ratio for *eirp-equal* and *eirp-unequal* systems [TGac-B channel model].

To check whether the MU-MIMO capacity always outperforms the SU-MIMO, we have evaluated the probability when the MU-MIMO capacity is lower than the SU-MIMO capacity. This is illustrated in Figure 3.16 for *eirp-equal* and *eirp-unequal* schemes versus the number of transmitting antennas.

Figure 3.16 shows that there are some channel snapshots for which the MU-MIMO is less efficient than SU-MIMO, particularly when n_T is equal to 4. The probability reaches 22% for equal power sharing between spatial streams. However, the unequal power sharing decreases this probability to 14%. We also observe on Figure 3.15 that the MU-MIMO capacity gain for unequal sharing is slightly greater than the one observed for a fair power distribution. Nevertheless, the gain is not significant: we have around 3% of capacity gain by contrast to high computational complexity. The probability is almost 0 ($\leq 1\%$) for $n_T = 6$ and is equal to 0 for $n_T \geq 8$.

These results can be explained by examining the overall system: for $n_T = 4$, the MU-MIMO system is composed of 4 antennas in the transmit and the receive sides with 4 spatial streams. This gives no diversity possibilities. The number of spatial streams becomes strictly less than the number of transmitting antennas when n_T increases. As a result, the system takes benefit from transmit diversity and shows probabilities which tend to 0.

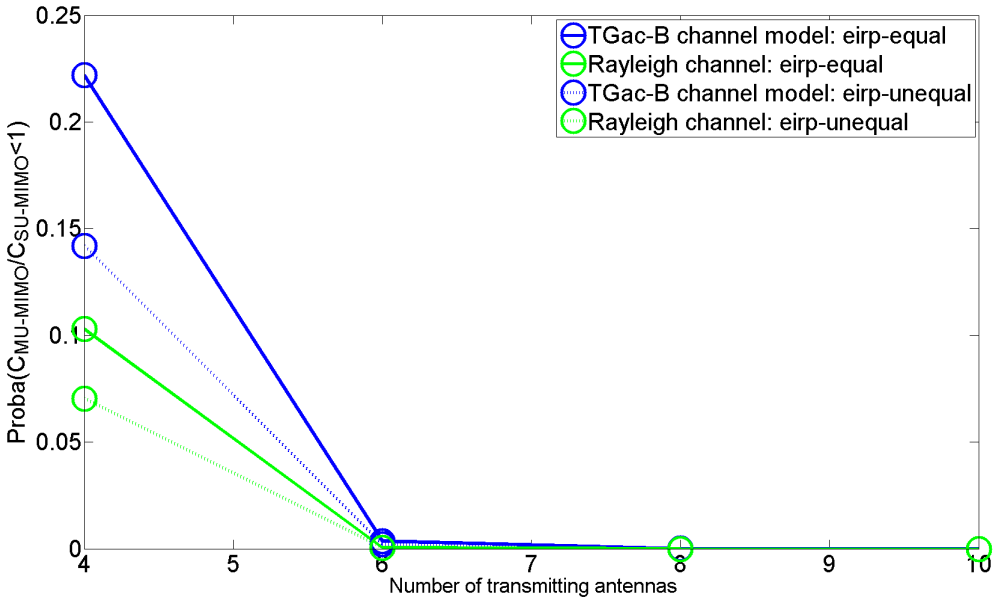

Figure 3.16 – Proba ($C_{MU-MIMO}/C_{SU-MIMO} < 1$) versus the number of transmitting antennas.

3.4.3.3 Antenna spacing effect

For additional results, different transmitting antenna spacings are evaluated for a system in NLOS conditions composed of a Tx with $n_T = 6$ antennas and $SNR_{EIRP} = 20$ dB. The evaluated values are: $0.25\ \lambda, 0.5\ \lambda, 0.75\ \lambda, 1\ \lambda, 1.25\ \lambda$ and $1.5\ \lambda$. Figure 3.17 shows an isolated and very low gain (37%) at $0.25\ \lambda$ due, inter alia, to the high correlation between the fading of the channels caused by the small spacing between the transmitting antennas. As the number of the transmitting antenna spacing is increasing, the MU-MIMO to SU-MIMO capacity gain for the residential environment (TGac-B) is around the value of the capacity gain of Rayleigh channel (57%). Antenna spacing has no effect on the Rayleigh channel since its MU-MIMO channel matrix elements are complex Gaussian random variables and independent. Considering a trade-off between the antenna size and the MU-MIMO capacity gain, the recommendation is to have the antenna spacing equal to $0.5\ \lambda$.

3.5 Conclusion

The purpose of this chapter is to give recommendations for radio engineering and system optimization. In this chapter, we have investigated the impact of antennas and propagation channel on the BD capacity gain for the 802.11ac MU-MIMO in home networks.

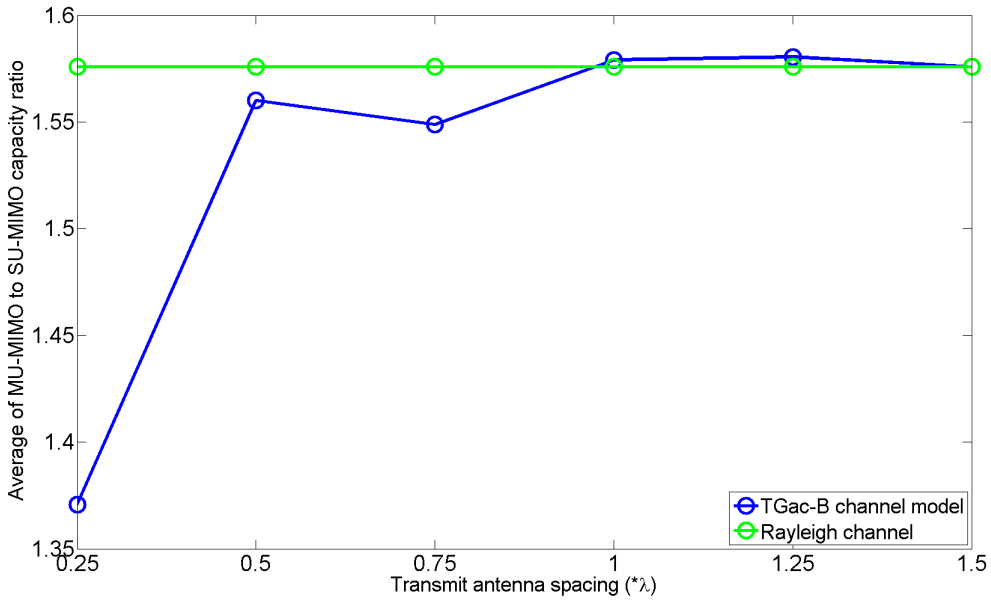

Figure 3.17 – Average of MU-MIMO to SU-MIMO capacity ratio versus transmitting antenna spacings.

In particular, we have proved that a small increase of the number of transmitting antennas compared to the total number of the transmitted spatial streams improves significantly the user channel de-correlation and the MU-MIMO capacity gain over SU-MIMO: for example a MU-MIMO gain over SU-MIMO of 45% is achieved for a 20 dB SNR, 4 spatial streams and 6 transmitting antennas. We have also highlighted a relevant channel correlation definition that is useful to decide whether MU-MIMO outperforms SU-MIMO and to select the users into a MU-MIMO user group [64]. Afterwards, we have formulated the optimization problem of the sum capacity for IEEE 802.11ac MU-MIMO systems, considering multiple spatial streams and antennas for each user and taking into account the EIRP constraint [65]. Then we have derived numerical results for a typical home network environment based on the spatially correlated IEEE 802.11ac channel models. Two transmit power allocation methods have been evaluated: equal and unequal sharing among the spatial streams under the same EIRP constraint. We have compared these two strategies with the common MU-MIMO BD linear under the total transmitted power constraint. We have shown that MU-MIMO precoding takes more benefit from the EIRP constraint. In particular, we have proved that under EIRP constraint, it is also recommended to have a number of transmitting antennas slightly greater than the total number of spatial streams to guarantee a MU-MIMO capacity gain over SU-MIMO with antenna spacing equal to 0.5 λ. These simulated results need to be confirmed in further work with real MU-MIMO measured propagation channels [66]. Table 3.3 summarizes the previous

conclusions and ends in proposing system recommendations.

Parameters	MU-MIMO **to** SU-MIMO **capacity gain**	**Recommendations for radio engineering**
SNR effect: $0 - 40$ dB	Till 80% of gain	The desired range is put forward
Transmit antenna spacing: $0.5\ \lambda\ -\ 1.5\ \lambda$	Insignificant gain of 2 %	$0.5\ \lambda$
Number of transmitting antenna n_T: $4 - 8$	40% of gain	n_T should be slightly greater than the number of spatial streams: 6 transmitting antennas for two two-antenna users and two SS per user
LOS or NLOS	almost the same gain (LOS gives a slightly high gain)	no recommendation
MU-MIMO with Water-filling algorithm	the same gain as equal power sharing	not recommended excepted if $n_T = n_R = N_{ss}$
EIRP constraint	10% of gain with 6 transmitting antennas	— Beneficial use — Power allocation strategy: equal power sharing for low complexity

Table 3.3 – Recommendations to optimize MU-MIMO.

No deployment conclusion could be drawn based on the relative positions of the AP and users since the TGac channel model is not geometrical. Next chapter will explore deployment recommendations. Moreover, the channel model is restricted to only simulate uniform linear antenna arrays. Other array geometries need to be evaluated based on measurements.

Chapter 4

MU-MIMO capacity based on propagation measurements in indoor environment

Contents

4.1 Introduction

This chapter presents the numerical results based on a measurement campaign conducted during the thesis in a residential environment typically encountered in home

networks. In order to have a meaningful comparison, we have performed a comparison between the TGac channel models and the measured environment. The first objective of this measurement campaign was to confirm the previous results and validate the radio engineering conclusions based on channel models, then to extend the results to different antenna array geometries and other potential parameters such as the path loss. We have also evaluated the impact of increasing the number of spatial streams and the SNR values. Afterwards, we have evaluated the measured path loss impact on MU-MIMO capacity gain using different channel access methods. Finally, we have drawn a comparative study between the simulated and measured results.

4.2 Experiment

In this section, we describe the performed measurements for MU-MIMO channels, based on which we evaluate the MU-MIMO performance. First, we present a state of the art of the previous studies based on measured data. We further describe the measurement environment, as well as the studied scenarios. Finally, we introduce the the measurement setup and the post processing.

4.2.1 Related work

Few articles have studied MU-MIMO capacity based on measured indoor MU-MIMO propagation channels (see Appendix C). In a narrow indoor corridor environment, the authors in [56] have analyzed DPC gain over linear processing for two single-antenna receivers and revealed that this gain is almost insignificant for low and high user channel orthogonality. Studies in [67, 48, 68] have focused on achieving capacity or throughput improvement through the use of various transmitting antenna arrangements, antenna designs and antenna configurations. It has been shown in [68] by evaluating channel capacity that a compact tri-polarization antenna cube combined with a simplified pattern circuit are suitable for MU-MIMO systems with antenna selection. It has been shown in [67], using one transmitter with 8 antennas and four single antenna receivers, that constraining the antenna arrangement to 7 λ is beneficial (a gain of 12.8 % of spectral efficiency is achieved) in an indoor environment (room), where λ indicates the wavelength of carrier frequency. However, none of these articles highlights the deployment recommendations or optimal system configuration of the MU-MIMO compared to SU-MIMO, or studies in details MU-MIMO capacity gain over SU-MIMO with multiple antennas receivers based on measurements in home networks.

4.2.2 Measurement scenarios

Figure 4.1 represents the environment of the experiment. It displays the 3D indoor residential scene used to perform measurements. It is a typical and real middle sized apartment with a 12 m $\times$7 m surface and European building materials and furniture. The ceiling is at 2.53 m. Both LOS and NLOS scenarios have been probed. Hereafter

only global results are displayed, more measurements would be necessary to compare LOS/NLOS statistics.

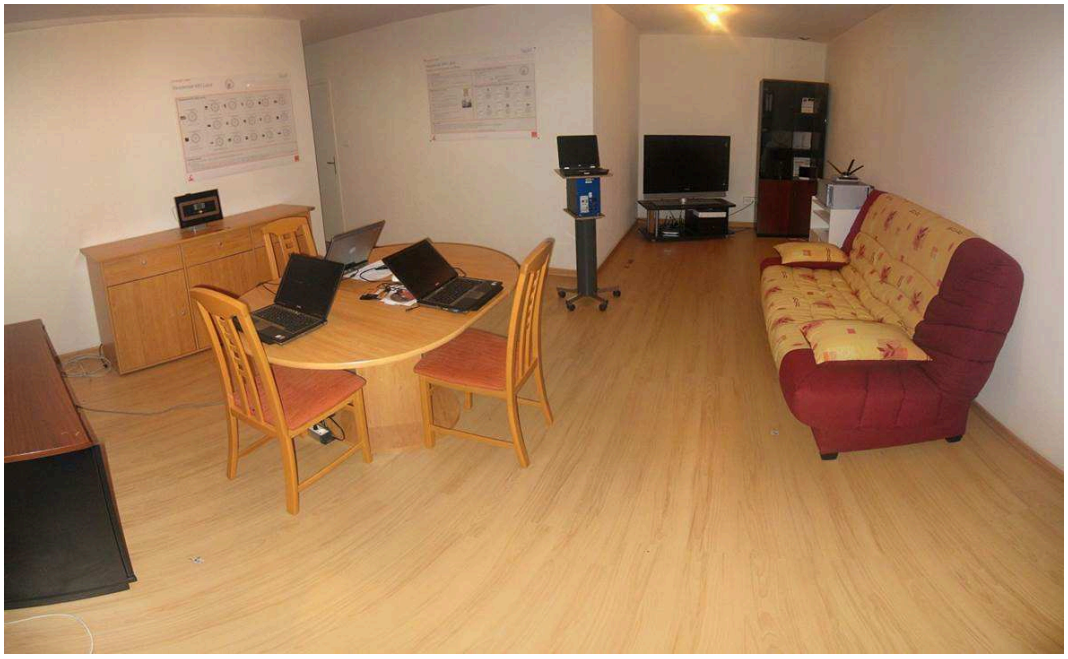

Figure 4.1 – Living room and corridor of the apartment.

Two locations of the Tx are considered, denoted as Tx_1 and Tx_2 in Figure 4.2. For each Tx position, multiple positions of the two receivers are evaluated. We denote by Rx_1 and Rx_2 the positions of the first and the second user respectively. During the measurements, nothing moved in the environment of the experiment to keep the same measurement conditions. Finally, the obtained measurement data base corresponds to 67 various 2−users configurations by combining the Tx and Rx positions.

4.2.3 Channel measurement setup

The MU-MIMO propagation channel is sounded using a Vector Network Analyzer (VNA) based on a frequency domain technique. We collect the S_{21} parameter since the propagation channel is the device under test. The VNA, depicted in Figure 4.4(a), is connected by cables of 10 m to the Tx, 20 m and 5 m to the first and second user respectively. Hence, the maximum distance between the Tx and Rx is 30 m. The VNA has probed $M = 2048$ frequency tones between 5.15 GHz and 5.40 GHz stepped by $\Delta f = 122.07$ kHz. This configuration permits a maximum propagation delay of $\frac{1}{\Delta f} = 8192$ ns. This value is well above the propagation delay that can be usually observed in such environment but it is useful to estimate the noise level of the measurement data for post-processing. The high number of frequency bins allows also to improve the dynamic (the difference between the peak power and noise level) of the CIR, which is between

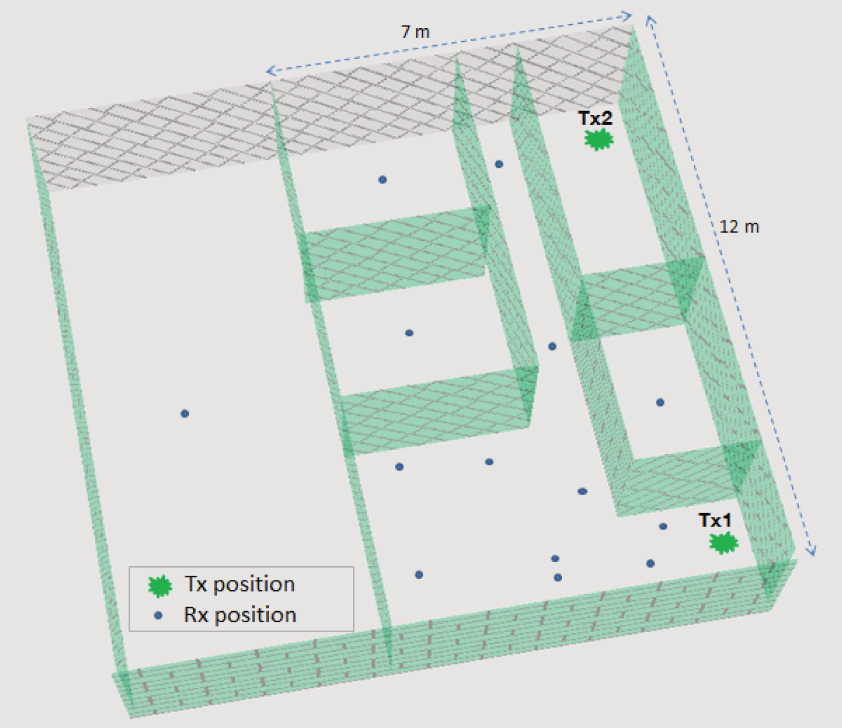

Figure 4.2 – The indoor environment: 2 positions of Tx with 12 positions of Rx.

20 dB and 65 dB in our experiment.

We used vertically polarized dipole antennas at the Tx and the Rx. The transmitting antenna pattern is depicted in Figure 4.3.

The Tx is composed of 8 antennas arranged in Uniform Linear Array (ULA) spaced by $\lambda/2$. The transmitting antenna gain is 5.13 dBi with 60° of vertical beamwidth. Two additional transmitting antennas are located at both ends to have symmetrical coupling effects as can be seen in Figure 4.5(b). The distance between the center of each transmitting antenna and the ground is 1.8 m. For each user as depicted in Figure 4.4(c), four antennas are arranged in a square horizontal array with a $\lambda/2$ side. The receiving antenna gain is 1.6 dBi, and the distance between the antenna center and the ground is fixed to 1.1 m. The transmitting antennas are mounted on a rotating arm to measure different antenna array geometries and to take into account fast fading effects as illustrated in Figure 4.5(b). A rotation step of 6° is selected. We come up to a total of $NACQ = 480$ virtual transmitting antennas as shown in Figure 4.4(d). For each position of the three devices, i.e. one Tx and two Rx, the channel is of dimension 480×8 for each subcarrier where $n_{Rx} = 8$ represents the total number of receiving antennas.

Two 8−to−1 switches at the Tx and the Rx respectively, are used to select the antennas. First, the channel is measured between the first transmitting antenna and the first receiving antenna by sweeping frequencies. The selected receiving antenna for

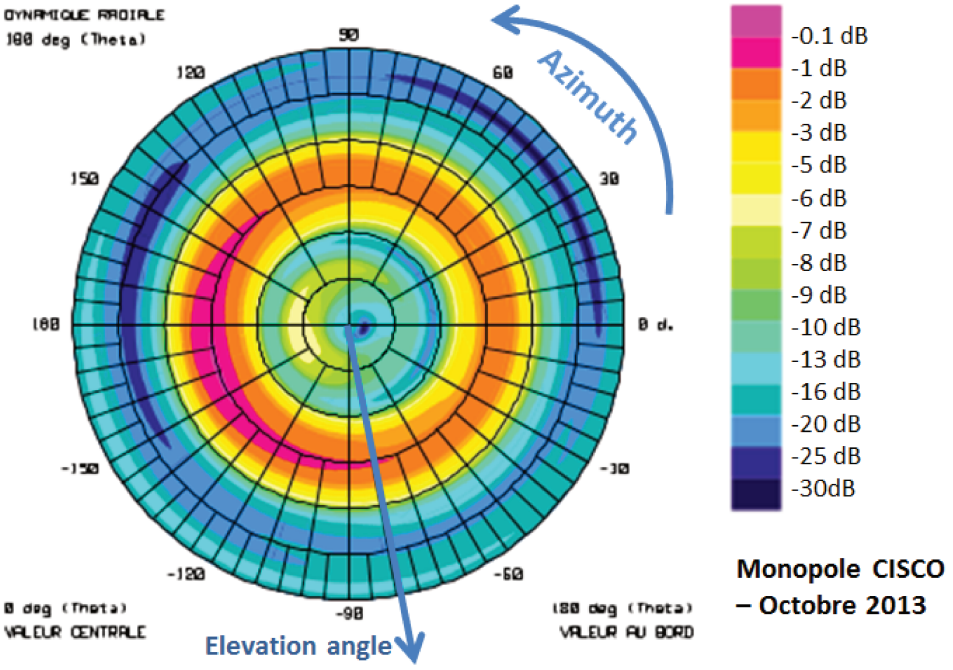

Figure 4.3 – 5 GHz transmitting antenna pattern - Energy pattern [Measurement made by Orange Labs].

measurement is then switched on using the receiving switch. Afterwards, we select the second transmitting antenna using the switch at the Tx. Note that the switching time is 5 ms for switching at the Tx and the Rx. Finally, after the 8×8 switching steps, the rotating arm is turned by 6°. We repeat the same processing till the rotating arm returns to the first position. It takes about 20 minutes with the VNA to record one measurement consisting of 480×8 channel sweeps over 2048 tones. All equipment (switches, VNA and rotating arm) are controlled by one laptop and connected through Ethernet cables.

4.2.4 Post-processing

The measured CIR were first calibrated using a reference measurement when the Tx and Rx ports where directly cable-connected. We afterwards apply in the frequency domain the Hanning window to reduce the leakage side lobes levels due to the limited measurement bandwidth window. Figure 4.5 gives an example of the measured average PDP before and after applying the calibration and the Hanning Window for the 8 receiving antennas. The figure shows two sets of curves. Each set corresponds to one user with its 4 antennas.

The collected CIRs have a dynamic arranged between 65 and 20 dB depending on whether the Rx is near or far from the Tx. The measurement noise level is estimated

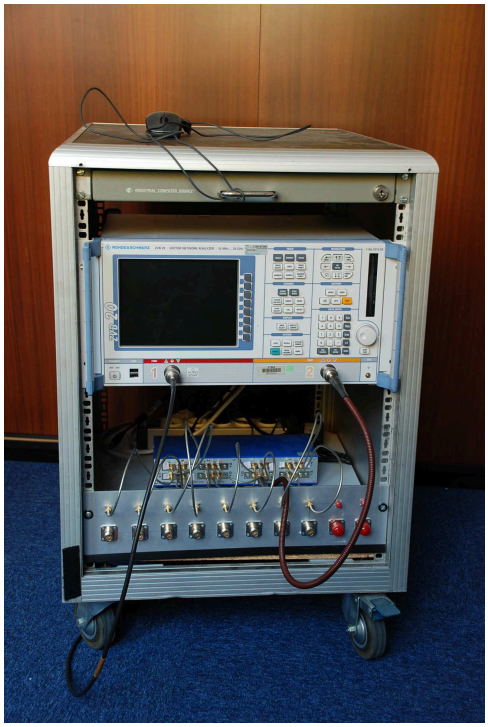

(a) VNA

(b) Tx

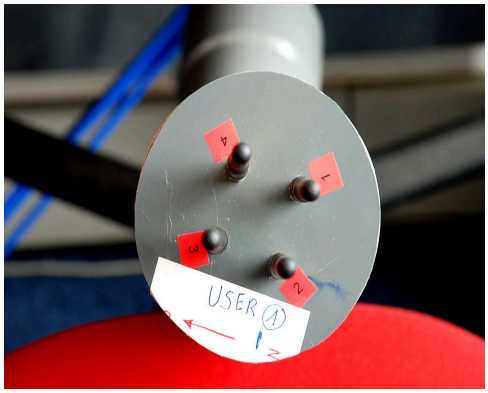

(c) Rx1

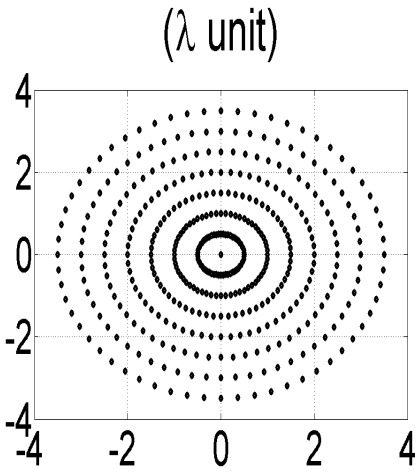

(d) Tx: 480 virtual antennas.

Figure 4.4 – Measurement equipment.

from the non physical delay area of the average PDP. We force to 0 the corresponding CIR complex samples with an average power below this noise level and also the sample corresponding to a dynamic greater than 30 dB in order to process measurements with

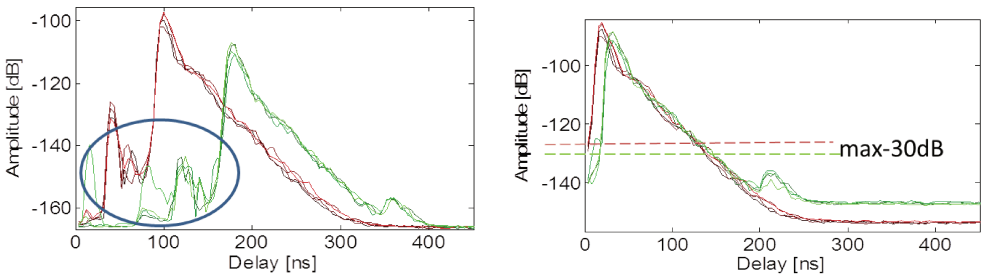

(a) Before (b) After

Figure 4.5 – Average PDP for each receiving antenna.

a comparable dynamic between 20 and 30 dB.

For each set of the 67 2−users configurations, the collected CIRs is of size of $480 \times 2048 \times n_R$. The average PDP $P_k(j\Delta T)$ for the k^{th} receiving antenna is thus computed for each set of 67 as in Equation 4.1

$$P_k(j\Delta T) = \frac{\sum_{i=1}^{NACQ} \mid h_{ki}(j\Delta T) \mid^2}{\sum_{j=1}^{2048} \sum_{i=1}^{NACQ} \mid h_{ki}(j\Delta T) \mid^2} \tag{4.1}$$

where h_{ki} is the CIR between the receiving antenna k and the transmitting antenna i and $\Delta T = \frac{1}{25010^6}$ [s].

The IEEE 802.11ac OFDM signal is divided into subcarriers with a subcarrier spacing equal to 312.5 kHz. Since the indoor propagation channel is frequency flat on such a small bandwidth, we choose the first measured frequency sample to be the multiple of 122.07 kHz which is the closest to the subcarrier spacing of IEEE 802.11ac (312.5 kHz). We exploit multiple 802.11ac 20 MHz subchannels (up to 10 sub-bands for 250 MHz probed by the VNA) as well as various Tx angular positions (up to 60 transmit angular positions of the rotating arm) in order to have representative statistical results.

4.3 Comparison of TGac channel models and measurements

The validity of a potential comparison between the measured and simulated results depends on the comparison of the channel characteristics. In this context, this section compares the channel parameters relying on: the delay spread, the MIMO transmit and receive correlation and the narrowband fast fading distribution.

4.3.1 Delay spread

The delay spread is a measure of the multipath richness of a communication channel. The DS (τ_{RMS}) is computed for each one of the k receiving antenna using the average

PDP over a 100 MHz bandwidth as in Equation 4.2. To get 100 MHz, the applied Hanning window was reduced accordingly.

$$\tau_{RMS}(k) = \sqrt{\frac{\sum_{j=1}^{2048} (j\Delta T)^2 P_k(j\Delta T)}{\sum_{j=1}^{2048} P_k(j\Delta T)} - \left(\frac{\sum_{j=1}^{2048} (j\Delta T) P_k(j\Delta T)}{\sum_{l=1}^{2048} P_k(l\Delta T)} \right)^2} \tag{4.2}$$

This choice is justified by the fact that the average PDP of TGac channels are by default computed over 100 MHz. The average PDP is computed over the 480 virtual antennas. In the LOS case, the computation gives a mean value of $\tau_{RMS} = 10.87$ ns, and $\tau_{RMS} = 17.93$ ns for the NLOS case. This result is in accordance with the numerical values in [69]. The LOS-NLOS refers to the case where one of the users is on LOS with the Tx and the other one on NLOS with Tx. It shows a middle case between the LOS and NLOS scenarios with $\tau_{RMS} = 13.5$ ns.

Figure 4.6 shows the delay spread of all measured channels compared to TGac channels. Despite of the dispersion of measured τ_{RMS}, the average value is equal to 15.433 ns. The TGac-B channel model is defined to have 15 ns. Thus, both environments show an average delay spread around 15 ns and can be considered to have a similar frequency selectivity .

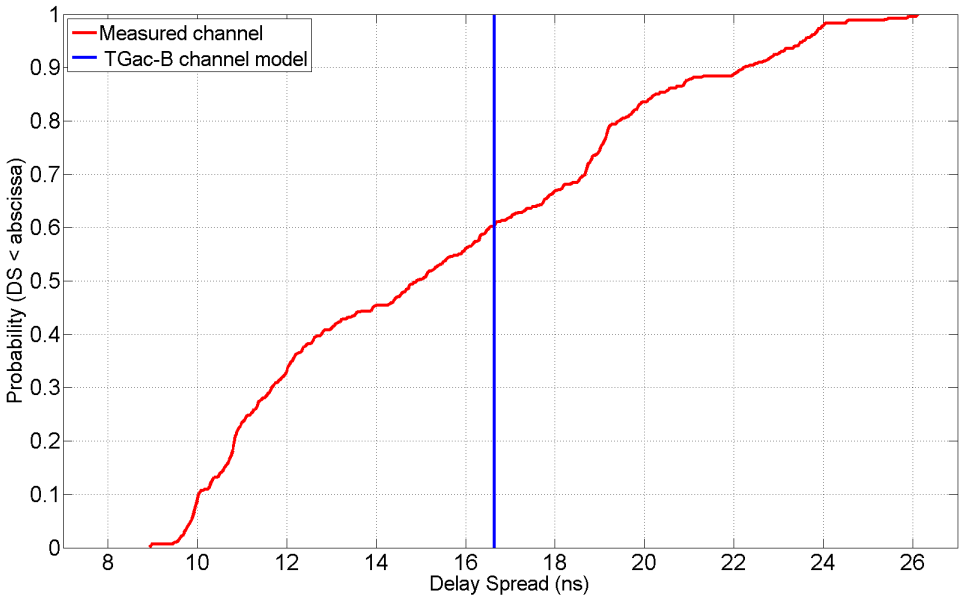

Figure 4.6 – Cumulative distribution function of the RMS delay spread [ns].

4.3.2 Superdiagonal of transmit and receive covariances

We study the coefficients r_{Tx} and r_{Rx} of the receive and transmit correlation matrices R_{Tx} and R_{Rx} as defined in [70][18] (Equation 4.3), of dimension $n_T \times n_T$ and $n_R \times n_R$ respectively, for NLOS scenario with $n_T = 8$ transmitting antennas arranged in linear array and two receivers with two antennas each.

$$\begin{cases} \mathbf{R}_{Tx} = \frac{1}{n_R} E \mid \mathbf{H}^T \bar{\mathbf{H}} \mid \\ \mathbf{R}_{Rx} = \frac{1}{n_T} E \mid \mathbf{H}\mathbf{H}^H \mid \end{cases} \tag{4.3}$$

The transmit and receive correlation matrices give insight to what extent the signals leaving the different transmitting antennas and the signals arriving at the different receiving antennas respectively are correlated. According to [30], it has been shown that in indoor and outdoor scenarios, almost no correlation can be measured at the receive side between the different users. However, at the transmit side, there is slightly, but not significantly more correlation. This has been shown to badly impact the MU-MIMO performance.

The correlation coefficient is featured to have *superdiagonal* form. The superdiagonal entry of a matrix is one that is directly above and to the right of the main diagonal. Each component shows the correlation between the antenna corresponding to its row and its adjacent antenna. The antennas are spaced by $\frac{\lambda}{2}$. We have based our computation on the second user channel matrix $\mathbf{H}_2$ because it includes all the various positions shown in Figure 4.2. The $n_T \times n_T$ transmit correlation matrix has the superdiagonal coefficients as $r_{Tx} = \frac{1}{n_R} E(\sum_{i=1}^{n_{R_2}} H_{ij} \bar{H}_{i(j+1)})$ for $j = 1, 2, \ldots, 7$. The superdiagonal of the $n_{R_2} \times n_{R_2}$ receive correlation is $r_{Rx} = \frac{1}{n_T} E(\sum_{j=1}^{n_T} H_{1j} \bar{H}_{2j})$, where the H_{ij} are the elements of the channel matrix $\mathbf{H}$.

Figure 4.7 shows the CDF of the average of the superdiagonal values of the transmit and receive correlation matrices. The first observation drawn from this figure is that the receive correlation shows lower values compared to the transmit correlation. The measured environment shows slightly less correlated values at the Tx and Rx side than the TGac-B channel model.

4.3.3 Fading

In this subsection, we evaluate the narrowband fast fading distribution.

We characterize the CDF of narrowband fading of the measured channel and we compare it to the Rayleigh distribution as illustrated in Figure 4.8. The figure shows that the fading in the measured environment fits exactly the Rayleigh distribution considered for the TGac-B channel model.

Analyzing the previous parameters, we have shown that the two environments meet the same trend. Hence, they are expected to give similar results.

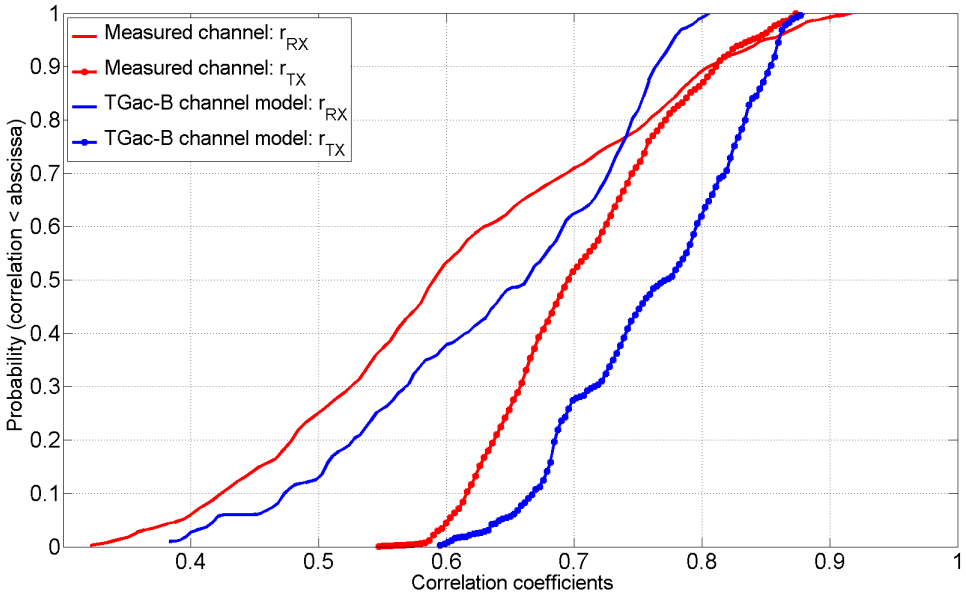

Figure 4.7 – CDF of the average of the superdiagonal values.

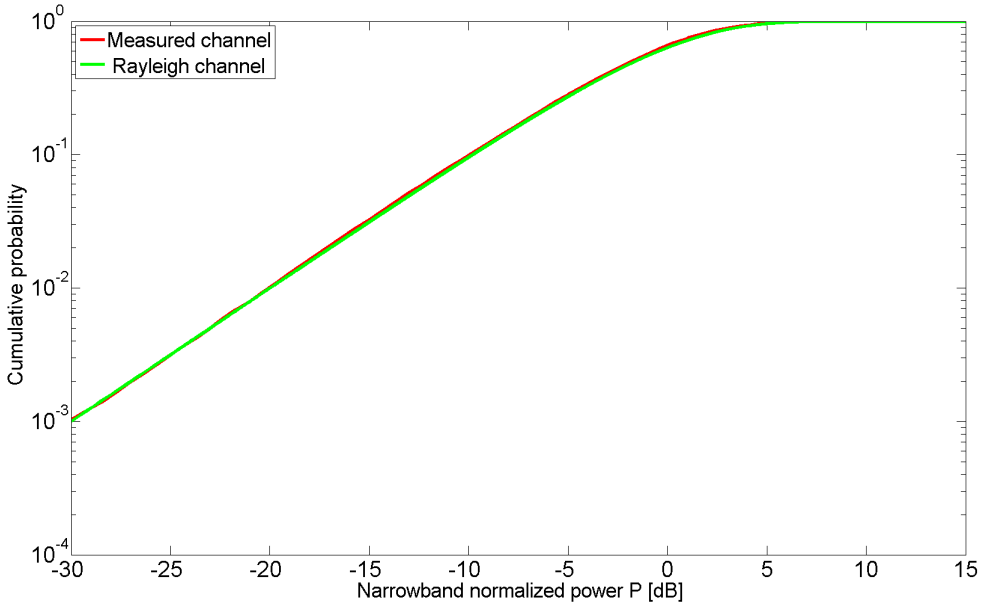

Figure 4.8 – Comparison of measured and Rayleigh fading CDFs [dB].

4.4 Statistical results

The measured data allows the study of various types of transmitting antenna array geometries using the 480 virtual antennas and an increased number of receiving antennas. This section first presents MU-MIMO results based on normalized 0 dB average path loss for each user. Afterwards, we consider measured path loss (non-normalized propagation channels). In this section, all numerical results are computed under the EIRP constraint ($EIRP = 23$ dBm). Note also that the power is equally shared among the spatial streams as well as subcarriers.

4.4.1 Impact of transmitting antennas considering a normalized channel

In this section, the effect of transmitting antennas (number and geometry of antennas) on MU-MIMO system with two receivers with two antennas each is analyzed based on a normalized channel. The reason of using the normalization is to keep only fast-fading effects so that the average SNR at the receiving antennas is set to a fixed value and can be easily adjusted as a parameter. The applied channel normalization in this article implies that the average propagation loss is set to 0 dB for both users [64]. The average SNR is defined as $SNR = EIRP/\sigma_n^2$ where $EIRP = 23$ dBm for this study, and is set to 20 dB. The aim is to assess the impact of transmitting antenna configuration on the BD capacity gain over SU-MIMO and to give recommendations to optimize MU-MIMO performance. To highlight the MU-MIMO capacity gain over SU-MIMO, most graphs below show the average of MU-MIMO to SU-MIMO capacity ratio.

4.4.1.1 Number of transmitting antennas

Figure 4.9 gives the average of MU-MIMO to SU-MIMO capacity ratio versus the number of transmitting antennas arranged in an ULA. It also includes 10% (q_{10}) and 90% (q_{90}) quantiles as a reference. The first observation drawn from Figure 4.9 is that the MU-MIMO capacity gain over SU-MIMO grows logarithmically with the number of transmitting antennas. It changes from 1.27 to 1.7 for the residential environment, i.e. around 43% of capacity gain. For 4 transmitting antennas, the quantile q_{10} of capacity gain is less than 1. This can be explained by the fact that we cannot benefit from transmit beamforming gain since the number of transmit antennas is the same as the total number of spatial streams.

Figure 4.10 shows the average capacity values for MU-MIMO and SU-MIMO systems. The capacity value for MU-MIMO increases more rapidly than SU-MIMO. It achieves 24 bits/s/Hz versus 14 bits/s/Hz for SU-MIMO with 8 transmitting antennas. In order to optimize the MU-MIMO capacity gain and have a less congested system, we recommend using 6 transmitting antennas in a system with two receivers and two antennas for each receiver. If we aim at reaching higher capacities, using 8 transmitting antennas allows 2 bits/s/Hz of capacity increase.

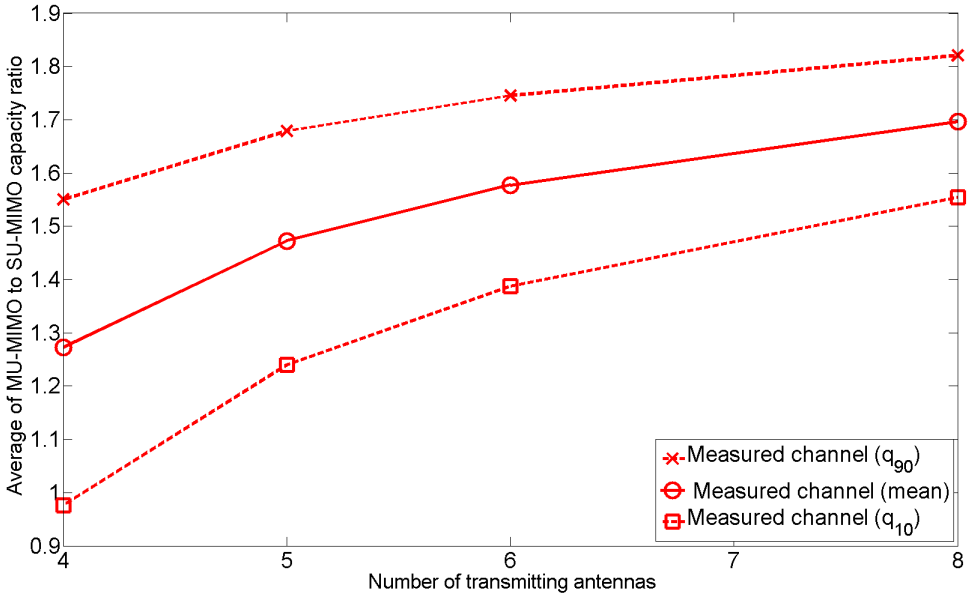

Figure 4.9 – Average of MU-MIMO to SU-MIMO capacity ratio versus the number of transmitting antennas.

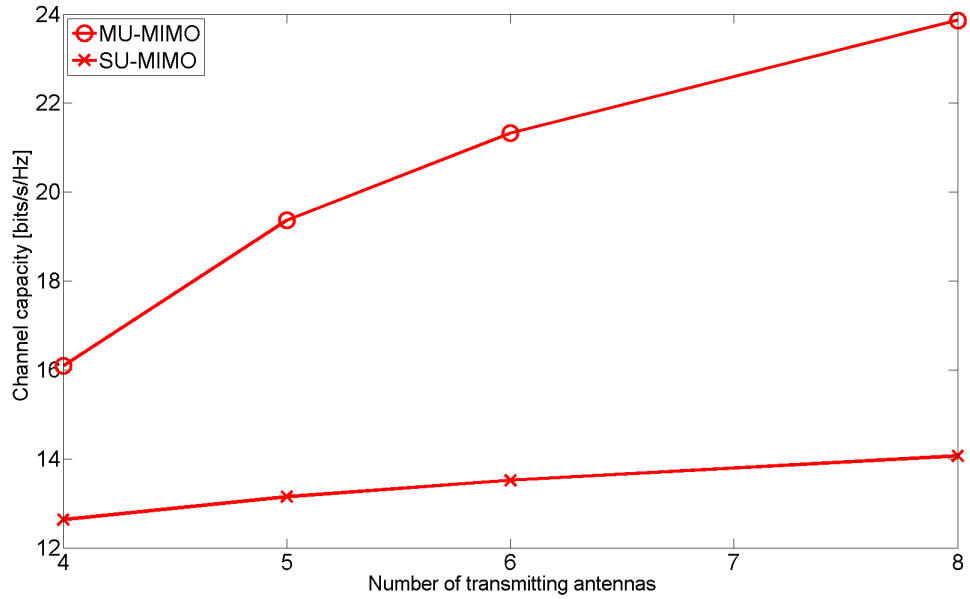

Figure 4.10 – Average MU-MIMO to SU-MIMO capacity values versus the number of transmitting antennas.

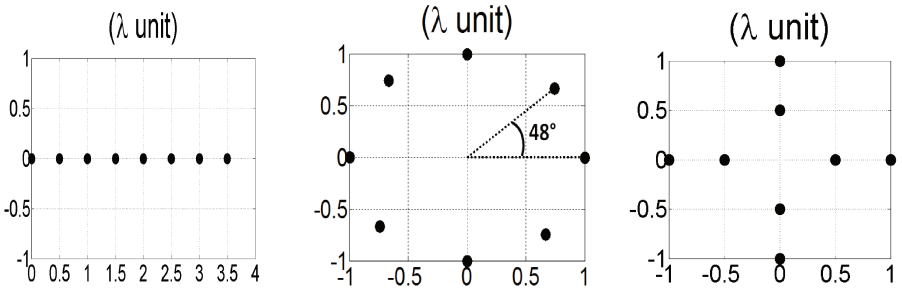

(a) ULA (b) ICA 1 λ (c) CCA

Figure 4.11 – Antenna array geometries.

4.4.1.2 Different antenna array geometries for 8 transmitting antennas

Before comparing the performance of MU-MIMO to SU-MIMO, we first define the analyzed planar and horizontal antenna array geometries. We evaluate a Tx with 8 antennas arranged in ULA, Crossed Circular Array (CCA) with 0.5 λ spacing, and Irregular Circular Array (ICA) with different radiuses as illustrated in Figure 4.11.

In Figure 4.11(b), the antennas are placed on the same circle and 48° is a multiple of the angular step of 6°. Four radiuses are considered: 0.5 λ, 1 λ, 2 λ and 3 λ. ICA 0.5 λ, ICA 1 λ, ICA 2 λ and ICA 3 λ denote the corresponding geometries. Note also that the results are presented based on the two-user channel correlation coefficient explored in Chapter 3, Equation 3.7. The ULA geometry is evaluated with mutual coupling since it is composed with physical antennas. However, ICA and CCA are evaluated without the coupling effect, both simulated with virtual antennas.

Figure 4.12 gives the average of MU-MIMO to SU-MIMO capacity ratio versus the average correlation coefficient. The highest MU-MIMO capacity gain over SU-MIMO is achieved with antennas arranged in CCA with relatively small correlation coefficient value. This confirms the results of [67] of reducing the span of an antenna array. All the simulated geometries show small correlation. This is explained by the number of the transmitting antennas [64]. In terms of capacity values, as in Figure 4.13, we achieve 23.45 bits/s/Hz with the CCA geometry, which is very close to the highest one shown in the graph with ULA but with a greater span. Hence, we recommend to use the CCA geometry since it has a small size and gives higher gain with relatively low correlation values.

We have chosen to deeply characterize a Tx with 8 transmitting antennas since it represents the maximum number of spatial streams defined in IEEE 802.11ac. In this context, we have launched two simulations with 1000 randomly distributed antennas in a span of 2 λ as shown in Figure 4.14. Figure 4.14(a) randomly draws 8 transmitting antennas in the 2 λ quadrant of the total number of virtual antennas, denoted hereafter *quadrant*. Figure 4.14(b) gives the chosen 8 antennas in a circle with a radius of 1 λ, labeled next *circle*.

Since computing capacity has relatively high time consumption, Figure 4.15 plots

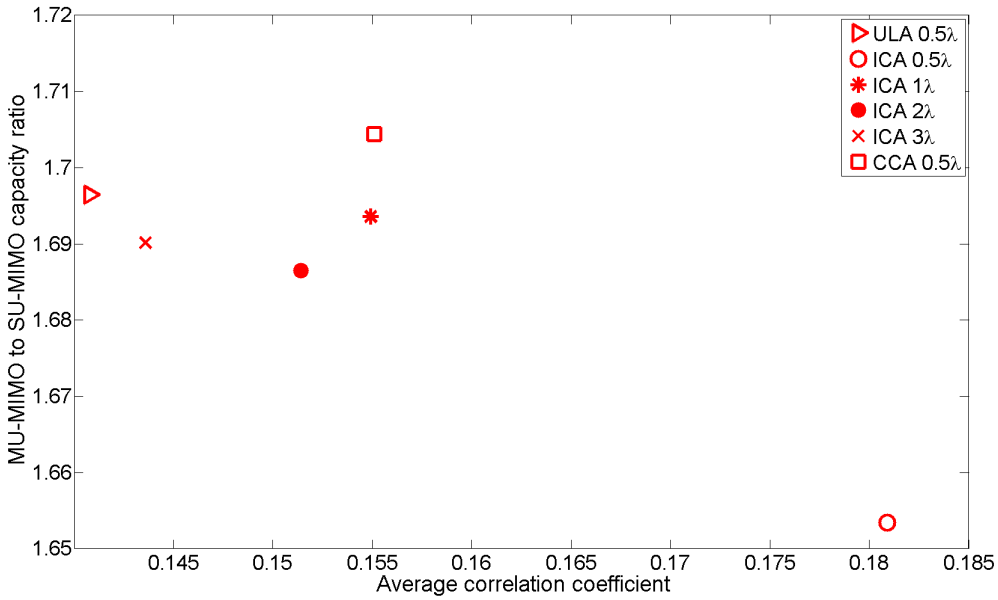

Figure 4.12 – Average of MU-MIMO to SU-MIMO capacity ratio versus the average correlation coefficient.

the CDF of the correlation coefficient values. The figure shows that the 1000 correlation coefficient values remain close to the regular geometries presented previously, i.e. around 0.14 of correlation. Only few draws show lower values of correlation coefficient (less than 15% draws show correlation coefficient less than 0.14). Further analysis could be made to identify the configuration that shows less correlation coefficient value. However, this optimization needs to be generalized to other environments and different Tx and Rx positions.

4.4.2 Impact of receiving antennas considering a normalized channel

In this section, the effect of the number of receiving antennas and the impact of the selected receiving antennas on MU-MIMO system with two receivers with two antennas each are analyzed based on a normalized channel.

4.4.2.1 Impact of selecting different receiving antennas

As can be seen in Figure 4.16, each user is equipped with four antennas. However, in the previous simulations we have evaluated a Rx with two antennas. In this subsection, we study the effect of selecting different receiving antennas on the MU-MIMO to SU-MIMO capacity gain and correlation.

Figure 4.17 gives the average of MU-MIMO to SU-MIMO capacity ratio versus the average correlation coefficient considering different receiving antenna arrangements. The

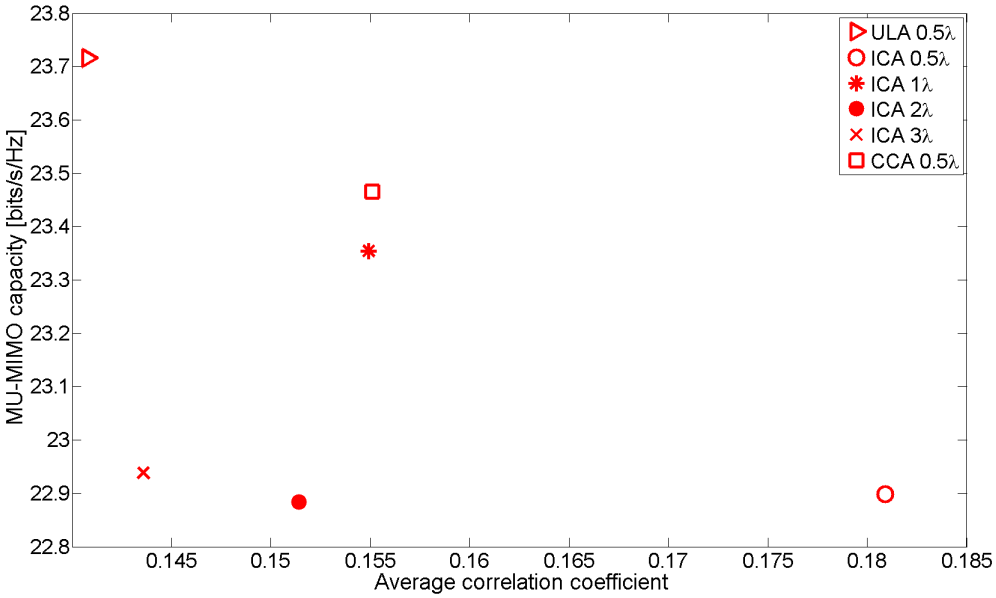

Figure 4.13 – Average MU-MIMO capacity values versus the average correlation coefficient.

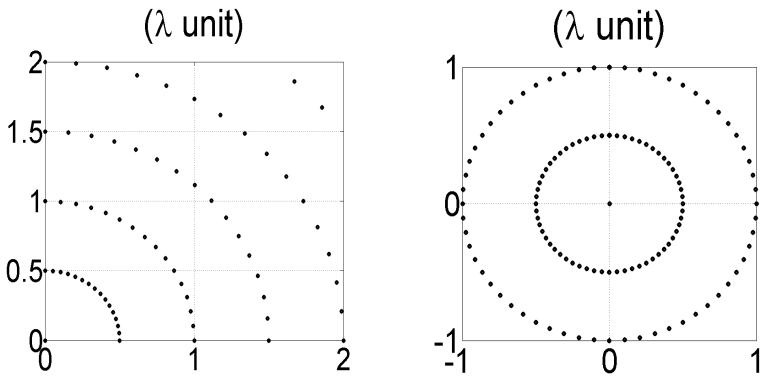

(a) Quadrant (b) Circle

Figure 4.14 – Random antenna array geometries.

highest MU-MIMO capacity gain over SU-MIMO is achieved with two antennas arranged in the diagonals across the square.

Additionally, this configuration extends the results of the previous chapter: spacing above 0.5 λ the receiving antennas increases slightly the MU-MIMO to SU-MIMO capacity gain: around 1% of capacity gain. All the cases show relatively small correlation of value: $0.18 - 0.19$. In terms of capacity values, as in Figure 4.18, we

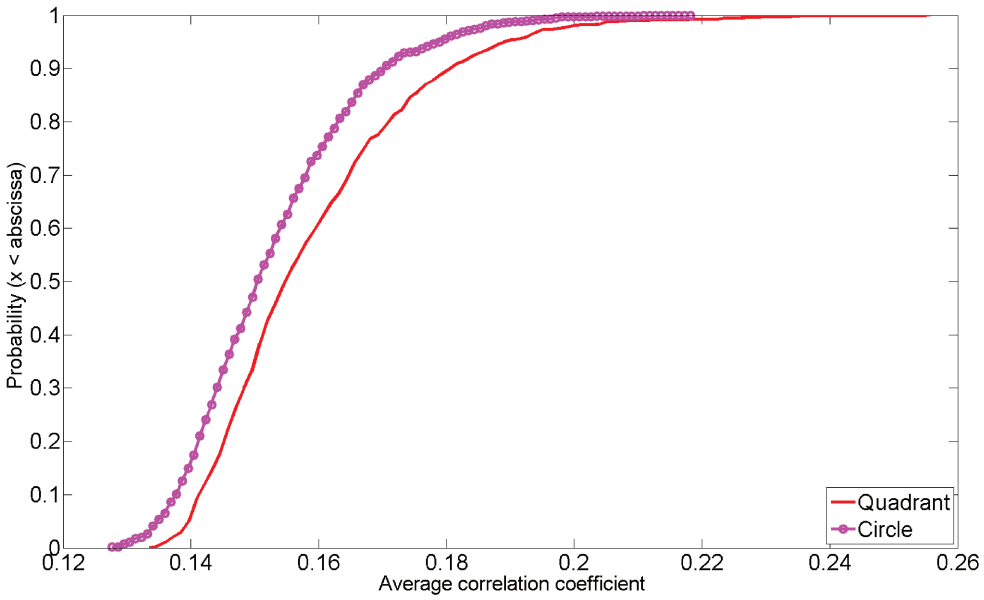

Figure 4.15 – CDF of the correlation coefficient.

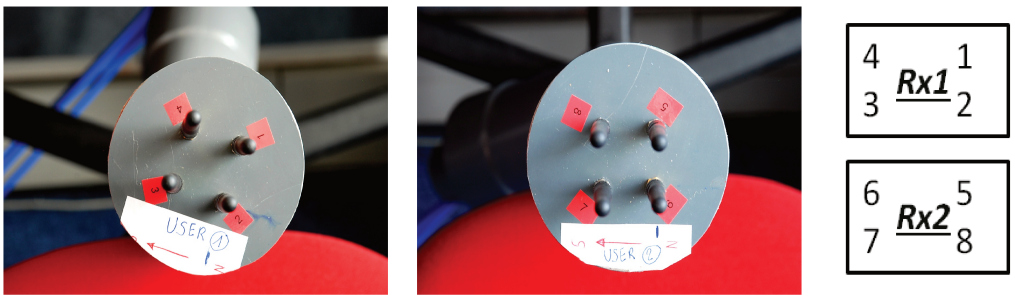

(a) Rx1 (b) Rx2 (c) Index

Figure 4.16 – The two users indices.

achieve 21.83 bits/s/Hz with the diagonal antennas, which is the highest one shown in the graph.

4.4.2.2 Impact of increasing the number of receiving antennas

In this subsection, we assess the impact of increasing the number of receiving antennas to $n_R = 3$ in optimizing the MU-MIMO techniques while keeping the total number of spatial streams $N_{ss} = 4$. Next subsection will highlight in details the impact of increasing the number of spatial streams. The evaluated system is composed of one transmitter equipped with $n_T = 4$ or $n_T = 6$ transmitting antennas arranged in ULA

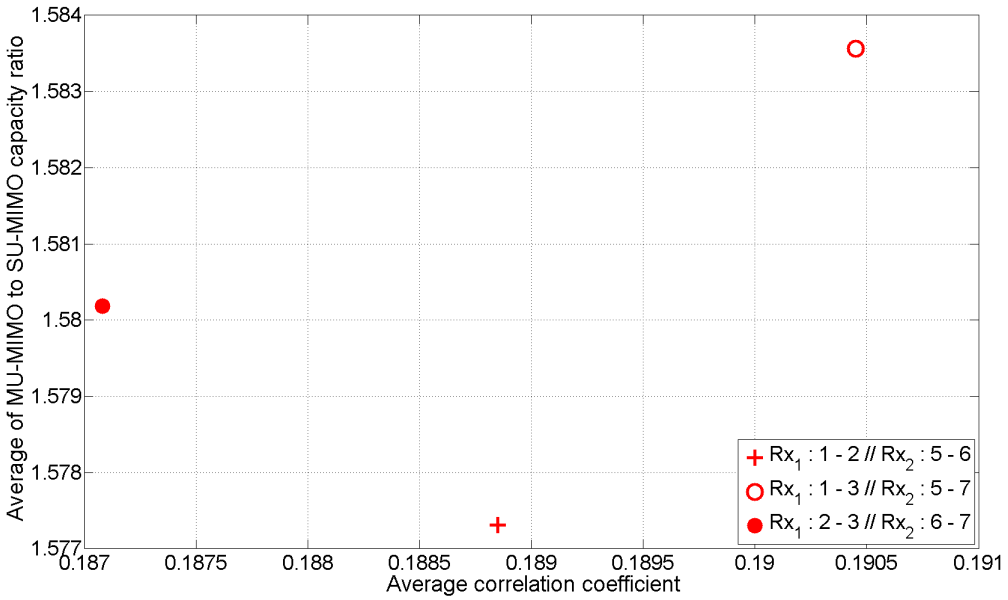

Figure 4.17 – MU-MIMO to SU-MIMO capacity ratio versus the average correlation coefficient ($n_T = 6$).

and two receivers with $n_R = 3$ antennas each. The average SNR is set to $SNR = 20$ dB. Figure 4.19 depicts the MU-MIMO to SU-MIMO capacity ratio versus the average correlation coefficient. The first observation drawn from Figure 4.19 is that the number of receiving antennas does not impact the correlation coefficient. This result is expected by the formula of the correlation coefficient proved in Equation 3.22 for Rayleigh channel. Increasing the number of receiving antennas increases the MU-MIMO to SU-MIMO capacity gain of 5%.

In terms of channel capacity values, Figure 4.20 shows an increase of about 3 bits/s/Hz for Tx with 4 or 6 antennas. Using a third antenna in a receiver will enlarge its design. Regarding the obtained performance, we do not recommend to increase the number of receiving antennas excepted if the number of spatial streams per user is 3. In the case of 2 spatial streams per user, it is preferable to increase the number of transmitting antennas and keeping 2 antennas at the receiver.

4.4.3 Impact of increasing the number of spatial streams

In this subsection, we highlight the effect of the number of spatial streams in optimizing the MU-MIMO techniques. Before giving the statistical results, we present the simulated system depicted in Figure 4.21. It is composed of one Tx with 4 transmitting antennas spaced with 0.5 λ and two receivers equipped with four antennas each: $n_{R_1} = n_{R_2} = 4$. As previously stated in Chapter 2, the MU-MIMO can

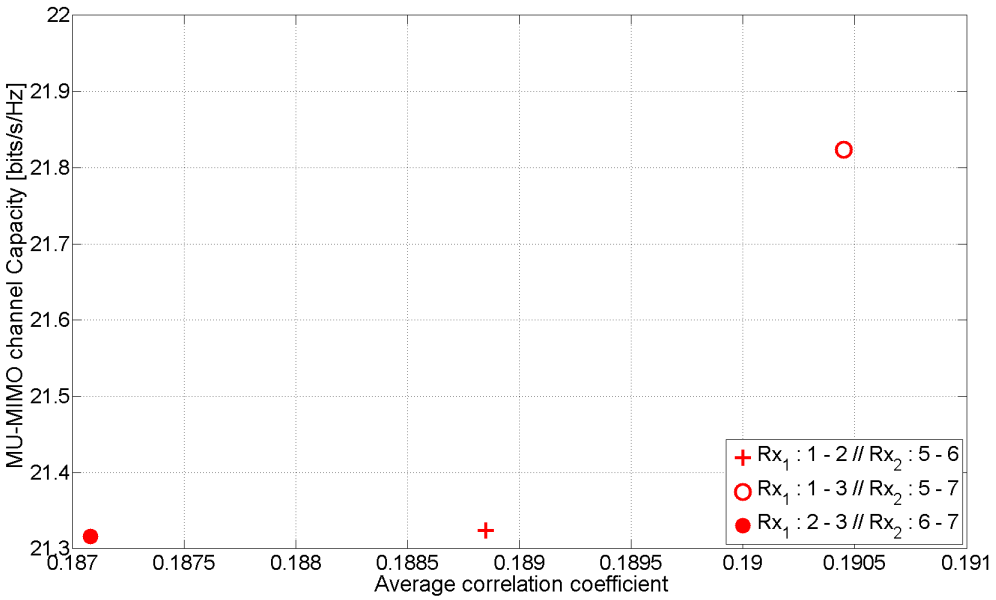

Figure 4.18 – Average MU-MIMO capacity values versus the average correlation coefficient ($n_T = 6$).

not be applied if the total number of spatial streams is greater than the number of transmitting antennas. Hence, we can simulate the MU-MIMO processing in the only case where the total of number spatial streams is 4 with $n_T = 4$ transmitting antennas. The SU-MIMO system is composed of 4 transmitting antennas and 4 receiving antennas. The objective here is to identify for which number of spatial streams, the MU-MIMO is preferable to SU-MIMO. The capacities are computed using five SNR values: $SNR = 15$; 20 ; 30 ; 45 dB and 60 dB. For numerical values, we have: $EIRP = 23$ dBm, 46.8 dB the free space path loss at 1 m range at 5.25 GHz and -93 dBm the noise power. We can expect SNR values till $SNR = 70$ dB.

Figure 4.22 shows the MU-MIMO channel capacity as a function of the SNR. The figure shows that MU-MIMO clearly outperforms the SU-MIMO channel capacity for two and three spatial streams. However, for a system with 4 spatial streams, the MU-MIMO is not recommended. It shows a slight decrease (2 bits/s/Hz) in the capacity value with an $SNR = 40$ dB compared to SU-MIMO. The MU-MIMO processing has in addition the channel sounding which is not assumed throughout this report. This validates the recommendation about using the MU-MIMO processing rather than the classical SU-MIMO techniques when the number of the transmitter antennas is greater than the total number of spatial streams. The number of spatial streams is generally limited by the number of receiving antennas of cheap devices.

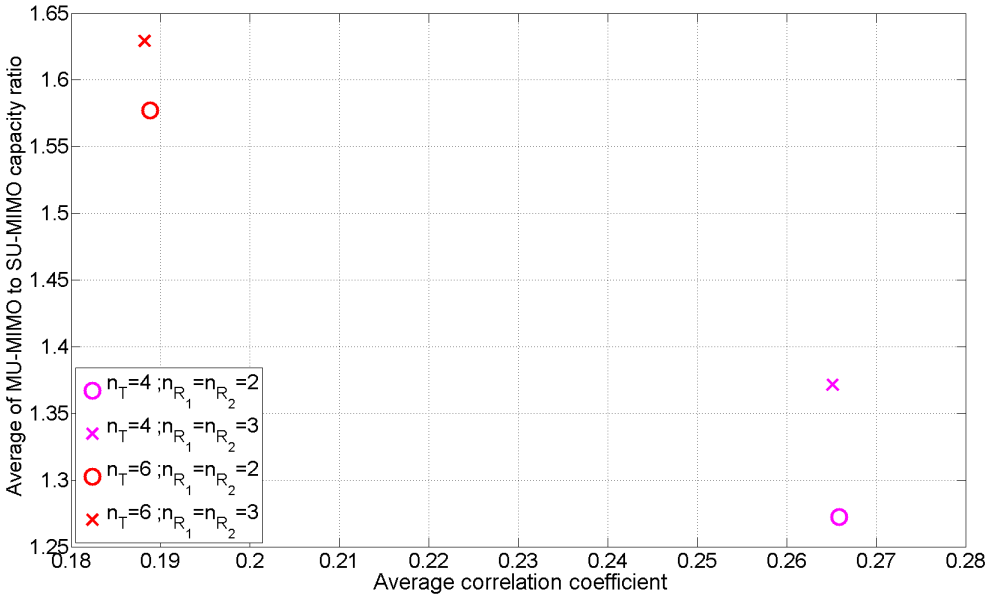

Figure 4.19 – Average MU-MIMO to SU-MIMO capacity ratio versus the average correlation coefficient.

4.4.4 Impact of the path loss difference on MU-MIMO gain

In this section, we consider the propagation channel including its measured path loss on a 20 MHz bandwidth. The $EIRP$ is equal to 23 dBm. The noise power is set to -93 dBm which corresponds to the noise temperature at $300°K$ for a 20 MHz band with a noise factor of 8 dB. The number of transmitting antennas is set to 6 arranged in ULA geometry. The SU-MIMO capacity is expressed considering TDMA and CSMA/CA channel access methods. The transmitter communicates with two receivers. Each receiver is equipped with two antennas spaced by $\frac{\lambda}{2}$. We consider the average received power at each user in dBm.

Figure 4.23 shows the average of MU-MIMO to SU-MIMO capacity ratio versus the absolute difference of the average received powers (in dB) denoted as ΔP by the two receivers Rx_1 and Rx_2. We observe that when ΔP is below 15 dB, both channel access methods give almost the same results. Nevertheless, compared to SU-MIMO CSMA/CA method, it is advantageous to group users with larger ΔP and use MU-MIMO: the capacity gain can be greater than 2. Actually, if C_1 is very small compared to C_2, then $C_{SU,CSMA}$ is penalized by C_1 [15] which is not the case of $C_{MU-MIMO}$. We also notice that the capacity gain in all cases is higher than 60% in a 12 m $\times$7 m apartment with a 23 dBm EIRP. This proves the benefit of using the MU-MIMO method rather than SU-MIMO.

Figure 4.24 includes the correlation parameter ρ in a 3D surface plot. The figure

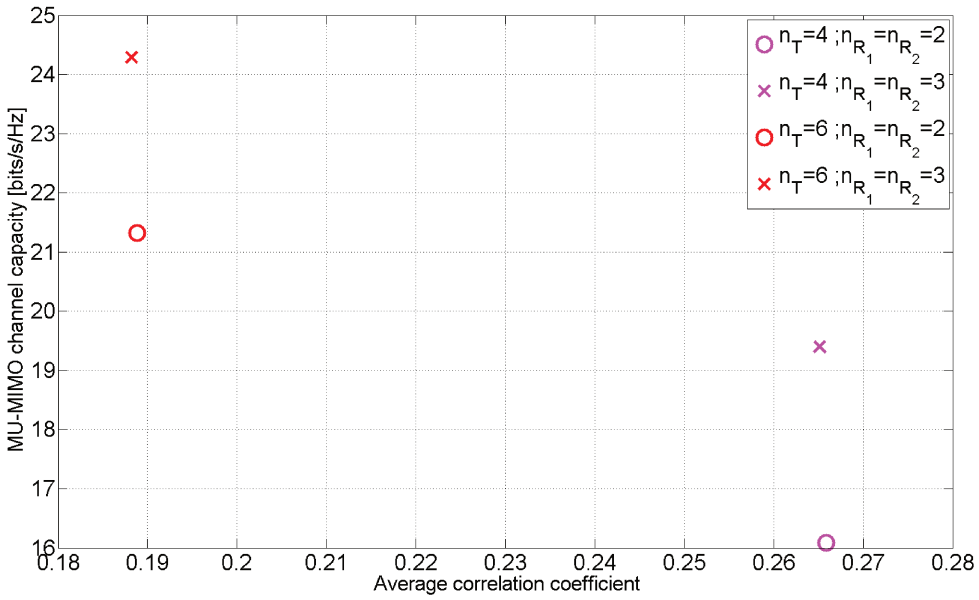

Figure 4.20 – Average MU-MIMO capacity values versus the average correlation coefficient.

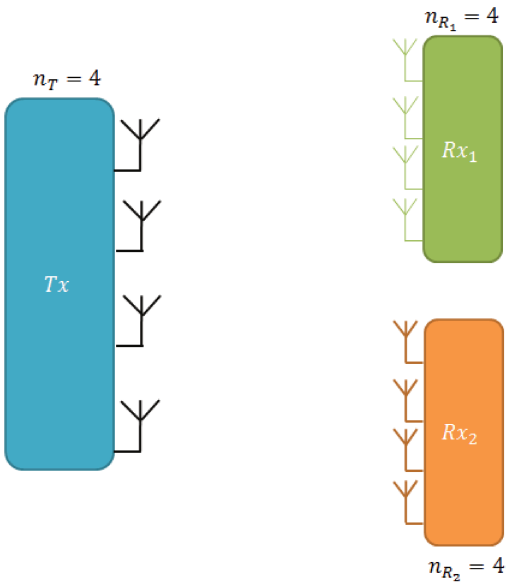

Figure 4.21 – MU-MIMO system model with $n_T = n_{R_1} = n_{R_2} = 4$.

shows that the best capacity MU-MIMO capacity gain is obtained for low correlation values and high ΔP. This is confirmed as detailed latter in Subsection 4.5.2 by the fact

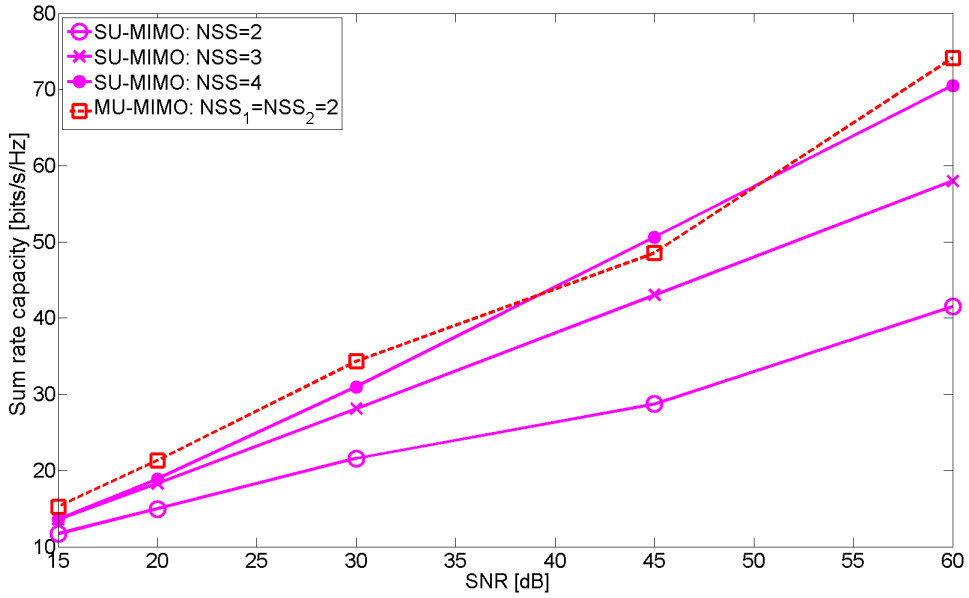

Figure 4.22 – Average MU-MIMO capacity values versus the SNR.

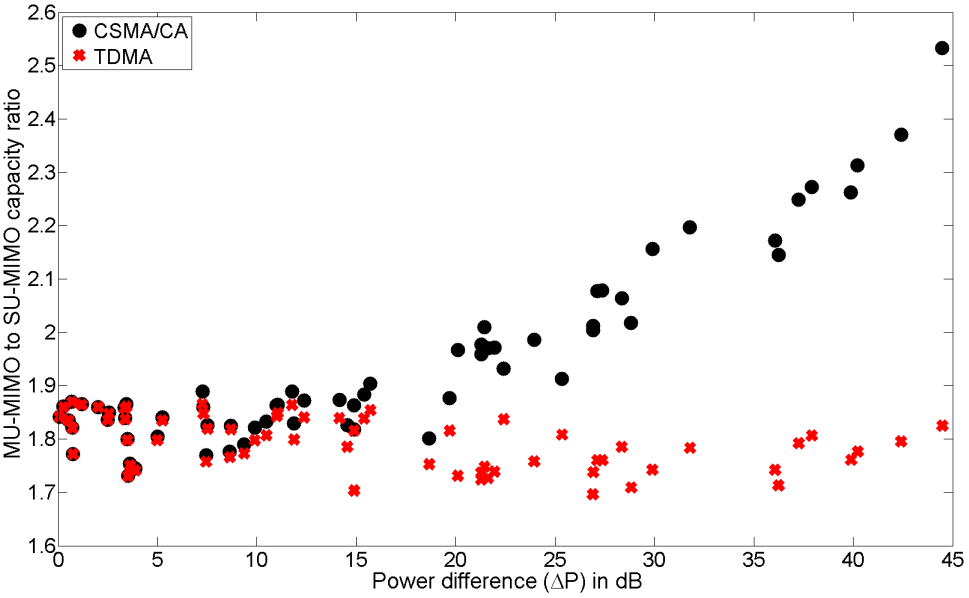

Figure 4.23 – Average MU-MIMO to SU-MIMO capacity ratio versus ΔP.

that high difference in the received powers means low level of similarity between the users' channels. Hence, the correlation coefficient is low.

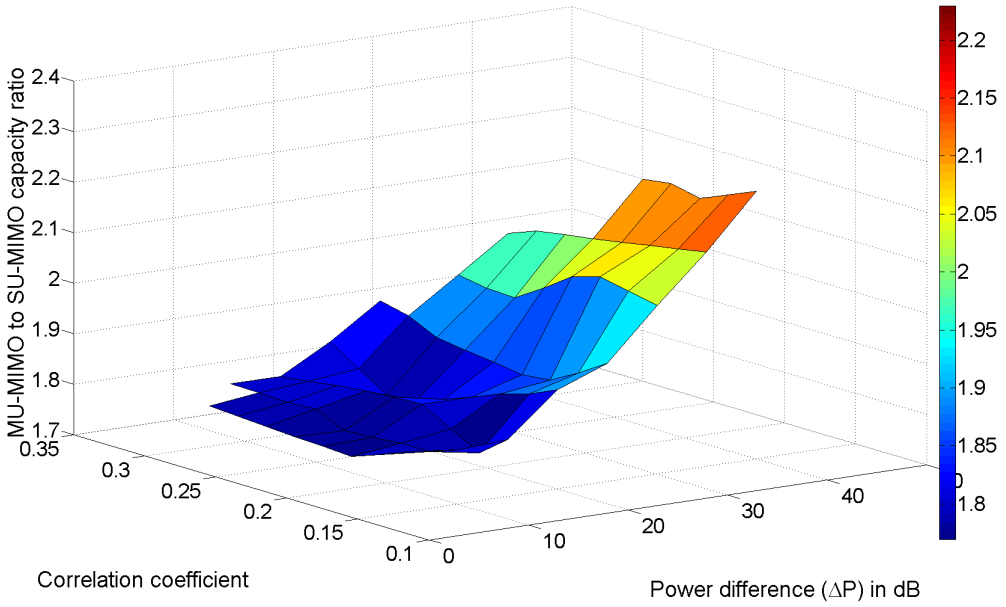

Figure 4.24 – MU-MIMO to SU-MIMO capacity ratio versus ΔP and correlation coefficient.

4.5 Measured versus simulated environments: numerical results

This section gives a thorough comparison between the numerical results based on simulated and measured channels. Since the TGac channel models simulate antennas arranged in ULA, we will confine the comparisons on evaluating a Tx with antennas arranged in ULA. We have presented in previous sections global statistical results including both LOS and NLOS cases. In this section, we will distinguish the two cases in order to have meaningful comparison with TGac simulation results.

The used notation for measurements comprises three cases. First, we denote the case where two receivers are in LOS with the transmitter as *"Meas. LOS"*. Second, the case where the two receivers are in NLOS with the transmitter is refereed to as *"Meas. NLOS"*. Finally, the case where one of the two users is in LOS and the other one is NLOS conditions with the Tx is denoted as *"Meas. LOS/NLOS"*.

Similarly, we denote the TGac-B channel model with users in LOS and NLOS with the Tx as *"TGac-B LOS"* and *"TGac-B NLOS"* respectively. The SNR is set to 20 dB and is based on the EIRP constraint.

4.5.1 MU-MIMO to SU-MIMO capacity gain

Figure 4.25 plots the values of the MU-MIMO capacity gain over SU-MIMO versus the number of transmitting antennas. We have considered a Tx with 4 to 8 transmitting antennas. The red curves correspond to values computed based on measurements, whereas blue curves show values with the TGac-B channel model. The reference values are showed based on Rayleigh channel in green color.

Clearly, the six curves show similar MU-MIMO to SU-MIMO capacity gain. The measured NLOS configuration (one of the receivers is on NLOS with the Tx) shows better performance for measured channels with 5 % of MU-MIMO to SU-MIMO capacity gain more than the configuration where the two users are on LOS with the Tx for measured channel with 4 or 5 transmitting antennas. The MU-MIMO to SU-MIMO gain difference is insignificant for further number of transmitting antennas for all the configuration.

The measured MU-MIMO to SU-MIMO capacity gain slightly overcomes the gain values with Rayleigh channels when one of the two users is in NLOS with the Tx. This can be explained by evaluating the channel capacity values in Figure 4.26.

It shows that the measured capacity values approach the references values computed based on Rayleigh channel for MU-MIMO SU-MIMO capacity values.

Indeed, the Rayleigh channel remains uncorrelated passing from SU-MIMO to MU-MIMO systems, whereas a measured environment becomes less correlated passing from SU-MIMO to MU-MIMO. Another explanation is given based on the correlation coefficient in the next subsection.

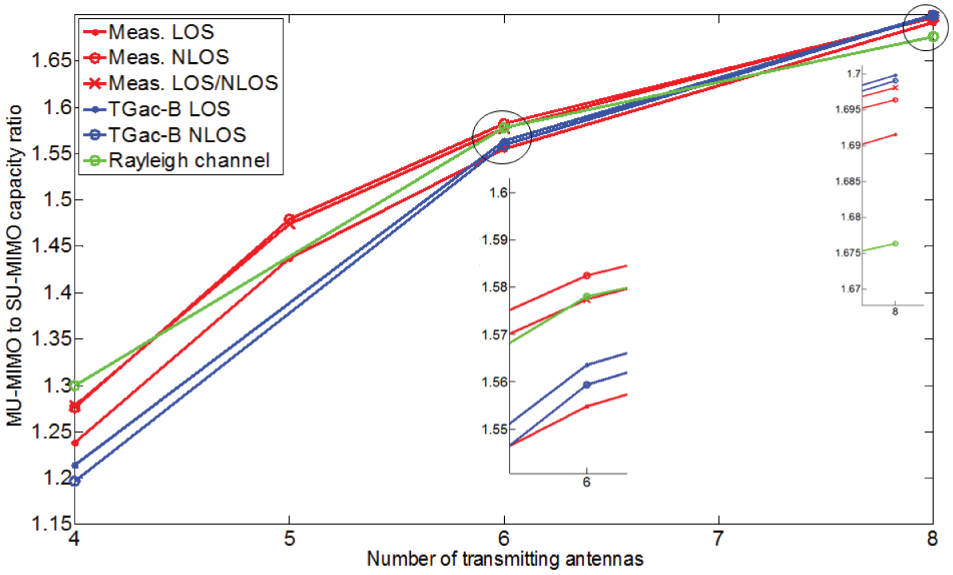

Figure 4.25 – Average MU-MIMO to SU-MIMO capacity ratio versus versus the number of transmitting antennas.

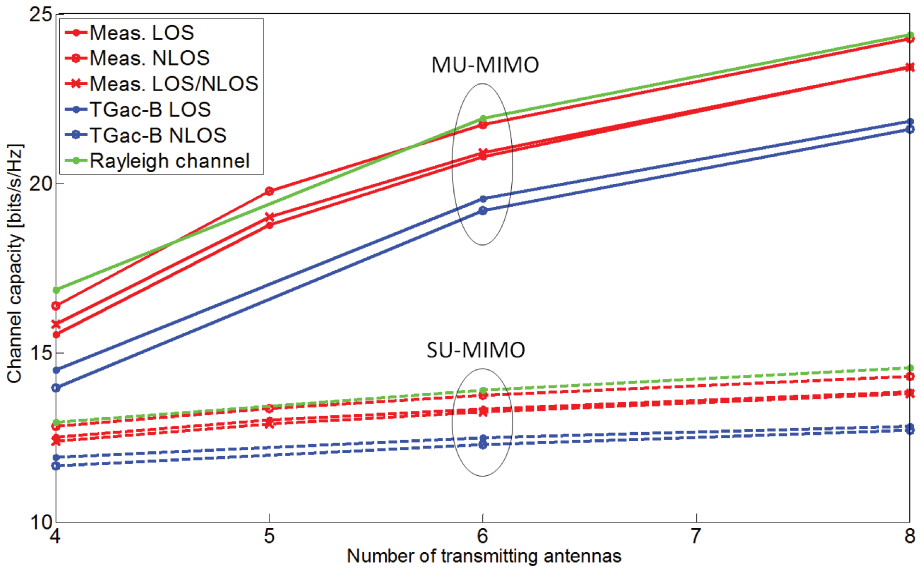

Figure 4.26 – Average MU-MIMO channel capacity versus the number of transmitting antennas.

4.5.2 Correlation coefficient

Figure 4.27 gives the average 2-user channel correlation coefficient versus the number of transmitting antennas. The measured channels show values of correlation approaching the correlation for i.i.d. Rayleigh channels when one of the two users on NLOS with the Tx. The channels are more correlated when the two users are in LOS with the Tx.

Figure 4.28 shows regression lines of MU-MIMO to SU-MIMO capacity gain versus the correlation coefficient for different transmitting antennas based on measurements. Hereafter only global results are displayed, more measurements would be necessary to deduce the regression parameters for separate cases: LOS and NLOS. Table 4.1 summarizes the numerical results defined in the previous chapter. We have computed the regression for the four values of the number of transmitting antennas arranged in ULA. The other geometries are studied in Appendix D.

n_T	a_0	a_1	r	RMSE
4	1.5525	-1.0471	0.8964	0.0292
5	1.6809	-0.9379	0.8838	0.0267
6	1.7458	-0.8899	0.9016	0.0213
8	1.8141	-0.8235	0.8863	0.0169

Table 4.1 – Numerical results of linear regression parameters for different transmitting antennas.

For comparison, Table 4.2 displays numerical results, which are different from the

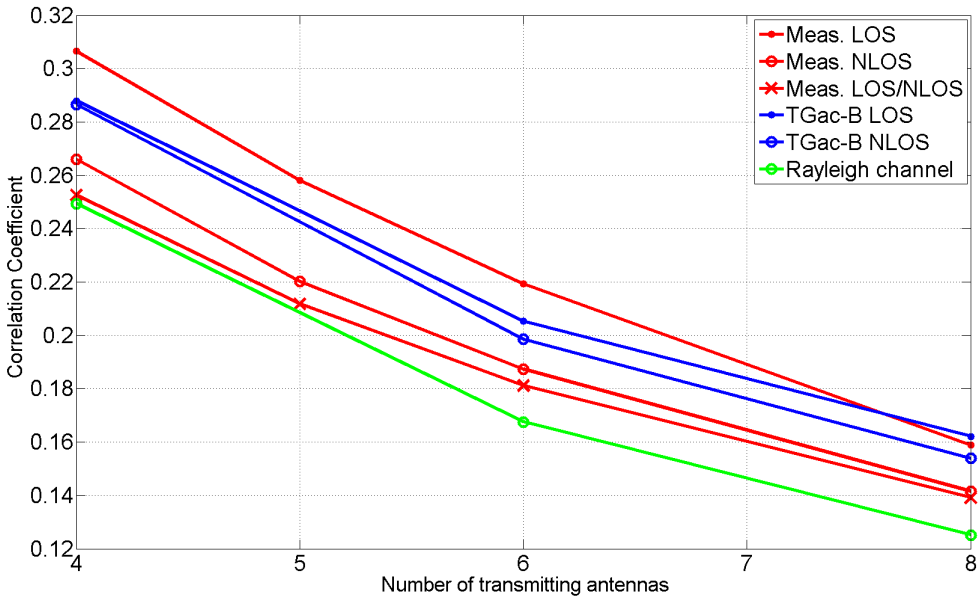

Figure 4.27 – Correlation coefficient versus the number of transmitting antennas.

ones showed in the previous chapter because the MU-MIMO to SU-MIMO capacity gain values are computed based on the EIRP constraint.

Scenario	LOS|NLOS	LOS|NLOS	LOS|NLOS	LOS|NLOS
n_T	a_0	a_1	r	RMSE
4	1.6864| 1.6719	-1.6373|-1.6553	0.9340| 0.9629	0.0487| 0.0302
6	1.8824|1.8741	-1.5518| -1.5817	0.9284| 0.9524	0.0435| 0.0294
8	1.9173 |1.9190	-1.3426|-1.4269	0.9327|0.9647	0.0331| 0.0203

Table 4.2 – Numerical results of linear regression parameters for different transmitting antennas [TGac-B channel model].

The expression of MU-MIMO to SU-MIMO capacity gain as a function of correlation coefficient motivates us to look for a simplified expression of the correlation coefficient as a function of the physical parameters such as users' relative position.

Figure 4.29 plots the correlation coefficient as a function of angles and distances for a Tx with $n_T = 4$ and two receivers in NLOS with $n_{R_1} = n_{R_2} = 2$ spaced by $\frac{\lambda}{2}$ as defined in TGac-B channel models. Indeed, for each drawing, four angles are drawn randomly by the TGac channel models. However, the points are dispersed and no conclusion could be drawn except that the points are randomly distributed and with a nearly periodicity.

Similarly, Figure 4.30 plots the correlation coefficient versus the users' position for a transmitter with $n_T = 8$ arranged in ULA based on measurements. We denote

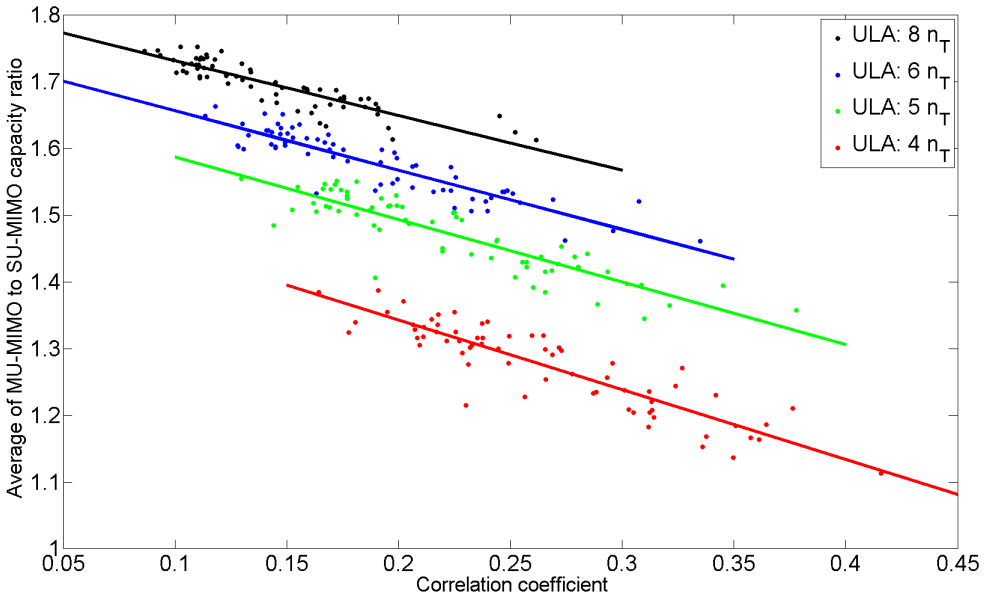

Figure 4.28 – Average of MU-MIMO to SU-MIMO capacity ratio versus the average correlation coefficient.

respectively the distance between each Rx_1 and Tx and Rx_2 and Tx as Tx−Rx_1, Tx−Rx_2. The angle in this case is defined as in Figure 4.31 The trend of the correlation coefficient gives an interesting result. It can approximately be expressed by the ratio of the distance between the first user and the Tx and the distance between the second user and the Tx. Table 4.3 gives the regression parameters for the studied configuration. The correlation coefficient is low. A better prediction would need other parameters to be included.

n_T	a_0	a_1	r	RMSE
8	0.1200	0.0139	0.4496	0.0350

Table 4.3 – Linear regression parameters for 8 transmitting antennas [Measured channel].

4.6 Conclusion

A MU-MIMO measurement campaign has been conducted in a residential environment for two users with two antennas each. The obtained sum rate capacity under the EIRP constraint results confirm that 6 is the recommended number of transmitting antennas to keep a compact size of the transmitting antenna arranged in

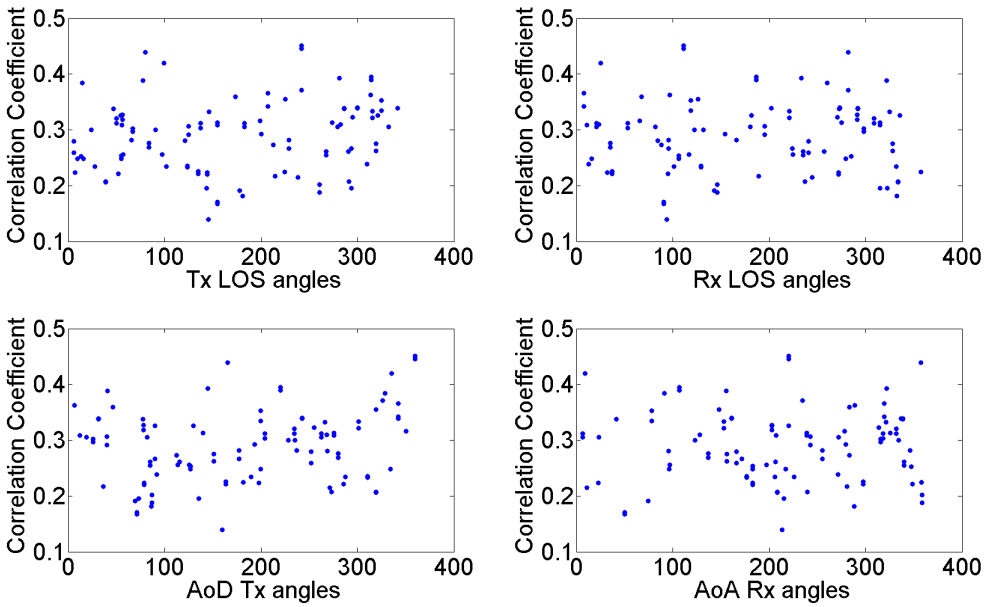

Figure 4.29 – Correlation coefficient versus the users' position [TGac-B channel].

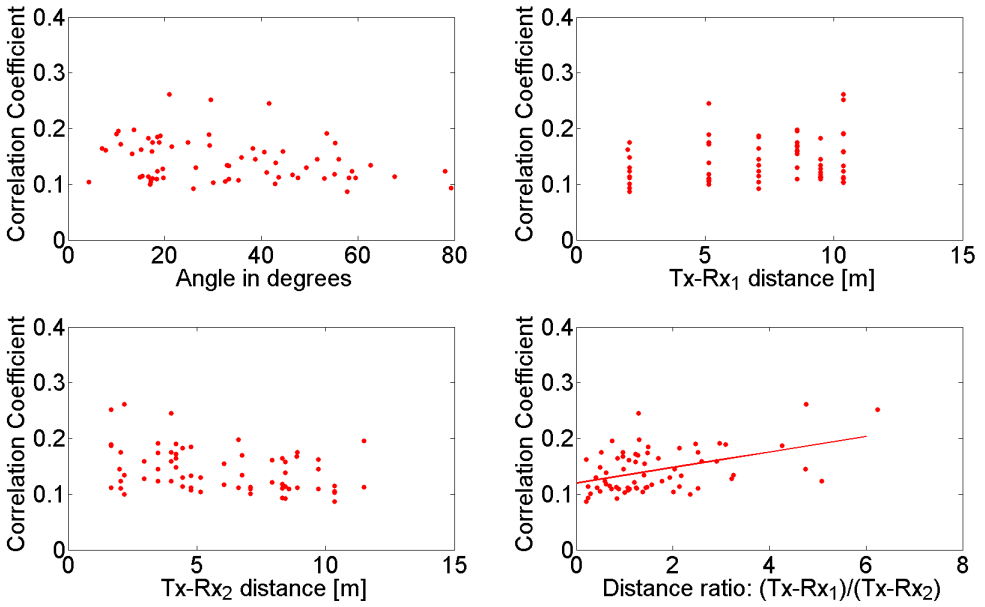

Figure 4.30 – Correlation coefficient versus the users' position [Measured channel].

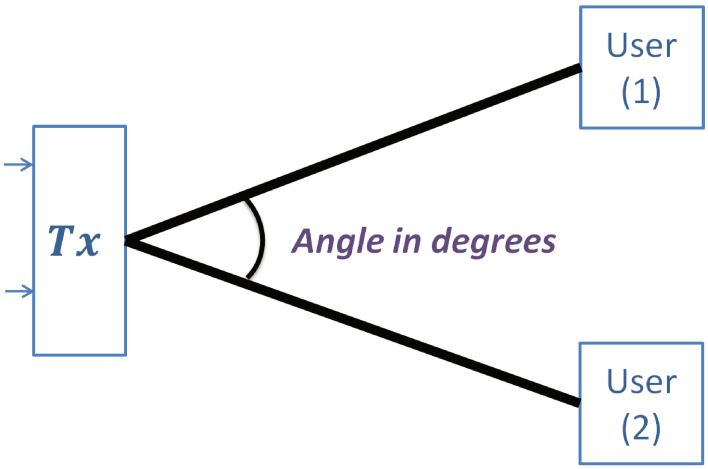

Figure 4.31 – Angles in degrees [Measured channel].

ULA: a gain of 58% is achieved for a 20 dB SNR. The experiment extends the study to various planar antenna array geometries. We recommend to use the CCA geometry.

We have evaluated the performance when increasing the number of receiving antennas and the number of spatial streams. However, this practice is not always possible as we need to keep the users as simple as possible.

Furthermore, we have studied the advantage of grouping users with a high path loss difference. In particular, in a typical indoor apartment with a 23 dBm EIRP, MU-MIMO is better than SU-MIMO based on IEEE 802.11ac CSMA/CA: the capacity gain goes beyond the double since SU-MIMO based on CSMA/CA is penalized when the gap between the received power of each user is high. These results have to be confirmed with real IEEE 802.11ac equipment and with non-perfect CSI and sounding protocol.

Furthermore, we have performed a comparison between these results and the ones based on the MU-MIMO channel model specified for 802.11ac presented in the previous chapter. In particular, we have confirmed the conclusions about approximating the MU-MIMO to SU-MIMO capacity gain using the correlation coefficient. Additionally, we have been able to approximate the correlation as a function of the users' relative distance to their AP.

Finally, the conditions LOS and NLOS are not relevant in a residential environment since they show similar numerical results.

Chapter 5

Transmit beamforming gain analysis for network planning tools based on propagation measurements

Contents

5.1 Introduction

The ability to accurately predict radio-propagation for wireless communication systems, is becoming crucial for system design and radio planning. In this context, the Wireless local Area Network Design and Analysis (WANDA) software has been developed by Orange Labs Belfort to design indoor WLAN. Figure 5.1 gives an example of Wi-Fi radio coverage proposed by WANDA. It has been simulated at

5 GHz in the apartment where the measurement campaign presented in the previous chapter were carried out. This coverage relies on a simple path loss model, taking into account only the building materials crossed by the direct line between the transmitter and the receiver. Note that ray tracing which considers reflected and diffracted path could be also used. This coverage map assumes that the AP has an independent antenna pattern of users' positions and is constant over time. This is also the case today of other commercial radio planning tools. However, the TxBF technique supposes a variable pattern. It shapes the effective radiation pattern of the antennas pointing towards the direction of the dominant multi-paths by controlling the power and the phase of the transmitted signals. This results in a significant variation on the radiated powers, received powers and interferences since the radiated power is expressed as a function of the precoding matrix which depends on the propagation channel (Chapter 3, Section 3.4, Equation 3.24).

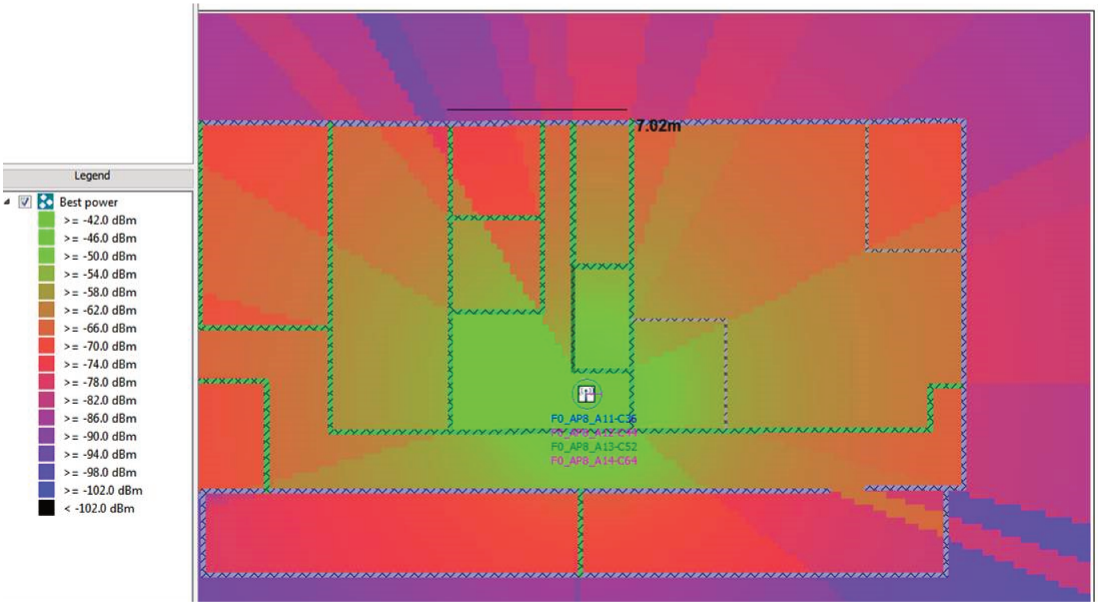

Figure 5.1 – Coverage map for a transmitter placed in the living room.

This chapter evaluates the transmit beamforming based on measured data in a SU-MIMO context. We have not considered the MU-MIMO context because in order to evaluate the interference level hereafter, we consider one user as *targeted user*, and the other one as *interfered*. In a MU-MIMO context, we would need at least the measurement data of three users to evaluate the interference level. Moreover, SU-MIMO is expected to have more TxBF gain compared to MU-MIMO since all the transmitting antennas are focusing the signal towards the same user. We first present in Section 5.2 the used metrics for the performance evaluation, and detail the methods of computation. In Section 5.3, we give the numerical and statistical results of the beamforming gain. We study the interference influence in Section 5.4. Finally, we draw

the conclusion and propose modeling for radio planning tools in Section 5.5.

5.2 Transmit beamforming analysis and modeling

5.2.1 Related work

Transmit beamforming is a feature of 802.11ac standard. It shapes the effective radiation pattern of the antennas pointing towards the direction of the dominant multi-paths by controlling the power and the phase of the transmitted signals. Various techniques may be used to implement the TxBF. There are phased antenna arrays (direction based beamformers), codes book (for Long Term Evolution (LTE)), dominant eigen mode selection (single beamforming technique with one antenna weighting vector and that carries only one spatial stream [71]), and the more general SVD-MIMO with one precoding matrix carrying all the spatial streams. This latter is selected in the 802.11ac standard and is studied in this chapter.

In the literature, TxBF has been studied in order to highlight its benefits compared to the use of a simple MIMO system using spatial multiplexing only. Most of the publications studied outdoor [72] or outdoor-indoor [73] environments based either on measurements made with equipment that implements TxBF or on a purely theoretical approach. Most of the results concern the dominant eigen mode TxBF. There are few results concerning the more general SVD-MIMO systems with multiple spatial streams [74][75], but they rarely concern typical European residential environments and European building materials. In fact, studies have analyzed several MIMO configurations in order to conclude on the relevance of a possible use of beamforming. The TxBF requires the knowledge of the MIMO propagation channel between the transmitter and the receiver. This implies frame exchanges between transmitter and receiver and an overhead in the frame control. For instance, in [76], it was shown that for small values of SNR (or high interference level) the dominant eigen mode Beamforming (BF) schemes can perform close to the MIMO system with singular value decomposition in terms of spectral efficiency, and can even outperform a MIMO system with CSI only at the receiver.

Other studies have focused on the comparison between introducing the dominant eigen mode and transmit diversity [77]. It was shown that, under ideal conditions (uncorrelated fading), transmit diversity has an advantage over a beamforming system. However, under handoff conditions, the beamforming system has both array gain and diversity, which improves its performance relative to transmit diversity.

The SVD, which is seen as one of the most relevant MIMO precoding techniques, is present in publications that address the topic of eigen beamforming with multiple streams. Indeed, the analysis in [78, 79, 80, 81] have focused on evaluating the impact of channel estimation error on the performance of MIMO system that implements SVD-MIMO technique. It was proved that in case of non-ideal channel knowledge and a limited accuracy in the channel matrix estimation, a reduced number of eigenmodes in the precoding process becomes an optimum and leads to an improved BER. A

typical system employing SVD shows capacity degradation when incorrect CSI is used to transmit data. Therefore, some papers propose a new linear processing architecture which reduces the effect of incorrect CSI at the transmitter.

Other approaches such as prototyping [82] have been also explored in order to assess the feasibility of an IEEE 802.11n transmit beamforming architecture before starting its mass production. However, it does not exploit the effect of the feedback delay to evaluate the added value of beamforming.

In the context of earlier studies, it was shown in [83] for example, that in the case of a single stream transported by a MIMO system with n_T transmitting antennas and n_R receiving antennas, a significant antenna array gain $n_T \times n_R$ can be achieved in LOS conditions i.e. in fully correlated received signals. For multiple streams and using the SVD-MIMO technique, a theoretical bound of the gain was defined in the case of a rich scattering environment (Rayleigh fading). This bound is $(\sqrt{n_R} + \sqrt{n_T})^2$. Other works such as [84] have also analyzed the diversity gain for such channels and SVD MIMO technique, and calculated that the achievable diversity order is $(n_T - N_{ss} + 1)(n_R - N_{ss} + 1)$ for N_{ss} spatial streams.

In [44], the transmit beamforming is analyzed based on simulations performed in a typical residential environment. The obtained results show that enabling TxBF increases the received power when n_T is important compared to N_{ss} (if $N_{ss} = n_T$, no power gain is achieved). Moreover, it was shown, for a given N_{ss}, that with TxBF enabled, it is more advantageous to increase the number of receiving antennas than the transmitting antennas number. Two optimal values of transmitting antenna spacing were proved to optimize the TxBF gain: around 0.5 λ and 1.25 λ. Accordingly, we have set the antenna spacing to 0.5 λ. Finally, it is proved that the TxBF can improve the transmission range especially when N_{ss} is sufficiently small compared to n_T. However, the published results are based on ray tracing tools, and no conclusion was carried out about the impact of the EIRP constraint on the numerical results.

In this chapter, we evaluate the TxBF performance under the EIRP constraint based on measured data in home environment. We reveal in particular the benefits of the introduction of this option compared to the use of a simple MIMO system with spatial multiplexing and spatial expansion. The comparisons have been performed using different metrics evaluated With Beamforming (W-BF) and Without Beamforming (Wo-BF) based on the SVD MIMO technique. This study addresses the impact of the overall MIMO configuration by varying the number of transmitting antennas, the number of receiving antennas and the number of spatial streams. Several transmitting antenna array geometries are compared to identify which one has the most important BF gain. The interference level reduction is then evaluated in order to investigate whether the introduction of TxBF can increase or reduce the interference generated by an AP with TxBF activated. Note that the TxBF as defined in 802.11ac standard is designed to optimize capacity but not to reduce or cancel interference to the undesired receivers.

5.2.2 System model

Let us consider a SU-MIMO system ($K = 1$). The number of receiving antennas and spatial streams are respectively $n_R = n_{R_1}$ and $N_{ss} = N_{ss1}$.

The $n_R \times n_T$ channel matrix is $\mathbf{H}_1$. The transmission scheme with n_T transmitting antennas system is equivalent to the system shown in Figure 5.2, where $\hat{\mathbf{V}}_k^{(1)}$ is defined in (Chapter 2, Subsection 2.5.5) as the right singular vectors of the channel matrix $\mathbf{H}_1$.

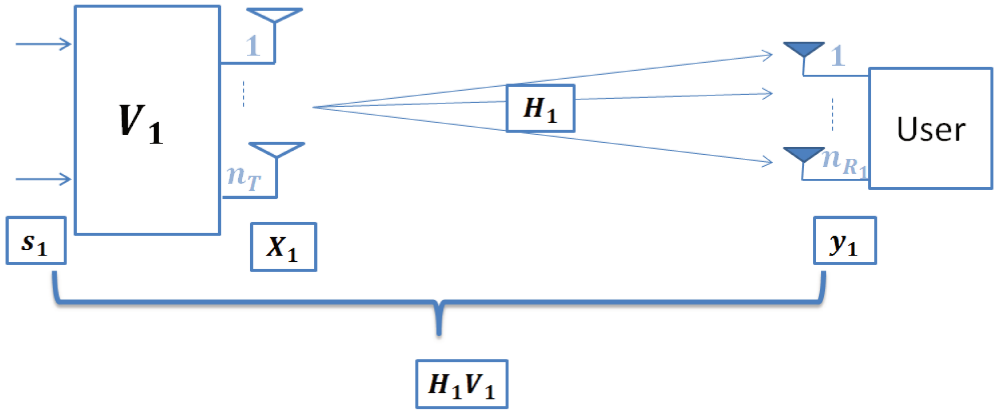

Figure 5.2 – Transmission scheme in case of an SVD based TxBF precoding.

The precoding technique transmits the matrix product $\mathbf{V}_1\mathbf{X}_1$, where $\mathbf{X}_1$ is the transmitted signal. Accordingly, the received signal in W-BF case $\mathbf{y}_{W-BF}$ is expressed as follows:

$$\mathbf{y}_{W-BF} = \mathbf{H}_1\mathbf{V}_1\mathbf{X}_1 + \mathbf{n}_1 \tag{5.1}$$

with $\mathbf{n} = \mathbf{n}_1$, column vector of n_R additive complex Gaussian noise with zero mean and equal variance for the independent real and imaginary components. It is also assumed that the noises noises at the receiving antennas are independent random variables. The total received power $P_{W-BF} = trace(E(\mathbf{y}_{W-BF}\mathbf{y}_{W-BF}^H))$ for a MIMO system applying TxBF is expressed as follows:

$$P_{W-BF} = \frac{P_{Tx}}{N_{ss}N} trace(\mathbf{H}_1\mathbf{V}_1\mathbf{V}_1^H\mathbf{H}_1^H) \tag{5.2}$$

We consider the TxBF under the EIRP constraint. We consider a 23 dBm EIRP and a total transmitted power P_{Tx} equally shared among the N_{ss} independent spatial streams. Hence, each spatial stream has the same average power $p_{SS} = \frac{P_{Tx}}{NN_{ss}}$.

In the case of a link not applying TxBF, the transmission scheme is given in Figure 5.3, where $\mathbf{Q}_1$ is the spatial mapping matrix used when there are more transmitting antennas than spatial streams ($N_{ss} \leq n_T$) [11] (see Appendix E). The received signal column vector $\mathbf{y}_{Wo-BF}$ is simply expressed as:

$$\mathbf{y}_{Wo-BF} = \mathbf{H}_1\mathbf{Q}_1\mathbf{X}_1 + \mathbf{n} \tag{5.3}$$

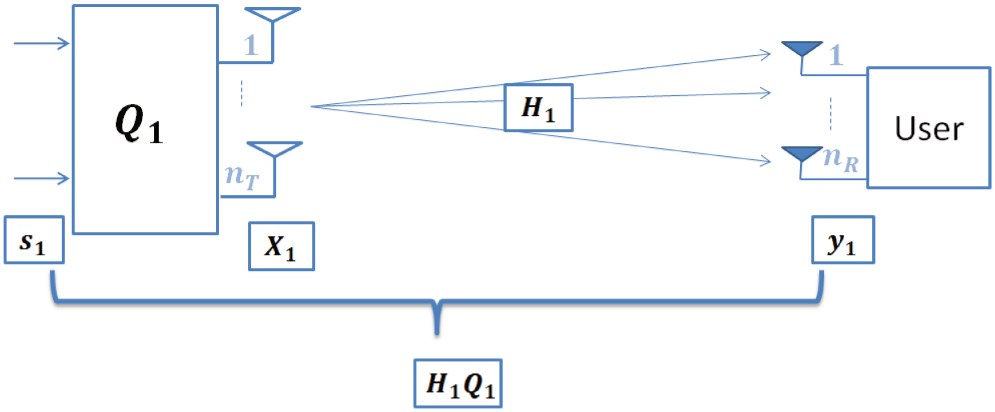

Figure 5.3 – Transmission scheme without TxBF (Wo-BF).

The received power without P_{Wo-BF} for a MIMO system without TxBF (Wo-BF) is expressed as follows:

$$P_{Wo-BF} = \frac{P_{Tx}}{N_{ss}} trace(\mathbf{H}_1\mathbf{Q}_1\mathbf{Q}_1^H\mathbf{H}_1^H) \tag{5.4}$$

Using Equations 5.2, 5.4, if the number of spatial streams is equal to the number of transmitting antennas, then $\mathbf{V}_1\mathbf{V}_1^H = \mathbf{I}$ and $\mathbf{Q}_1\mathbf{Q}_1^H = \mathbf{I}$ and the received power with TxBF is identical to the one received without TxBF, i.e. if $N_{ss} = n_T$, then $P_{W-BF} = P_{Wo-BF}$.

5.2.3 SNR gain

In this subsection, we present the SNR gain to achieve the same capacities as a metric to evaluate the transmit beamforming gain.

The first step consists of evaluating the SU-MIMO capacity satisfying the EIRP constraint: $EIRP = 23$ dBm (Chapter 3, Section 3.4) for several values of path loss. Actually, using the 67 various 2 users configurations, we normalize the channel to have a path loss in the range $[\![45 \text{ dB}, 110 \text{ dB }]\!]$ since 46.8 dB is the free space path loss at 1 m range at 5.25 GHz. For each value of path loss, the median value of SU-MIMO is computed. Since the median SU-MIMO capacity reveals a linear decrease as a function of path loss (in dB), we have applied a linear regression as depicted in Figure 5.4. The figure illustrates an example of the regression lines of the SU-MIMO capacity with (blue line) and without (red line) beamforming for a system $n_T = 2, n_R = 1, N_{ss} = 1$ as a function of path loss. For numerical examples, as in previous chapters, we have considered the noise temperature at $300°K$ for a 20 MHz band with a noise factor of 8 dB. The value is then: $\sigma_n^2 = -93$ dBm.

The SNR gain is defined as the SNR difference between the regression lines in dB as can be seen in the figure.

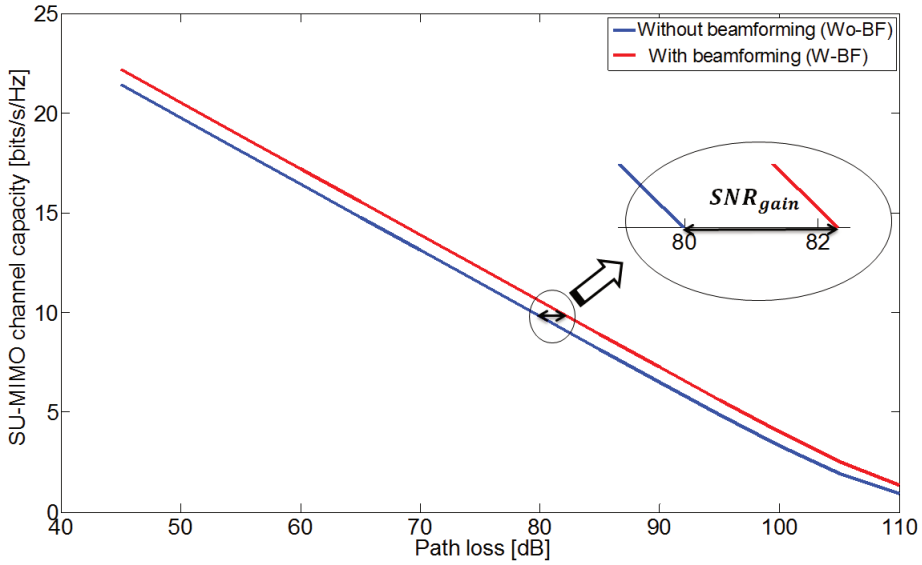

Figure 5.4 – SU-MIMO capacity as a function of path loss.

5.2.4 Beamforming and interference

One other relevant aspect to be addressed about transmit beamforming is its ability to reduce interference. It modifies the radiation pattern of the emission and favors the targeted receiver, but it is unclear if the power level received by other users has increased or decreased, as this depends on the multipath, the number of antennas and the beam directivity. Basically, 802.11ac is not designed to minimize the interference. The received power and interference level are important parameters determining the transmission quality. In fact, BER decreases as the received power increases, which helps maintaining a high data rate. Otherwise, the degradation of the bit error rate causes a switching to a modulation and coding scheme that reduces the bit rate. Enabling the beamforming option can compensate a possible decrease of the received power due to a deterioration of transmission conditions. The powers received by all the receiving antennas using or not using the TxBF are computed.

Figure 5.5 illustrates the used interference model. We have exploited the measured data for the MU-MIMO system with two users. We have simulated the activation of the beamforming towards one user, labeled *targeted user*. We next compute the received powers using or not using beamforming towards the second user labeled *Interfered* user.

$$\begin{cases} P_{Wo-BF}^{Interfered} = \frac{P_{Tx}}{NN_{ss}} trace(\mathbf{H}_2\mathbf{Q}_1\mathbf{Q}_1^H\mathbf{H}_2^H) \\ P_{W-BF}^{Interfered} = \frac{P_{Tx}}{NN_{ss}} trace(\mathbf{H}_2\mathbf{V}_1\mathbf{V}_1^H\mathbf{H}_2^H) \end{cases} \tag{5.5}$$

where $\mathbf{V}_1$, $\mathbf{Q}_1$ are the precoding matrix for the *targeted user* with and without TxBF.

The interference level difference I_{level} is defined as the average difference between the received power (expressed in dB) without TxBF and with TxBF for the same MIMO

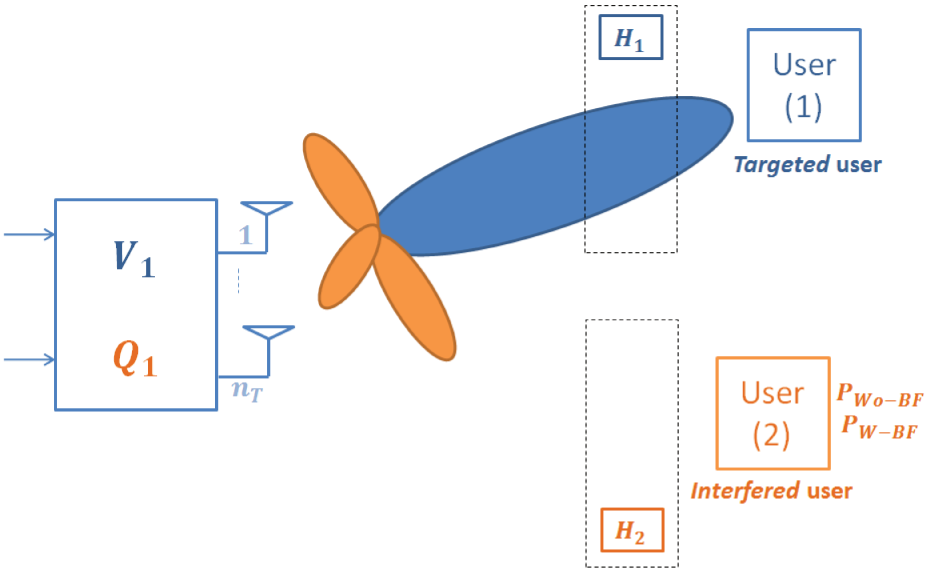

Figure 5.5 – Transmission scheme quantifying interference.

configuration in this case as follows:

$$I_{level} = 10 \log_{10} \frac{E(P_{Wo-BF}^{Interfered})}{E(P_{W-BF}^{Interfered})} \tag{5.6}$$

5.3 Statistical results of transmit beamforming gain

In this section, we give numerical results of transmit beamforming gain quantified in terms of SNR gain. The SNR gain is evaluated as a function of the number and the geometry of antenna arrays as well as the number of spatial streams.

5.3.1 Impact of the number of antennas

In this subsection, we evaluate a transmitter with various number of transmitting antennas. The transmitting antennas are arranged in ULA. The number of transmitting antenna varies in $n_T = 2, n_T = 4, n_T = 6, n_T = 8$.

First, we evaluate the SNR gain considering **one spatial stream** $N_{ss} = 1$. The number of receiving antennas varies in $n_R = 1, n_R = 2, n_R = 4$. Figure 5.6 gives the SNR gain as a function of the number of transmitting antennas for $N_{ss} = 1$. The SNR gain increases with the increase of the number of transmitting antennas, whereas it decreases when the number of receiving antennas increases. This is explained by evaluating the two system Wo-BF with $n_R = 1$ and $n_R = 3$. The system with $n_R = 3$ benefits already from diversity Wo-BF. Moving to TxBF, less SNR gain is achieved

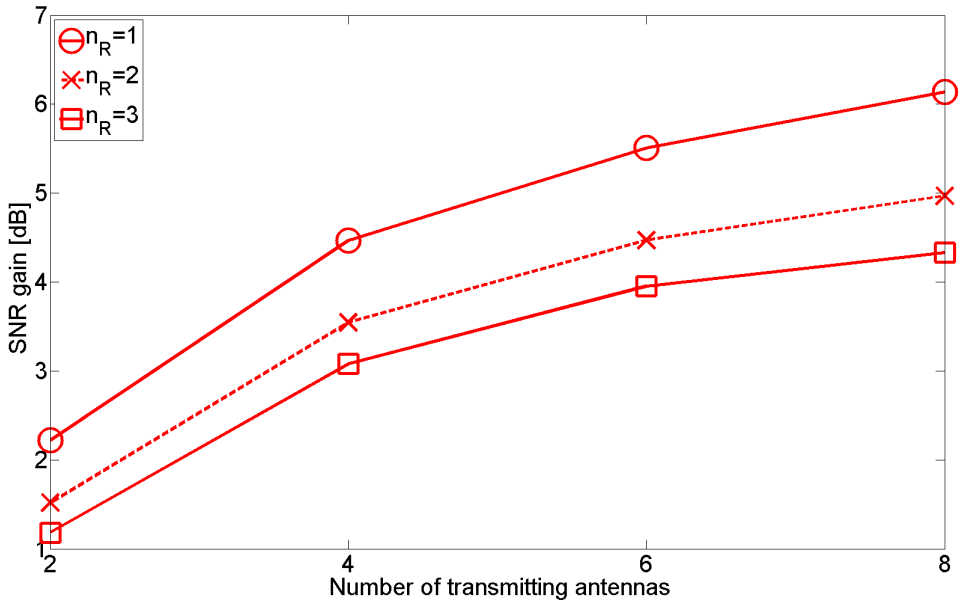

Figure 5.6 – The SNR gain as a function of the number of transmitting antennas for $N_{ss} = 1$.

compared to a system with one receiving antenna ($n_R = 1$) which does not show any diversity.

Moreover, the figure shows that even under the EIRP constraint, the transmit beamforming still achieves gain. It changes from 2 dB to 4 dB. The highest SNR gain 6 dB is achieved with a transmitter equipped with $n_T = 8$ antennas and a receiver with $n_R = 1$ antenna. Hence, we can fully benefit from the TxBF when the number of transmitting antennas is largely greater than the number of receiving antennas and spatial streams, whereas the SNR gain is null when $n_T = N_{ss}$.

Secondly, we evaluate **two spatial streams** $N_{ss} = 2$ to assess its impact on TxBF. The number of receiving antennas varies in this case in $n_R = 2, n_R = 3$. Figure 5.7 gives the SNR gain as a function of the number of transmitting antennas for $N_{ss} = 2$. The same conclusion about the number of the transmitting and receiving antennas is drawn from Figure 5.7. Moreover, Figure 5.7 shows that increasing the number of spatial streams decreases the SNR gain. Indeed, the highest value of SNR gain is achieved by $n_T = 8, n_R = 2$.

Therefore, with TxBF, increasing the SNR gain is possible when we increase the number of transmitting antennas, decrease the number of receiving antennas, or decrease the number of spatial streams compared to the number of transmitting antennas, even under the EIRP constraint. The beamforming gains are in the range of 1 to 6 dB which is very interesting to extend the WLAN coverage.

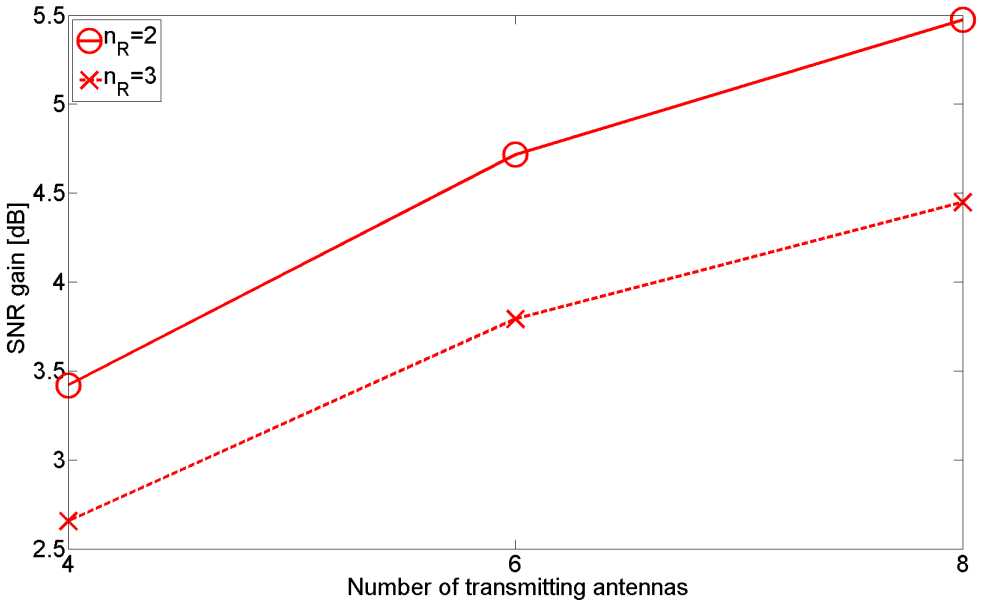

Figure 5.7 – The SNR gain as a function of the number of transmitting antennas for $N_{ss} = 2$.

5.3.2 Impact of the geometry of transmitting antenna arrays

In this subsection, we assess the impact of antenna array geometries on the SNR gain. We simulate different antenna array geometries as in previous chapter (Chapter 4, Figure 4.11). The transmitter is composed of $n_T = 8$ transmitting antennas arranged in 5 different geometries: CCA with 0.5λ spacing, and ICA with different radiuses: ICA 0.5λ, ICA 1λ, ICA 2λ and ICA 3λ.

We study the case of **one spatial stream** $N_{ss} = 1$. The number of receiving antennas varies in $n_R = 1, n_R = 2, n_R = 3$. Figure 5.8 gives the SNR gain as a function of the receiving antennas for different antenna array geometries. The figure confirms that an increase in the number of receiving antennas decreases the SNR gain of almost 1 dB for all antenna array geometries except the ICA 1λ where it decreases by more than 1 dB. The ICA 1λ achieves the highest SNR gain 6 dB with a receiver equipped with $n_R = 1$ receiving antenna. For $n_R = 2$ and $n_R = 3$ receiving antennas, the ICA 1λ shows the highest SNR gain with $4,3$ dB and $3,6$ dB respectively.

All antenna array geometries show almost the same SNR gain values. The variation is less than 0.5 dB which is insignificant regarding the difference between SNR gain values when varying the number of transmitting antennas.

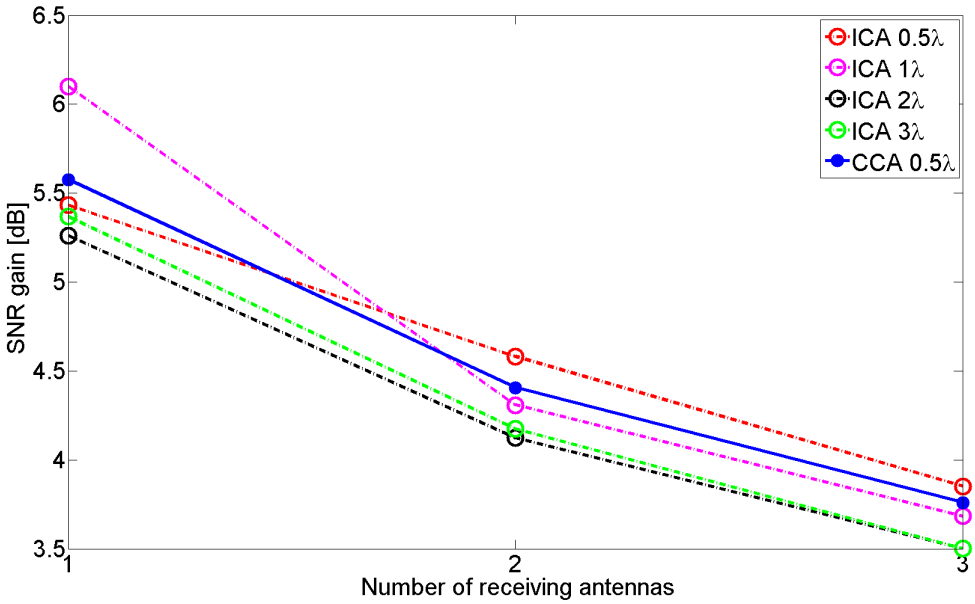

Figure 5.8 – The SNR gain as a function of the number of receiving antennas for $N_{ss} = 1$.

5.4 Statistical results of interference level reduction

In this section, we give numerical results of interference reduction to see whether the introduction of TxBF increases or reduces the interference difference generated by the AP. The interference reduction is evaluated as a function of the number and the geometry of antennas as well as the number of spatial streams.

5.4.1 Interference level

In this section, we study the average value of the interference reduction for the various 2-user measurement configurations. The transmitter has the antennas arranged in ULA.

At first, we study the case with one spatial stream. Figure 5.9 gives the average of the interference reduction as a function of the average of SNR gain for one spatial stream. Increasing the number of transmitting antennas decreases the interference level. The interference level is reduced from 1.5 dB to almost 3 dB when the number of transmitting antennas increases from $n_T = 2$ to $n_T = 8$. However, increasing the number of receiving antennas does almost not impact the interference level. The interference reduction values slightly increase (less than 0.5 dB) passing from $n_R = 1$ to $n_R = 3$. The highest value of interference reduction 3.5 dB in this case ($N_{ss} = 1$) is achieved by a system with $n_R = 3, n_T = 8$.

Secondly, we set the number of spatial streams to $N_{ss} = 2$. Figure 5.10 gives the average of the interference level difference as a function of the average of SNR gain for

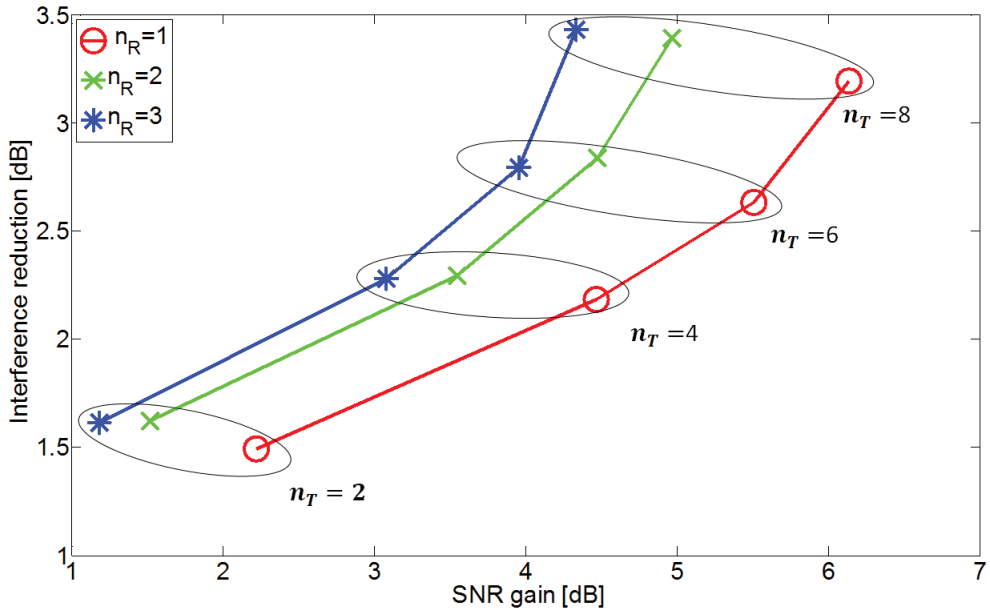

Figure 5.9 – The interference level as a function of the average of SNR gain for $N_{ss} = 1$.

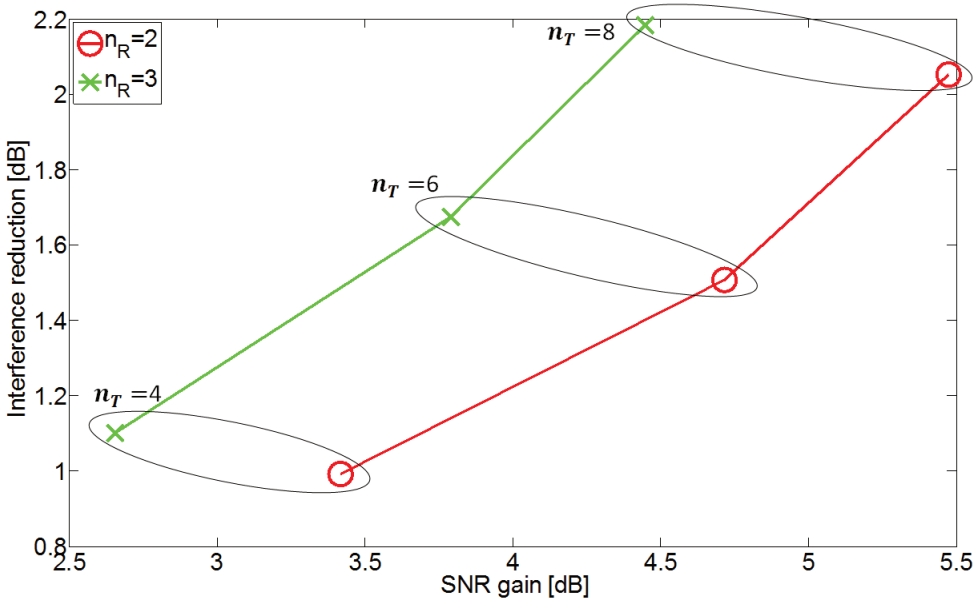

Figure 5.10 – The interference level as a function of the average of SNR gain for $N_{ss} = 2$.

two spatial streams ($N_{ss} = 2$). The number of transmitting antennas varies in $n_T = 4, n_T = 6, n_T = 8$, whereas the number of receiving antennas varies in $n_R = 2, n_R = 3$. The interference reduction value for a system with $n_R = 3, n_T = 8$, which represents the

configuration of the best reduction level, is 2.2 dB. This value is less than the achieved value with $N_{ss} = 1$ and the same configuration. This shows that increasing the number of spatial streams increases the interference level.

5.4.2 Interference level reduction map

For more readable graphs, we give in this section interference level reduction maps for several configurations and user' positions. By activating the TxBF towards the *targeted* user, we compute then the received powers at the different positions of the *Interfered* user. Using cubic interpolation, we approximate the values in the other positions of the map. Hence, we derive a continuous surface, namely interference level reduction map.

First, we draw the interference level reduction map for a system with $n_T = 4$ transmitting antennas, $n_R = 3$ receiving antennas, and $N_{ss} = 1$ spatial stream as illustrated in Figure 5.11. The *black* points refer to the positions where measurements have been made computed with exact and non-interpolated values. The color bar refers to the interference reduction level in dB. The figure gives an example where the *targeted* user is in LOS with the Tx. It plots LOS scenario with the first position of the transmitter. The worst case is logically when the *interfered* user is placed in the proximity of the *targeted* user where the interference reduction values are below 1 dB. We can also observe that there is no interference increase next to the *targeted* user.

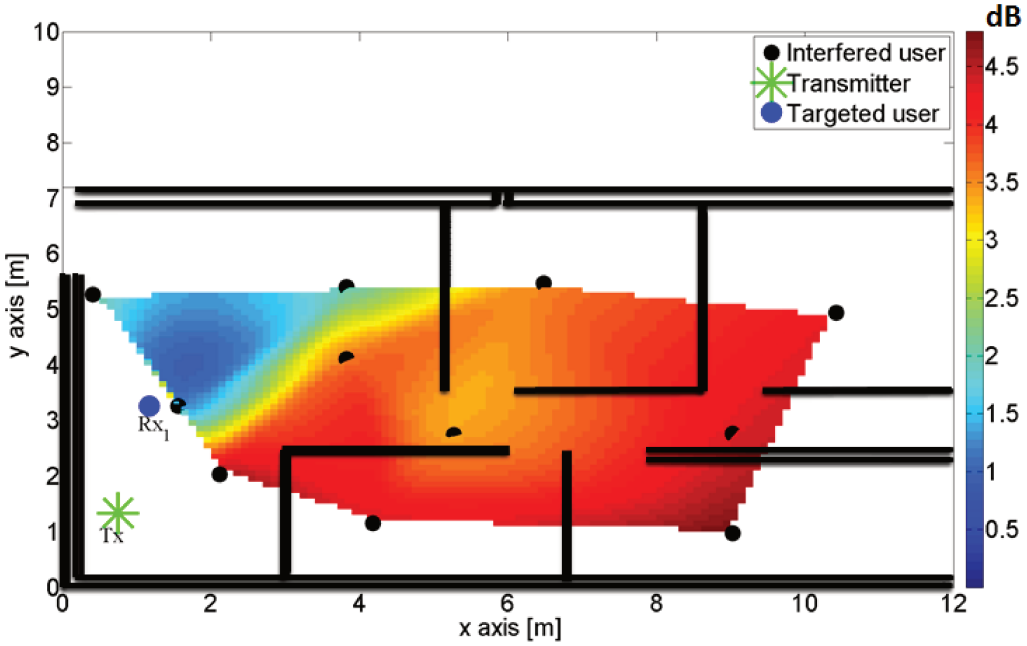

Figure 5.11 – Interference level reduction map for a MIMO system with $n_T = 4$ arranged in ULA, $n_R = 3$, and $N_{ss} = 1$ [LOS scenario with Tx_1].

Figure 5.12 gives the interference level reduction map when the *targeted* user in in NLOS with the transmitter. In this case, we keep the same MIMO configuration: $n_T = 4$, $n_R = 3$ and $N_{ss} = 1$, but we change the position of the transmitter. The interference level reduction map shows clearly that when the *interfered* user is on the direction of the *targeted* user, the interference reduction level is very low. This result is confirmed when we change the position of the *targeted* user as depicted in Figure 5.13. Moreover, this example shows that the radiated power is not maximal on the direct line path but in another dominant path: probably the reflected or diffracted path in this case.

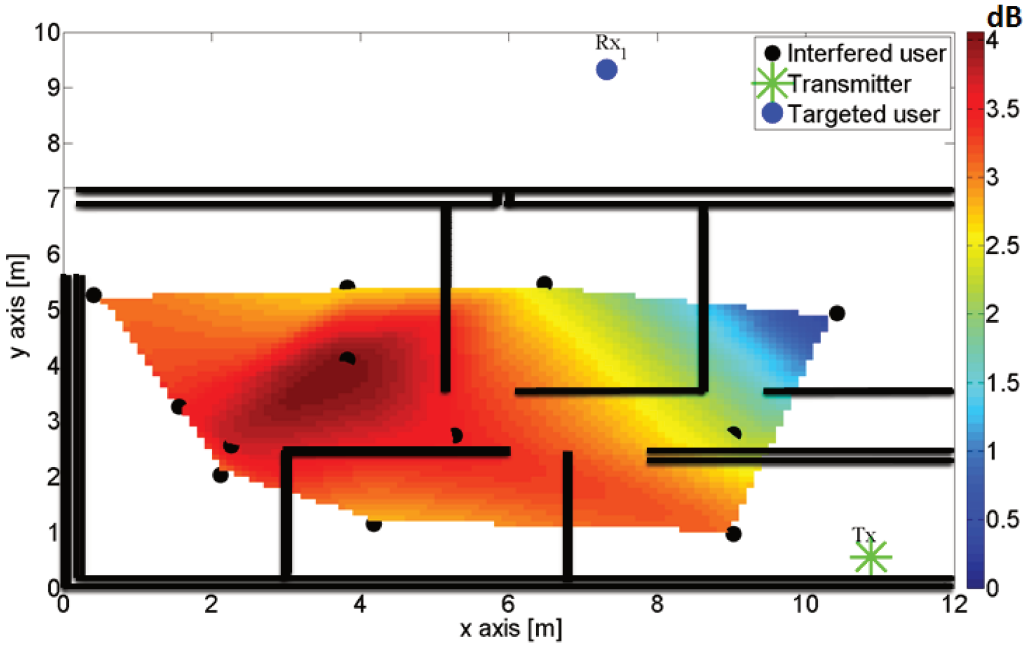

Figure 5.12 – Interference level reduction map for a MIMO system with $n_T = 4$ arranged in ULA, $n_R = 3$, and $N_{ss} = 1$ [NLOS scenario with Tx_2].

Afterwards, we increase the number of transmitting antennas to $n_T = 8$. The number of receiving antennas is $n_R = 3$, and the number of spatial streams is $N_{ss} = 1$. Figure 5.14 plots the interference level reduction map for a *targeted* user in LOS scenario with the first position of the transmitter. The first observation drawn from this figure is that all interference reduction values are higher than 2 dB, which is beneficial for wireless communications. Since, the *targeted* user benefits from a greater interference reduction, greater than 5 dB.

Finally, we consider a transmitter with $n_T = 8$ transmitting antennas arranged in CCA. The number of receiving antennas is $n_R = 3$, and the number of spatial streams is $N_{ss} = 1$. Figure 5.15 plots the interference level reduction map for a LOS scenario with the first position of the transmitter. It shows that CCA offers a less *clean* environment than the ULA with interference reduction values around 5 dB. Figure 5.16 plots the interference level reduction map for a NLOS scenario with the second position of the

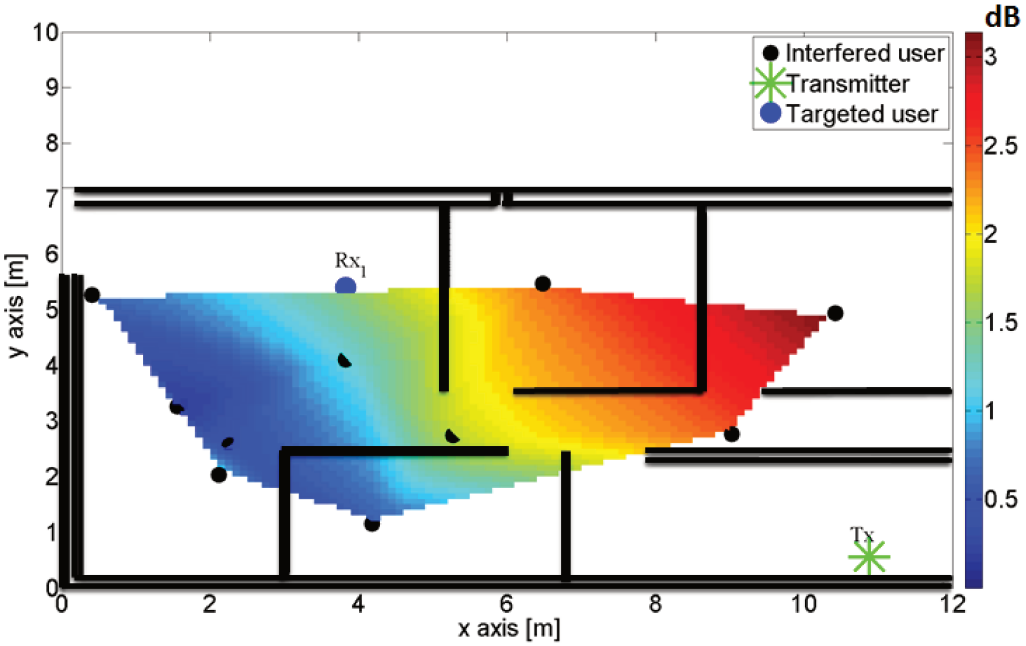

Figure 5.13 – Interference level reduction map for a MIMO system with $n_T = 4$ arranged in ULA, $n_R = 3$, and $N_{ss} = 1$ [NLOS scenario with Tx_1].

transmitter with the same MIMO configuration: $n_T = 8$, $n_R = 3$ and $N_{ss} = 1$. The transmitting antennas are arranged in CCA. Compared to LOS, this scenario shows lower values of reduction interference level.

5.5 Conclusion and proposed model for radio planning tool

Several MIMO configurations (number of transmitting and receiving antennas, number of spatial streams, antenna array geometries) have been compared to identify which one has the most important impact on the TxBF quantified in terms of received power.

In particular, we have proved that increasing the SNR gain is possible when we increase the number of transmitting antennas, decrease the number of receiving antennas, or decrease the number of spatial streams. The computed gain can be used to correct and update the beamformong gains of the coverage maps in the current planning tools.

Moreover, we have investigated whether the introduction of TxBF increases or reduces the effect of interference. We have been able to show that TxBF reduces the interference in the environment from 0 to 6 dB in the best cases. Moreover, increasing the number of transmitting antennas can improve this interference reduction: for example, an increase of 2 dB is achieved when we increase the number of transmitting antennas from $n_T = 2$ to $n_T = 8$ for a system with one spatial stream $N_{ss} = 1$. Finally,

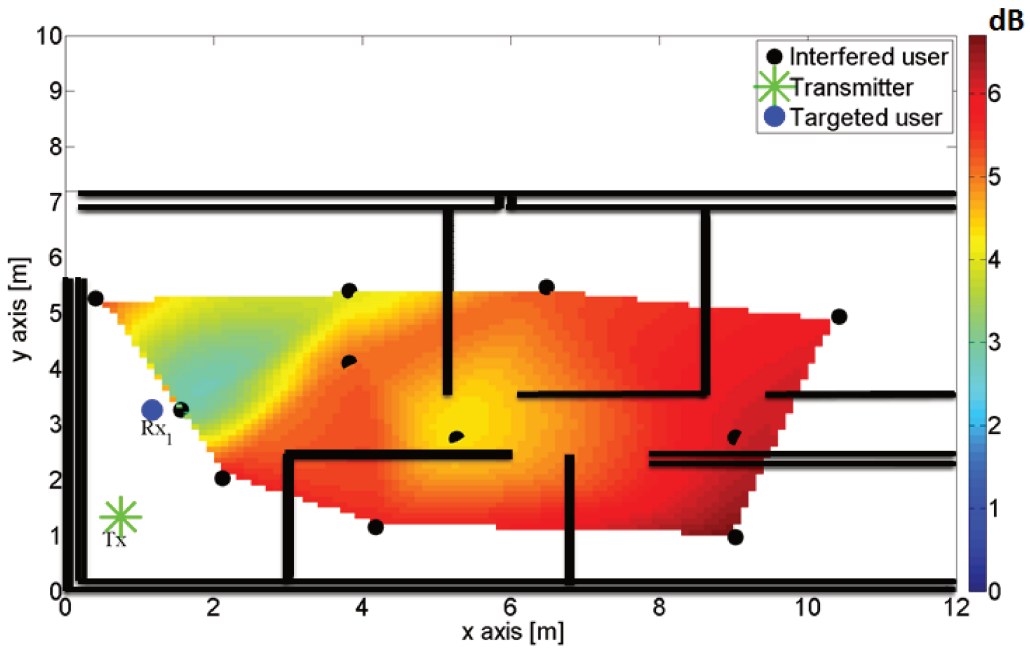

Figure 5.14 – Interference level reduction map for a MIMO system with $n_T = 8$ arranged in ULA, $n_R = 3$, and $N_{ss} = 1$ [LOS scenario with Tx_1].

we have shown that the antenna array geometry has no significant impact on TxBF with less than 1 dB of SNR gain and less 1 dB of interference reduction.

Since we generally consider the worst case in updating the interference reduction in the planning tools, no correction is proposed at this stage. Indeed, planning tools when simulating the radio coverage takes into account a certain margin of error in order to guarantee that for example in 90% of cases, the true interference level is lower than the predicted values. In our results, there is not interference reduction in 100% of cases.

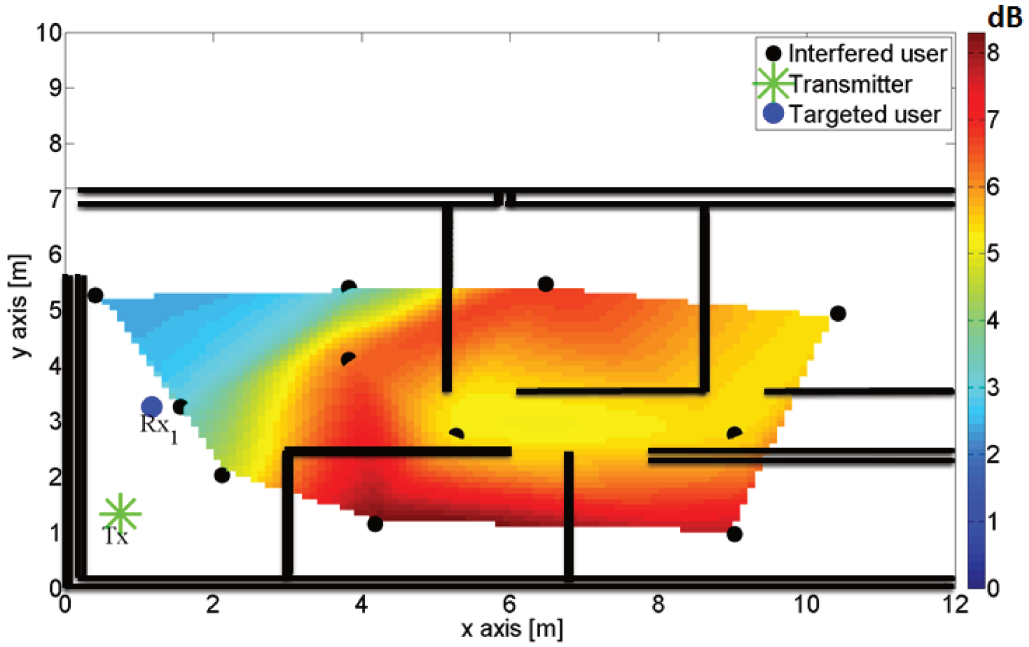

Figure 5.15 – Interference level reduction map for a MIMO system with $n_T = 8$ arranged in CCA, $n_R = 3$, and $N_{ss} = 1$ [LOS scenario with Tx_1].

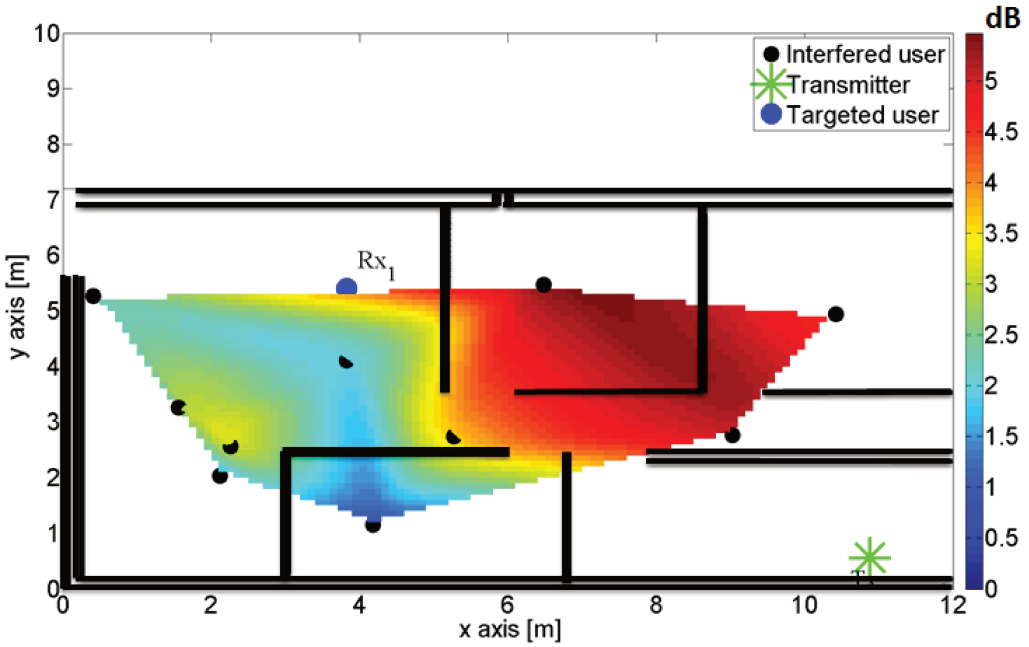

Figure 5.16 – Interference level reduction map for a MIMO system with $n_T = 8$ arranged in CCA, $n_R = 3$, and $N_{ss} = 1$ [NLOS scenario with Tx_2].

Chapter 6

Conclusion and perspectives

Contents

6.1 Conclusion

In the recent years, MIMO has attracted considerable attention for its potential to increase channel capacity. The MU-MIMO techniques have been proposed to further increase the capacity by spatial reuse. However, no study gives explicit answers to whether using MU-MIMO or SU-MIMO is the best choice in a residential environment, or gives optimal configurations to benefit fully from these techniques. In addition, current network planning tools need to be reviewed taking into account the beamforming gains. In this thesis, we have addressed these issues related to MU-MIMO and smart antennas.

Firstly, the physical features of the new standard 802.11ac as well as the basic propagation mechanisms have been summarized in Chapter 2. The MIMO channel models have also been presented. We have highlighted in particular the TGac channel models. The MU-MIMO system model, the precoding techniques and their related capacities have been next recalled. Indeed, we have given in this chapter a short state of the art of the MU-MIMO techniques. For our studies, we have selected BD technique for the MU-MIMO processing.

In Chapter 3, we have proposed recommendations to optimize MU-MIMO performance based on TGac simulations in terms of channel propagation parameters and users' configuration: LOS, NLOS, distances... A particular interest has been paid to study the power control required to meet the European regulation for WLAN in the 5 GHz frequency band in terms of EIRP. First, we have given a detailed description of the simulation process, the evaluated channel model and its parameters. Next, we have provided simulation results in function of antennas and propagation channels parameters on the BD capacity gain over SU-MIMO. In particular, we have proved

that a small increase in the number of transmitting antennas compared to the total number of transmitted spatial streams improves significantly the user channel de-correlation and the MU-MIMO capacity gain over SU-MIMO. We have also highlighted a relevant channel correlation definition that is useful to decide whether MU-MIMO outperforms SU-MIMO and to select the users into a MU-MIMO user group [64]. Afterwards, we have formulated the optimization problem of maximizing the sum capacity under the EIRP constraint for the IEEE 802.11ac MU-MIMO. In our formulation, we have looked for the power value which maximizes the sum capacity for each spatial stream of each user [65]. We have compared these two strategies with the common linear MU-MIMO BD under the total transmitted power constraint. We have shown that MU-MIMO precoding takes benefit from the EIRP constraint. The MU-MIMO to SU-MIMO capacity gain increases under the EIRP constraint.

In Chapter 4, we have presented the results of a measurement campaign using the VNA. This campaign has been conducted during the thesis in a residential environment typically encountered in home networks at Orange Labs Belfort. The first objective of this measurement campaign was to confirm the previous results and validate the radio engineering conclusions based on channel models, then to extend the results to different antenna array geometries and other potential parameters such as the propagation path loss. Obtained results confirm the recommendations based on TGac simulations. Furthermore, we have extended the conclusions to study the impact of receiving antennas and the number of spatial streams and the SNR values. In particular, increasing the number of receiving antennas increases the MU-MIMO to SU-MIMO capacity gain by only 5%. Moreover, selecting receiving antennas spaced by 0.5λ or $0.5\sqrt{2}\lambda$ has no significant impact on MU-MIMO to SU-MIMO capacity gain. Afterwards, we have compared the measured propagation path loss impact on MU-MIMO capacity gain using TDMA and CSMA/CA channel access methods.

Finally, in Chapter 5, we have evaluated the transmit beamforming gain based on measured data in a SU-MIMO context. The performance evaluation has been made based on the SNR gain and interference reduction. Several MIMO configurations (number of transmitting and receiving antennas, number of spatial streams, antenna array geometries) have been compared to identify which one has the most important impact on the TxBF quantified in terms of received power. In particular, we have proved that increasing the SNR gain is possible when we increase the number of transmitting antennas, decrease the number of receiving antennas, or decrease the number of spatial streams. These conclusions have been drawn to correct and update the beamforming gains of the coverage maps in the current planning tools. Moreover, we have investigated whether the introduction of TxBF can increase or reduce the effect of interference generated by an interfering link. We have been able to show that TxBF reduces the interference in the environment but not for the 100% of locations.

6.2 Future work

In this thesis, many issues related to MU-MIMO system have been addressed. However, multiple suggestions have not been explored and can be the topics for future studies:

- This thesis assumes a perfect channel state of information at the transmitter. It is relevant to assess the impact of an imperfect CSI on the obtained results.
- A deep analysis of spatial characteristics (AoA, AoD) of the propagation channel could be done to compare the results between TGac MIMO channel models and measurement campaign.
- It would be interesting to conduct a measurement campaign with a compacted antenna array including the antenna coupling effect. In our measurement campaign, we have evaluated only the case with 8 transmitting antennas arranged in ULA.
- It is possible to go further in analyzing the random draws of 8 transmitting antennas to propose an optimized array geometry and to test it in other residential environments.
- It is relevant to develop rapid algorithm simulating the antenna processing in the case of ray tracing or ray launching models in order to predict the beamforming gains in each point of the coverage map instead of a global statistical correction.
- An accurate prediction of the correlation coefficient as a function of the users' locations would be interesting to decide about the benefit of MU-MIMO.

Appendix A

All detailed parameters of TGac-B channel

The following figures (A.2, A.3 A.4 A.5 A.6) present the amplitude of the channel taps, the PDP, the CDF, the spatial correlation properties and the Doppler spectra respectively of a SU-MIMO set-up with $n_T = 2, n_R = 2$ working at 5.25 GHz carrier frequency, with $\frac{\lambda}{2}$ wavelength spacing at the transmitter and receiver, using IEEE 802.11 TGac channel model TGac-B. It is sampled in time domain at 2500 Hz to simulate fading with NLOS conditions. 512 FadingNumberOfIterations, where each iteration has a length of 55 CoherenceTimes, have been generated. In order to reduce the set of output samples, a downsampling factor of 48 has been applied. Per block, one sample has been stored. Dashed red curves/markers correspond to the reference values, whereas the blue curves/markers are the outcomes of the simulation. Moreover, in the Doppler plot, the green curve represents the Welch periodogram[85]. Figure A.1 gives an example of display of simulation parameters at the start of a simulation. The highlighted parameters are the ones that can be modified. The match between reference curves and simulation results is satisfactory in Figure A.3. Considering the LOS conditions, the achieved tap power distributions in Figure A.3 fit the reference PDP [85]. The addition of the LOS component causes the achieved PDP of models TGac-B to be shifted with respect to the reference one, up to the value of the K factor (in this case K is equal to 0). In Figure A.5, the spatial correlation coefficients of the simulated impulse responses match the coefficients computed during the initialization phase. The spatial correlation tends to be significant for certain taps. This is partly due to the small spacing (half a wavelength) between the two receive antenna elements. Finally, the simulated Doppler spectra shown in Figures A.6 reproduce the bell shape spectrum selected by IEEE 802.11 TGac Channel Model Special Committee. On these figures, the red vertical lines are drawn at $+/- frequency_{Doppler}$. The upper green line is set at the maximum of the Doppler spectrum, and the lower green line lies 10 dB below. Ideally, the Doppler spectrum should meet the crossing of the red and green lines. This would be the case, should the jitter be removed from the sampled spectra presented.

```
Simulation length: 55 coherence times
32 vectors of 512 fading samples generated @ 1750 Hz will be used internally
to produce 23392 interpolated samples @ 2500 Hz
Oversampling factor of the fades = 2500/1750 = 1.4286
487 interpolated samples will be collected in H and stored in tmp.mat
Sampling frequency of H samples = 2500/48 = 52.0833 Hz
```

Figure A.1 – Display example of simulation parameters at the start of a simulation.

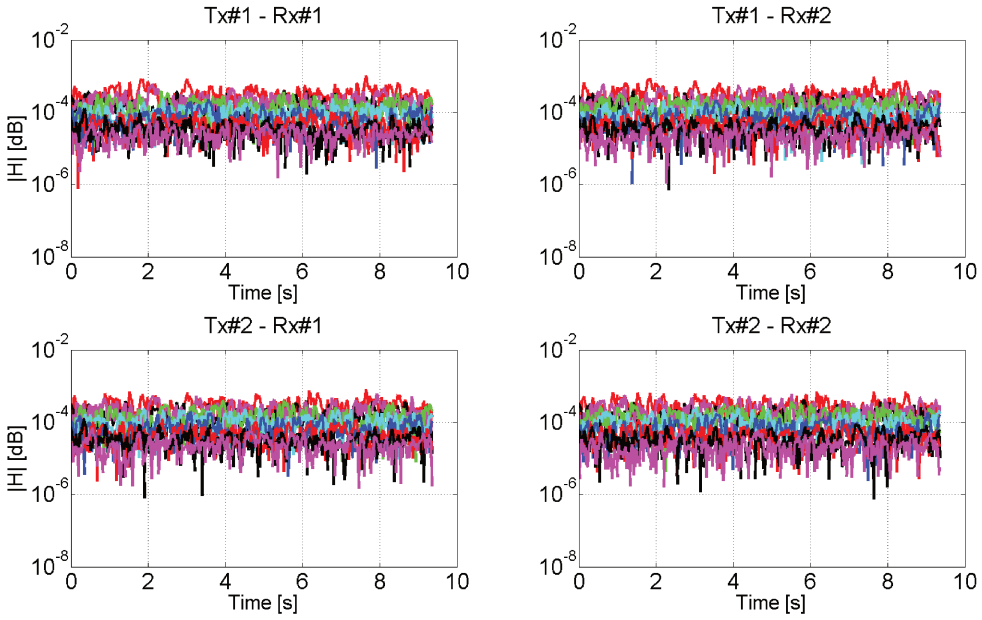

Figure A.2 – Amplitude of the channel taps versus times of the IEEE 802.11 channel model case B (9 taps).

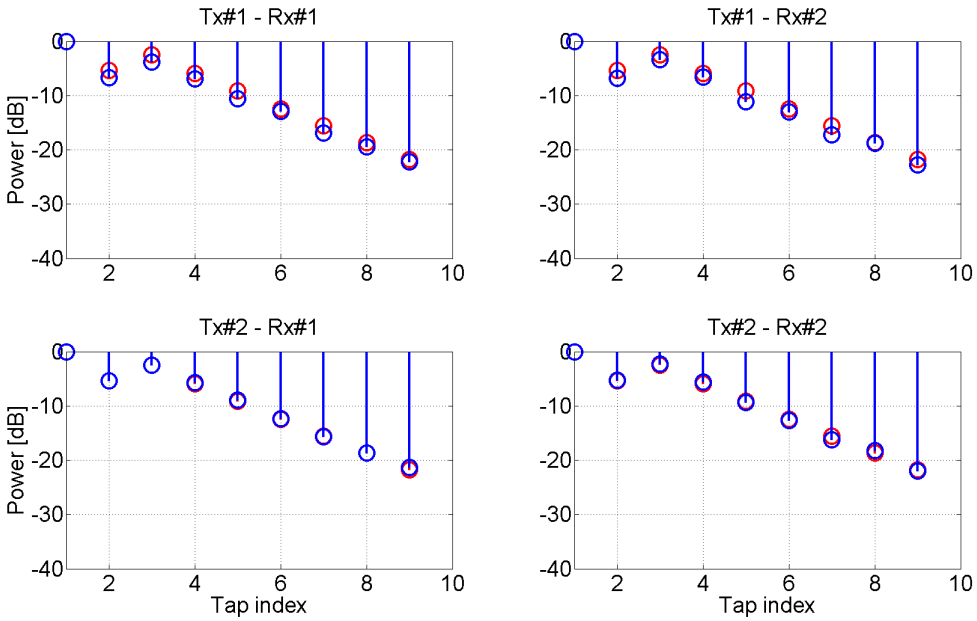

Figure A.3 – The PDP of IEEE 802.11 channel model case B (9 taps).

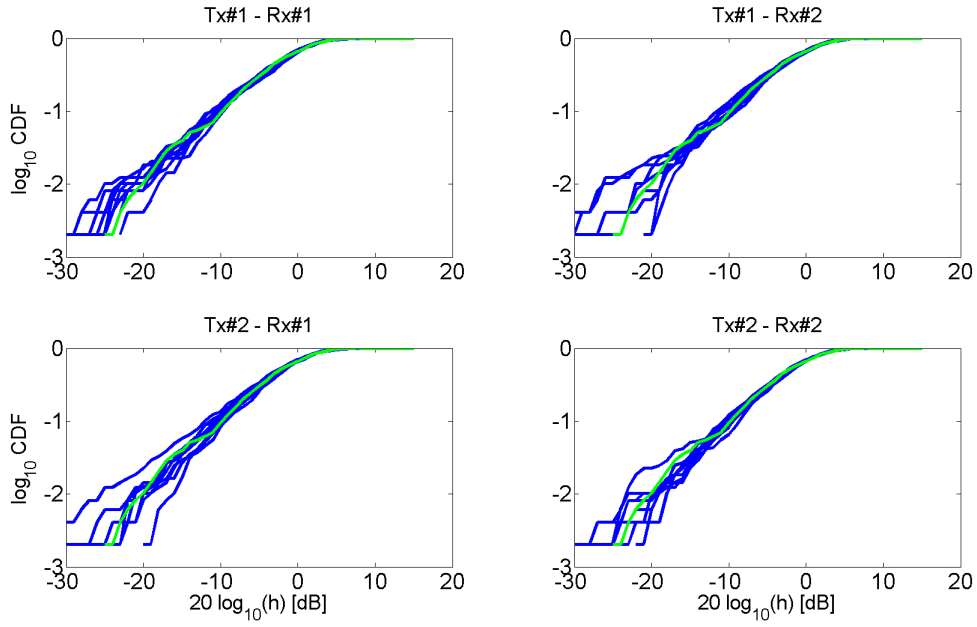

Figure A.4 – The CDF of the taps of the IEEE 802.11 channel model case B (9 taps).

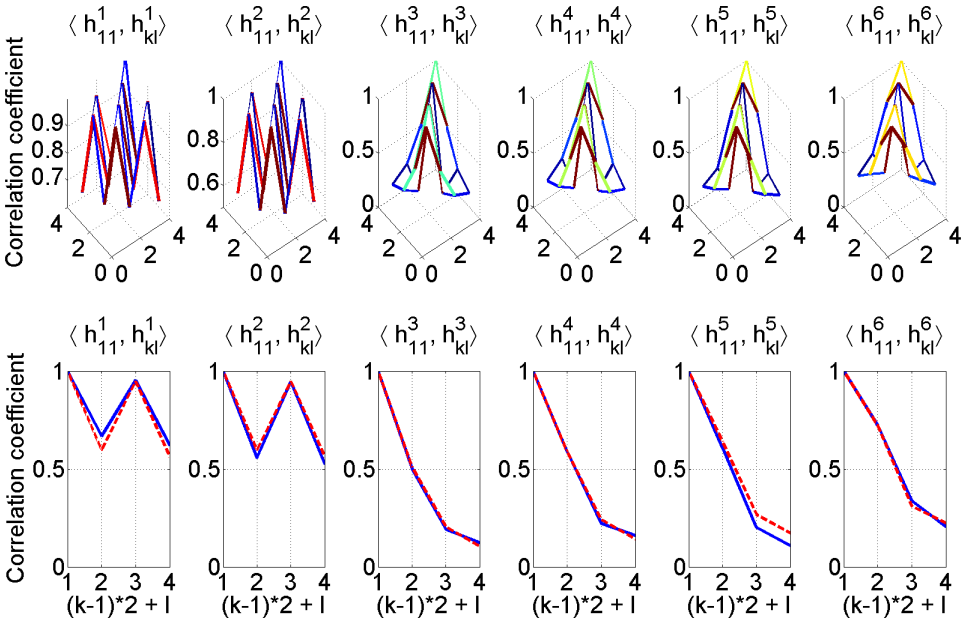

(a) The first six taps

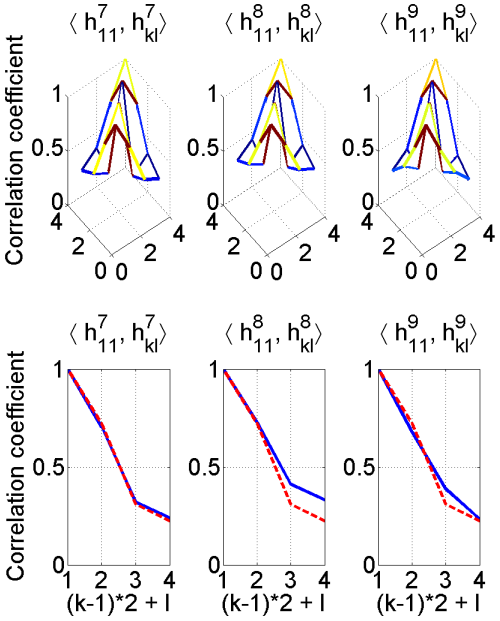

(b) The last three taps

Figure A.5 – Spatial correlation of the taps of the IEEE 802.11 channel model case B (9 taps).

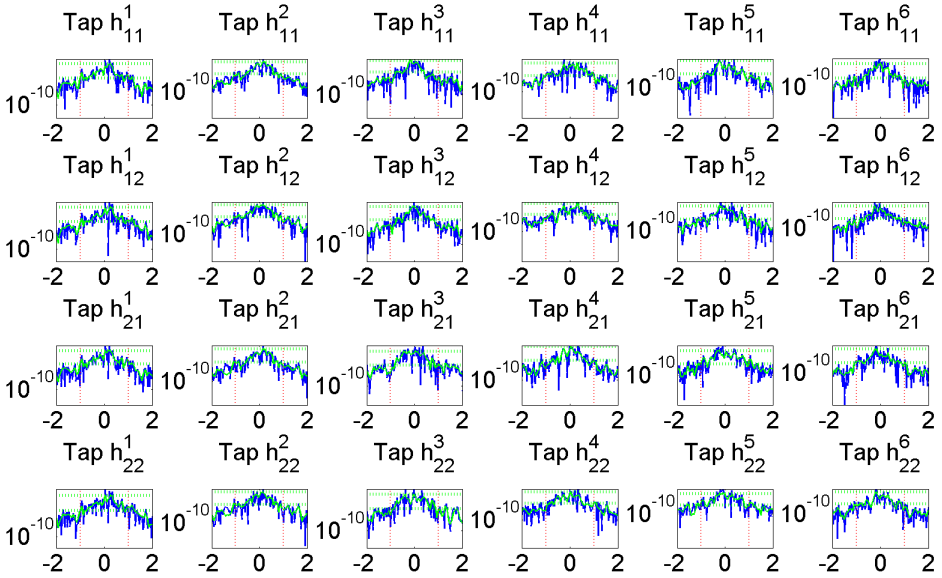

(a) The first six taps

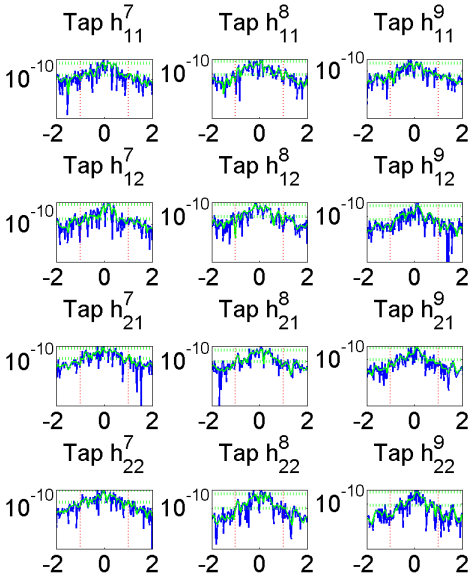

(b) The last three taps

Figure A.6 – Doppler spectra of the taps of the IEEE 802.11 channel model case B (9 taps).

Appendix B

Comparison of TDMA SU-MIMO, DPC, and BD sum rate capacity using MU-MIMO and spatially correlated channels

We study the MU-MIMO broadcast channel and the achievable throughput for the optimal strategy of dirty paper coding. We compare its performance to that achieved with block diagonalization with lower complexity based on correlated channels.

It was found in [43] that dirty-paper coding is optimum capacity achieving for the broadcast MU-MIMO channel. In [86], two iterative algorithms have been proposed to find the optimum sum capacity bound for the multiple-antenna broadcast channel. The authors have used the fact that the Gaussian broadcast and multiple-access channels are dual. This means that their capacity regions, and therefore their sum rate capacities, are equal. These algorithms compute the sum rate capacity achieving for the dual multiple-access channel. This can be converted to the equivalent optimal strategies for the broadcast channel. The algorithms employ a simple iterative Water-filling procedure that probably converges to the optimum. The two algorithms use the single-user Water-filling procedure in each iteration. Based on this algorithm and Water-filling, we find the sum capacity of the multiple-antenna broadcast channel.

Figure B.1 illustrates the performance of the BD algorithm using or not Water-filling and the sum-rate bound computed with DPC for a case involving $n_T = 6, n_{R_1} = n_{R_2} = 2$ and $SNR = 20$ dB. The SNR here is defined as in Chapter 3, Section 3.3 without the EIRP constraint. We have also plotted the SU-MIMO capacity to compare. The results are based on the correlated TGac-B channel model and the cumulative distribution function of the capacity achieved by each method is plotted. Block diagonalization with equal power sharing among the spatial streams is labeled *MU-MIMO BD*, whereas *MU-MIMO BD WF* refers to the BD algorithm employing the optimal power allocation via Water-filling. *SU-MIMO* refers to the case with equal power sharing with no precoding

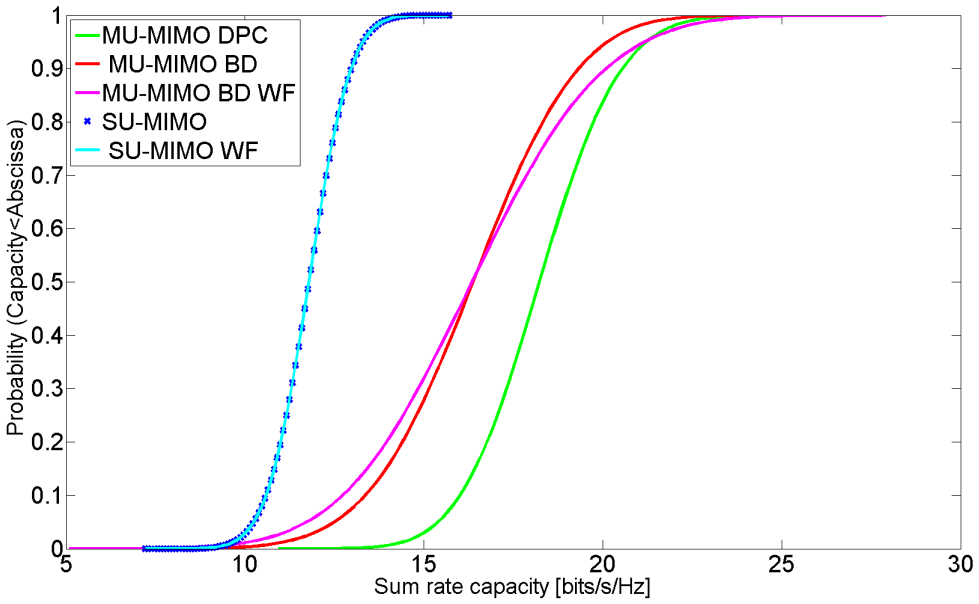

Figure B.1 – Cumulative distributions of the sum rate capacity for $n_T = 6, n_{R_1} = n_{R_2} = 2$ achieved by several MU-MIMO strategies.

algorithm. Finally, *SU-MIMO WF* employs Water-filling algorithm.

The first observation drawn from the Figure B.1 is that SU-MIMO show similar capacity values with equal power sharing and Water-filling algorithm. The MU-MIMO gives almost the same values. Furthermore, it can be seen that MU-MIMO DPC gives the highest values of capacity as expected. The gap between the average values of DPC (18.4739 bits/s/Hz) and BD (15.5096 bits/s/Hz) capacities is 3 bits/s/Hz.

The expected loss in Rayleigh fading due to block diagonalization compared to DPC is given by [35]:

$$loss_{DPC-BD} = (\log_2 e) \sum_{k=0}^{K-1} \sum_{n=0}^{n_{R_1}-1} \sum_{i=kn_{R_1}+1}^{(K-1)n_T} \frac{1}{n_T - n - i} \qquad [bits/s/Hz] \qquad \text{(B.1)}$$

In our case when $K = 2$, $n_T = 6$ and $n_{R_1} = n_{R_2} = 2$, $loss_{DPC-BD} = 1.5$ bits/s/Hz in Rayleigh channels.

Appendix C

Measurement campaigns synthesis

Table C.3 gives a non-exhaustif survey of the main measurement campaigns conducted to evaluate MU-MIMO techniques. It shows that only a limited amount of channel measurements and analysis of such MU-MIMO systems are available, even less in the 802.11ac context. It mainly concerns outdoor areas or indoor to outdoor areas. Note that the measurement campaigns conducted in Eurecom Institute have resulted in many publications, we have mentioned only few of these papers [46][30][87][32].

Environment and equipment	Configurations and parameters	Evaluated parameters and conclusions
[VNA] [54] LOS and NLOS cases in a meeting room at 5.2 GHz	$K = 2$, $n_T = 4$, $n_{R_1} = n_{R_2} = 2$ omnidirectional colinear antennas with coupling spaced by $\frac{\lambda}{2}$, $d_{Tx-Rx_1} = 4$ m, $d_{Rx_1-Rx_2} = 3$ m.	Doppler spectrum and BER dependent on the array orientation and the direction of the receiver motion. In NLOS, Doppler spectrum is quite different from the theoretical U-shaped spectrum in the Jakes' model. BER performance is much degraded due to a channel change.
[Sounder EMOS [1]] [46] LOS and NLOS in outdoor vicinity of Eurecom, Sophia-Antipolis, France at 1917.6 MHz. BW: 4.0625 MHz	$n_T = 2$, $K = 2$, $n_{R_1} = n_{R_2} = 2$. Tx: antennas arranged in two cross-polarized pairs. Rx: 3G Panorama Antennas	A characterization of the (dis-)similarity of the channels of different users using: spatial separation of the user's, correlation matrices, co-linearity of the MIMO channel matrices and correlation of large scale fading. The structure of the MIMO channel matrices changes significantly with the inter-user distance [captured by the co-linearity measure]. The transmit and the full correlation matrix also show some dependence on the inter-user distance. Receive correlation matrices are independent of the inter-user distance. The shadowing correlation was found to be very low in all cases even when the nodes are quite close.
[49] Indoor conference room LOS/NLOS VNA at 5 GHz.	SU-MIMO: $n_T = 4$, $n_R = 4$ MU-MIMO: $n_T = 4$, $K = 2$, $n_R = 2$ two linear array orientations spaced by $\frac{\lambda}{2}$. Antenna coupling effect	BER: LOS is better than NLOS (much higher SNR is given by the direct path) MU-MIMO system is sensitive to channel change (it causes the IUI).

Table C.1 – Survey of measurement studies [Part I].

[30] [Sounder EMOS] *near* and *far* outdoors vicinity of the Eurecom, Sophia-Antipolis [predominantly present LOS] and NLOS indoor: Tx in the neighboring building [strong reflections] and Rx in the same room.	Frequency: 1917.6 MHz (BW:4.8 MHz). Linear methods with perfect CSI: CI and RCI $n_T = 4$, $K = 4$, $n_{R_k} = 1$, $SNR = 10$ dB with fairly sharing proportional in a round robin fashion. Tx:arranged in two cross-polarized pairs. Rx: 3G Panorama Antennas.	The performance of MU-MIMO precoding drops drastically when the users are close together in an outdoor scenario due to the strong correlation at the transmitter. MU-MIMO provides a higher throughput than SU-MIMO. In outdoor scenarios with a LOS, the capacity drops significantly when the users are close together, due to high correlation at the transmitter side of the channel.
[Sounder EMOS][87]: -vicinity of the Eurecom institute in Sophia-Antipolis outdoo. -LOS and NLOS indoor at 1917.6 MHz.	Outdoor: $n_T = 4$, $K = 4$, $n_{R_k} = 1$. Indoor: $n_T = 2$, $K = 2$, $n_{R_k} = 1$. $SNR = 10$ dB, 4.8 MHz of bandwidth. Tx: 2 cross-polarized pairs. Rx: 3G Panorama Antennas. OFDM	Distance VS the capacity of linear precoding schemes: the further apart the users are, the higher the capacity. Hence, spatial separation of users has a very strong impact on the performance of linear precoding schemes In particular, the performance of a CI precoder drops significantly in outdoor scenarios, when the users are close together. The performance of limited feedback MU-MIMO schemes crucially depends on the codebook.
[32] EMOS outdoors in the vicinity of the Eurecom institute LOS most of time	$n_T = 4$ (2 cross polarized), $K = 4$, $n_{R_k} = 1$, $N_{ss} = 4$ $SNR = 10$ dB. 1917.6 MHz, BW:4.8 MHz Antenna selection	The results show that MU-MIMO provides a higher throughput than SU-MIMO. However, the throughput in the measured channels is by far worse than the one in channels without spatial correlation. Of all the evaluated linear precoding schemes, the RCI precoder performs best in the measured channels.

Table C.2 – Survey of measurement studies [Part II].

[26] Indoor and indoor-outdoor scenarios with multiples base stations in the Royal Institute of Technology (KTH) using DSP DA Converter at 1766.6 M̃Hz (BW: 9.6 kHz).	4 Tx and 4 Rx. Rx: 4-monopole array. Tx: dual-polarized sectorial antennas with directive pattern in elevation with high gain (Outdoor), and dual-polarized patch antennas with low profile and low gain (Indoor). Different noise and interference levels	Downlink with no CSI with close antenna elements, in both indoor and outdoor locations, performs very similar to a channel with CSIT (slightly higher in indoor). Spatially, separated locations for Base Station (BS) shows slightly lower average capacity and non-Gaussian distribution for the measured environment.
[48] LOS scenario in a conference room at the NTT DOCOMO RD Center in Yokosuka, Japan using an implemented LTE-Advanced transceiver	$K = 2$, $n_T = 4$, $n_{R_k} = 2$. 3.92625 GHz, BW: 90 MHz Antenna arrangements at Tx: CAA and DAA. Tx and Rx:dipole antennas with omni-directional beam patterns in azimuth with 2 dBi of gain.	Peak throughput greater than 1 Gbit/s is achieved for the CAA. Throughput of approximately 700 to 950 Mbps is achieved for DAA. MU-MIMO is robust against the antenna separation. moving speed, antenna separation (fading correlation), and transmitter antenna arrangement on the achievable throughput of MU-MIMO.
[47] indoor environment (a room) using MU-MIMO testbed according to 802.11a standard	4.85 GHz BW: 100 MHz MU-MIMO: $n_T =$, $K = 4$, $n_{R_k} = 4$ Tx and Rx: Sleeve antennas are used for the transmitter and receiver antennas arranged in linear arrays spaced by 1.0 and 0.5 wavelengths, respectively.	Frequency utilization of over 43.5/50 bits/s/Hz (0.87/1Gbps) when SNR is 31 and 36 dB, respectively for $n_T = 16$, $n_R = 4$ $K = 4$. The frequency utilization ($K = 4$): 2.4 to 3.3 times higher compared to the eigenvector beamforming method in SU-MIMO, when $n_T = 16$ and n_R changes from 2 to 4.

Table C.3 – Survey of measurement studies [Part III].

Appendix D

Capacity gain versus correlation coefficient

The regression line of MU-MIMO to SU-MIMO capacity gain as a function of correlation coefficient for $n_T = 8$ transmitting antennas arranged in CCA with 0.5 λ spacing is depicted in Figure D.1. Their regression parameters are summarized in Table D.1.

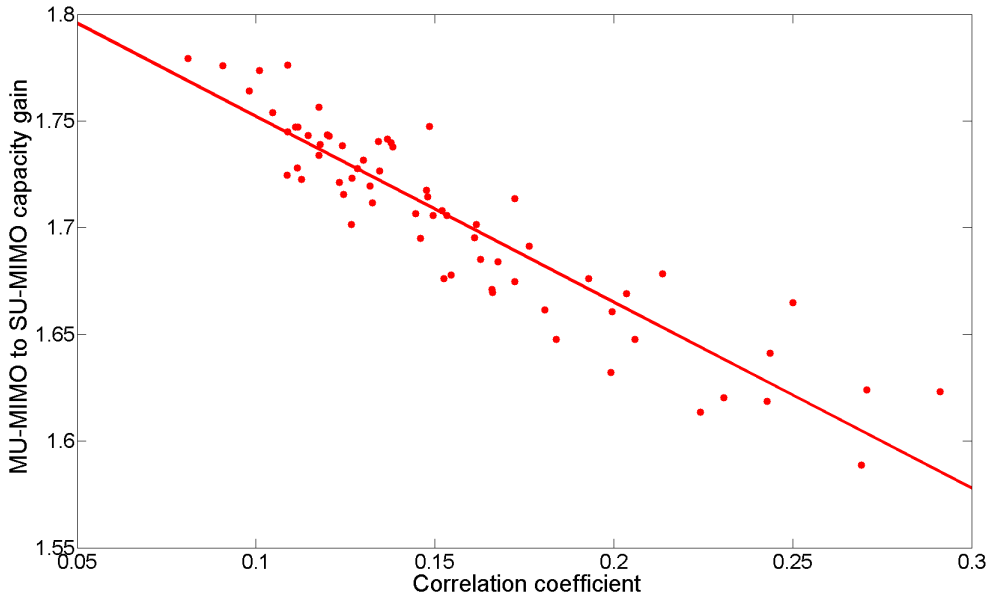

Figure D.1 – Average of MU-MIMO to SU-MIMO capacity ratio versus the average correlation coefficient ($n_T = 8$).

Next, the following figures (D.2, D.3, D.4, D.5) show the regression lines of

n_T	a_0	a_1	r	RMSE
4	1.5525	-1.0471	0.8964	0.0292
5	1.6809	-0.9379	0.8838	0.0267
6	1.7458	-0.8899	0.9016	0.0213
8	1.8141	-0.8235	0.8863	0.0169

Table D.1 – Numerical results of linear regression parameters for different transmitting antennas for CCA with $n_T = 8$.

MU-MIMO to SU-MIMO capacity gain as a function of correlation coefficient for different number of transmitting antennas arranged in ICA with different radiuses: ICA 0.5 λ, ICA 1 λ, ICA 2 λ and ICA 3 λ. Table D.2 summarizes the related regression parameters.

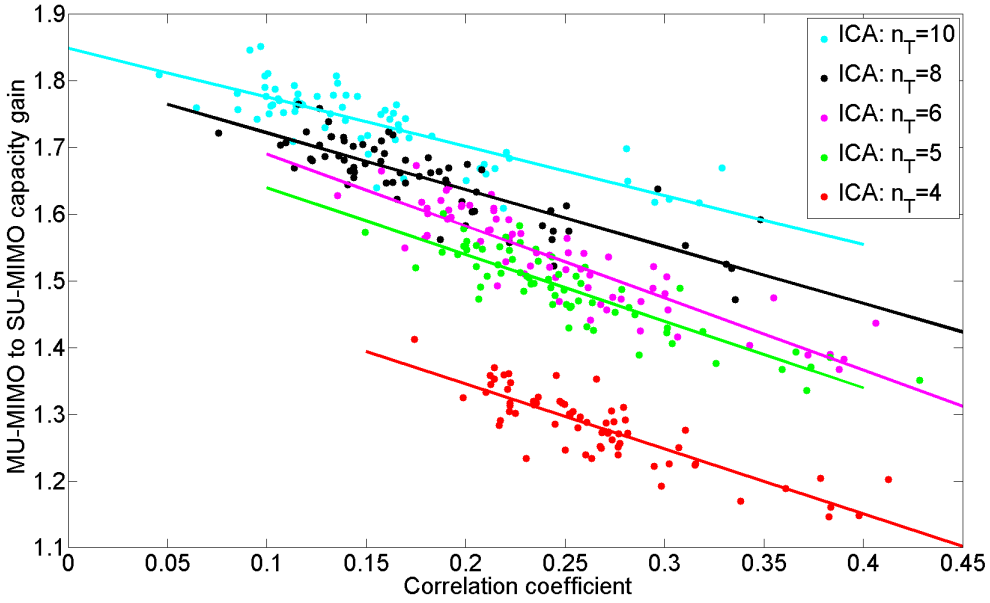

Figure D.2 – Average of MU-MIMO to SU-MIMO capacity ratio versus the average correlation coefficient (ICA 0.5 λ).

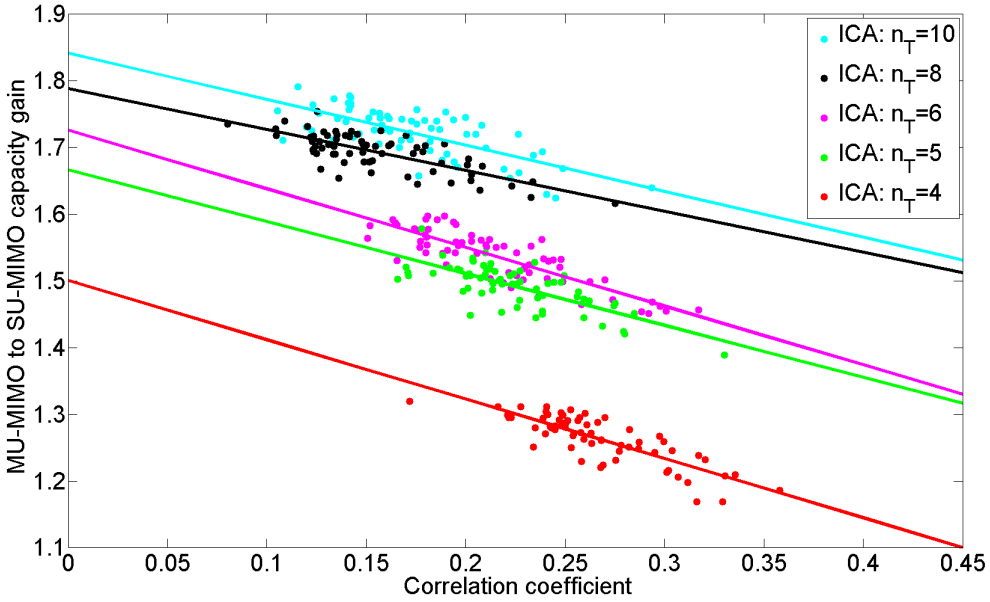

Figure D.3 – Average of MU-MIMO to SU-MIMO capacity ratio versus the average correlation coefficient (ICA 1 λ).

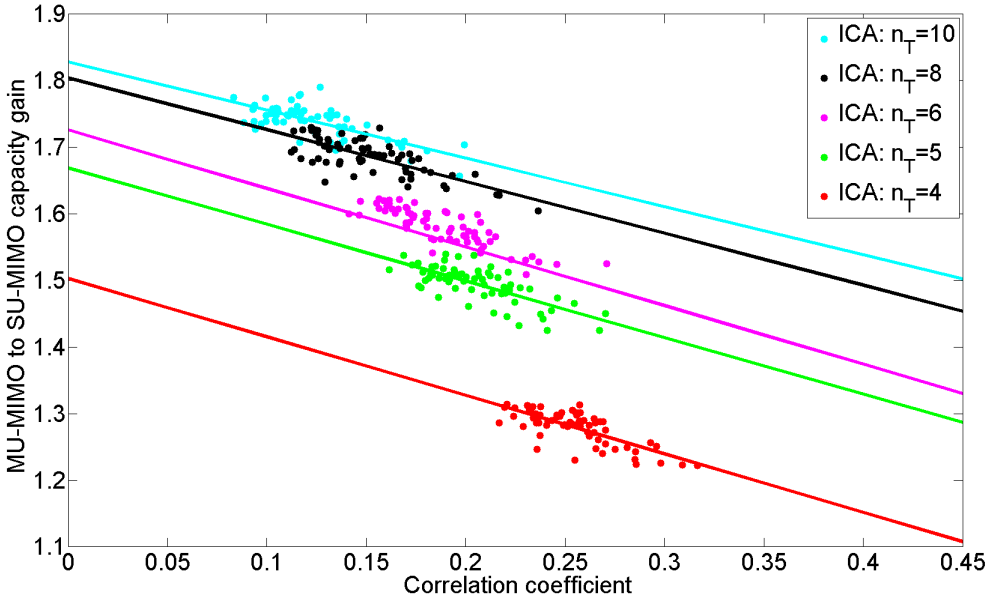

Figure D.4 – Average of MU-MIMO to SU-MIMO capacity ratio versus the average correlation coefficient (ICA 2 λ).

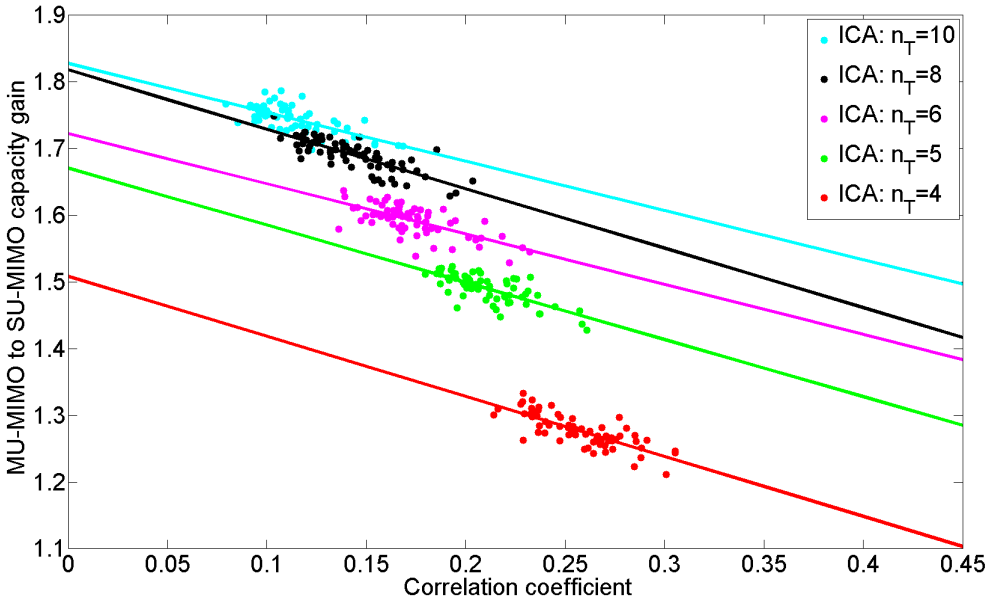

Figure D.5 – Average of MU-MIMO to SU-MIMO capacity ratio versus the average correlation coefficient (ICA 3 λ).

n_T	a_0				a_1				r				RMSE			
	ICA 0.5 λ	ICA 1 λ	ICA 2 λ	ICA 3 λ	ICA 0.5 λ	ICA 1 λ	ICA 2 λ	ICA 3 λ	ICA 0.5 λ	ICA 1 λ	ICA 2 λ	ICA 3 λ	ICA 0.5 λ	ICA 1 λ	ICA 2 λ	ICA 3 λ
4	1.54	1.5	1.503	1.509	-0.974	-0.89	-0.879	-0.9	0.03	0.02	0.017	0.015	0.853	0.829	0.755	0.782
5	1.74	1.667	1.669	1.671	-1	-0.778	-0.85	-0.858	0.03	0.022	0.019	0.015	0.875	0.739	0.723	0.731
6	1.757	1.726	1.726	1.722	-1.339	-0.88	-0.88	-0.753	0.04	0.021	0.021	0.017	0.897	0.852	0.852	0.687
8	1.807	1.789	1.804	1.818	-0.853	-0.615	-0.779	-0.892	0.034	0.019	0.019	0.015	0.835	0.755	0.746	0.795
10	1.849	1.841	1.828	1.828	-0.737	-0.689	-0.723	-0.736	0.033	0.026	0.018	0.015	0.807	0.716	0.723	0.698

Table D.2 – Numerical results of linear regression parameters for ICA with n_T passing from 4 to 10 and different radiuses.

Appendix E

Spatial expansion precoding matrix

Cyclic Shift Delay (CSD) and spatial expansion versus antenna mapping are applied at the transmitter, when no beamforming scheme is considered. It is necessary because closely spaced antennas act as beamforming arrays without wide phase spacing, and it is possible to inadvertently create signal maxima and minima over receive antennas due to interference patterns. This is avoided by giving each transmit antenna's signal a large phase shift relative to the others. Below are examples of spatial mapping matrices that might be used [88]. There are many other alternatives; implementation is not restricted to the spatial mapping matrices shown. The examples are:

— Direct mapping $\mathbf{Q}_k$ is a diagonal matrix of unit magnitude complex values that takes one of two forms:

1. $\mathbf{Q}_k = \mathbf{I}$, the identity matrix
2. A CSD matrix in which the diagonal elements represent cyclic shifts in the time domain.

— Indirect mapping: $\mathbf{Q}_k$ may be the product of a CSD matrix and a unitary matrix such as the Hadamard matrix or the Fourier matrix.

— Spatial expansion: $\mathbf{Q}_k$ is the product of a CSD matrix and a square matrix formed of orthogonal columns.

In our implementation, we have evaluated the spatial expansion scheme [88].The spatial expansion may be performed by duplicating some of the N_{ss} streams to form the n_T streams, with each stream being scaled by the normalization factor $\sqrt{\frac{N_{ss}}{n_T}}$. The spatial expansion may be performed by using, for instance, one of the following matrices, denoted $\mathbf{D}$, left-multiplied by a CSD matrix, denoted $\mathbf{M_{CDS}}(k)$, and/or possibly multiplied by any unitary matrix. The resulting spatial mapping matrix is then $\mathbf{Q}_k = \mathbf{M_{CDS}}(k).\mathbf{D}$, where $\mathbf{D}$ may take on one of the following values:

— $n_T = 2$, $N_{ss} = 1$, $\mathbf{D} = \frac{1}{\sqrt{2}} \begin{bmatrix} 1 & 1 \end{bmatrix}^T$

— $n_T = 3$, $N_{ss} = 1$, $\mathbf{D} = \frac{1}{\sqrt{3}} \begin{bmatrix} 1 & 1 & 1 \end{bmatrix}^T$

— $n_T = 4$, $N_{ss} = 1$, $\mathbf{D} = \frac{1}{2}\begin{bmatrix}1 & 1 & 1 & 1\end{bmatrix}^T$

— $n_T = 3$, $N_{ss} = 2$, $\mathbf{D} = \sqrt{\frac{2}{3}}\begin{bmatrix}1 & 0\\ 0 & 1\\ 1 & 0\end{bmatrix}$

— $n_T = 4$, $N_{ss} = 2$, $\mathbf{D} = \frac{1}{\sqrt{2}}\begin{bmatrix}1 & 0\\ 0 & 1\\ 1 & 0\\ 0 & 1\end{bmatrix}$

— $n_T = 4$, $N_{ss} = 3$, $\mathbf{D} = \frac{\sqrt{3}}{2}\begin{bmatrix}1 & 0 & 0\\ 0 & 1 & 0\\ 0 & 0 & 1\\ 1 & 0 & 0\end{bmatrix}$

The values of the cyclic shifts to be used are specified in Table E.1 [88].

Number of space-time streams	Cyclic shift for space-time stream 1 [ns]	Cyclic shift for space-time stream 2 (ns)	Cyclic shift for space-time stream 3 (ns)	Cyclic shift for space-time stream 4 (ns)
$N_{ss} = 1$	0	−−	−−	−−
$N_{ss} = 2$	0	−400 ns	−−	−−
$N_{ss} = 3$	0	−400 ns	−200 ns	−−
$N_{ss} = 4$	0	−400 ns	−200 ns	−600 ns

Table E.1 – Cyclic shift values.

Bibliography

[1] Cisco: Technical white paper. 802.11ac: The fifth generation of Wi-Fi. `http\protect\kern+.2222em\relax//http://www.cisco.com/c/en/us/products/collateral/wireless/aironet-3600-series/white_paper_c11-713103.html`, 2014.

[2] V. Jones and H. Sampath. Emerging technologies for WLAN. *Communications Magazine, IEEE*, 53(3):141–149, March 2015.

[3] IDC: Analyze the future. Press release: worldwide WLAN market growth. `http://www.idc.com/getdoc.jsp?containerId=prUS24466913`, 2013.

[4] Wireless LAN market to expand nearly 50 percent in five years. `http://www.cellular-news.com/story/58452.php`, 2013.

[5] G. Breit and et al. Multi-user MIMO channel measurements. Technical Report Doc.: IEEE 802.11-09/0574r0, IEEE P802.11 Wireless LANs, 2009.

[6] G. Breit and et al. Multi-user AoD diversity measurements. Technical Report Doc.: IEEE 802.11-09/0699r0, IEEE P802.11 Wireless LANs, 2009.

[7] B-J. Kwak and et al. Channel measurements in corridors for TGac. Technical Report Doc.: IEEE 802.11-09/0542r0, IEEE P802.11 Wireless LANs, 2009.

[8] B-J. Kwak and et al. Measured channel capacity and AoD estimation for Multi-user MIMO scenarios. Technical Report Doc.: IEEE 802.11-09/0543r0, IEEE P802.11 Wireless LANs, 2009.

[9] G. J. Foschini and M. J. Gans. On limits of wireless communications in a fading environment when using multiple antennas. *Wireless Personal Communications*, 6:311–335, 1998.

[10] T. K. Sarkar, Z. Ji, K. Kim, A. Medouri, and M. Salazar-Palma. A survey of various propagation models for mobile communication. *Antennas and Propagation Magazine, IEEE*, 45(3):51–82, June 2003.

[11] E. Perahia and M. X. Gong. Gigabit wireless LANs: an overview of IEEE 802.11ac and 802.11ad. *Mobile Computing and Communications Review*, 15(3):23–33, 2011.

[12] Institute of Electrical, Electronics Engineers, IEEE Computer Society. LAN/MAN Standards Committee, IEEE Standards Association, and IEEE Standards Board. *IEEE Standard for Information Technology - Telecommunications and Information Exchange Between Systems - Local and Metropolitan Area Networks - Specific Requirements: Part 11: Wireless LAN medium access control (MAC) and physical layer (PHY) specifications. Amendment 3: Specification for operation in additional regulatory domains*. IEEE (std.). IEEE, 2001.

[13] R. Van Nee, V.K. Jones, G. Awater, A. Van Zelst, J. Gardner, and G. Steele. The 802.11n MIMO-OFDM standard for wireless LAN and beyond. *Wireless Personal Communications*, 37(3-4):445–453, 2006.

[14] Quantenna announces world's first 802.11ac 10g wave 3 Wi-Fi product line. Press Release 09-08-15, September 2015. `http://www.quantenna.com/pressrelease-09_08_15.html`.

[15] M. Heusse, F. Rousseau, G. Berger-Sabbatel, and A. Duda. Performance anomaly of 802.11b. In *22nd Annual Joint Conference of the IEEE Computer and Communications, IEEE Societies (INFOCOM)*, pages 836–843, March 2003.

[16] G. Redieteab. *Cross-layer optimization for next generation Wi-Fi*. PhD thesis, INSA de Rennes, Rennes, France, 2012.

[17] H. Sizun. *La propagation des ondes radioelectriques*. Collection technique et scientifique des telecommunications. Springer France, 2002.

[18] T. Zhijun, Y. Liyuan, Y. Juan, and H. Ping. The impact of multi-path angular spread of MIMO system capacity. In *Proceedings of 14th Youth Conference on Communication*, 2009.

[19] L. Schumacher, K.I. Pedersen, and P.E. Mogensen. From antenna spacings to theoretical capacities - guidelines for simulating MIMO systems. In *The 13th IEEE International Symposium on Personal, Indoor and Mobile Radio Communications*, volume 2, pages 587–592, Sept 2002.

[20] V. Erceg and et al. Tgn channel models. Technical Report Doc.: IEEE 802.11-03/940r4, IEEE P802.11 Wireless LANs, 2004.

[21] G. Breit and et al. TGac channel model addendum. Technical Report Doc.: IEEE 802.11-09/0308r12, IEEE P802.11 Wireless LANs, 2010.

[22] H. P. Bui, Y. Ogawa, T. Nishimura, and T. Ohgane. Performance evaluation of a multi-user MIMO system with prediction of time-varying indoor channels. *Antennas and Propagation, IEEE Transactions on*, 61(1):371–379, Jan 2013.

[23] S.P.T. Kumar, B. Farhang-Boroujeny, S. Uysal, and C.S. Ng. Microwave indoor radio propagation measurements and modeling at 5 GHz for future wireless LAN systems. In *Asia Pacific Microwave Conference*, volume 3, pages 606–609, 1999.

[24] J. Lee and N. Jindal. Dirty paper coding vs. linear precoding for MIMO broadcast channels. In *Asilomar Conference on Signals Systems and Computers*, pages 779–783, Oct 2006.

[25] Z. Pan, K.-K. Wong, and T.-S. Ng. Generalized multiuser orthogonal space-division multiplexing. *Wireless Communications, IEEE Transactions on*, 3(6):1969–1973, Nov 2004.

[26] L. Garcia-Garcia, B. Lindmark, N. Jalden, and L. de Haro. Multi-user MIMO capacity from measurements in indoor environment with in- and outdoor base stations. In *The Second European Conference on Antennas and Propagation (EUCAP)*, pages 1–7, Nov 2007.

[27] C.B. Peel, B.M. Hochwald, and A.L. Swindlehurst. A vector-perturbation technique for near-capacity multiantenna multiuser communication-part I: channel inversion and regularization. *Communications, IEEE Transactions on*, 53(1):195–202, Jan 2005.

[28] C.B. Peel, Q.H. Spencer, A.L. Swindlehurst, M. Haardt, and B.M. Hochwald. *Space-Time Processing for MIMO Communications (chapter:Linear and Dirty-Paper Techniques for the Multi-User MIMO Downlink).* Wiley, 2005.

[29] I. E. Telatar. Capacity of multi-antenna gaussian channels. *European Transactions on Telecommunications*, 10:585–595, 1999.

[30] F. Kaltenberger, D. Gesbert, R. Knopp, and M. Kountouris. Correlation and capacity of measured multi-user MIMO channels. In *IEEE 19th International Symposium on Personal Indoor and Mobile Radio Communications (PIMRC)*, pages 1–5, Sept 2008.

[31] M. Kamal and K. Iqubal shahi. Multiuser MIMO downlink system capacity analysis in wireless communication for time varying channel. *International Journal of Scientific and Engineering Research*, 6:2229–5518, 2015.

[32] F. Kaltenberger, M. Kountouris, L. Cardoso, R. Knopp, and D. Gesbert. Capacity of linear multi-user MIMO precoding schemes with measured channel data. In *IEEE 9th Workshop on Signal Processing Advances in Wireless Communications (SPAWC)*, pages 580–584, July 2008.

[33] Q.H. Spencer, A.L. Swindlehurst, and M. Haardt. Zero-forcing methods for downlink spatial multiplexing in multiuser MIMO channels. *Signal Processing, IEEE Transactions on*, 52(2):461–471, Feb. 2004.

[34] L.U. Choi and R.D. Murch. A transmit preprocessing technique for multiuser MIMO systems using a decomposition approach. *Wireless Communications, IEEE Transactions on*, 3(1):20–24, Jan. 2004.

[35] J. Lee and N. Jindal. High SNR analysis for MIMO broadcast channels: Dirty paper coding versus linear precoding. *Information Theory, IEEE Transactions on*, 53(12):4787–4792, Dec 2007.

[36] M. Morales Cespedes, A. Garcia Armada, and J. Gutierrez Teran. Achievable throughput with block diagonalization on OFDM indoor demonstrator. In *Proceedings of the 21st European Signal Processing Conference (EUSIPCO)*, pages 1–5, Sept 2013.

[37] D. Nojima, L. Lanante, Y. Nagao, M. Kurosaki, and H. Ochi. Performance evaluation for multi-user MIMO IEEE 802.11ac wireless LAN system. In *14th International Conference on Advanced Communication Technology (ICACT)*, pages 804–808, Feb 2012.

[38] N. Ravindran and N. Jindal. Limited feedback-based block diagonalization for the MIMO broadcast channel. *Selected Areas in Communications, IEEE Journal on*, 26(8):1473–1482, October 2008.

[39] K. Yamaguchi, T. Nagahashi, T. Akiyama, H. Matsue, K. Uekado, T. Namera, H. Fukui, and S. Nanamatsu. Transmission performance evaluation for downlink MU-MIMO system: Computer simulation with block diagonalization algorithm and field experiments based on mobile WiMAX system. In *International Conference on Information Networking (ICOIN)*, pages 242–247, Jan 2015.

[40] V. Stankovic and M. Haardt. Multi-user MIMO downlink precoding for users with multiple antennas. In *Proceedings of 12th Wireless World Research Forum (WWRF)*, Nov. 2004.

[41] V. Stankovic and M. Haardt. Generalized design of Multi-User MIMO precoding matrices. *Wireless Communications, IEEE Transactions on*, 7(3):953–961, March 2008.

[42] F. Boccardi and H. Huang. A near-optimum technique using linear precoding for the MIMO broadcast channel. In *IEEE International Conference on Acoustics, Speech and Signal Processing (ICASSP)*, volume 3, pages 17–20, April 2007.

[43] M. H. M. Costa. Writing on dirty paper (corresp.). *Information Theory, IEEE Transactions on*, 29(3):439–441, May 1983.

[44] A. Bouhlel, V. Guillet, G. El Zein, and G. Zaharia. Transmit beamforming analysis for mimo systems in indoor residential environment based on 3d ray tracing. *Wireless Personal Communications*, 82(1):509–531, 2015.

[45] F. Kaltenberger, L. Cardoso, M. Kountouris, R. Knopp, and D. Gesbert. Real-time multi-user MIMO channel sounding and capacity evaluations. In *4th Management comitee meeting, COST 2100*, 2008.

[46] F. Kaltenberger, L. Bernado, and T. Zemen. On the characterization of MU-MIMO channels. In *International ITG Workshop on Smart Antennas (WSA)*, 2009.

[47] K. Nishimori, R. Kudo, N. Honma, Y. Takatori, and M. Mizoguchi. 16x16 multiuser mimo testbed employing simple adaptive modulation scheme. In *IEEE 69th Vehicular Technology Conference (VTC Spring 2009)*, pages 1–5, April 2009.

[48] Y. Kakishima, T. Kawamura, Y. Kishiyama, H. Taoka, and H. Andoh. Indoor experiments on 4-by-2 multi-user MIMO employing various transmitter antenna arrangements in LTE-advanced downlink. In *IEEE Vehicular Technology Conference (VTC Fall)*, pages 1–5, Sept 2012.

[49] Y. Ogawa, H. P. Bui, T. Nishimura, and T. Ohgane. An overview of actual SU- and MU-MIMO performances in a measured indoor channel. In *International Symposium on Antennas and Propagation (ISAP)*, pages 1–4, 2010.

[50] S. Loyka and G. Levin. On physically-based normalization of MIMO channel matrices. *Wireless Communications, IEEE Transactions on*, 8(3):1107–1112, March 2009.

[51] N. Jindal and A. Goldsmith. Dirty-paper coding versus TDMA for MIMO broadcast channels. *Information Theory, IEEE Transactions on*, 51(5):1783–1794, May 2005.

[52] J. Saavedra. *Multidiffusion et diffusion dans les systemes OFDM sans fil*. PhD thesis, Univ. Paris-Sud, Paris, France, 2012.

[53] S. Krusevac, P. B. Rapajic, and R. A. Kenneddy. Mutual coupling effect on thermal noise in multi-element antenna systems. *Progress In Electromagnetics Research*, 59:325–333, 2006.

[54] H.P. Bui, Y. Ogawa, T. Nishimura, and T. Ohgane. Measurement-based evaluation of a multiuser MIMO system in an indoor time-varying environment. In *Vehicular Technology Conference (VTC Fall)*, pages 1–5, Sept 2010.

[55] D.P. Palomar and J.R. Fonollosa. Practical algorithms for a family of waterfilling solutions. *Signal Processing, IEEE Transactions on*, 53(2):686–695, Feb 2005.

[56] F. Rusek, O. Edfors, and F. Tufvesson. Indoor multi-user MIMO: Measured user orthogonality and its impact on the choice of coding. In *6th European Conference on Antennas and Propagation (EUCAP)*, pages 2289–2293, March 2012.

[57] M. Herdin, N. Czink, H. Ozcelik, and E. Bonek. Correlation matrix distance, a meaningful measure for evaluation of non-stationary mimo channels. In *IEEE 61st Vehicular Technology Conference (VTC 2005 Spring)*, volume 1, pages 136–140, May 2005.

[58] N. Czink, B. Bandemer, G. Vazquez-vilar, L. Jalloul, and A. Paulraj. Can multi-user mimo measurements be done using a single channel sounder? 2008.

[59] S. Zukang, C. Runhua, J.G. Andrews, R.W. Heath, and B.L. Evans. Sum capacity of multiuser mimo broadcast channels with block diagonalization. *Wireless Communications, IEEE Transactions on*, 6(6):2040–2045, June 2007.

[60] Q.H. Spencer and A.L. Swindlehurst. Channel allocation in multi-user MIMO wireless communications systems. In *IEEE International Conference on Communications*, volume 5, pages 3035–3039, June 2004.

[61] L. Zhao, Y. Wang, and P. Charge. Efficient power allocation strategy in multiuser MIMO broadcast channels. In *IEEE 24th International Symposium on Personal Indoor and Mobile Radio Communications (PIMRC)*, pages 2591–2595, Sept 2013.

[62] A.M. Kuzminskiy. Downlink beamforming under EIRP constraint in WLAN OFDM systems. In *14th European Signal Processing Conference*, pages 1–5, Sept 2006.

[63] S. Grant, M.; Boyd. Matlab software for disciplined convex programming. March 2014.

[64] K. Issiali, V. Guillet, G. El Zein, and G. Zaharia. Impact of antennas and correlated propagation channel on BD capacity gain for 802.11ac multi-user MIMO in home networks. In *The International Conference on WIreless Technologies embedded and intelligent Systems (WITS)*, April 2015.

[65] K. Issiali, V. Guillet, G. El Zein, and G. Zaharia. Impact of EIRP Constraint on MU-MIMO 802.11ac Capacity Gain in Home Networks. In *Mediterranean Conference On Information and Communication Technologies (MedICT)*, pages 1–10, May 2015.

[66] K. Issiali, V. Guillet, G. El Zein, and G. Zaharia. IEEE 802.11ac multi-user MIMO capacity and impact of antenna array geometry based on indoor measurements. In *IEEE International Symposium on Personal, Indoor and Mobile Radio Communications (PIMRC)*, pages 1–5, Aug 2015.

[67] M. Fushiki, Y. Hatakawa, and S. Konishi. Experimental evaluations of multiuser MIMO with two-dimensional antenna configuration. In *Wireless Communications and Mobile Computing Conference (IWCMC)*, pages 195–200, Aug. 2014.

[68] J. Zheng, X. Gao, Z. Zhang, and Z. Feng. Performance examinations of multi-user MIMO systems with a compact antenna cube. In *IEEE International Symposium on Antennas and Propagation (APSURSI)*, pages 55–58, July 2011.

[69] J.T.E. McDonnell, T.P. Spiller, and T.A. Wilkinson. RMS delay spread in indoor LOS environments at 5.2 GHz. *Electronics Letters*, 34(11):1149–1150, May 1998.

[70] H. Ozcelik, N. Czink, and E. Bonek. What makes a good mimo channel model? In *IEEE 61st Vehicular Technology Conference (VTC 2005 Spring)*, volume 1, pages 156–160, May 2005.

[71] H.T. Nguyen, J.B. Andersen, and G.F. Pedersen. On the performance of link adaptation techniques in MIMO systems. *Wireless Personal Communications*, 42(4):543–561, 2007.

[72] V. Desai, J.F. Kepler, and F.W. Vook. Field data showing the downlink adaptive beamforming gains in an experimental IEEE 802.16e-2005 OFDMA system. In *IEEE Radio and Wireless Symposium*, pages 619–622, Jan 2008.

[73] C. Hermosilla, R.A. Valenzuela, L. Ahumada, and R. Feick. Empirical comparison of MIMO and beamforming schemes for outdoor-indoor scenarios. *Wireless Communications, IEEE Transactions on*, 8(3):1139–1143, March 2009.

[74] G. K. Tran, N. D. Dao, K. Sakaguchi, K. Araki, H. Iwai, T. Sakata, and K. Ogawa. Performance analysis of MIMO-OFDM systems using indoor wideband mimo channel measurement data. In *IEEE 63rd Vehicular Technology Conference (VTC Spring)*, volume 6, pages 2868–2872, May 2006.

[75] H. Nishimoto, Y. Ogawa, T. Nishimura, and T. Ohgane. Measurement-based performance evaluation of MIMO spatial multiplexing in a multipath-rich indoor environment. *Antennas and Propagation, IEEE Transactions on*, 55(12):3677–3689, Dec 2007.

[76] C. Hermosilla, R.A. Valenzuela, L. Ahumada, and R. Feick. Empirical comparison of MIMO and beamforming schemes. In *IEEE International Conference on Communications (ICC)*, pages 4226–4229, May 2008.

[77] B. Friedlander and S. Scherzer. Beamforming versus transmit diversity in the downlink of a cellular communications system. *Vehicular Technology, IEEE Transactions on*, 53(4):1023–1034, July 2004.

[78] H. Busche, A. Vanaev, and H. Rohling. SVD-based MIMO precoding and equalization schemes for realistic channel knowledge: Design criteria and performance evaluation. *Wireless Personal Communications*, 48(3):347–359, 2009.

[79] G. Lebrun, T. Ying, and M. Faulkner. MIMO transmission over a time-varying channel using svd. In *IEEE Global Telecommunications Conference (GLOBECOM)*, volume 1, pages 414–418, Nov 2002.

[80] G. Morozov, A. Davydov, and A. Papathanassiou. A novel combined CSI feedback mechanism to support multi-user MIMO beamforming schemes in TDD-OFDMA systems. In *International Congress on Ultra Modern Telecommunications and Control Systems and Workshops (ICUMT)*, pages 896–900, 2010.

[81] X. Sun, Q. Wang, L.J. Cimini, L.J. Greenstein, and D.S. Chan. ICI/ISI-aware beamforming for MIMO-OFDM wireless systems. *Wireless Communications, IEEE Transactions on*, 11(1):378–385, January 2012.

[82] S. Quadri and R.J. Haines. Industrial prototyping: A common architecture and case study of IEEE 802.11n transmit beamforming. In *IEEE 69th Vehicular Technology Conference (VTC Spring)*, pages 1–5, April 2009.

[83] J.B. Andersen. Array gain and capacity for known random channels with multiple element arrays at both ends. *Selected Areas in Communications, IEEE Journal on*, 18(11):2172–2178, Nov 2000.

[84] E. Sengul, E. Akay, and E. Ayanoglu. Diversity analysis of single and multiple beamforming. *Communications, IEEE Transactions on*, 54(6):990–993, June 2006.

[85] L. Schumacher and B. Dijkstra. Description of a Matlab implementation of the indoor MIMO WLAN channel model. Technical Report Implementation note version 3.1, IEEE 802.11 TGn Channel Model Special Committee, 2004.

[86] N. Jindal, W. Rhee, S. Vishwanath, S.A. Jafar, and A. Goldsmith. Sum power iterative water-filling for multi-antenna gaussian broadcast channels. *Information Theory, IEEE Transactions on*, 51(4):1570–1580, April 2005.

[87] F. Kaltenberger, M. Kountouris, D. Gesbert, and R. Knopp. On the trade-off between feedback and capacity in measured MU-MIMO channels. *Wireless Communications, IEEE Transactions on*, 8(9):4866–4875, September 2009.

[88] IEEE standard for information technology – telecommunications and information exchange between systems local and metropolitan area networks – specific requirements part 11: Wireless LAN medium access control (MAC) and physical layer (PHY) specifications. *IEEE Std 802.11-2012 (Revision of IEEE Std 802.11-2007)*, pages 1–2793, March 2012.

INSA de RENNES
Service des Formations

AVIS DU JURY SUR LA REPRODUCTION DE LA THESE SOUTENUE

Titre de la thèse:
Prise en compte des antennes adaptatives et techniques MIMO multiutilisateurs pour l'ingénierie et les outils d'ingénierie radio indoor

Nom Prénom de l'auteur : ISSIALI KHOULOUD

Membres du jury :
- Monsieur DIOURIS Jean-François
- Madame BAUDOIN Geneviève
- Madame AMIS CAVALEC Karine
- Monsieur LOUZIR Ali
- Monsieur GUILLET Valéry
- Monsieur EL ZEIN Ghais
- Monsieur ZAHARIA Gheorghe
- Monsieur SIBILLE Alain

Président du jury : Geneviève BAUDOIN

Date de la soutenance : 08 Décembre 2015

Reproduction de la these soutenue

Thèse pouvant être reproduite en l'état
~~Thèse pouvant être reproduite après corrections suggérées~~

Fait à Rennes, le 08 Décembre 2015

Signature du président de jury

G. Baudoin

Le Directeur,

M'hamed DRISSI

INSTITUT NATIONAL des SCIENCES APPLIQUÉES - RENNES -

Résumé

La facilité de déploiement et la flexibilité des technologies sans fil ont permis une évolution considérable des normes IEEE 802.11. L'arrivée de la fibre optique à la maison a également motivé des études de recherche pour accroître les débits et la capacité. Dans ce contexte, la dernière norme IEEE 802.11ac ratifiée en 2014 a normalisé de nouvelles technologies pour atteindre des débits maximaux au-dessus de 1 Gbit/s. En particulier, 802.11ac propose le Multiple Input Multiple Output Multi-Utilisateurs (MIMO-MU) et le Transmit Beamforming (TxBF). Ces technologies d'antennes intelligentes supposent un diagramme d'antenne d'émission qui dépend de la position des utilisateurs et des caractéristiques du canal de propagation multi-trajets correspondant. Cependant, les outils d'ingénierie et de planification radio actuels simulent une carte de couverture fixe et indépendante de tout traitement d'antennes adaptatives côté émission.

Cette thèse étudie l'impact de ces techniques MIMO-MU et TxBF et propose des solutions adaptées pour l'ingénierie radio et l'optimisation du système ainsi que pour les outils de planification radio. En effet, la première partie de cette thèse consiste à affiner les gains de capacité en identifiant les configurations et les paramètres système optimaux. La deuxième partie aborde les gains de beamforming en termes du gain sur le rapport signal à bruit (SNR) et sur la réduction du niveau d'interférence pour avoir une modélisation réaliste de la couverture radio.

Par conséquent, nous avons tout d'abord analysé le gain de capacité MIMO-MU par rapport au MIMO Single User (MIMO-SU) en se basant sur les modèles de canaux standardisés pour le contexte MIMO-MU corrélés 802.11ac. En analysant les résultats, nous avons proposé des optimisations du système pour maximiser les gains de capacité MIMO-MU dans un environnement résidentiel, principalement liées à la configuration du système, telles que le nombre d'antennes d'émission, l'espacement d'antennes, un compromis entre le nombre d'antennes et le nombre de flux spatiaux, la géométrie du réseau d'antennes... Un coefficient de corrélation entre canaux a été mis en évidence pour expliquer les gains obtenus. En outre, nous avons formulé le problème d'optimisation convexe de maximisation de capacité dans le cadre d'un système MIMO-MU équipé de plusieurs antennes de réception tout en tenant compte de la contrainte de la puissance isotrope rayonnée équivalente (PIRE) pour un réseau local sans fil (WLAN) en Europe.

Nous avons ensuite mené une campagne de mesures de canaux de propagation avec deux utilisateurs dans un environnement résidentiel pour confirmer et compléter les résultats obtenus avec des canaux simulés. Nous avons été en mesure d'étendre cette étude à d'autres paramètres pouvant potentiellement influencer le gain de capacité MIMO-MU par rapport au MIMO-SU, tels que l'atténuation de propagation et la géométrie des réseaux d'antennes.

Enfin, à partir de ces mesures nous avons évalué les performances de la technique du TxBF en analysant le gain sur le SNR ainsi que la réduction d'interférence. Cette partie propose finalement une modélisation statistique pour intégrer la prise en compte des gains de beamforming dans la simulation des couvertures radio avec un outil d'ingénierie.

Abstract

The deployment facility and flexibility of wireless technologies have allowed considerable evolution of IEEE 802.11 standards. The arrival of the optical fiber to the home has further motivated the research studies to increase data rates and capacity. In this context, the latest IEEE 802.11ac standard ratified in 2014 proposes new technologies to achieve maximum data rates above 1 Gbit/s. In particular, 802.11ac includes the Multi-User Multiple Input Multiple Output (MU-MIMO) and Transmit Beamforming (TxBF). These smart antenna technologies assume a variable transmit antenna pattern in function of the users' position and the corresponding multipath propagation channel characteristics. However, the actual radio planning tools give a fixed coverage map independent of any adaptive or smart antenna processing.

This thesis studies the impact of the MU-MIMO and TxBF techniques on radio engineering, system optimization as well as radio planning tools. Indeed, the first part of this thesis deals with refining the sum rate capacity gains by identifying interesting system configurations and optimal system parameters. The second part addresses the beamforming gains in terms of the Signal-to-Noise Ratio (SNR) gain and interference level to have realistic radio coverage modeling.

Hence, we have firstly analyzed the MU-MIMO to Single User MIMO (SU-MIMO) sum rate capacity gain based on the 802.11ac correlated MU-MIMO channel models. By analyzing the results, we have proposed system recommendations to optimize the MU-MIMO in a residential environment, mainly related to system configuration such as the number of transmitting antennas (antenna spacing, tradeoff between antenna number and number of spatial streams, antenna arrangement...). A correlation coefficient between channels has been highlighted to explain the obtained gains. Moreover, we have formulated the convex optimization problem of maximizing the capacity in a MU-MIMO context with multiple receiving antennas taking into account the Equivalent Isotropically Radiated Power (EIRP) constraint for Wireless Local Area Network (WLAN) in Europe.

Secondly, we have conducted a 2-user Multiple-Input Multiple-Output (MIMO) propagation channel measurement campaign in a residential environment to confirm the obtained radio engineering and system optimization recommendations. We have been able to extend this study to other potential parameters to have influence on MU-MIMO to SU-MIMO capacity gain such as path loss and antenna array geometries.

Finally, we have evaluated the performance of TxBF by analyzing the Signal-to-Noise Ratio (SNR) gain as well as the interference reduction. This part identifies the system parameters which have the biggest influence on the realistic radio coverage simulation. It proposes a statistical modeling to predict the beamforming gains achieved by the antenna processing.

N° d'ordre : **15ISAR 32 / D15 - 32**

Institut National des Sciences Appliquées de Rennes
20, Avenue des Buttes de Coëmes • CS 70839 • F-35708 Rennes Cedex
Tel : 02 23 23 82 00 - Fax : 02 23 23 83 96